Micromechanics of gel rupture

Akash Singh

To cite this version:

Akash Singh. Micromechanics of gel rupture. Physics [physics]. Université de Lyon, 2021. English. NNT : 2021LYSE1294 . tel-03729090

HAL Id: tel-03729090
https://theses.hal.science/tel-03729090

Submitted on 20 Jul 2022

N° d'ordre NNT: XXX

THÈSE DE DOCTORAT DE L'UNIVERSITÉ DE LYON

Opérée au sein de

l'Université Claude Bernard Lyon 1

Ecole Doctorale N° 52
Physique et Astrophysique de Lyon

Spécialité de doctorat : Physique

Soutenue publiquement le 08/12/2021, par :

Akash SINGH

Micromécanique de la Rupture des Gels

Devant le jury composé de :

Roberto CERBINO Professeur, Université de Vienne	**Rapporteur**
Jean COLOMBANI Professeur, Université Lyon 1	**Examinateur**
Emanuela DEL GADO Professeure, Université de Georgetown, Washington	**Rapporteure**
Marie-Hélène FAMELART Chargée de Recherche,INRAE Rennes	**Examinatrice**
Loic VANEL Professeur, Université Lyon 1	**Directeur de thèse**
Mathieu LEOCMACH Chargé de Recherche, CNRS	**Co-Directeur de thèse**

N° d'ordre NNT: XXX

THESIS SUBMITTED TO THE UNIVERSITY OF LYON

Operated within

Claude Bernard University Lyon 1

Doctoral school N° 52
Physics and Astrophysics

Doctoral specialty : Physics

Publicly defended on 08/12/2021, by :

Akash Singh

Micromechanics of Gel Rupture

The jury members :

Roberto CERBINO Professor, University of Vienna	**Reporter**
Jean COLOMBANI Professor, Université Lyon 1	**Examinator**
Emanuela DEL GADO Professor, University of Georgetown, Washington	**Reporter**
Marie-Hélène FAMELART Chargée de Recherche,INRAE Rennes	**Examinator**
Loic VANEL Professor, Université Lyon 1	**PhD supervisor**
Mathieu LEOCMACH Chargé de Recherche, CNRS	**PhD co-Supervisor**

Contents

Abstract

> panta rhei
> Everything flows
>
> Heraclitus

Fracture is an important phenomena in our day to day life, from the ease of cracking open an egg after inducing a small flaw on the surface, to the mind nerving slow breaking of the charger cable. Exactly a century ago, A. A. Griffith expressed a criteria that relates the size of the critical defect in a brittle material to the critical stress required for fracture. The presence of microscopic flaws explains why the stress required to break an 'intact' material is orders of magnitude lower than the theoretical stress predicted from breaking the atomic bonds. Despite significant progress in the field of fracture mechanics since Griffith, we still do not have a complete understanding of the why, when or where the failure will happen. This is because failure is a multi-scale phenomena: An example of this is the fracture of solid wood: from molecular to cellular scale to growth ring scale and finally the breaking of a branch. Understanding of the connection between these different scales is crucial to comprehend their complex, nonlinear and spatio-temporal response. Thus going down in scale to the precursor or the structural unit within the material where the failure originates can lead to development of reliable models for better engineering of these materials.

In crystalline systems, the structural precursor is a competition between motion of dislocation and grain boundary mediated plasticity. This model is not valid in amorphous systems. Furthermore, solids that have an heterogeneous structure bring yet another level of difficulty in pinpointing the precursor events. In my thesis, I studied the fracture of gels, solids that are made of two intertwined phases: a solid network and a liquid medium. In gels, the complex coupling of viscoelasticity and plasticity makes it difficult to understand the driving force behind fracture as most of the theoretical models are based on understanding of elasto-plastic systems. The importance of gels in our daily experience, from the 'mouth-feel' of yogurt to the usage of gel as biomimetic material, requires the advancement in understanding their fracture precursors.

In this work we try to find fracture precursors in gel by combining shear rheology to 3D confocal microscopic observation. This means we have to use a gel system which has microstructure large enough to be observable with optical resolution. Larger microstructure implies softer materials and thus low stresses that are difficult to apply reliably. Thus the first part of this thesis consists in developing a cantilever based setup for shear rheology of very soft solids under constant stress or strain. This setup has a sensitivity of 6 mPa in stress measurement and can reliably apply strain or stress control in both shear and normal directions. The gel system we work with is sodium caseinate, a protein gel with a microstructural length scale of order 10 µm. We describe the physical chemistry, mass transport and rheological characterization of our system to develop a fast in-situ gelation technique.

In the next part, we perform controlled strain and stress experiments with this system until failure. In the case of incremental control strain steps, direct microscopic visualization combined with 2D phase correlation describes the existence of a soft layer near the maximum shear zone to be the precursor to fracture. For the long duration creep experiment, the 3D stroboscopic view observes visuals of the strand breaking events which are spatially scattered. We develop analysis based on estimation of small displacement to detect these events to observe their spatio-temporal profile. We observe that strand breaking events occur way before the catastrophic failure, and we are able to detect their nucleation which leads to failure. The spatial correlation of the principle shear component leads us to discover the elastic coupling of eshelby nature i.e. the existence of a shear transformation zone as inclusion within a large elastic medium.

keywords: Gels, fracture, confocal microscopy, microstructure, precursor, rheology, soft matter, amorphous, image correlation.

Résumé

La physique de la fracture est omniprésente dans notre vie quotidienne, qu'il s'agisse de la facilité avec laquelle on peut ouvrir un œuf une fois fêlé ou de la lente agonie d'un câble de chargeur. Il y a exactement un siècle, A. A. Griffith a lié la taille du défaut critique dans un matériau fragile à la contrainte critique requise pour la rupture. La présence de défauts microscopiques explique pourquoi un matériau “intact" rompt à des contraintes inférieures de plusieurs ordres de grandeur à la contrainte prédite par la rupture des liaisons atomiques. Malgré les progrès réalisés dans le domaine de la mécanique de la rupture depuis Griffith, nous n'avons toujours pas une compréhension complète de pourquoi, quand et où la rupture se produira. C'est dû au caractère multi-échelle de la rupture. La fracture du bois massif en est un exemple : des molécules, aux cellules, à l'anneau de croissance jusqu'à la branche. Il est essentiel de comprendre la connexion entre ces différentes échelles pour appréhender leur réponse spatio-temporelle complexe et non linéaire. Ainsi, zoomer à l'échelle du précurseur ou de l'unité structurelle du matériau d'où provient la fracture conduit à des modèles fiables pour une meilleure ingénierie de chaque matériau.

Dans les cristaux, le précurseur structurel est une compétition entre mouvement des dislocations et plasticité dans les joints de grain. Ce modèle ne s'applique pas dans les systèmes amorphes. De plus, les solides structurellement hétérogène apportent encore un autre niveau de difficulté dans l'identification des précurseurs. Dans ma thèse, j'ai étudié la rupture des gels, qui sont des solides constitués de deux phases entrelacées : un réseau solide et un milieu liquide. Dans les gels, le couplage complexe de la viscoélasticité et de la plasticité rend difficile la compréhension des raisons de la rupture, car la plupart des modèles théoriques sont basés sur la compréhension de systèmes élasto-plastiques. L'importance des gels, de la consistance du yaourt à l'utilisation des gels comme matériau biomimétique, nécessite de mieux comprendre leurs précurseurs de fracture.

Dans ce travail, nous essayons de trouver les précurseurs de fracture dans les gels en combinant rhéologie et observation 3D par microscopie confocale. Nous devons donc utiliser un gel de microstructure plus grande que la résolution optique, ce qui implique un matériau très mou et donc des contraintes faibles qui sont difficiles à appliquer de manière contrôlée. Ainsi, nous avons développé un dispositif basé sur un cantilever permettant d'étudier la réponse rhéologique de solides très mous sous contrainte ou déformation constante. Sa sensibilité de 6 mPa en contrainte permet de contrôler précisément la contrainte ou la déformation dans les directions normale et de cisaillement. Le système de gel avec lequel nous travaillons est le caséinate de sodium, un gel de protéines dont la microstructure est de l'ordre de 10 µm. Nous décrivons la physico-chimie, le transport de masse et la rhéologie de notre système afin de développer une technique rapide de gélification in-situ.

Ensuite, nous réalisons des expériences de déformation et de contrainte contrôlées avec ce système jusqu'à la rupture. Dans le cas de marches de déformation incrémentale, la visualisation microscopique directe combinée à la corrélation d'images 2D détecte l'existence d'une couche de cisaillement maximale comme étant le précurseur de la rupture. En fluage, la vue stroboscopique 3D permet d'observer des ruptures de brins éparses. Nous développons une analyse basée sur l'estimation des petits déplacements pour détecter ces événements et observer leur profil spatio-temporel. Nous observons que les ruptures de brin se produisent bien avant la rupture catastrophique, et nous sommes capables de détecter leur nucléation qui conduit à la rupture. La composante principale du cisaillement présente des corrélations de type Eshelby, c'est-à-dire un couplage élastique.

Mots clés : Gels, fracture, microscopie confocale, microstructure, précurseur, rhéologie, matière molle, amorphe, corrélation d'images.

Acknowledgement

This three-year journey of becoming a researcher through doctoral studies has been a really enriching experience for me in terms of not just the research competence but also personal development. Definitely, this would have been impossible without the help and contribution from a number of people.

First and foremost, I would like to express my sincerest gratitude to my supervisor Dr. Mathieu Leocmach, and Prof. Loic Vanel for molding me into an independent researcher from the crude state I came in after my Master's. Dr. Mathieu Leocmach was the principal director of the project with a clear vision of what we wanted to achieve. He not only helped in the development of my experimental and computational skills but also provided moral support and motivation especially when the going got tough: in the time when our setup ICAMM went all ICANT, or the long discussions during the long isolation period of the pandemic. I would like to thank Prof. Loic Vanel for providing the fundamental insight from fracture mechanics perspectives to this project as well as helping move forward the project, especially when we were blocked and needed redirection. I wish I can become a researcher with the kind of rigorous and patient guidance both of you provided me during the thesis.

I would also extend my thanks to Gilles Simon, who fabricated and helped in designing the ICAMM setup. He was always ingenious and without him, the realization of this setup would not have been possible. I would also thank Prof. Catherine Barentin, for her help with the rheometer characterization. She is such a wonderful teacher, and I really liked how she instigated to look at the rheometer measurement as a tool beyond characterizing just the mechanical properties. I would also thank Dr. Michio Tateno, who worked during an internship on this setup before me and passed on his wisdom during another short visit to Lyon. I am also thankful to Dr. Mehdi Bouzid and Dr. Alexandre Nicolas for providing their time to discuss certain observations in this project and providing their insight into the analysis.

I would like to acknowledge the effort of the referees, Prof. Emmanuela Del Gado and Prof. Roberto Cerbino for going through the arduous process of reading this thesis and am thankful to them for providing their valuable feedback. I will also extend my thanks to the rest of the jury members, Dr. Marie-Hélène Famelart and Prof. Jean Colombani for their insightful comments and discussion during the defense. The diverse background of the jury definately provided some good insights into this interdisciplinary work.

I would really like to thank the Liquid and Interface team and in extension, the biophysics team who were instrumental in not only proper conduction of the lab but also ensuring the team stays connected, and the exchanges continue smoothly even during the peak of the pandemic. My friends and colleagues, with who I can fill up an entire page, helped me in some way or another not just with the scientific discussion, but also integrate into the lab and in general the French society. I will always remember our good (sometimes hot) discussion on physics but also the time outside of work, sharing the diverse cultural aspect of coming together from different corners of the world. The same goes for all my flatmates and friends outside the lab, the time spend with you was always enriching, fun, and invaluable.

Finally, but never least, I would like to thank my family: My parents, my sister, and my brother-in-law for always supporting my dreams and reaching out to me throughout this journey. They were always encouraging about all my decisions and my parents should definitely be proud of nurturing two different kinds of doctors in a family which, in all our extended relationship, have seen none to date. Extending my thanks to Marine, who was my direct support during the quite grueling and tough last lap of this thesis. You provided a sense of comfort and calmness which was crucial to finish this thesis right.

Chapter 1

Introduction

> What do we mean by soft matter? Americans prefer to call it "complex fluids". This is a rather ugly name, which tends to discourage the young students
>
> Pierre-Gilles de Gennes

These lines from De Gennes's Noble lecture in 1991 [1] remind me of my undergraduate Chemical engineering days, when I was eager to pursue more courses in fluid mechanics and in contrast, ended up taking my first course in complex fluids. Gradually, the course translated from shear thinning of blood to talk about how mountains flow! The coining 'Soft Matter' for such materials in fact originated as a joke by M. Veyssié in the 1970s [2]. Getting away from the terminology soft matter (or complex fluids) are materials that deform easily compared to their hard solid counterpart (or defer from simple fluids in their flow properties). For some of them, called viscoelastic materials, their solid-like or liquid-like behavior is dependent on the time scale we look at. Soft matter, show this on an experimental time scale and hence, they are also called viscoelastic materials. This array of rich behavior stems from the role entropy plays in these systems due to the weak nature of interactions, and structural units much larger than the atomic scale. Thus, the structure of soft materials can relate to the wide range of macroscopic phenomena they display.

On the other hand, fracture is a phenomenon that we encounter in our daily life and are often eager to avoid. Studies on fracture mechanics predate the development of science in soft matter, dating back to the Renaissance period [3]. But its ubiquitous nature means that we have been dealing with it since prehistoric times when the genus homo began to fracture stones to make tools. However, preventing or controlling fractures are problems that are actively been pursued to date as scientists try to link the different scales of this multi-scale phenomena while trying to link the varying observations in different materials.

A younger me would have never imagined these two widely different issues can be coupled. But this is the essence of this thesis: to observe failure in a soft matter system akin to yogurt: casein gel. This system surprisingly shows characteristics of brittle fracture, similar to many hard solids and (harder) soft systems. Its large microstructure can help us understand the growth of fracture from its origin (precursor) state at structural scale, to the final catastrophic fracture we see at the macroscopic scale. In this chapter, I describe the basic linear description of the two sciences: fracture and viscoelasticity so that people familiar with one (or none) can appreciate the more involved development in the non-linear physics of the two. For fracture, I describe the theories and models of crack nucleation and propagation. On the soft matter side, I describe the recent developments in the non-linear rheology of the colloidal gel system, the class to which casein gel belongs. Finally, I describe the efforts to find fracture precursors in these systems from probing of microstructure, which remains a challenge we will try to address in this thesis.

1.1 Material Fracture

Material failure is generally thought of as an undesirable event and can put human life at risk, economic losses, and interfere with our life. However, in our day-to-day life, we encounter several events where the fracture is desirable. Breaking an egg is facilitated if we make a small notch at the surface. More sophisticated examples can be breaking of gelified wax causing clogging in oil pipelines [4] or the use of directed crack formation to form the desired pattern in nanofabrication [5]. Fractures not only can occur in the bulk of the material but also at the interface between two materials such as rupture of adhesion which we encounter from our usage of pressure-sensitive tape or the movement of lizards [6]. Fracture belongs to catastrophic phenomena like earthquakes or crashes of the stock market, that everyone would like to predict [7]. However, we are far from a universal model able to predict such sudden events. Similar reasoning can lead to or prevent failure: The fracture of the hull of the Boeing 737 plane happened due to cracks initiated near the rivet by corrosion and grew under pressure change imposed by flying and landing, while rivets were found to be responsible for the prevention of crack growth and failure in American cargo ships during World War 2 [8].

This unpredictability stems from two characteristic behaviors of fracture: delayed rupture and volume effect. Material can fracture immediately on application of an impulsive force, for example, the shattering of glass. But, many materials on application of a load will not break immediately but after a delay. This phenomenon is known as creep rupture for a constant load and fatigue rupture for an oscillatory one. Vicat studied the creep of iron wire under different loads, which break after 'some time' even when corrosion was prevented [9]. The 'some time' for Vicat's experiment meant three years! This delayed rupture is a system-dependent phenomena and is not only a characteristic of metals but brittle materials such as crystalline solids [10], composites such as wood [11] and fiber [12], very soft disordered solids as gels [13] and glass [14], as well as geological phenomena such as earthquakes and avalanches [15]. The reasoning for delayed failure is quite complicated and remains one of the core questions we address in this thesis with respect to gels.

Volume effect in fracture is linked to the argument presented by Griffith that real materials are inherently 'flawed'. Almost five centuries ago, Leonardo Da Vinci described in his notes [16] an experiment to test the strength of an iron wire by increasing the load until it fractures and observing the location of the fracture [3]. His observation was that on reducing the length (by half consecutively), the weight carried by the wire until fracture was increased. However, continuum mechanics shows that since the tensile stress in the material remains the same on keeping the same area, the strength of the material should not be affected by the length. The earlier assumption behind this observation was that Da Vinci might have meant a relatively 'increase in diameter' when he meant 'smaller length' [17]. However, later interpretations see Da Vinci's experiments as an early observation of the volume effect in fracture. Indeed, continuum mechanics treat the material as homogeneous while in the real world most of the materials are disordered, and hence, there is a distribution of strength in a material due to the local flaws. It has now been well established that the strength of a material is volume dependent and linked to the distribution of the weakest element as a function of sample volume [18]. Weibull established the proof based on the statistic of distribution of extreme values for many non-interacting cracks in a material [19]. Thus, the explanation for Da Vinci's observation can be the usage of a thin wire with pre-existing microcracks and voids linked to the forging techniques of the Renaissance period [20].

The presence of flaws means that fracture is a multi-scale phenomenon. One can look at several scales: For example fracture in wood can be observed at not only the macro-scale but also narrowed down to growth-ring scale, further by looking at crack advancement at cellular scale and finally at the complex molecular makeup of amorphous lignin and semi-crystalline cellulose [11]. This multi-scale nature of the failure is not only a material property but also observed in catastrophic natural phenomena such as avalanches, where failure has been studied from the size of the snow grains to the scale of a mountain slope [15]. The detection of entities responsible for the origin of fracture at a length scale similar to or slightly larger than the structural unit of the material is known as precursor detection and the entity is called a precursor [2]. Precursors cause damage accumulation and understanding how the material accumulates damage followed by nucleation and final crack propagation can be used to link the different scales of fracture and hence, improve their understanding. In atomic crystals, it has been long known that the precursor to fracture is the movement of dislocation [21]. However, dynamic monitoring of this motion is not possible due to the atomistic length-scale of these defects. In such a case colloids have been a revelation due to their ability to mimic atomistic structures but at micro-scale in a crystal, glass, and gel state. The dynamics of motion of dislocation has been studied in colloidal crystals [22] and has been found to be in competition with grain boundary mediated plasticity in crystals with smaller grain size [23] as the source of fracture. However, systems with large heterogeneity such as glasses and gels provide additional challenges: Their structure is quite heterogeneous and it is difficult to locate these inherent flaws under quiescent conditions. Besides, a continuous description of materials such as gel fails at a scale lower than the largest pore size of the network. Hence, a combination of micro-structural probing with simultaneous macroscopic deformation is important to understand the multi-scale nature of the failure in these materials.

Due to the application of material fracture in engineering since ancient times, macroscopic understanding has progressed more than understanding microscopic precursor formation. I explain the top-down approach through the most general theory of fracture growth known as the linear elastic fracture mechanics (LEFM) [24], and the elastic/viscoplastic model for time-dependent nucleation of the cracks [25]. Although vastly different from the gels we look at, due to the absence of viscoelasticity or large-scale plasticity, as well as simultaneous crack nucleation, it lays the essential foundation and provides us with relevant length and time scales important to understand growth and nucleation of fracture.

1.1.1 Basics of fracture mechanics

The fracture process can be broken down into three stages: damage accumulation due to precursors, nucleation of one or multiple cracks from the damage followed by uncontrolled crack growth. The nature of these three stages vary from material to material but can be broadly characterized in two kind of failure mode: ductile or fragile. Ductile fracture leads to plastic deformation in the vicinity of the crack. Generally, the process is slow as the material deforms to the applied force and resists the tendency to fracture. There will be an appearance of deformation at the macroscopic surface: when we crush a bottle of packaged water, the bottle does not break, but we see the signs of this deformation. Brittle fracture is characterized by very little plastic deformation near the crack that spreads rapidly as in the case of shattering of glass.

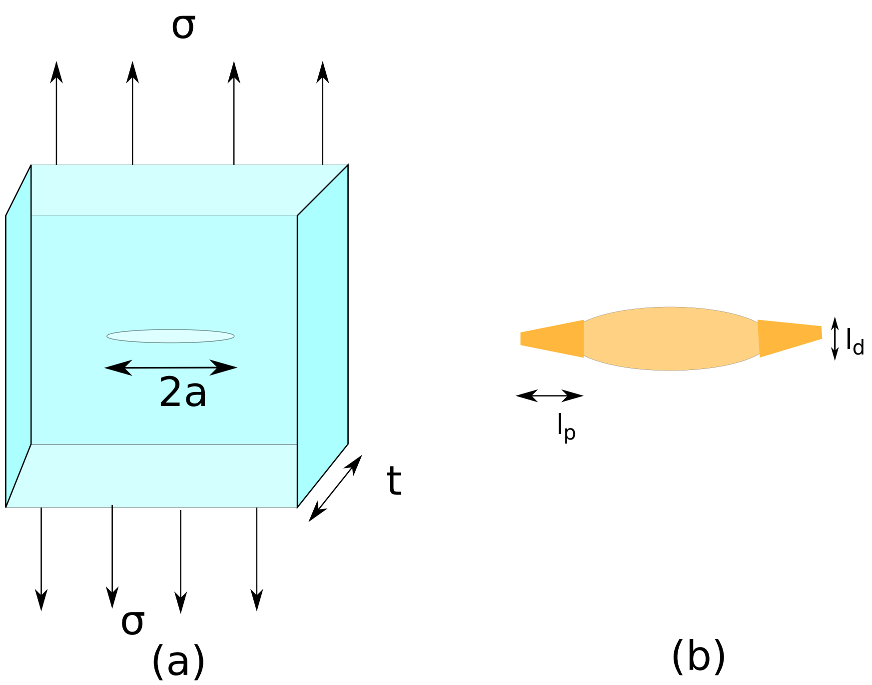

FIGURE 1.1: Schematic of (a) a thin elliptical crack of length $2a$ in an elastic solid under a stress σ and (b) The two relevant length scales: l_p is the plastic zone due to deformation at the crack tip and l_d is the crack opening displacement between the lips of the crack due to the plasticity.

Crack propagation

The first notion of crack propagation based on the atomic nature of matter was to think of crack propagation as breaking of atomic bonds. However, this model is quickly invalidated by experiments: materials are observed to break at stresses orders of magnitude lower than the atomic cohesion. Here is where the concept of stress concentration at the crack tip comes into the picture. Griffith proposed that materials are inherently flawed, i.e. there are defects that act as nucleation sites for fracture to grow [26]. The tip of these cracks has a high concentration of stress compared to the bulk material. This non-linear stress at the tip is hard to quantify. Griffith, instead of relying on atomic forces developed criteria based on thermodynamic energy balance [26]. As a crack propagates, two new surfaces are created which give rise to surface energy while elastic energy is lost due to the breaking of the material. For the case of a thin elliptical crack, as shown in Fig. 1.1a, above a certain crack length, the critical stress ($\sigma = \sigma_c$) defined from the equilibrium of the two energy is given by

$$\sigma_c = \sqrt{\frac{2E\Gamma}{\pi a}} \tag{1.1}$$

where E is the elastic modulus, Γ is the surface energy per unit area. This comes from an unstable equilibrium condition implying if the stress is larger than σ_c the material will undergo uncontrolled crack growth to fracture. For plastic materials, this can be modified by including a Γ_p which is the plastic work done per unit area for the crack to grow.

$$\sigma_c = \sqrt{\frac{2E(\Gamma + \Gamma_p)}{\pi a}} \tag{1.2}$$

The physical interpretation is that the plastic deformation at the tip reduces the stress concentration by increasing the curvature at the crack tip. These fundamental contributions are significant in the study of fracture and led to the development of linear elastic fracture mechanics (LEFM). The assumption of LEFM is that the material has inherent cracks of size smaller than the size of the material i.e. the bulk material behaves elastically everywhere except a very small region near the crack tip [24, 27]. Some important results from LEFM are that the stress field near the crack trip depends on the inverse of the square root of the radial distance and there are two important physical length scale l_p and l_d as seen in Fig.1.1b. In small scale yielding of the crack tip l_p ($l_p << a$), the stress is limited by the yield stress σ_y and the length scale of the plastic zone at crack propagation is given by

$$l_p \propto \frac{\Gamma E}{\sigma_y^2} \tag{1.3}$$

Due to the plasticity a relative displacement of the crack lip occurs whose length scale is given as

$$l_d \propto \frac{\Gamma}{\sigma_y} \tag{1.4}$$

This is known as the critical crack opening displacement [28]. This length scale can provide a broad idea of the applicability of LEFM to any material. For example silicate glass, which shows brittle fracture, with typical experimental value of E, σ_y and Γ has a $l_p \approx 7\,\text{nm}$ and $l_d \approx 1\,\text{nm}$. On the other hand, steel which displays relatively ductile fracture has $l_p \approx 8\,\text{mm}$ and $l_d \approx 40\,\mu\text{m}$ [27]. For the application of LEFM to steel, we will require a macroscopic volume of the material. The application of this model requires that the sample size is much larger than l_p and l_d. Also, if the length scale of the plastic zone is greater than the defect, it will blunt out the stress near the tip and the crack will not grow. Another factor limiting LEFM applicability is the difficulty to get the quantities like Γ, E, and Γ_p experimentally.

1.1.2 Nucleation of fracture

Fracture in the material can occur on the application of stress smaller than the σ_c and show a delay between stress application and fracture growth. As proposed by Griffith below the critical stress an energy barrier exists for the nucleation of the crack. The rupture is modeled to be thermally activated [25] and hence, the failure time takes the Arrhenius form $\tau = \tau_o \exp(\frac{E_A}{k_b T})$, where E_A is the activation energy barrier for the nucleation to happen. As stated above, in the case of a brittle fracture, the activation energy comes from the balance between elastic energy lost and interfacial energy gained, and thus behaves as $E_A \propto \sigma^{-2}$ for a 2D fracture. Pomeau et al. made an extension to 3D of this global energy balance (GEB) model [25] and obtained $E_A \propto \sigma^{-4}$ [29]. This approach assumes that the material behaves elastically until rupture (= brittle) and has been observed in hard systems such as fiberglass composites [30] and surprisingly soft systems such as polymer gels [31].

However, several materials show large plastic damage before failure and the rupture in these systems has been modeled as the consequence of viscoplastic creep [25] such that $E_a = E_o - \sigma V$, where E_o, V are parameter characteristic energy barrier and activation volume. This is known as the BBZ model and has been used to predict rupture in fiber bundle [32], glassy polymer [33], poly-crystalline metals and alloys [34]. The drawback with the model based on GEB or viscoelastic flow is that experimentally they are based on either following the growth of a single crack or application of in-homogeneous stress. In a heterogeneous system without any large flaws, fracture is a gradual process with multiple damage accumulation happening simultaneously. By contrast, amorphous systems such as composites and gels have large heterogeneity in their structure and can have local variations in stress concentration. Besides, the creep observed in some of these systems is related to linear viscoelasticity [13, 12].

Fiber bundle models are a tool to model how damage is accumulated in heterogeneous systems. The initial framework for the Fiber bundle by H. A. Daniels is purely statistical. In material science, it is modeled as stretching of parallel fibers under the application of stress or strain and some criteria for the breaking of the fiber and redistribution of the stress. This offers possibilities on the model assumptions based on the constitutive laws of the fibers, for example elastic [35], elasto-plastic [12], or viscoelastic [36, 37], distribution in strength of the fibers [35, 12], variation of the applied stress or strain [38], whether the load sharing is mean field [39, 12] or local [37]. However, the basis for these assumptions can lead to variation in response of the bundles, and in some cases, widely different assumptions lead to similar results as pointed out by Jagla et al. [37]. The broad panel of possibilities offered by fiber bundle models enables the description of the failure of heterogeneous systems well beyond the original bundle of fibers. Constitutive elements can be fuse in an electrical circuit, as well as microscopic regions in a composite, or strands in a gel network.

Thus, the bottom-up approach of understanding what are the structural origin of the fracture phenomena is important to understand how these local damages accumulate and interact before and during their nucleation. Ultimately, coupling of both macroscopic and microscopic measurement can provide simultaneous information, offering the possibility to compare with the model predictions. To understand the behavior of gels and in general soft materials under a force, it is necessary to define standard shear rheology and the linear response. I give here a general description of the linear behavior of viscoelastic material under small deformation and the experimental methods to probe the linear and non-linear behavior of gels.

1.2 Basics of macroscopic shear rheology

Rheology, as indicated from the Greek root, is defined as the study of the flow of matter. Initially used for studying the flow of fluid and deformation of solid, today it is used to describe the complex behavior of material due to a combination of viscosity, elasticity, and plasticity governed by the experimental time scale. Many materials in our daily life show a rich combination of these phenomena rather than just behaving as a pure Newtonian liquid or a pure elastic solid. Silly putty is a common example: It behaves like a solid when bounced off the wall but flows like a liquid when left long enough on the table. Its description as a solid or liquid depends on what time scale we are looking at! This is linked to the fact that structural rearrangement inside the material can take a finite time. The rearrangement time can be scaled in terms of a dimensionless Deborah number such that

$$N_D = \frac{\tau_{\text{mat}}}{\tau_{\text{expt}}} \tag{1.5}$$

where τ_{mat} is the relaxation time of the material and τ_{expt} is the experimental time scale. A pure viscous material will amount to $N_D = 0$ since the rearrangements are fast and all the deformation energy is converted to heat by the viscous dissipation,

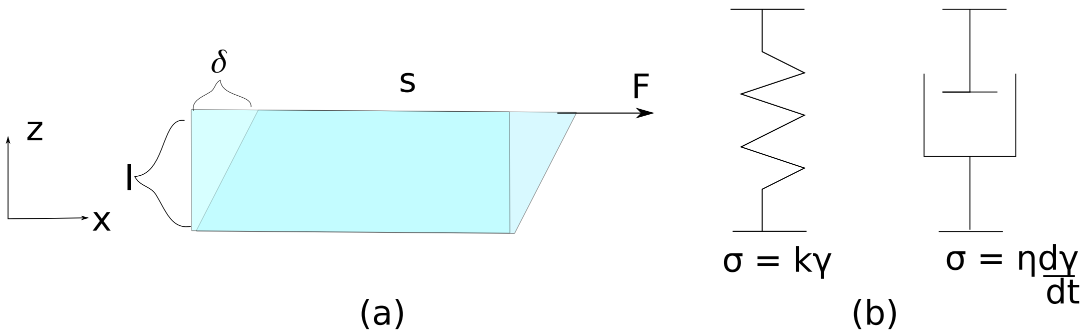

FIGURE 1.2: (a) Schematic representation of a cuboid (front view) before and after a deformation δ of the top surface due to a force F. The stress is defined as $\sigma = \frac{F}{s}$ where s is the cross-section area of the top surface. The shear strain deformation in such case is defined as $\gamma = \frac{\delta}{l}$ where l is the gap between the top and the stationary bottom surface. (b) The schematic modeling of a pure elastic solid as a spring and a liquid as dash-pot.

while for a pure elastic material it is equal to infinity and the energy is stored through the elastic stretching of the system. However, real materials exist between extremes and as we will show, do not exhibit a simple single relaxation time.

Shearing is the deformation of a material in which parallel plane in the material slide past each other similar to a deck of card. Shear is a widely studied method of deformation as most complex fluids are incompressible. Here I describe the tensorial description of shear and the experimentally used simple shear deformation which is a scaler quantity. This section is designed for someone looking for a general introduction to rheology. People who already know these basics can skip to the part. 1.2.4

1.2.1 Shear deformation

Stress is a 2^{nd} degree tensor define as the force per unit area over a continuum material such that

$$\sigma_{ij} = \frac{F_i}{A_j} \tag{1.6}$$

Indices i and j represents directions in a orthogonal space, F_i represents the force vector and is parallel to direction i, and A_j is the area of the surface normal to direction j. The material under stress undergoes a deformation. If the material is a solid continuum, we can define the strain as the symmetric component of the displacement gradient

$$\gamma_{ij} = \frac{1}{2}\left(\frac{\partial u_i}{\partial x_j} + \frac{\partial u_j}{\partial x_i}\right) \tag{1.7}$$

$\vec{u}$ is the displacement vector field. We can define the strain rate as the symmetric component of the velocity gradient:

$$\dot{\gamma}_{ij} = \frac{1}{2}\left(\frac{\partial v_i}{\partial x_j} + \frac{\partial v_j}{\partial x_i}\right) \tag{1.8}$$

Here $\vec{v}$ is the velocity vector field inside the material. The symmetric component is taken to avoid pure rotation of the body which results in zero deformation (The rotational component is the anti-symmetric part of the displacement gradient tensor). Generally the relation between the stress and strain (or strain rate) can be quite complicated tensorial equation and depends on the position x_j. But for certain specific geometry of deformation, the form of relation simplifies. This is the case of simple shear. As seen in Fig. 1.2 for a schematic cuboidal material , the shear stress on application of a force F acting on the top surface of area s (perpendicular to z) is given by a single component $\sigma_{xz} = \frac{F}{s}$. If deformation in the material is uniform and the displacement of the top surface is δ, its gradient is given by $\begin{pmatrix} 0 & \frac{\delta}{l} \\ 0 & 0 \end{pmatrix}$, where l is the perpendicular distance between the top and the stationary bottom surface. Thus the shear strain γ_{xy} from the (Eq. 1.7) is given by $\begin{pmatrix} 0 & \frac{\delta}{2l} \\ \frac{\delta}{2l} & 0 \end{pmatrix}$

In the traditional definition of simple shear, it is easier to define strain as deformation gradient so that both the stress and strain can be described by a scalar quantity. Thus the simplicity of the simple shear lies in the scalar description of $\sigma = \frac{F}{s}$ and simple shear $\gamma = \frac{\delta}{l}$. Note here again that the scalar γ is different from the pure shear γ_{ij} and is actually a combination of pure shear plus rotation. The same goes for the shear rate: if the top plate is moving with a velocity V, the simple shear rate can be defined by a scalar $\dot{\gamma} = \frac{V}{l}$. In the case of a pure hookean solid with shear modulus G, the shear stress and strain are related as

$$\sigma = G\gamma \tag{1.9}$$

The pure solid signifies the conversion of the mechanical energy due to shear into the elastic internal energy of the material and the rearrangement of the microstructure takes infinite time. For modeling purpose, it is easy to visualize solid as a perfectly elastic Hookean spring of spring constant k as shown in Fig. 1.2b. For a pure Newtonian fluid the relation is given by

$$\sigma = \eta\dot{\gamma} \tag{1.10}$$

where η is the viscosity of the fluid and is a constant for a given temperature. On application of shear, the rearrangements within the fluid are faster than the time scale of shear and all the energy is lost through viscous dissipation. A Newtonian fluid is modeled as a dash-pot in a fluid as shown in Fig. 1.2b. Thus from here on when we talk of macroscopic stress and strain, it is the scalar quantity σ and γ unless stated otherwise.

1.2.2 Linear viscoelasticity

Viscoelastic material show rich and complex behavior which is a combination of the two ideal scenarios described above. Under the assumption of small deformation, the complex viscoelasticity can be assumed to be linear. Mathematically, linear means that the stress, $\sigma(t)$ and the strain, $\gamma(t)$ are linearly connected and follow the following rules:

- If the strain is multiplied by a constant factor, the stress will scale by the same factor (vis-versa).
- The stress response (or the strain response) to an arbitrary combination of strain (or stress) is given by the the linear combination of response to the individual strain.

The earliest effort to describe linear viscoelasticity through a constitutive equation was done by O.Meyer in 1874 [40, 41] where a combination of (Eq. 1.9) and (Eq. 1.10) yields a form

$$\sigma = k\gamma + \eta \frac{d\gamma}{dt} \tag{1.11}$$

This was reintroduced by W. Voigt to model the viscoelasticity using a parallel combination of the spring and the dash-pot shown in Fig. 1.2b. Later known as the Kelvin-Voigt model, the representation is similar to an electric circuit with a resistor: energy loss device (the dash-pot here similar to a piston moving in oil) and a capacitor (the energy storing device) in parallel. The strain is equivalent to the voltage and the stress is similar to the current. Since in parallel, the strain (voltage) is the same, while the stress is the combination of stress experienced by both the elements,

$$\gamma = \gamma_E = \gamma_V \tag{1.12}$$

$$\sigma = \sigma_E + \sigma_V \tag{1.13}$$

Substituting $\sigma_E = k\gamma$ and $\sigma_V = \eta\dot{\gamma}$, we get (Eq. 1.11). The relaxation time for this model is given by $\tau_{\text{mat}} = \frac{\mu}{k}$. Another such simple model is known as the Maxwell model obtained by applying the spring and dash-pot in series. Here the stress experienced by the elements remains the same and the strain is equal to the sum of the individual strains for the ideal elements. Thus we get the final equation

$$\frac{d\gamma}{dt} = \frac{1}{k}\frac{d\sigma}{dt} + \frac{\sigma}{\eta} \tag{1.14}$$

Here as well $\tau_{\text{mat}} = \frac{\eta}{k}$. However, note that this model description is quite simplistic and most materials do not have a single characteristic relaxation time. More fitting models can be generated by adding more elements to the stress/strain circuit. A more general constitutive equation while remaining in the linear domain can be given by adding higher-order differentials [41].

$$\sum_{n=0}^{\infty} u_n \frac{d^n\sigma(t)}{dt^n} = \sum_{m=0}^{\infty} q_m \frac{d^m\gamma(t)}{dt^m} \tag{1.15}$$

where u_n and q_m are constant coefficients.

1.2.3 Standard experimental method for linear rheology

Experimentally, a rheometer is used to measure $\sigma(t)$ and $\gamma(t)$. The device has a stator which is a stationary component and a rotor, in which the torque is controlled in case of a stress-controlled rheometer and the angular position is controlled in case of a strain-controlled one. The material is sandwiched between the two and experiences shear. Based on the geometry, the torque and deflection are calibrated as stress and strain respectively. Also custom designed shear cells with plate-plate geometry are quite often used based on their ease of combining with other microstructural probe such as microscopes. A common method to describe the systems viscoelastic property is to apply small amplitude sinusoidal stress (or strain) on the material and get the strain (or stress) response. This is also called small-amplitude oscillatory shear (SAOS). If the behavior is linear viscoelastic, the response will be sinusoidal too with a shift in phase. The shift is 0° for a pure elastic material and is 90° for a pure viscous fluid. In general, for an oscillatory strain $\bar{\gamma}(t) = e^{i\omega t}$, the stress is related to the strain as $\bar{\sigma}(t) = G^* e^{i\omega t}$ where G^* is the complex modulus, given by

$$G^* = G' + iG'' \tag{1.16}$$

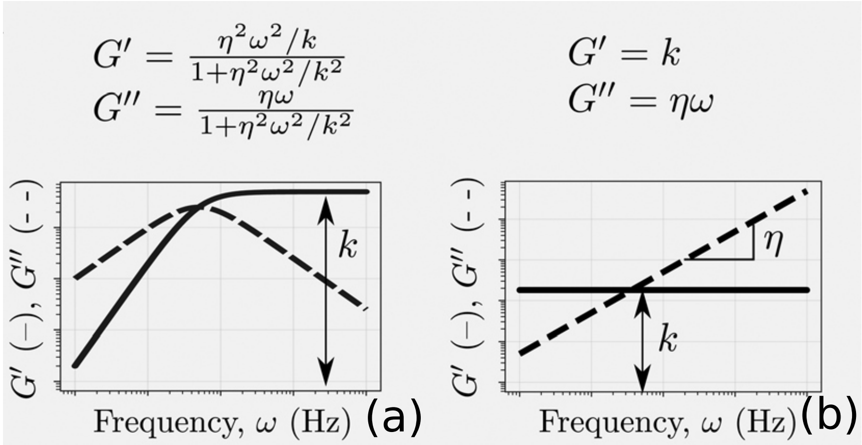

FIGURE 1.3: The resultant elastic (G') and viscous (G'') modulus obtained for the case of (a) Maxwell model and (b)Kelvin-Voigt model. The point where G' and G'' is the characteristic relaxation frequency of the material $\omega_{\text{mat}} = \frac{1}{\tau_{\text{mat}}}$. Above the frequency Maxwell material show solid like behavior while the response for Kevin-Voigt is predominantly liquid-like. Image adapted from [42].

where G' is the elastic or storage modulus while the G'' is the viscous or loss modulus. Linear oscillatory methods are quite practical since the modulus only depends on the frequency. The response for Maxwell and Kelvin-Voigt on solving (Eq. 1.11) and (Eq. 1.14) for a sinusoidal input are shown in Fig. 1.3.

Other methods to measure linear temporal response include applying small step stress and measuring the increase in strain known as a creep; or measuring the stress relaxation after the application of a step strain. These methods can give crucial information about the transient response of the material. Especially the measurements from small time scales can be used to extend the spectrum of frequency dependence in oscillatory tests for large frequencies inaccessible due to practical limitations.

For a step strain γ_o, the relaxation in stress is given by $\sigma(t) = G(t)\gamma o$, where $G(t)$ is the relaxation modulus. Similarly, for a step stress of σ_o, the creep in strain is given by $\gamma(t) = J(t)\sigma_o$, where $J(t)$ is the creep compliance. The responses for the Kelvin-Voigt model and Maxwell model based on solving (Eq. 1.11) and (Eq. 1.14) for the $G(t)$ and $J(t)$ are shown in Fig. 1.4. Notice that the nature of decay and growth is exponential for the relaxation modulus for the Maxwell model and the compliance in Kelvin-Voigt model.

Beside the differential representation of the constitutive linear viscoelastic equation, another description considers the integral over the whole history. This is based on the 2^{nd} rule of the linear description. Any imposed strain or stress history on a material can be divided into infinitesimal step strain or stress given by the Heaviside step function. The stress (or strain) response at time t imposed at an arbitrary time τ can be given by the sum of the response to all the small infinitesimal step strains. Over the limit of these step sizes tending towards 0, we can represent the sum with an integral such that

$$\sigma(t) = \int_0^t G(t-\tau)\frac{d\gamma(\tau)}{d\tau}d\tau \tag{1.17}$$

$$\gamma(t) = \int_0^t J(t-\tau)\frac{d\sigma(\tau)}{d\tau}d\tau \tag{1.18}$$

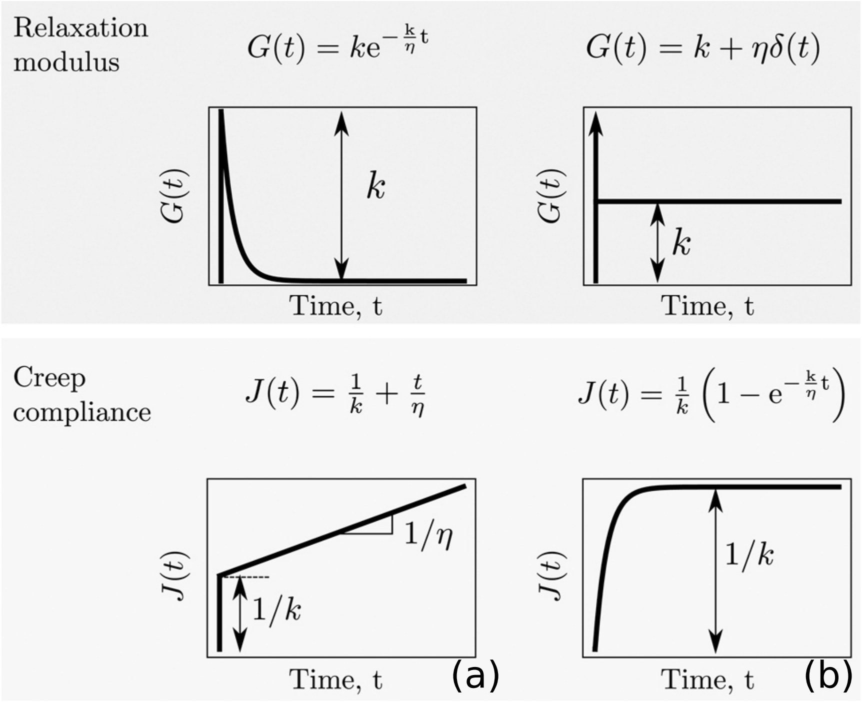

FIGURE 1.4: The resultant stress relaxation modulus ($G(t)$) and creep compliance ($J(t)$) obtained for the case of (a) Maxwell model and (b)Kelvin-Voigt model. Image adapted from [42].

1.2.4 Fractional viscoelastic model

As seen in the previous section, the two linear viscoelastic models discussed until now are quite elementary and contain a single relaxation time $\tau = \frac{\eta}{k}$. Time scales are important as they can describe physical relaxation processes. For more complicated systems with multiple relaxation times, the additional elements can be put for example a generalized Maxwell model where we have n number of series springs and dash-pot parallel to each other.

Some materials show a continuous distribution of time scales where n is practically infinite. This is the case for example of the so-called 'power-law materials' which display power-law dependence of moduli and compliance on frequency or time:

$$J(t) \propto t^{\alpha} \tag{1.19}$$

$$G(t) \propto t^{-\alpha} \tag{1.20}$$

$$G', G'' \propto \omega^{\alpha} \tag{1.21}$$

where, $0 < \alpha < 1$. Such power-law behaviour has been observed in several viscoelastic materials such as cross-linked polymer [43], foam [44], hydrogels [45], protein and colloidal gels [13, 46, 47]. Materials displaying power-law mathematically show the continuous distribution of time scales and not discrete numbers [42]. The power-law behavior can be fitted with the generalized Maxwell model. By increasing the value of n, the fitting can be improved and the number of relaxation times increases. For the best fitting $n \rightarrow \infty$. However, such a fitting with a large number of parameters makes any physical description of the material complicated. Also the best fitting is optimized to a limited time window and outside it might no longer match the data [43, 42]. This calls for a modeling approach away from the general spring, dash-pot paradigm.

Since for a power law fluid, $G(t) = At^{-\alpha}$, we can substitute it in the integral definition of the stress relaxation (Eq. 1.17) so that,

$$\sigma(t) = A \int_0^t (t-\tau)^{-\alpha} \frac{d\gamma(\tau)}{d\tau} d\tau \tag{1.22}$$

The right-hand side is similar to the definition of fractional calculus given by

$$\frac{\mathrm{d}^\alpha f(t)}{\mathrm{d}t^\alpha} = \frac{1}{\Gamma(1-\alpha)} \int_0^t (t-\tau)^{-\alpha} \frac{\mathrm{d}f(\tau)}{\mathrm{d}\tau} \mathrm{d}\tau \tag{1.23}$$

Thus a constitutive equation based on power-law [48] can be defined such that

$$\sigma(t) = C_\alpha \frac{\mathrm{d}^\alpha \gamma}{\mathrm{d}t^\alpha} = \frac{C_\alpha}{\Gamma(1-\alpha)} \int_0^t (t-\tau)^{-\alpha} \frac{d\gamma(\tau)}{d\tau} d\tau \tag{1.24}$$

Here $A = \frac{C_\alpha}{\Gamma(1-\alpha)}$, C_α, α are constants representing quasi-steady property of the material describing the 'firmness' of the material in dynamic condition such as creep. The constitutive equation can be modeled as a spring pot: An element containing the property of both the spring and dash-pot such that $\sigma = C_\alpha \frac{\mathrm{d}^\alpha \gamma}{\mathrm{d}t^\alpha}$. For the limiting case of $\alpha = 0$ and $\alpha = 1$, it reduces to an equation representing ideal elastic solid or Newtonian fluid. This opens the case for understanding of several practical systems showing power-law rheology using the fractional constitutive equation [42]. It was developed by Scott Blair to understand the behavior of food materials like milk curd [49]. Recently, it has been used to model the linear step strain response of protein gel made of sodium caseinate [47]. Further modeling can be improved by implementing a series of spring-pots as in the Fractional Maxwell used in the case of colloidal [50] and carbopol gels [51] and Fractional Kelvin-Voigt used in case of modeling potato starch gel [52].

1.2.5 Standard non-linear shear tests

Beyond the linear regime, the linear viscoelastic constitutive equation stops holding true. The response may stay reversible but amplitude dependant, become plastic or show brittle failure. There are multiple methods to probe these non-linear dynamics. Fig. 1.5a shows the schematic of the change in strain rate for a creep response extended over a long duration of the applied stress. The initial response, shaded in blue, is generally a power-law explained by linear viscoelasticity [13, 53] or plasticity [54]. At the end of the linear regime the strain rate undergoes a minimum followed by an asymptotic increase signifying rupture. Another method can be to impose a shear startup, where the strain rate is kept constant so the strain increases linearly as shown in Fig. 1.5b. Soft material such as gels shows quite a rich behavior after the linear regime which needs to be discussed in details and will be covered in Section. 1.4.1. After the linear regime, the stress reaches a characteristic maximum and the failure is signaled by the sudden drop in the stress value. Large amplitude oscillatory shear (LAOS) with either stress or strain imposed offer several possibilities as they are frequency-resolved. If the amplitude is kept constant, we have a response, which is called fatigue as shown in Fig. 1.5c and Fig. 1.5d. For a sinusoidal

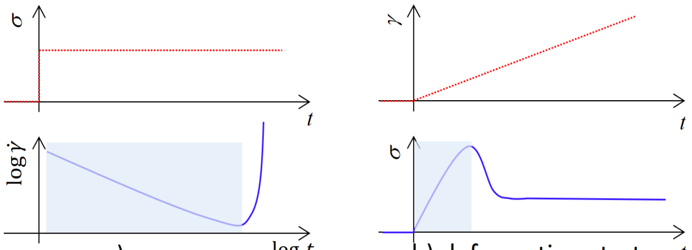

a) creep

b) deformation startup

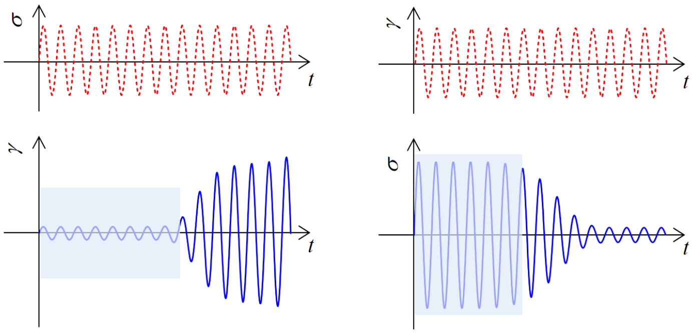

c) LAOS, σ imposed

d) LAOS, γ imposed

FIGURE 1.5: Schematic of different mode of rheology and crude macroscopic response until failure in soft condensed matter extracted from [2]. The imposed parameter is at the top in red and the expected response is below in blue. The shaded region corresponds to the region where we expect to see structural precursor before the material undergoes macroscopic fracture.

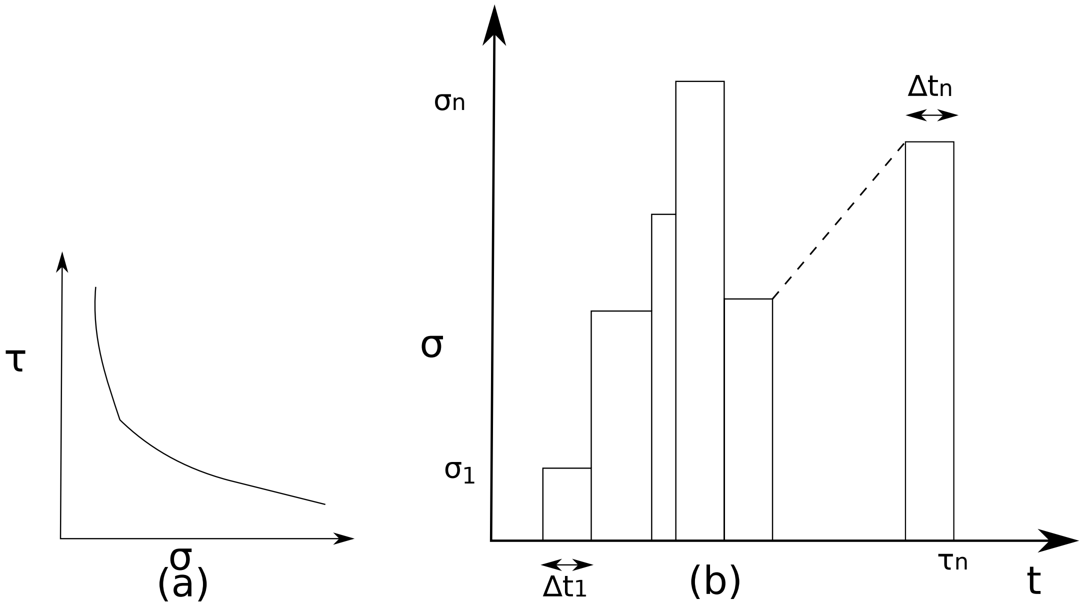

FIGURE 1.6: Schematic to understand the Baileys' rupture criteria for Markovian process under certain assumptions. (a) schematic of the stress dependence of failure time τ for a subcritical stress experiment. (b) Any random test where a sequence of step stress are applied to the material. The material fail after the n^{th} step at time τ_n.

input, the initial response is non-linear and non-sinusoidal. Furthermore, after some time the material starts to accumulate significant damage until failure and we see changes in the oscillation magnitude as indicated by the increasing amplitude in stress-controlled vs decrease in strain-controlled.

Other quantities which can be extracted are the dependence of the time to fracture τ_f on the applied stress in either static (creep), or dynamic (fatigue) sub-critical stress (schematically represented by (Fig. 1.6a)). One such dependency other than the activated Arrhenius-like is Basquin's law which predicts a power-law $\tau_f \propto \sigma^{-\beta}$ where $\beta > 0$. First seen by Basquin [55] for tests on different metal alloys under cyclic loading, this power-law dependence has been observed in heterogeneous systems such as composites [56] and biopolymer gels [13]. This is different than exponential dependence and has a strong relation to damage accumulation.

An important criteria which comes out of such dependence is the Bailey's rupture criteria [57]. Bailey observed that on increasing the applied shear-rate to glass, the critical point (σ_c, γ_c) to rupture increases. This he explained through a simple model of damage accumulation. Suppose a material under a constant stress σ accumulates damage and breaks at time $\tau(\sigma)$ given by Fig. 1.6a. If a stress of σ_1 is applied over a duration of Δt_1, the fraction of the total damage (to failure) it accumulates can be given as $\Delta t_1/\tau_f(\sigma_1)$. In general for any incremental step in Fig. 1.6bthe fraction of the total damage is $\Delta t_i/\tau_f(\sigma_i)$. Thus, the total damage accumulated before rupture in the incremental step stress (Fig. 1.6b) up to rupture at τ_n should be equal to

$$\sum_{i=1}^{i=n} \frac{\Delta t_i}{\tau_f(\sigma_i)} = 1 \tag{1.25}$$

for $\Delta t_i \to 0$ this turns into an integral

$$\int_0^{\tau_n} \frac{\mathrm{d}t}{\tau_f(\sigma(t))} = 1 \tag{1.26}$$

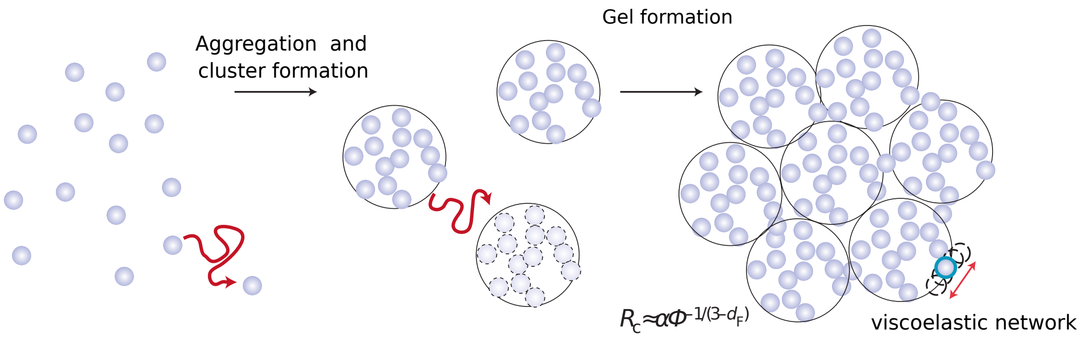

FIGURE 1.7: Schematic of the fractal aggregation model extracted from [60].

It has been shown by Freeds and Leonav [58] that the criterion is stochastically a Markovian process and its application requires that the damage is irreversible, the various damage accumulation in the material happens independently and have no memory of the previous accumulation. This criterion has been found valid in several hard materials such as metals, glasses [57] and polymer liquid [59].

1.3 Particulate gels

Gels are materials composed of bi-continuous phases of a solid network inside a liquid. The interplay between the two structures governs their rich viscoelastic behavior displaying a non-zero yield stress and incompressibility. This finds application in several industries ranging from food materials, for example yogurt and cheese which are gels obtained from aggregation of casein micelles to ceramics, where sol-gel transition of SiO_2 is used in the formation of ceramic structures [60]. The mechanical behavior of this system plays an important role in their utility: developing sustainable food based material for example a soy substitute of milk-based yogurt requires engineering the breaking or the 'mouth feel' sensation of the substitute material to remain the same. Waxy crude oil forms a gel and causes clogging in pipelines which can affect the transportation of oil and hence, the need creates a demand to characterize their yielding [4]. Also due to their unique makeup, gels are being explored as structural materials. For example, studies on double network hydrogels with their high water content show that they have the right mechanical properties to act as cartilage replacement [61]. Understanding their behavior under non-linear deformation can help accelerate application of these materials. Based on the nature of bonding between the sub-units, gels can be divided into two classes: *chemical gels* where the bonds are covalent and *physical gels* where the nature of interaction are weak and reversible, produced by van der Waals, electrostatic or hydrogen bonding. There is a lot of research on the understanding of macroscopic fracture of gels especially in chemical gels such as polymer gels [31] and hydrogel [62, 27] due to their widespread applications and high stiffness. However, the micromechanics has relatively lagged due to the viscoelastic nature of these materials as well as the heterogeneous structure. The length scale of the heterogeneity in such chemical gels is quite small to be probed at a structural scale. As such, a special class of gels called colloidal or particulate gels with particle size ranging from 10 nm to a few micrometers offers the possibility to not only explain fracture origin in the various example of these gels we encounter from the manufacturing of ceramic to food product like yogurt but also harder system such as polymer gels where the structural origin of fracture has never been observed.

In polymer gels, restoring forces on the application of stress are entropic in nature. The elasticity of polymer gels is typically modeled using entropy [Flory model 1953]. By contrast in colloidal gels, the attractive interaction are at the origin of their elasticity. At the end of the 1980s, the fractal aggregation model became popular to describe formation of colloidal gels and their properties [63, 64]. The model is described schematically by Fig. 1.7, where the colloidal particles undergoing Brownian motion, on increasing their attractive interactions, start to aggregate and form cluster, which aggregates with each other as well. Once the volume fraction of particles inside becomes the same as that of the system and no more changes occur among the particles in an aggregate, the aggregates touch and form a continuous network. The clusters are fractal in nature i.e. they are self-similar at a scale smaller than the fractal cluster size. From the model, the scaling of the cluster size R_c can be defined as

$$R_c = a\phi^{-1/(3-d_F)} \tag{1.27}$$

where a is the effective colloid radius and d_F is the fractal dimension which can be obtained from scattering experiments or microscopy. The elasticity in gel is modeled as arising from the elastic backbone of the cluster which has the same size R_c but a smaller fractal dimension d_b, with $d_b < d_F$. Generally $d_b \approx 1.1 - -1.3$. The elasticity of the cluster is given by [63]

$$K_c \propto \frac{1}{R_c^{2+d_b}} \tag{1.28}$$

However, newer developments in gelation physics have started looking at gels through other perspectives such as the arrested phase separation for colloidal gels with intermediate attraction and concentration [65]. The structure of gel and its mechanical properties are very system-dependent. In the case of non-linear rheology, it is rather complicate and requires detailed introspection in the specific studies, covered in Section. 1.4. However, these scaling laws related to the fractal structure of gels have been proven for a lot of gel materials [66, 64].

To summarize, particulate gels are the perfect candidate for advancing the science of failure in gels due to their characterized linear mechanics and large microstructural size. Also, certain gels [13, 47, 53] show non-linear behavior and rupture similar to brittle fracture observed in hard solids and thus can help in the understanding of fracture in these other amorphous systems where the microstructure cannot be probed. However, classical methods to understand fracture in elastic solids such as LEFM (Section. 1.1.1) fail as the size l_p and l_d for gel systems are of the scale of a few mesh size, violating the assumptions required for the application. Besides, the energy landscape is complicated by the added viscous effects, multiple damage accumulation and lack of understanding of how these damages interact and nucleate. Hence, we proceed with reviewing some advances made in the macroscopic and microstructural understanding of the non-linear rheology of gels.

1.4 Non-linear rheology and fracture in gels

The actual response of gel depends not only on the method described in Section. 1.2.5, but also on the type of gel system under shear. For example, the difference between the response of gels which undergo fluidization on failure which is reversible on removal of shear-like carbon black, from those gels showing irreversible brittle solid

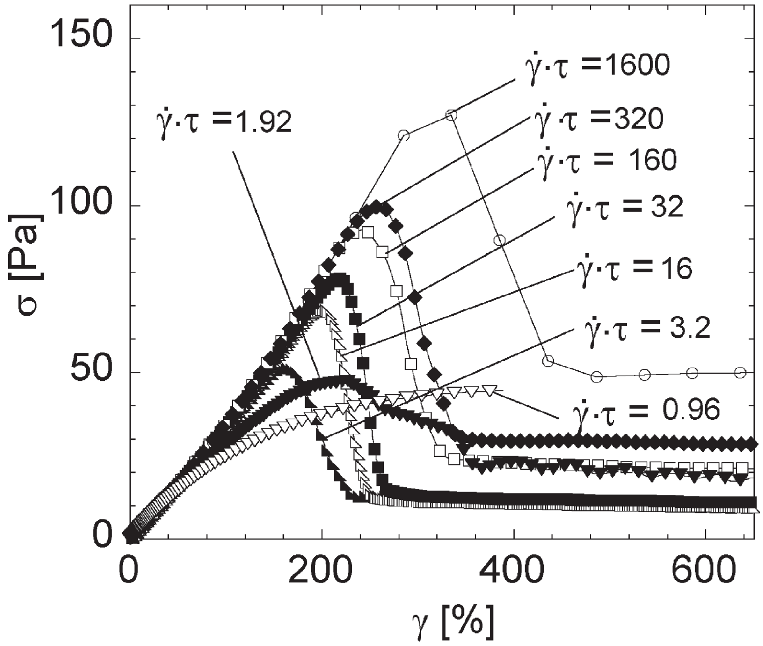

FIGURE 1.8: Stress response of a physically cross-linked polymer gel at different shear rates expressed in terms of reduced shear rate ($\dot{\gamma}\tau$) extracted from [68].

like rupture, for example, casein [67]. The non-linear response is also rich in macroscopic behavior such as strain hardening and softening which are linked to the microstructure and hence important in the study of failure in these materials.

1.4.1 Behavior of gels under strain control: shear startup and strain step

Step strain and shear startup experiments are quite straightforward to perform and the failure time can be controlled by the deformation/deformation-rate imposed either by using a shear cell or a rheometer. The characteristic behavior under such deformation can be summarized by Fig. 1.8. The experiments by [68] are performed on a bio-polymer gel which is gelified through cross-links formed by physical interaction (electrostatic here) and is reversible even after failure. An interesting aspect of their work is that the system shows Maxwell behavior (see Section. 1.2.3), allowing to define a characteristic relaxation time τ. Thus, after the initial linear regime, the gel shows a variety of rich responses based on the applied shear rate. At low shear rates when the experimental time scale probed ($1/\dot{\gamma}$) is larger than τ, the stress increases gradually towards a steady-state value behaving like a viscous fluid. This is because the system has enough time to relax and the material behaves like a fluid. At intermediate experimental time scale just smaller than τ ($\dot{\gamma}\tau = 3.2$), ductile like behavior is observed where a smooth transition from linear to non-linear regime occurs and a quasi-plateau is observed before failure. The stress deviates downwards from the linear value as plastic relaxation dissipates the elastic energy. On the other hand, for higher shear rates, the linear to the non-linear regime is initially governed by a weak strain hardening: an increase in the instantaneous elastic modulus, followed by a maxima in stress and a fast sudden drop in stress which is a characteristic of brittle fracture.

A change in the fracture mechanism based on shear rate is difficult as τ is complex and unlike the gel described above, most colloidal gels do not follow a simple constitutive model as seen before for power-law gels, which are better represented

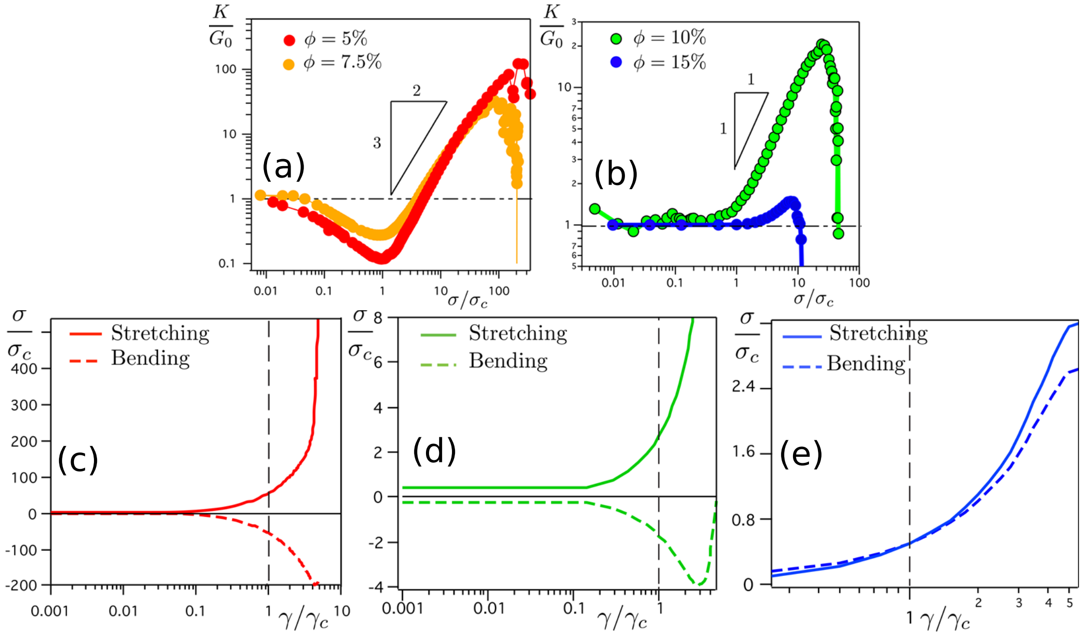

FIGURE 1.9: Numerical simulation of an incremental step strain experiment. (a) and (b) The normalized instantaneous elastic modulus denoted by K (G_0 is the elastic modulus in linear regime) as a function of gel volume fraction. (c), (d) and (e) The contribution of stretching and bending to the stress normalized by σ_c, the stress at the start of non-linear (stiffening in Fig. 1.8) for ϕ = 5,10,15 respectively. Adapted from [72].

by a fractional spring-pot model with a continuous description of relaxation time [42, 13, 53]. Also, there can be relaxation mechanism happening not in the bulk but at the interface as wall-slip is a possibility [69, 70, 71].

What is the microscopic picture behind the strain hardening or softening?

A more pronounced strain hardening behavior compared to Fig. 1.8 has been reported in other colloidal gel [66, 73, 47], simulation [74, 72], and for polymer gel [75]. In polymer gels, this has been attributed to the semi-flexibility of the network: before stretching fully, their bending stiffness is high enough to favor stretching in competition to the reduction of free energy by coiling up and increasing the entropy. This non-linear stretching is also responsible for the negative normal stress observed in these systems [76]. In the case of fractal colloidal gels, it is the stretching of the fractal backbone that transmits the stress [66]. This model is also valid for the observation by Keshavarz et al. [47] in casein gel. In the work by the group of Del Gado et al. [72] on incremental step strain experiments with athermal particle, they observe a concentration dependence of the strain hardening as seen in Fig. 1.9a and Fig. 1.9b. This is attributed to the added topological constraint on increasing the concentration and the gel structure becomes more homogeneous, resulting in hardly any non-linear behavior for the highest fraction ($\phi = 0.15$) in Fig. 1.9b.

Strain softening is less common and is often attributed to a coupling between stretching and other deformation modes. For example, in Fig. 1.9a the system of Bouzid et al. at low concentration is showing a softening before the hardening. This is from the competition between stretching and bending as seen in Fig. 1.9c, Fig. 1.9d and Fig. 1.9e. At low concentration, the gel is sparsely connected and on imposing shear, the gel can release internal stresses by unbending, leading to the softening behavior (Fig. 1.9c). At intermediate concentration, topological effects kick in strong

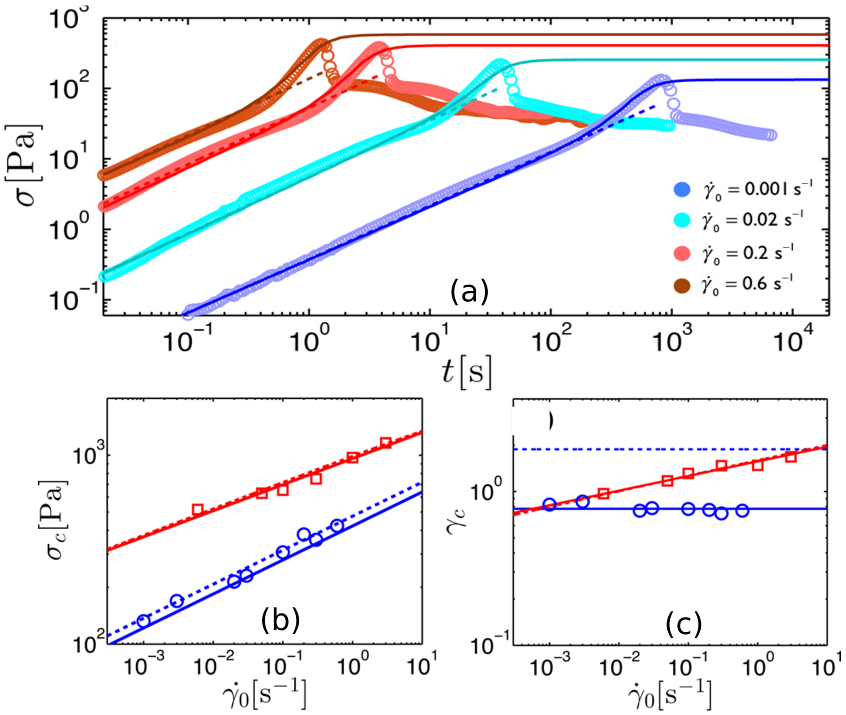

FIGURE 1.10: (a) Shear startup response of 4% casein gel at different shear rates. The solid line represents the fitting up until the critical point with the K-BKZ formulation. (b) and (c) The critical stress and the corresponding critical strain plotted as a function of strain rate as circles for 4% and squares for 8%. The dashed line corresponds to prediction combining bailey's failure criteria and linear response while the solid line is using the full K-BKZ relationship accounting for the hardening and softening. Adapted from [47].

enough to prevent unbending while allowing the stretching out of the strands until they stiffen. At the highest ϕ, the topological constraints lead to more homogeneous stress distribution, preventing localization, and both stretching and bending contribute positively to the stress. Experimentally, Keshavarz et al. [47] on applying step strain (non-incremental) observed reversible softening after hardening on increasing the amplitude of the step. An hypothesis for this (credit to Thibaut Divoux) can be the buckling of the locally compressed strand which has been observed in fibrin gel [77] and in hydrogel [78]. This hypothesis can be probed experimentally by combining the test with microscopy experiments. Also, the observation in simulation is another aspect that can be verified with the experiment, keeping in mind gelation still happens at low concentrations.

Fracture prediction through non-linear constitutive equations

Can fracture be predicted just from the macroscopic rheology? Yes! Extending on their work (Section. 1.4.1), Keshavarz et al. perform shear startup experiments on the same casein gel. The stress response is plotted in Fig. 1.10a for different shear rates. The gel shows strain hardening after a linear regime, followed by brittle irreversible failure. The macroscopic behavior observed remains the same across the different shear rates probed implying that the experimental time scale is faster than any relaxation frequencies. They predict the entire non-linear viscoelastic stress response until the critical stress combining the K-BKZ formulation with the linear fractional viscoelastic constitutive equation (Eq. 1.18) as seen in Fig. 1.10a. The formulation requires a "damping function" which they estimate accounting for both the strain hardening and softening observed in the step strain experiment (Section. 1.4.1). The critical stress σ_c is the point of maxima in macroscopic stress. For their experiment, it is also the point in time where they observe the first macroscopic fracture appearing in the gel. The K-BKZ requires the strain field to remain homogeneous (at macroscale) and thus cannot account for the behavior after the critical point where the start of macroscopic growth of fracture is observed. Fig. 1.10b and 1.10c plot the locus of the critical stress and strain for two concentrations of the gel which are appropriately predicted by combining the K-BKZ predicted behavior with Bailey's rupture criteria [57]. As seen in Section. 1.2.5, this implies that the macroscopic failure is a result of damage accumulation due to local events which are independent and irreversible. It opens up an interesting perspective on the relation of brittle fracture observed in these soft gels to those observed in much stiffer systems such as glass [57] and elastomers [59] for which Bailey's failure criteria was successfully established earlier. Application of Bailey's criteria to the casein gel means that damage accumulation until the start of local rupture nucleation should show no temporal correlation.

A prediction for fracture based on macroscopic rheology can be significant to estimate the life cycle of the material. But it is subjected to whether the material can be described by a similar kind of modeling addressed in the work of Keshavarz et al. The K-BKZ kind of formalism requires that the deformation remains homogeneous throughout the material which might not always be true for example the wall slip observed in [70]. Also, Bailey's criteria for critical stress requires the knowledge of time dependence of failure under creep. The nature of the plastic events as well as the hypothesis of independent events accumulating needs to be verified with local structural observation as well as spatial and temporal correlation.

1.4.2 Behavior of gels under sub-critical stress

Creep or static fatigue

Shear startup experiments are comparatively easy to perform due to control over the time duration over which the experiments are carried out. Also, the control parameter is the displacement, easier to measure and control than forces. This can be seen in the wide variety of shear cell devices developed compared to stress-controlled custom shear cells [79, 80]. The problem with strain controlled method is that the shear history of the material is significantly different than what is observed in real life, where most of the processes are stress-controlled. For example, the breaking of a cable wire, the loss of adhesion in sticky notes due to the slow creep under gravity are situations where we do not have control over the deformation. Besides, many of the models describing failure are for material under a constant stress [37, 12, 36].

As stated above (Section 1.2.5), many materials display a power-law response to creep, although for very different microscopic mechanisms. Andrade creep observed in crystalline solids is due to collective motion of dislocations, that is plasticity [21, 54]. Plasticity also explains the creep response of gels showing reversible yielding [70] (Fig. 1.11a). However in this thesis, we will focus on a gel system where the power-law creep can be explained by the linear viscoelasticity of the material,

Creep study on irreversible fracturing of gel formed by acidification of sodium caseinate show power-law with $\dot{\gamma} \propto t^{0.85}$ as shown in the Fig. 1.11b. The exponent observed is different than the one in crystalline solid ($t^{-\frac{2}{3}}$). The linear viscoelastic behavior, tested by performing frequency sweep in SAOS shows that the G', $G'' \propto \omega^{0.15}$. As seen in Section 1.2.4, this relates the two moduli through the power-law ($\alpha = 0.15$) and hence, the observed creep is linear-viscoelastic in nature.

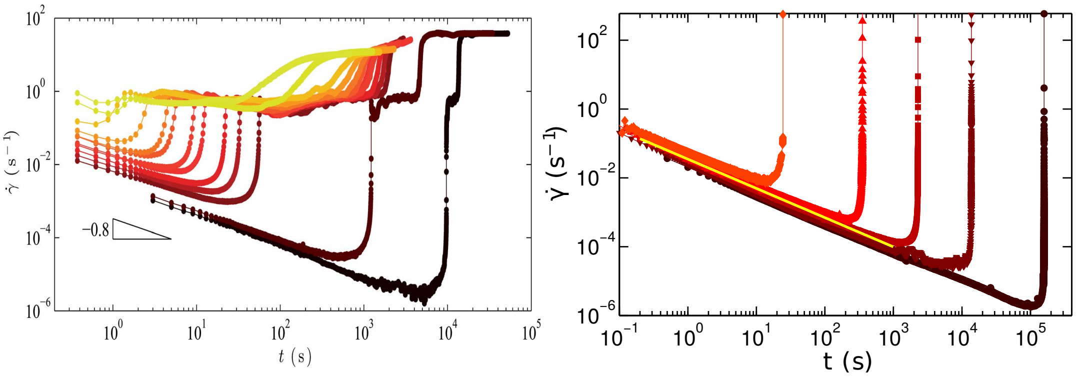

(a) (b)

FIGURE 1.11: Creep test showing strain rate as a function of time on (a) 8 wt% carbon black gel showing reversible fracture and (b) 4 wt% sodium caseinate gel showing irreversible fracture for different applied stresses (σ increasing from 24 to 80 Pa for (a) and 200 to 1000 Pa in (b)). The initial regime is a power-law $\dot{\gamma} \approx t^{-\alpha}$ with $\alpha \approx 0.8, 0.85$ in the two case. (a) extracted from [Grenard 2014], and [67] with original data from [13].

An irreversible gel formed by silica nano-particle [53] also showed that the power-law is accounted by the fractional Maxwell model. To test if the creep is recoverable, Leocmach et al. perform successive loading and unloading test on their gel and observed that only a small fraction of the strain is not recovered while the linear viscoelastic properties remain unchanged, signaling no significant damage to the structure. After the creep regime referred to as primary and defined by Andradre's law, the dynamics pass into a second regime with a minima in strain rate. This secondary regime is quite long and in fact, may correspond to 80% of the total creep time [13]. The minimum in $\dot{\gamma}$ has been observed in fiber composite materials [12] and have been modeled precisely using FBM [37]. Simultaneous macroscopic observation of the gel in cylindrical Couette cell shows the initiation of an observable fracture growing in the vorticity direction around the time $\dot{\gamma}$ reaches the minimum.

On entering the tertiary regime, where the strain rate is growing, the behavior between the two kind of gels starts to deviate. The reversible gel goes through two plateau of fluidization as seen in Fig. 1.11a. The reason for the two relaxations in the response is hard to pinpoint just from the macroscopic response. As for the casein gel, it shows a rapid increase in strain with a power-law dependence given by $\dot{\gamma} \propto (\tau_f - t)^{-1}$. In fact, when fitting the full creep behavior using a linear combination of the two phenomena: the linear viscoelastic creep and the crack growth from the macroscopically observed fracture, a complete collapse for the different σ is observed, implying a smooth transition from the primary to the tertiary regime where the secondary regime implies a microscopic picture combining linear viscoelasticity and crack growth.

As mentioned earlier, the three regimes, a primary Andrade creep, followed by minima and a tertiary acceleration, have been observed in creep experiments on fiber composite material [12]. Similar trend were observed in the acoustic emission (AE) where an emitted crackling noise is linked to plastic rearrangements. To explain this and assuming that the crackling is associated with pure plastic activity, Nechad et al. [12] proposed a fiber bundle model where each fiber is nonlinear, the fibers strength is nonuniform, and mean-field coupling between the fibers. The model captures quite well the primary creep as well as the tertiary behavior. However, the Andradre creep has been observed in other FBMs with totally different assumptions. For example, Pradhan et al. [38] used a fiber bundle model where the dynamics is controlled by an external increase in load with no internal temporal dynamics. Jagla [37], recovers the three regimes using a totally different elastic spring plus a dash-pot element of uniform stiffness where the reason for primary creep involves both the effect of both plastic events and viscoelasticity. He points out some issues with the model proposed by [12]: 1) The use of a non-linear element might seem realistic but makes the modeling more coarse-grain and does not explain phenomena at the microscale, 2) The temporal breaking of fibers (constitutive element) is one by one and happens independently and does not account for local coupling which causes avalanche or burst of breaking due to nearby events. Thus, it seems different models based on widely different microscopic pictures can account for the macroscopic rheology observed. Thus, the microscopic nature of these non-linear behavior needs independent experimental verification to progress with understanding which kinds of assumptions are valid in the models.

Dynamic fatigue

Oscillatory tests are extensively used to quantify frequency-dependent linear viscoelasticity by separating elastic and viscous components. The response in nonlinear regime under large amplitude becomes quite complicated as the assumption that the response will be sinusoidal fails. For example in the strain sweep test transitioning from small to large oscillation, the G' and G'' no longer remain independent but become dependent on the magnitude of the strain in the non-linear regime. The change in magnitude can give an idea of the yielding point, especially at the crossover between G' and G'' but it does not provide any time-resolved information. This can be done by using rigorous analysis [5]. One such analysis method is the Fourier transform rheology [81] where the response can be seen as a sum of sinusoids with different amplitude and phase differences. Strain-controlled LAOS using the FT rheology have been able to differentiate polymer with different branching [82]. However, an issue with LAOS as pointed out by Perge et al. [69] is the assumption that the oscillation happens over a dynamic steady state, i.e. there is no change in material property from one oscillation cycle to another. This means that the characteristic relaxation time of the material τ_{mat} is significantly smaller than the time scale of the applied frequency, $\frac{1}{\omega_{expt}}$. This as we have seen is quite untrue for a lot of soft material due to lack of a single characteristic time scale of relaxation and material showing thixotropy, i.e the response of the material is time-dependent.

I will discuss the most classical approach to studying oscillatory non-linear response called dynamic fatigue, the oscillatory equivalent of creep. [1]. On application of oscillatory stress just above the linear limit, the response is non-linear and not pure sinusoidal as seen in the inset of Fig. 1.12a. However on applying a Fourier transformation, we can extract the fundamental frequency and define G' and G'' as seen in Fig. 1.12a and can extract the magnitude of γ for this first harmonic (Fig. 1.12b middle). The experiments are carried out in a Talor-Couette geometry similar to the experiment described in Fig. 1.11. During the initial phase, the strain amplitude γ_o increases very slowly, but as soon as the gel enters the non-linear regime, it undergoes an abrupt change. The point of transition in time is referred to as τ_w. Finally a strain rate relaxation occur at time τ_f as shown in Fig. 1.12b. This double transition

---

[1] The history of fatigue is intriguing and in the 19th century, largely remained a mystery as the cyclic process results in not so large plastic deformation. The cause of the Versailles train disaster is associated with the fracture of the axle which was a recurring problem caused by fatigue [83]

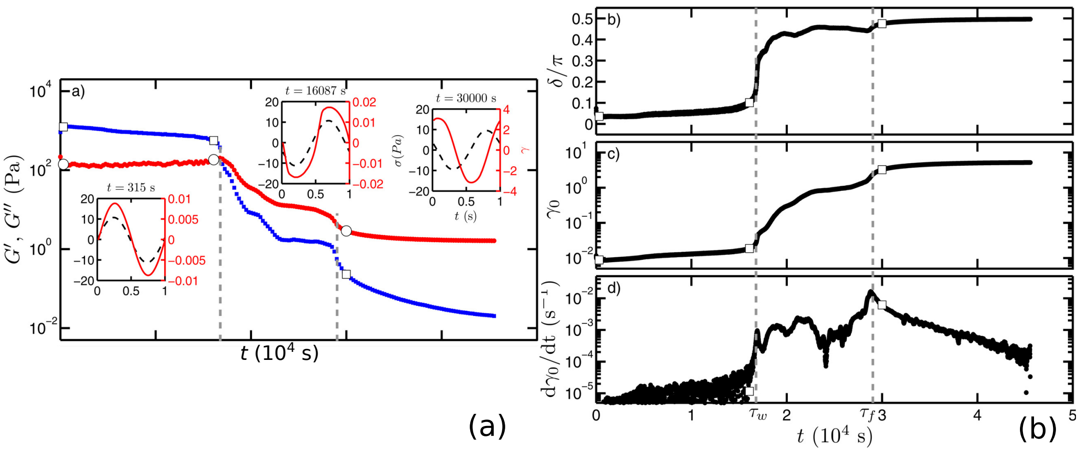

FIGURE 1.12: Fatigue experiment on 6% carbon black gel in a Taylor-Couette geometry at $\sigma = 11\,\mathrm{Pa}$ and frequency $f = 1\,\mathrm{Hz}$ adapted from [69]. (a) evolution of the elastic modulus (G', blue square) and loss modulus (G'', red circles). In inset the instantaneous strain response (red, solid) for the imposed stress at the moment (black, dotted) for three points markedwith circles. (b) The evolution of phase shift $\delta = \tan^{-1}(\frac{G''}{G'})$ of the first harmonic. (c) Evolution of the amplitude of strain γ_o from the first harmonic and (d) time derivative $\frac{d\gamma_o}{dt}$ of the strain amplitude in (c). The dotted line represent the two crossover time, t_w corresponding to the apparent yielding when $G' \sim G''$ and t_f corresponds to the fluidization time.

is similar to the creep response of the same gel in Fig. 1.11a and is a characteristic of colloidal gel showing reversible fluidization [84, 85]. The hypothesis for the two characteristic time scales are based on inter-cluster and intra-cluster bond breaking [86]. The microscopic probing using ultrasound offers more insight as will be discussed in Section. 1.4.3). LAOS performed on 6 wt% casein gel reveal brittle fracture similar to the case of static fracture in Fig. 1.11b. However, fatigue experiment can provide additional information through the harmonics which are not accessible in static creep.

Rupture criteria from harmonics analysis of LAOS

An example of the functionality of the oscillatory shear rheology is demonstrated by the work of Saint Michael et al. [87] where alongside the fatigue at constant stress, they perform increasing amplitude oscillatory stress for 10 cycles to determine empirical criteria for rupture. As seen in Fig. 1.13 when they plot the amplitude of the odd harmonics (even harmonics are negligible due to boundary condition of no-slip) against the normalized stress σ/G' for different concentrations, all the curves collapse perfectly. They identify three zones: linear viscoelastic regime where $\gamma_1 = \sigma_1/G'$ (negligible harmonics), a non-linear viscoelastic regime where the amplitude of the harmonics increase as power-laws with exponents larger than one, and a damaged regime, where the increase of the harmonics become slower than their respective power-law. On extrapolating the respective power laws from the nonlinear viscoelastic regime, they observe a common intersection point that corresponds to the critical stress at which the sample breaks immediately. In this system, it is thus possible to measure the critical stress from measurements in the nonlinear viscoelastic regime, i.e. without damaging the material.

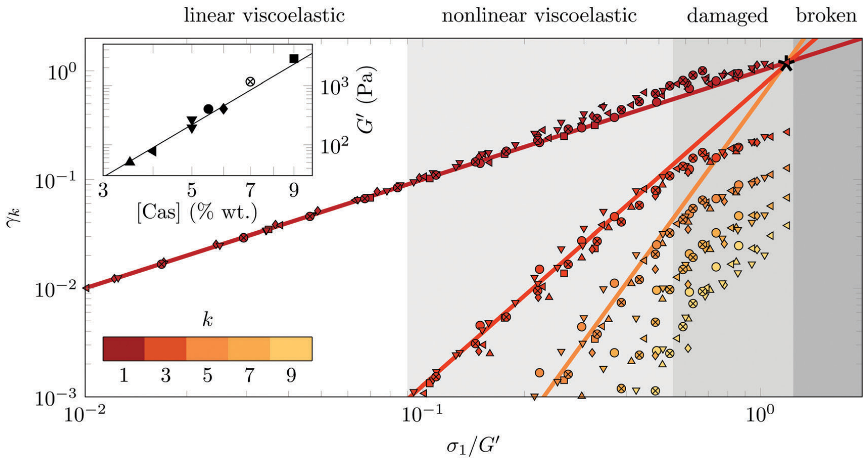

FIGURE 1.13: Magnitude of the harmonic γy_k of the strain response to an increasing oscillatory stress until 10 oscillations for different concentrations of casein as a function of normalized stress amplitude $\frac{\sigma}{G'}$, where G' is the elastic modulus in the linear response whose variation with the concentration of casein is shown in the inset. The straight lines are power-law fit for for the viscoelastic regime ($\frac{\sigma}{G'}$). Image taken from [87].

Failure time link to a rupture mechanism

For reversible gels, the time to fluidize either in creep Fig. 1.11a or in fatigue Fig. 1.12 shows an exponential Arrhenius type dependence on the applied stress magnitude such that $\tau_f \propto \exp(\frac{\sigma}{\sigma^*})$, where σ^* represent the elastic barrier required needed to be crossed to break a bond. This means rupture is an activated process and is a competition between bond formation and breaking under the influence of an external stress. The observation of this Arrhenius type dependence in other reversible gel fracture [84], as well as simulation [85] implies the role of particle interaction and gelation process on the fracture mechanism observed.

By contrast, the irreversible fracture time in casein gel τ_f show a power-law dependence on the applied stress σ in both creep [13] and fatigue test [87, 67]. This is similar to the Basquin law of fatigue [55] which was found for hard heterogeneous material under cyclic deformation (Section 1.2.3. Jagla et al. [37] also observed this in their FBM. This means that unlike in reversible gels, fracture is not governed directly by the thermally activated process, but is also linked to the amount of damage the material can accumulate. The exponent reported are in the range 1 to 10, and are an order of magnitude larger than those for other hard solids [55] implying that soft caseinate gel is more prone to damage accumulation. Besides the Andrade creep and the brittle fracture observed, this adds another consistent result relating fracture in these soft gel to hard materials.

How heterogeneous materials, let alone gels, accumulate damage until the nucleation of a critical fracture is still unclear [25, 2]. Below, we report the previous attempts to identify fracture precursors in gels.

1.4.3 Microscopic probing for fracture precursors

As seen in Section 1.4, the macroscopic mechanics combined with models and numerical simulations is informative but does not provide a full microscopic picture of the failure in these materials. The link between the brittle fracture of casein gels and

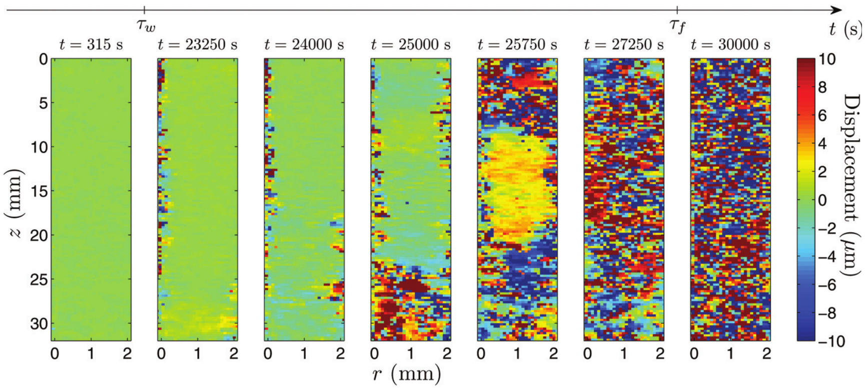

FIGURE 1.14: Time resolved displacement field $\Delta(r, z, t)$ for the same experiment describing Fig. 1.12, where r is the radial distance from the inner cylinder and z is the direction of vorticity. t_w and t_f are the time corresponding to apparent yield corresponding to wall slip and bulk fluidization respectively. Retrieved from [69].

hard solids although intriguing, opens up several questions: Are there any microscopic plastic events that cause local topological changes but do not impact the overall dynamics of the gel in the primary regime? The match with the Bailey rupture criteria might suggest locally independent events accumulating progressively. Besides, numerical simulations on reversible gels have highlighted the limited impact of microscopic plastic events on the gel structure that lead to failure in fatigue [88] and creep tests [89]. If so, how does fracture nucleate and transition to the accelerated growth regime? An understanding of those events will help develop better assumptions for future models and engineering the fracture of these systems. In the case of reversible yielding such as in carbon black gels, the reason for the two-step relaxation is hard to decipher macroscopically and as we will see, can be answered by mesoscale probing. Besides, a microscopic understanding can help understand the difference in the nature of the interaction of the fracture precursors which leads to the difference in the macroscopic rheology in these two kinds of gel failure.

Here, I elaborate on the different methods used for microstructural probing and the major inferences from these studies.

Ultrasound Velocimetry

Ultrasound velocimetry techniques to probe heterogeneities in strain and sometimes in mechanical properties have been extensively developed by the group of Sébastien Manneville in ENS Lyon [90, 91, 13, 70, 69, 87, 71]. Ultrasound velocimetry has the advantages of a high temporal resolution and of being able to probe opaque materials. However, they have a resolution of 30 to 50 µm depending on the wavelength of the ultrasound used, which is large with respect to gel microstructure.

Perge et al. [69] used ultrasound imaging to look at local inhomogeneity arising during the experiment described in Section. 1.4.2. The meso-scale displacement field displayed in Fig. 1.14 shows no sign of rearrangement for time $t < t_w$ inferring that the gel behaves like an elastic solid. This might also be an implication of the low resolution of the ultrasonic method compared to the typical size of carbon black aggregates (~ 500 nm). At $t \sim t_w$, the gel yields at the inner cylinder and subsequently leads to wall slip. Hence, this explains the first relaxation in G', G'' observed in Fig. 1.12a. Between the time corresponding to this wall slip and fluidization, there is noisy region of uncorrelated large displacement corresponding to macroscopic fluidized zone which is progressively invading into the still solid-like domain. Finally

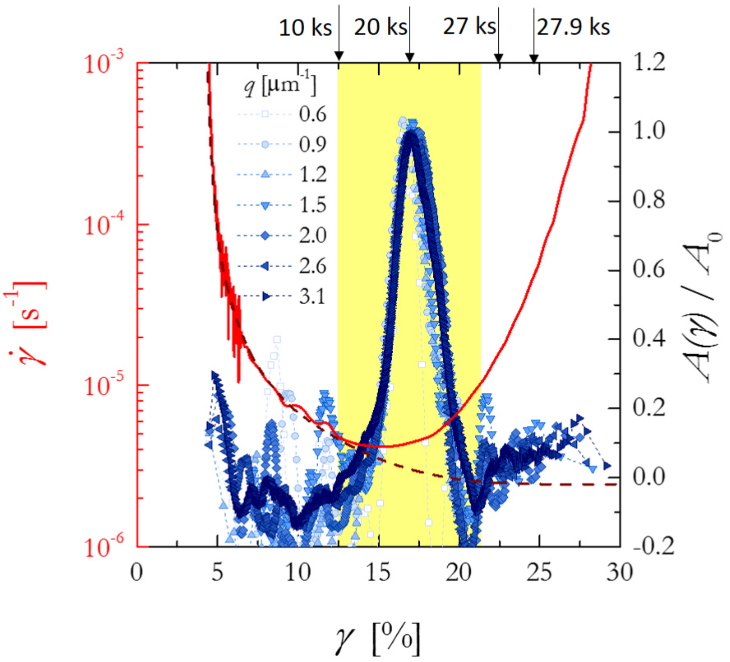

FIGURE 1.15: Creep experiment and irreversible fracture of silica gel: Left axis: $\dot{\gamma}$ as a function of the cumulative strain plotted as the red line. The dotted line represents the linear viscoelastic fit for the primary creep regime using the Fractional Maxwell Model. The blue curves are the measure of scaled plastic activity obtained from dynamics measured using light scattering for different wave vectors (q). The time at the top correspond to experimental time corresponding to the strain. Obtained from [2] with original data from [53]

after t_f the whole gel is fluidized, corresponding to the last step of constant strain amplitude in Fig. 1.12c.

In the case of creep experiment on casein gel by Leocmach et al. [13] (see Fig. 1.11a), no heterogeneity is observed in the primary regime. Again it might point to either no plastic activity or activities at scales lower than the resolution of the method. The second reason is more likely since the typical mesh size in 4% wt sodium caseinate is a few microns. During the secondary regime, macroscopic fracture nucleates near the top and bottom of the Couette cell and grows in the vorticity direction. Due to the limit of the size of the sample probed, they could not observe the heterogeneity associated with this fracture, but observed spatial fluctuation due to the elastic interaction in the gel. Finally, in the tertiary regime, the fracture enters the region in the range of the ultrasound probe and the displacement field registers heterogeneity at the tip of this macroscopic fracture growth. Unfortunately, like seen in the case of the reversible gel, the resolution is too coarse to detect the precursors, and it's hard to extract what the spatial heterogeneity associated with the growth of fracture corresponds to.

Light scattering

To probe the microstructure, time-resolved light scattering techniques can be coupled with mechanical tests [92, 93, 53]. They have the advantage of being fast and can provide ensemble-averaged information of the microstructure on a wide range of scales, well below the diffraction limit. For a system of reversible fractal colloidal gel, Mohraz and Solomon [92] coupled small-angle light scattering to a shear startup

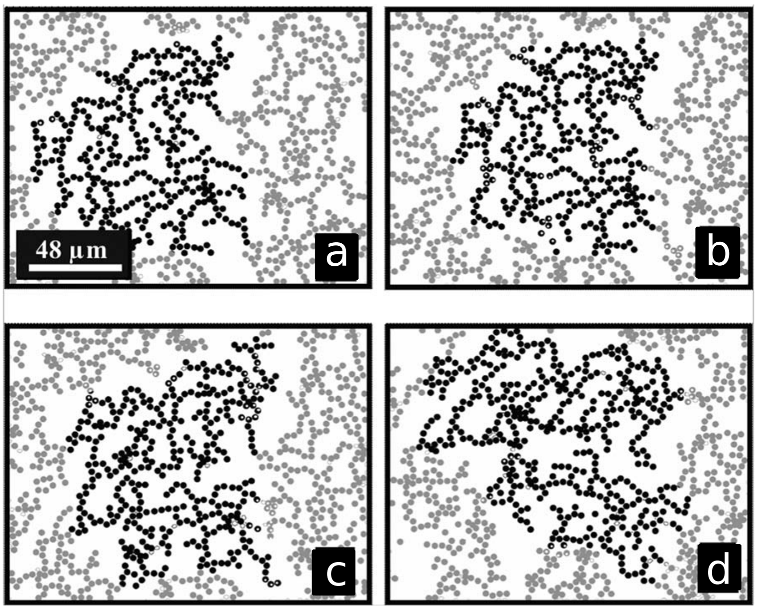

FIGURE 1.16: Microscopy image of a cluster yielding of a 2D 3.1 μm particle size polystyrene particle gel of $\phi = 0.4$ adsorbed at an oil-water interface in a shear startup experiment with $\dot{\gamma} = 0.05\,\mathrm{s}^{-1}$ at strain (a) $\gamma = 0.25$, (b) 0.5, (c) 0.75 and (d) 1.25. Adapted from [94].

experiment to observe structural anisotropy in the velocity gradient direction. They infer three regimes from it: structural orientation, network breakup near the stress maximum, and cluster densification after failure. However, the anisotropy was related to the orientation of the gel following the same trend as the strain γ without providing any other information. This highlights the issue with finding structural changes associated with damage accumulation using scattering: the rare precursor phenomena are hard to detect due to the ensembled averaging nature of the scattering method. Similar issues were encountered while probing the structural changes in the study by Roger et al. [93] and Aime et al. [53].

Aime et al. [53] discovered that microstructural dynamic changes or 'dynamic precursors' can serve as a warning for the weakening of the gel well before its catastrophic failure. In a creep experiment on a silica gel showing irreversible fracture, they probe the system dynamics at wave vector corresponding to the mesh size of the gel in the direction perpendicular to the shear plane. They observe a localized fastening related to plastic rearrangements way before the catastrophic failure as seen in Fig. 1.15. These observations proved to be a benchmark in the research on studying fracture precursors in gels.

However, the nature of these dynamic precursors still remains a mystery. Dynamics measurement might miss out on the local strand breaking with the very small signal as these events hardly impact their local topology, which may be a reason for no plastic activity measured during the initial viscoelastic creep. Also, their spatial distribution or nature of interaction cannot be extracted from scattering methods and hence, requires Spatio-temporal resolved microscopic observation

Microscopic observation

To obtain details about each microscopic plastic event, visualization with an optical microscopy can be done. Masschaele et al. [94] studied this using a gel mono-layer of attractive colloidal particles trapped in an oil-water interface which show fractal

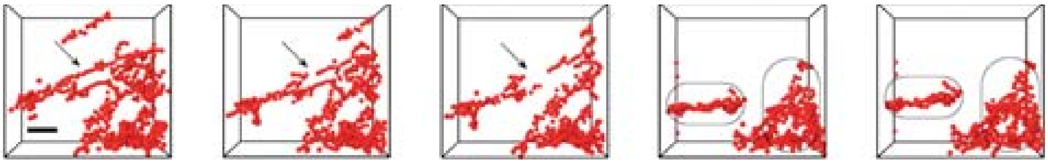

FIGURE 1.17: 3D rendered evolution of microstructure of 1 µm sized sterically stabilized PMMA colloidal gel at a strain rate of $\dot{\gamma} = 7 \times 10^{-2}$ s$^-1$ during the intermediate time stage before global rupture. The scale bar is of size 7.5 µm. Adapted from. [95].

clusters of size observable by microscope. Away from the traditional rheometer and shear cells, the shear on the gel is purely through the hydrodynamic interaction due to velocity gradient in the fluids. For an experiment of particle surface volume fraction $\phi = 0.2$, after an initial elastic and affine response, localized rearrangements corresponding to bond-breaking events of the size of local heterogeneity are spotted at $\gamma \approx 0.15$, well before the gel macroscopic rupture ($\gamma > 1$). This demonstrates the advantage of optical observation over other microscopic probing methods [92, 13, 69, 53] where such localized plastic activities remain hard to detect. At around $\gamma \approx 0.7$, contrary to the Bailey's hypothesis applied to irreversible fracture in casein gel [47], the breaking happens as a cascade or 'avalanche' indicating correlations through elastic coupling. Its also in line with the observation by Jagla [37] who proposed the model to account for avalanche effect in breaking. Finally for $\gamma > 1$, heterogeneity becomes larger due to cluster densification also seen in [92] which happens due to the breaking bond either folding into the backbone or reconnecting with other dangling ends. The study relies solely on microscopic observation to define the different regimes as they do not have a measurement of the macroscopic stress.

For a higher fraction $\phi = 0.4$, Fig. 1.16 details the breaking away of an individual cluster which suffers localized strand breaking event (Fig. 1.16a to Fig. 1.16(c)) and breaks apart from the network while maintaining its integrity. This shows the strong fractal nature of the gel as length scale of the breaking cluster is the same as the one before the percolation by diffusion-limited cluster aggregation. The effect of the increase in concentration is seen in the structure of the gel as the size of heterogeneity reduces and deformation becomes more localized leading to more localized cluster breaking, spanning from several diameters at $\phi = 0.2$ to the order of a diameter at $\phi = 0.5$. This is expected as the size of the fractal aggregate is expected to reduce with the volume fraction [63].

One issue with optical visualization is having 3D time-resolved imaging. Due to recent advances in technology, confocal microscopy has emerged as a powerful tool to visualize 3D spatially resolved microstructure of gels under shear [96, 97, 95]. It enables to detect local deformation and rearrangements especially for out-of-plane motion. Hsiao et al. [97] applied high step strain to rupture a colloidal gel of PMMA particles and immediately freeze the position of the particles by photopolimerization. This prevents the rearrangements usually seen in this system known for its reversible yielding. After the failure, they observe the existence of an eroded cluster which provides some elasticity to the failed gel. The only time-resolved shear experiment exploring 3D yielding visualization till date has been the work of Rajaram and Mohraz [95]. They perform a shear startup experiment on a reversible colloidal gel using a custom shear cell of cone and plate geometry. Unfortunately, there is no possibility of relating the microstructural visualization to macroscopic rheology as there is no measurement of stress in their experiments. For the shear startup experiment where the gel is anchored to the plate and cone, they observe initially orientational anisotropy similar to the one in Ref. [92] in their scattering due to orientation of gel in extensional direction. During the intermediate stage, there is a slowing down of the velocities leading to an arrested anisotropic state. However, during this stage, there are regular but scattered local rearrangements. Fig. 1.17 demonstrates one breaking event where during the arrested anisotropic phase, a continuous chain of the gel breaks inducing local translation before getting reattached to the main backbone resulting in the formation of local cluster and densification as marked in the last two images. Finally, in the third stage, they observe yielding as structural rearrangement cannot accommodate the global stress. It was observed that although local rupture and clustering are happening all across the gel, but the movement is local and the gel structure remains arrested during the process as opposed to the global rupture indicating yielding and fluidization.

The work of Rajaram and Mohraz [95] are in line with what was observed in the case of 2D gel with additional information of an arrested phase where local plasticity compensate for the added strain while the global structure remains arrested. They also emphasize the importance of boundary conditions as for similar experiments with no anchoring, there is no intermediate transition stage. Further investigation has to be done to couple with global stress measurement to understand these microstructural changes. Also, the use of cone-plate geometry makes it possible only to visualize a small section of the gel thus lacking statistics and understanding of how the rupture events impact the gel rheology. Visualization of fracture in irreversible gel can give a comparison of how the microstructural evolution compares to the one in the above reversible gel system.

Numerical simulations

Numerical simulations can also provide information at micro or mesoscale. However, until recently most gel simulations were only able to reproduce the phenomenology of reversible gels. Bouzid and Del Gado, have shown that the irreversible gel phenomenology could be reproduced provided both bending rigidity and low temperature are considered [98]. At low temperatures, a strand breaking event triggers other events through elastic propagation. Events are correlated. By contrast, at high temperatures, this correlation is lost in the random background of the temperature-activated breaking events.

This is reminiscent of recent results by Ozawa et al. [99] on an analytical mean-field elastoplastic model and in MD simulations of a purely repulsive dense system (i.e. not a gel). They have shown that the degree of annealing was a key parameter controlling the ductile to brittle transition. This analogy at the mesoscale however sheds no light on the nature of precursors to brittle failure in gels.

We come back to the work of Bouzid et al. [72] in Section. 1.4.1. As the concentration increases (See Fig. 1.9), the gel transitions from a largely deformable, rich non-linear behavior at low concentration, to a gel hardly showing any non-linear stiffening and transitioning to a ruptured state reminiscent of brittle fracture seen in the irreversible fracture of casein gel. This is attributed to the more homogeneous microstructure at higher concentration leading to homogenous stress distribution due to the local elastic coupling. This again can be related with the simulation works discussed above as a transition from heterogeneous to a more homogeneous structure (high degree of annealing and less disordered state) [98, 99]. These observations can be interesting to confirm experimentally. In the work of Masschaele et al. [94], they explore the effect of concentration but the lack of macroscopic stress measurement make it hard to infer anything.

1.5 Aim and challenges

To summarize, fracture study through non-linear rheology combined with microscopic probe provides a window to understanding how fracture precursors originate, not just in gels, but other soft materials as well. Combining macroscopic rheology with scattering technique, acoustic measurement using ultrasound and observation with microscope are some popular method to obtain local information. Coupling with ultrasound techniques can provide information about the dynamic precursors from the Spatio-temporal fluctuation of local velocity. However, these fluctuations correspond either to the late solid-fluid transition [69, 87] or the onset of visible cracks in the material [13], and it is difficult to clarify their structural origin. Scattering techniques have the advantage of being fast and can provide ensemble-averaged information of the microstructure. Aime et al. [53] using light scattering, measured an increase in dynamic activity associated with plastic rearrangements long before the actual failure in silica gels [53]. However, due to the volume averaging in scattering analysis, it is difficult to identify the structural precursors because generally, these heterogeneities are rare and too small to detect, that they get lost in the ensemble-averaging. Optical microscopy, especially with the advances in confocal microscopy technology, can surpass these roadblocks due to the ability to obtain spatial and temporal resolution at particle level despite their inherent limitation such as type of sample, and compromise between resolution, imaged volume, and acquisition rate.

1.5.1 Simultaneous microscopy and rheology

Coupling a confocal microscope with a commercial or custom rotational rheometer seems to be the most straightforward way to observe in real space the microstruture evolution upon mechanical stimulation. This solution is well adapted to study samples under a steady shear rate [100, 101, 95, 102, 103], oscillatory shear [104] or constant stress [105, 85, 106, 14]. The cone-plate geometry is often chosen in rotational rheometers in order to achieve homogeneous shear [100, 107, 95, 105, 106]. However in such geometry the only way to observe the whole thickness of the gap and thus quantify the effect of wall slip is to observe very close to the axis of the (truncated) cone, where the shear is actually not homogeneous [108].

Translational shear cells with plate-plate geometry offer homogeneous shear and are better suited to integrate with optical microscopy due to their simpler and less expensive design. Thus, they have been widely used to study yielding transition in soft solids [109, 104, 107, 97, 110, 86, 111, 112, 79, 80]. However, shear cells usually have a small plate surface area to achieve a high degree of parallelism, leading to a small and thus difficult to measure net force. Indeed, most translational shear cells lack stress measurement. Only a few works [79, 80] have explored the possibility to have stress measurement and, to our knowledge, stress control is only available in the setup proposed in Ref. [80]. However, this control is less sensitive than in rotational stress-controlled rheometer, restricting its usage to rather large stresses ($> 1\,\mathrm{Pa}$). Furthermore, normal stress cannot be controlled and is never measured and as we have seen, normal stress plays an important role in the rheology of non-linear stretching observed in these gels.

To be observed with confocal microscopy, the microstructure needs to be at least a micrometer large. Elasticity scales with the typical microstructure size ξ as $k_\mathrm{B}T/\xi^3$, (k_B: Boltzmann constant, T: temperature. For colloidal gels similar scaling, see

Eq. 1.27), soft solids with microstructure observable by optical microscopy have usually very small elastic modulus and are too soft to be stressed in a controlled way. For instance, a colloidal gel made of micron-size particles with 10 µm structural pore size will have moduli of the order of 10 mPa and yield stress closer to 1 mPa [113]. Such stresses are too low to be reliably applied by most commercial rheometers, and even less so by shear cells. That is why most rheo-confocal studies on colloidal gels have been performed by controlling the strain or the strain rate, with no measure of the stress response [104, 85, 95, 97]. Indeed, the stress response is often extrapolated from quantitative measurements done on similar systems with much smaller building blocks [114, 85].

Thus, the first aim of this dissertation will be to develop a setup of high precision in stress measurement and control, which can be combined with a confocal microscope to extract 3D microstructural data. Inspired by the design of the atomic force microscope (AFM) [115] we have come up with a device that uses the principle of deflection of a cantilever to measure and control stresses in a soft solid system. The detail of the design is covered in Chapter 2.

1.5.2 Irreversible rupture in colloidal gels

Besides stress controlled measurements, experiments coupled with microscopic observations are not explored in the domain of soft colloidal gels like casein showing irreversible fracture. This is because unlike a lot of colloidal gel systems [95], refractive index matching in these water based gels is difficult. However, if we are able to develop a setup of precise and sensitive stress control, we can choose lower concentrations of the gel than generally used in previous studies, decreasing the impact of refractive index mismatch. Coupled with the high resolution confocal microscopes, a depth of order of 100 µm should be possible to scan with this combination. The literature on the study of irreversible fracture in these gels has progressed significantly at the macro-scale. The parallel with hard solid rupture drawn from Bailey's rupture criteria, the power-law dependence of rupture time on the applied creep or prediction of the behavior through Fiber-bundle models originally designed for composites, require a microscopic explanation to understand the origin of these phenomena. Besides, colloidal gels with their large microstructure serve as a model material to understand fracture origin at structural scales in these hard amorphous systems as well as polymer gels. The slow phenomenon of creep fracture dominates the rupture phenomena we observe in our daily life. Thus, **the second aim of this study will focus on irreversible fracture of protein gels such as casein under controlled sub-critical stress, to understand the precursor origin of the creep macroscopically linked to linear viscoelasticity and how they interact to cause crack nucleation and failure in these materials**. Ultimately, understanding the nature of precursor correlation and nucleation, we can work on developing better assumptions to model the behavior and the energy landscape of fracture in soft heterogeneous materials.

1.6 Outline of the thesis

The thesis is broken into 7 chapters starting from this introduction. In Chapter 2, we discuss the design and engineering of a mechanical setup integrated with a confocal microscope, key to explore the micromechanics of gel rupture. This setup is able to measure and apply stress with high sensitivity in both shear and normal direction.

Chapter 3 discusses the physical chemistry and rheology of our model irreversible gel system with large microstructure: an acid-induced sodium caseinate gel. We discuss various improvements we brought to this system, and how we adapted it to our experimental needs.

In Chapter 4, we benchmark the setup on the gel system to verify whether we can perform the stress and strain control, and measurements that we claim in Chapter 2. We perform incremental step strain experiments and observe the microstructure simultaneously to pinpoint the source of rupture using simple image correlation techniques.

Chapter 4 also demonstrates the ability of our setup to perform controlled creep experiment. We acquire continuous 3D images of our gel under creep and visually recognize strand breaking events from these image in the regime defined by macroscopic linear viscoelasticity. However, these strand-breaking events are rare and with the huge amount of time-resolved 3D data, we need to develop sophisticated methods to locate these events.

In Chapter. 5, we describe in detail the analysis method we use to locate the strand breaking precursor events. One is based on the estimation of small displacement and the other on extracting the network topology.

In Chapter. 6, we use the methods defined in Chapter. 5 to locate the strand breaking events and their nucleation for the creep experiment introduced in Chapter. 4. We try some spatial correlations to understand the elastic coupling between the intact gel and the precursor ’defects’ existing within the material.

Finally, Chapter 7, summarizes the findings from our study and the various possibilities with it to address the open questions we discussed in this introduction.

Chapter 2

> Mechanics is the paradise of mathematical science because here we come to the fruits of mathematics
>
> Leonardo da Vinci

ICAMM: Immersed Cantilever Apparatus for Mechanics and Microscopy

A cantilever is defined as a structure fixed at one end while having the other end unsupported. We see cantilever structures quite often in our daily life such as apartment balconies, airplane wings, road signs etc. Cantilevers have been a subject of interest since ages. Galileo, in his book "Two New Sciences" (translated name) [116] however erroneously, quantified the force required to break a cantilever bar loaded at its free end. He also discovered the scaling problem: the strength of the beam decreases on increasing the length unless we increase the breadth and width at a higher rate. Due to one end being free, cantilevers are subjected to deflection. This deflection can be used to quantify forces and measure mechanical properties, from geological [117] to atomic scale. It is at the basis of atomic-force microscopy [115], surface-force apparatus [118, 119], and several biosensors [120]. Combining AFM with confocal microscopy allows local probing of forces and visualization from molecule to cell scale with the advantage of combining the spatial resolution in AFM with the chemical specificity offered by fluorescence microscopy [121]. In the heterogeneous system, it offers the possibility of decoupling force response in methods such as deep indentation [122]. However, AFM applies force at a very local level and cannot apply stress homogeneously over the confocal field of view.

Based on this principle of deflection of a cantilever, we have developed a novel apparatus that can perform both shear and normal tests while capturing 3D microstructure by confocal microscopy. This device, named “Immersed Cantilever Apparatus for Mechanics and Microscopy” (ICAMM). The setup offers stress and strain measurement, and can apply controlled stress or strain independently in shear and normal direction using PID loops. Section 2.1 looks at the initial inspiration device and explains the working principle and design of our setup. Section 2.2 details the mechanics behind cantilever deflection which affects our choice of material and geometry. Section 2.3 looks at the various calibration method and calculations required for the measurement of stress, strain, and the sensitivity of our measurements. Finally, Section 2.4 summarizes the PID method and how we use it to control stress and strain with ICAMM.

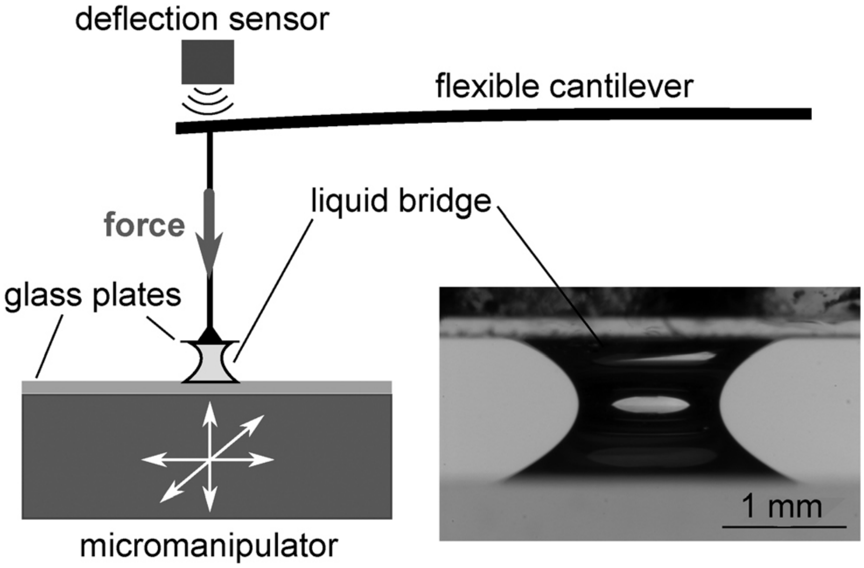

FIGURE 2.1: Schematic of the tensiometer device extracted from [127] which applies vertical force on a material (carbopol here) to measure change in surface tension on application of force in yield-stress fluids.

2.1 Design of the setup

2.1.1 Initial design inspiration

A decade before my PhD, Hélène Delanoë-Ayari designed in the lab a tensiometre to quantify the viscosity of cell aggregates. Using this compression and stretching device based on a decimeter-long cantilever blade for which deflection was measured by an eddy current sensor has successfully quantified the viscosity of cell aggregates [123, 124]. Later, Hélène and Catherine Barentin successfully used it successfully to quantify the surface tension of liquids, biological tissues, and yield-stress fluids [125, 126, 127]. Furthermore, they have coupled this apparatus to the observation of the microstructure (although, not in 3D) [123, 125]. A schematic of the setup used for surface tension measurement in yield stress fluid is shown in Fig. 2.1. This bridge tensiometer device can create normal strain in the yield stress fluid by changing the position of the micromanipulator which is attached to the bottom plate. The force measurement is obtained by the deflection in the cantilever attached to the upper plate using a sensor.

In AFM, the deflection of the cantilever is measured by the reflection of a laser on its tip [128]. For centimetric cantilevers where displacements are larger and in possibly turbid environments, eddy current sensors and capacitive sensors offer a good trade-off between precision and compactness. Compared to capacitive sensors, eddy current sensors offer a larger dynamic range and are unperturbed by changes in medium conductivity. Thus, the selection of non-contact eddy-based sensors as in the case of tensiometer device serve as the optimum choice.

The tensiometer device is limited in its usage for performing mechanics. First, since the sample is in contact with air, the theoretical sensitivity of 0.1 mPa on bulk stress is never reached as surface tension forces are dominating. Second, the setup can only perform a vertical traction test since it uses a flat beam cantilever which exploits deflection only in a single direction. Thus, even if the concept of using cantilever as force measurement apparatus is quite old, its usage for shear rheology of soft yield stress solids combined with confocal microscopy observation has not

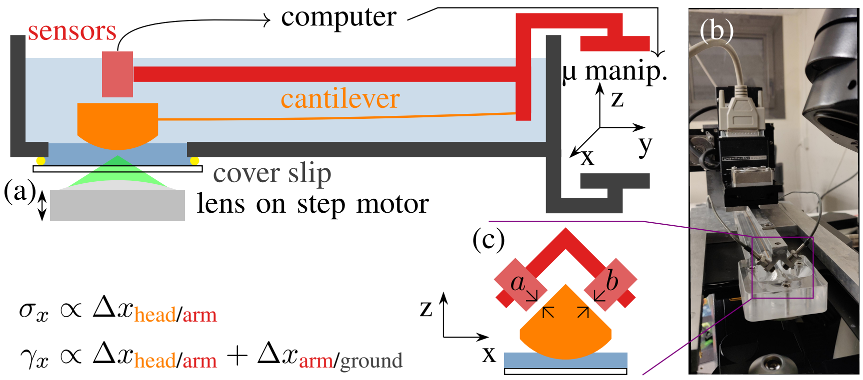

FIGURE 2.2: Design of the ICAMM with (a) a schematic side section view, (b) an angled front view of the actual device, and (c) a schematic front section view. The distances *a* and *b* measured by the sensors are highlighted by pairs of facing arrows. In the schematics, elements are colored with respect to their reference frame: orange for the head and the cantilever, red for the sensors and the arm, dark gray for the tank (ground frame). The gel sample is shown in blue, whereas the liquid permeating it and surrounding the head is shown in light blue.

been reported. Taking into account these limitations we have come up with a two-sensor-based immersed setup 'ICAMM'.

2.1.2 Working principle and design specifications

The apparatus design and main components are shown in Fig. 2.2. The working principle is based on measuring the deflection of a cantilever to obtain the stress applied to the sample. At the end of the cantilever, a rigid 'head' (orange in Fig. 2.2) has its bottom in contact with the top of the sample. Two metallic targets of 8 mm width and 0.3 mm thickness are glued at 45° on both sides of the head (Fig. 2.2c). The distance *a* and *b* to each of these targets is measured by an eddy current position sensor (EPS08-C3.5-A/M, Micro-Epsilon, light red on Fig. 2.2) respectively in ferromagnetic or non-ferromagnetic target mode. Indeed, using different modes and targets (stainless steel and aluminum respectively) is necessary to avoid interference between the sensors. Both sensors are mounted on a rigid (10 kN/m) 'arm' using a sensor holder as seen in Fig. 2.3 (red on Fig. 2.2), a fixing plate (Fig. 2.4) to which the base of the cantilever is also clamped. Sensor readings thus give direct access to the position of the head of the cantilever with respect to its base, that is to say, the deflection of the cantilever.

The arm is mounted on a micromanipulator (MP285, Sutter Instrument), allowing three-axis translation with respect to the ground frame via step motor (16 steps per µm). Thus, the position of the head with respect to the ground frame (e.g. $x_{\text{head/ground}}$) is obtained by summing the displacement of the micromanipulator (e.g. $x_{\text{arm/ground}}$) with the displacement of the head obtained from the sensors (e.g. $x_{\text{head/arm}}$). Since the bottom of the sample is fixed with respect to the ground frame, the position of the head with respect to the ground frame can be converted to a macroscopic strain, knowing the geometry.

The deflection of the cantilever can be converted to a force. However, further conversion to stress in the volume of the sample is in general made more complicated by the contribution of interfacial forces acting between cantilever, sample, and air [127]. Since we are dealing with gel samples permeated by a solvent, we are able to get rid of surface tension effects by fully immersing the sample (dark blue on Fig. 2.2a), the cantilever, and its head into the same solvent (light blue on Fig. 2.2a).

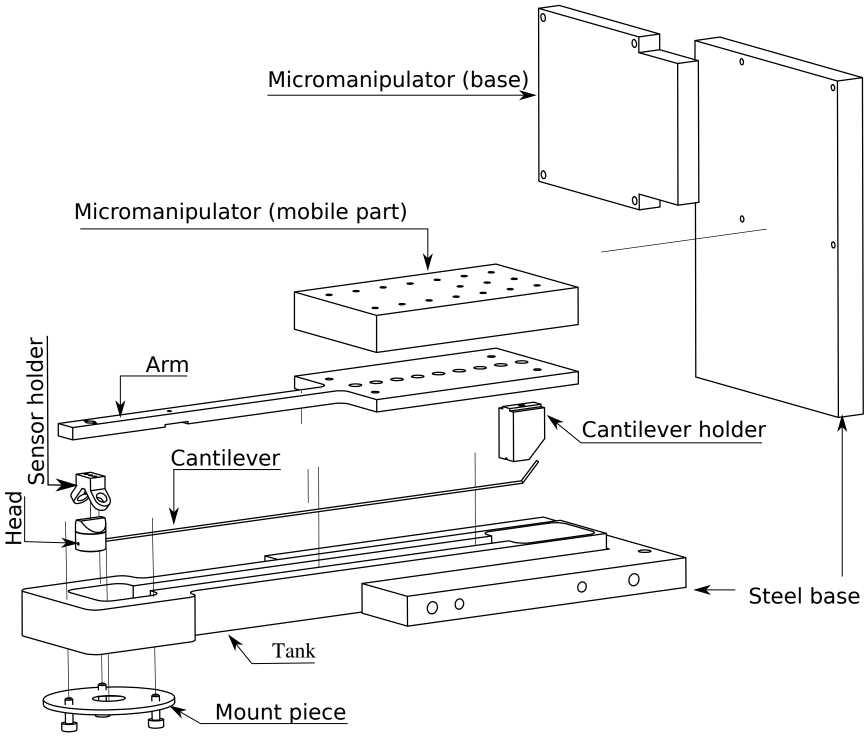

FIGURE 2.3: Exploded view of the different component of ICAMM.

Provided a fine-tuning of the solutes in this solvent (see Chapter 3), the gel network can maintain its mechanical properties while immersed. A collateral benefit of the immersion is a buoyancy force acting on the head, that partially counteracts its weights, providing the opportunity to use a softer cantilever without experiencing its plastic bending.

The solvent is contained by a machined PMMA tank as seen in Fig. 2.3 (dark gray in Fig. 2.2). The choice of PMMA as tank material is based on the criteria that it is transparent, quite inert to chemicals, does not absorb water, is rigid and does not deform easily under force, cheap, and easily machinable. The bottom of the tank (2 mm thick) has a circular (15 mm diameter) hole to allow observation with an inverted optical microscope. This hole is reversibly mounted and sealed (Teflon tape $>$ 0.1 mm thickness) with a glass coverslip (30 mm diameter, 0.17 mm thickness) pressed by an inverted conical stainless steel mount piece attached to the tank by three screws (Fig. 2.6). The gel sample is sandwiched between this coverslip and the head of the cantilever, as sketched in Fig. 2.2a. The whole apparatus can be used either alone for purely mechanical measurements or mounted on an inverted microscope. As seen in Fig. 2.3, the micromanipulator and the tank are connected to a rigid stainless steel base(tank support in Fig. 2.5) that can be screwed to a standard XY microscope stage, here the motorized stage of a Leica SP5 confocal microscope. The whole apparatus weighs approximately 3 kg. Mounting and unmounting from the stage can be done in a few minutes.

The output of each sensor is read and digitized by DT3100-SM (Micro-Epsilon) electronics. Digital readings from the sensors (ethernet) and the micromanipulator (serial) are centralized on the host PC by a Python program that also actuates the micromanipulator. Source code of the program can be found at [1].

---

[1] https://doi.org/10.5281/zenodo.4892987

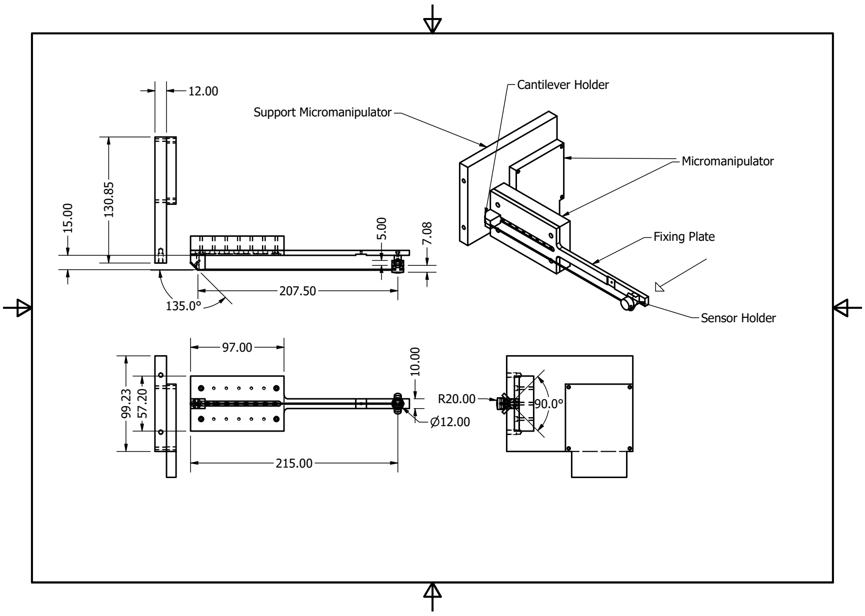

FIGURE 2.4: From top left to top right clockwise: projected side, projected bottom, projected front and orthogonal view of the cantilever, cantilever fixing plate, micromanipulator support and head. All length dimensions are in mm and angles in °

Fig. 2.4, 2.5 and 2.6 show the engineering design of all the components and their dimensions and can be useful for someone looking to recreate the setup.

2.2 Choice of cantilever

The choice of the cantilever is crucial in the current apparatus to get the right measurements. In order to obtain the same stiffness in every direction of flexion, we settled to a circular section. The dependence of deflection on the force applied on the head can be obtained by solving the moment-curvature equation:

$$\frac{1}{R} = \frac{M}{EI} \tag{2.1}$$

where R is the radius of curvature, M is the bending moment, E is the young's modulus and I is the area moment of inertia of the cantilever. For a circular cross-section cantilever of diameter D, it is given by

$$I = \frac{\pi D^4}{64} \tag{2.2}$$

The radius of curvature of any function $y = f(x)$ is given by

$$\frac{1}{R} = \frac{\frac{\mathrm{d}^2 y}{dx^2}}{(1 + (\frac{\mathrm{d}y}{\mathrm{d}x})^2)^{\frac{3}{2}}} \tag{2.3}$$

Assuming small elastic displacement y and substituting (Eq. 2.3) and (Eq.2.2) in (Eq. 2.1), gives

$$\frac{\mathrm{d}^2 y}{\mathrm{d}x^2} = \frac{64M}{\pi E D^4} \tag{2.4}$$

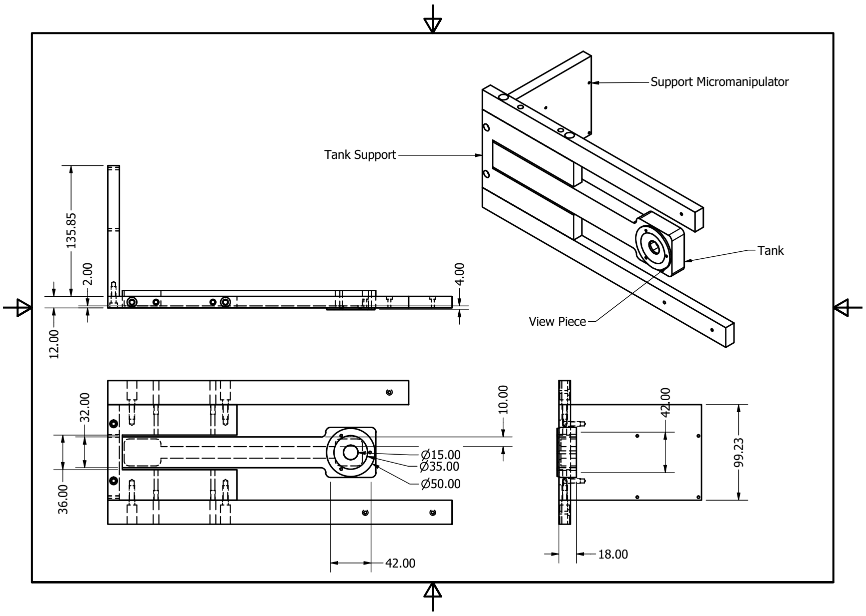

FIGURE 2.5: From top left to top right clockwise: projected side, projected bottom, projected front and orthogonal view of the tank, tank support, and viewing piece. All length dimensions are in mm and angles in °

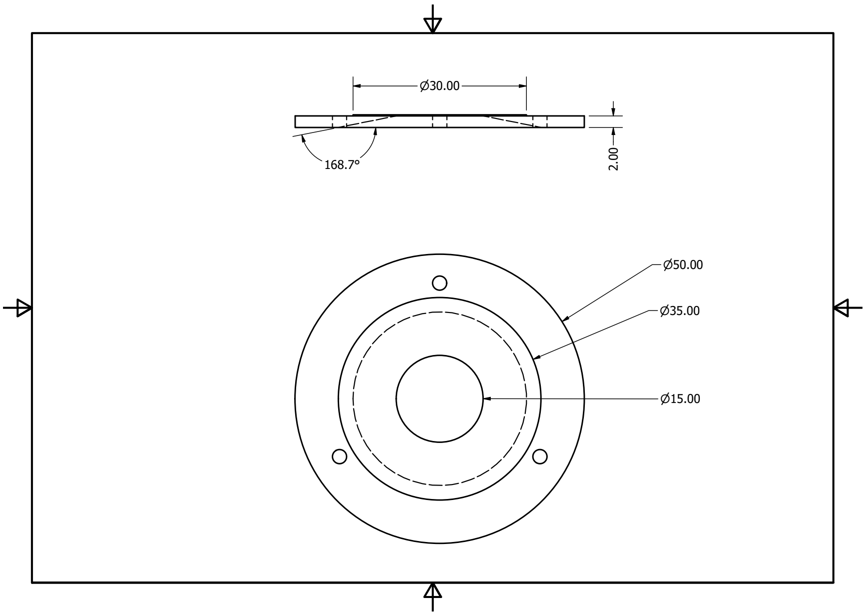

FIGURE 2.6: Top: projected side and bottom projected bottom-view of viewing piece and coverslip used. All length dimensions are in mm and angles in °

Solving this differential for the case of force F acting on the head for a cantilever of length L, the equilibrium deflection δ is

$$\delta = \frac{64L^3}{3\pi ED^4}F \tag{2.5}$$

Aside from flexion, a circular cantilever can display torsion that may disturb our measurements. The angular rotation at equilibrium around the axis due to a torque τ is given by

$$\theta = \frac{\tau L}{GJ} \tag{2.6}$$

Where G is the shear modulus and J is the polar moment of inertia. For a force F applied tangentially to the bottom of the head at a distance ℓ_b from the axis of the cantilever, $\tau = F\ell_b$. The sensors placed at distance ℓ_s from the axis of the cantilever will measure a displacement due to torsion $\delta_T = \ell_s\theta$. Thus substituting $G = \frac{E}{2(1+\nu)}$ and $J = \frac{\pi D^4}{32}$ for a circular cross-section beam we get

$$\delta_T = \frac{64\ell_b\ell_s L}{\pi D^4}\frac{1+\nu}{E}F, \tag{2.7}$$

where ν is the Poisson ratio of the material. Combining (Eq. 2.5) and (Eq. 2.6) we have

$$\frac{\delta}{\delta_T} = \frac{1}{3(1+\nu)}\frac{L^2}{\ell_b\ell_s} \tag{2.8}$$

This ratio is ≈ 500 for $L = 20\,\text{cm}$, $\ell_b = 2\,\text{mm}$, $\ell_s = 10\,\text{mm}$ and $\nu = 0.3$. Therefore, the torsion mode is negligible in our measurements but could be an issue for shorter cantilevers.

We have tried cantilevers in pure copper and stainless steel, however they showed too narrow elastic domain for our purpose. We finally settled to copper-beryllium alloy (Cu 98 % and Be 2 %, GoodFellow CU075340, $\nu = 0.3$ and $E = 120\,\text{GPa}$-$160\,\text{GPa}$) for its large elastic domain. In the following, we further characterize a cantilever of length $L \approx 20\,\text{cm}$ and diameter $D = 1.0\,\text{mm}$.

2.3 Calibrations and measurements

2.3.1 Geometric calibration

On each mounting of the cantilever or the sensors, we perform a geometric calibration so that the reading of the sensors (a, b) is properly converted to the (x, z) coordinate system. The displacement of the cantilever head along the arm (y direction) is negligible since the cantilever length ($L = 20\,\text{cm}$) is much larger than the typical movement of cantilever head ($< 100\,\mu\text{m}$). We physically block the head against an obstacle normal to x, make the micromanipulator move by a known distance along x and take the sensor readings 10 times, averaging them to record (a, b). We repeat this procedure every $10\,\mu\text{m}$ up to $200\,\mu\text{m}$ and perform the same along z. A typical set of results is shown in Fig. 2.7 as scattered data. The error in this plot depends on the repeatability of our measurement. For the sensors, the specified repeatability is $< 0.5\,\mu\text{m}$.

If we assume that the cantilever behaves linearly, then the displacements $\Delta x_{\text{head/arm}}$ and $\Delta z_{\text{head/arm}}$ should be given as a linear combination of both Δa and Δb. This can

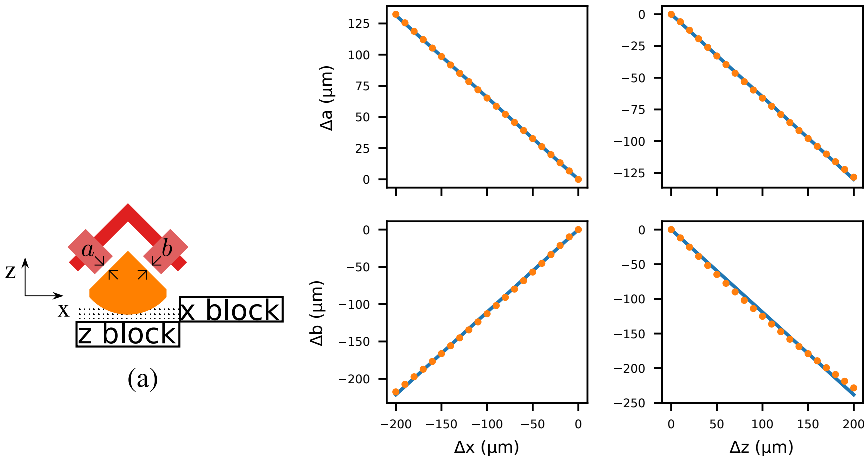

(a)

(b)

FIGURE 2.7: (a) Schematic representation of the geometric calibration of the sensor distances from the head (a, b) to the lab frame of reference (x, z) (b) a typical calibration result represented by scattered points. The error in both x and y direction are smaller than the plotted points. A linear fit (line) and matrix inversion gives the value of the calibration matrix M as $\begin{pmatrix} -0.793 & -0.433 \\ 0.736 & -0.437 \end{pmatrix}$.

be represented by the matrix multiplication:

$$\begin{bmatrix} \Delta x_{\text{head/arm}} \\ \Delta z_{\text{head/arm}} \end{bmatrix} = M \begin{bmatrix} \Delta a \\ \Delta b \end{bmatrix}, \tag{2.9}$$

where M is a (2×2) matrix. The four coefficients of M^{-1} are obtained from a linear least square fit of data shown in Fig. 2.7. We can then inverse the matrix to get M. The geometric coefficients are of order 0.4-0.7, whereas their uncertainties are of the order of 10^{-5}. We can thus consider that the relative uncertainty added by the referential change is of order 5×10^{-4}.

2.3.2 Stiffness calibration (k)

Provided the large dynamic range of eddy current sensors (from 80 nm to 800 µm), forces four orders of magnitude larger than the resolution can be reliably applied. Therefore in our case, a scale precise to 0.01 g (Denver Instrument, MXX-612) is enough to calibrate the stiffness of the cantilever. We start from a position where the head is just touching the scale plate and tare the scale. Then, we lower down the micro-manipulator by a known height, which gives the deflection of the cantilever, while the force is read from the scale. The linearity of the reading is shown in Fig. 2.8 and persists as long as the sensors are not physically touching the head. From a linear fit, we obtain the stiffness coefficient, typically $k = 2.059(9)\,\text{N/m}$. The value matches with the theoretically expected one from (Eq. 2.5) if E is assumed to be 130 GPa, which is within the range of the specification. Furthermore, the cantilever stiffness is at least three orders of magnitude lower than the stiffness of the scale measured independently to 10 kN/m, which validates the calibration method.

2.3.3 Force to stress

In order to avoid parallelism issues, the part of the head of the cantilever in contact with the gel is a spherical cap of the radius of curvature $R_0 = 20\,\text{mm}$, with a base of

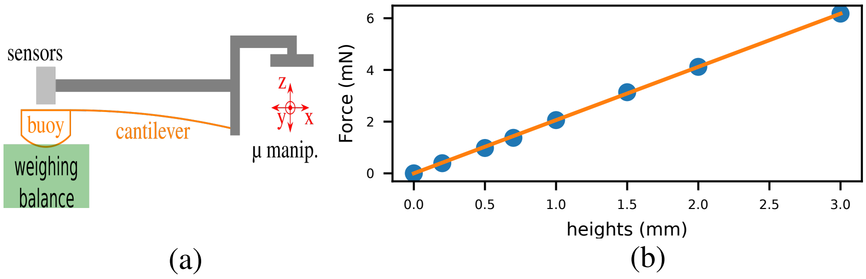

FIGURE 2.8: Cantilever stiffness calibration: (a) schematic of the test and(b) the measured force as function of height. The error in weight are quiet small compare to the actual measurements and hence not visible in the plot. The stiffness coefficient obtained from the linear fit is $2.059 \pm 0.009 N/m$.

radius $r_c = 6\,\mathrm{mm}$. Between the bottom of the head and the coverslip, we thus have a sphere-plane geometry of minimum gap h_0, with h_0 typically 0.1 mm.

Confocal observations will be centered on the vertical axis of the head, with a size of the field of view similar to $h_0 \ll R_0$. Therefore, within the field of view, the stress can be considered locally uniform. To further quantify this zone of uniform strain we can do some order analysis on the parameter shown in Fig. 2.9. By simple geometric solution h at any point x away from the center 'o' is given by

$$h = h_o + R_o \left(1 - \sqrt{1 - \left(\frac{x}{R_o}\right)^2}\right) \tag{2.10}$$

Where R_o is the radius of curvature of the head. For $x << R_o$ applying Taylor series expansion gives the relation

$$h = h_o + \frac{x^2}{2R_o} \tag{2.11}$$

We can define a critical value x_c for x when curvature becomes important such that $\frac{x^2}{2R_o} \approx h_o$. Thus

$$x_c = \sqrt{2R_o h_o} \tag{2.12}$$

For $h_o = 0.1\,\mathrm{mm}$ and $R_o = 20\,\mathrm{mm}$, $x_c = 2\,\mathrm{mm}$, thus quite larger than the zone of focus with the microscope.

For the calculation of effective area for stress calculation, assume a small shear displacement μ applied to the head. If we take a small ring element of size $\mathrm{d}s \approx \mathrm{d}x$, the stress on it due to the sheared material can be written assuming locally homogeneous strain

$$\mathrm{d}\sigma = \frac{G\mu}{h(x)} \tag{2.13}$$

where G is the elastic modulus of the material. The total force on the ring is then

$$\mathrm{d}F = 2\pi x \mathrm{d}x G \frac{\mu}{h(x)} \tag{2.14}$$

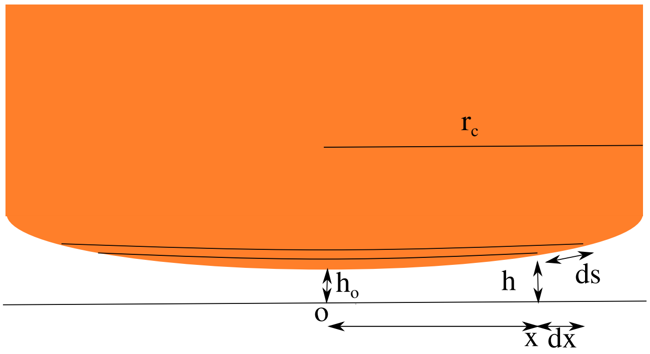

FIGURE 2.9: Schematic representation of the curvature of the head surface for effective area (A_{eff}) calculation and the ring element of radius x .

$h(x)$ is given by the (Eq. 2.11). Integrating this equation between 0 and r_c, which is the radius of the cylindrical cross-section of the head, the total force F is

$$F = 2\pi G R_o \mu \ln\left(1 + \frac{r_c^2}{2R_o h_o}\right) \tag{2.15}$$

We want to find the equivalent plane geometry of height h_o and effective area A_{eff}, which on application of a displacement μ gives the same force.

$$F = G A_{eff} \frac{\mu}{h_o} \tag{2.16}$$

Comparing (Eq. 2.15) and (Eq. 2.16), we get

$$A_{\text{eff}} \approx 2\pi R_0 h_0 \ln\left(1 + \frac{r_c^2}{2R_0 h_0}\right) \tag{2.17}$$

For our geometrical parameters, $A_{\text{eff}} \approx 29\,\text{mm}^2$. This will be useful to get the stress from any arbitrary force measured by the deflection of the cantilever.

2.3.4 Systematic and relative uncertainties

Systematic uncertainties on the stress come from the respective calibrations of M, k and A_{eff} and sum up to about 10% uncertainties on the absolute magnitude of the stress measurable with the present apparatus. However, relative uncertainties between two measurements done with the same set of calibrations stem linearly from the resolution of the sensors, $\delta a = \delta b = 80\,\text{nm}$ for a static measurement. The resolution in stress is thus $\delta\sigma = k\delta a / A_{\text{eff}} \approx 6\,\text{mPa}$. This is similar to catalog specifications of commercial stress-controlled rheometers (e.g. Anton-Paar MCR 502 with a $R = 25\,\text{mm}$ cone-plate) and at least an order of magnitude better than published shear-cells [79, 80]. Furthermore, our apparatus has an equivalent resolution in normal stress, whereas rheometers more often have normal stress resolutions in the range of 1 Pa and shear-cells are to our knowledge not able to measure or to control normal stress. Also, from (Eq. (2.5)), we deduce that the stiffness coefficient of the cantilever scales with the diameter and length as $k \propto D^4 L^{-3}$. In principle, we can bring down the precision to order of 1 µPa using a thinner and longer cantilever. This can be useful to study the sub-critical stress behavior in soft colloidal gels.

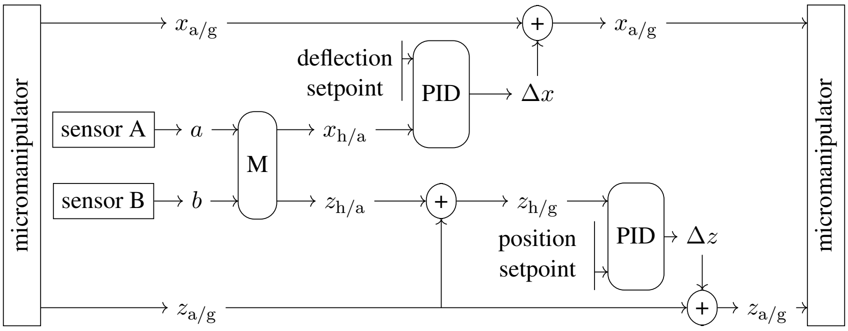

FIGURE 2.10: Diagram of the control loops in the case of a constant shear stress and a constant normal position. For the sake of space, names of reference frames are shortened to their initials.

2.4 Action: PID control loops

Mechanically, ICAMM is neither a stress-controlled or strain-controlled setup. Indeed in most practical cases, the stiffness of the cantilever is close to the equivalent stiffness of the studied sample. For example, a gel with $G' \approx 7\,\mathrm{Pa}$ in our geometry has an equivalent stiffness of $k_{\text{gel}} = G'A_{\text{eff}}/h_0 \approx 2\,\mathrm{N/m}$, similar to the stiffness of the cantilever. That is why we need to introduce a feedback control on either the position of the head with respect to the ground or the deflection in order to obtain a strain-controlled, respectively stress-controlled test. As shown in Fig. 2.10, we can set this mode on both axes independently. In the example, we show stress control in the x direction, maintaining a constant gap thickness $z_{\text{head/ground}}$ corresponding to a strain control in the vertical direction.

The PID controller acts by calculating the error $e(t)$, which is the difference between the setpoint and the process variable, and acting on this $e(t)$ using a proportional (P), integral (I), derivative (D) correction so as to minimize the quantity

$$PV = K_p e(t) + K_i \int_0^t e(t^{'})d(t^{'}) + K_d \frac{de(t)}{dt} \tag{2.18}$$

where K_p, K_i and K_d are the coefficient of the P, I and D control respectively.

In Fig. 2.10, we have the sensors providing the distances a, b which are converted to the reference frame coordinate using the calibration matrix M, as shown in Section 2.3.1. For the stress control in x, it is inputted into the PID and compared with the deflection setpoint to obtain the error, and the control action according to (Eq. 2.18) is sent to the micromanipulator to act on. Similarly, the PID acts on z but here the input to the PID is obtained from both the micromanipulator and sensor as $z_{\text{arm/ground}} + z_{\text{head/arm}}$.

Since the micromanipulator moves in steps of finite size ($\epsilon = 62.5\,\mathrm{nm}$), a purely proportional controller ($K_p > 0$, $K_i = K_d = 0$) cannot correct an error such that $|e(t)| < e_p$, where $e_p = \epsilon/(2K_p)$ is the steady-state error of the proportional controller. This error can be improved by using a larger value of K_p or by introducing an integral controller which keeps adding the error over time. Each of these actions can lead to overshoot and instability in the control loop and hence, a further differential controller can be added, which anticipates the rate of change in $e(t)$ and dampens it. Also, the frequency of our control loop is limited by the frequency of action of the micromanipulator which is 10 Hz.

The testing of this setup will be performed on a sodium caseinate gel, the methods and characterization of which are discussed in Chapter 3. All the details are discussed in Chapter. 4.

Key concepts of the chapter: This chapter contains the working principle and all the design details of the setup ICAMM which can perform controlled stress or strain experiments on soft solids while having simultaneous microscopic visualization:

1. The stress is measured using eddy-based sensors.
2. To get rid of surface tension forces, the sample and cantilever are immersed in a solvent.
3. We explain the different calibrations required to convert sensor reading to deflection and deflection to stresses and strain.
4. Both the stress and strain are controlled by applying PID control loops on measured quantities and changing position using a micromanipulator.
5. With this apparatus, we can independently apply shear and normal stress, or strain, with the same precision.

Chapter 3

> The ability to reduce everything to simple fundamental laws does not imply the ability to start from those laws and reconstruct the universe
>
> More is different (1972), P.W. Anderson

Gel System Characterization and Experimental Methods

The model gel system we work with is acid-induced gel of sodium caseinate. Similar to hard solids, casein gels show brittle irreversible fracture [13]. This fracture mechanism is prevalent in several important polymer-based gel [129], hence, understanding the phenomena can widen the engineering application for a broad class of network materials including polymer gels and protein gels. The casein gel we study here has a large micro-structure with mesh size typical of $\approx 10\,\mu\text{m}$ order [130] making microscopic observation viable. In addition, the food grade of the gel makes it easy to handle. Specific safety measures are not required. In this chapter, the introduction on casein gel covers the physical chemistry and mechanism behind the gelation. I further introduce a method to fasten the gelation process by the addition of acetate buffer. Later, I elaborate on the chemical composition and procedure for in-situ gelation in ICAMM. Finally, I characterize the gel rheology using a standard rheometer and address the mass transfer between the surrounding solution and the gel through experiment and model.

3.1 Casein Gels

Casein (Caseus in Latin for Cheese) is a natural occurring protein in mammalian milk, existing in mainly four structural form (α_{s1-}, α_{s2-}, $\beta-$ and $\kappa-$). It is present in a micelle structure with thousands of casein molecules associating with calcium phosphate [131]. The $\kappa-$ casein coats the micelle and hence, stabilizes it via electrostatic and static repulsion. A method to induce gelation is by the addition of proteolytic enzymes as in the case of cheese (rennet), which cut off the $\kappa-$ casein responsible for steric stability thus resulting in aggregation. Another method is to slowly reduce the pH using bacterial culture (as in yogurt). Casein and in general proteins are made up of amino acids which can be acidic or basic in nature. At neutral pH, casein has a net negative charge while at its isoelectric pH of 4.6, it carries no net charge. The bacterias in the culture convert the lactose in milk to lactic acid, slowly acidifying the suspension, resulting in the arrested state of gel around the isoelectric point of pH 4.6.

What happens to casein on acidification? To qualitatively explain this I take the experimental data from [132]. In the experiment, they add a 1 M HCl solution to a 4% sodium caseinate solution and after centrifugation, obtain the amount of unaggregated casein. As seen in Fig. 3.1, initially the casein is stabilized by the electrostatic repulsions at high pH. The amount of free casein begins to drop and reaches zero at a pH $\approx$ 5. In addition, the food grade of the gel makes it easy to handle. Specific

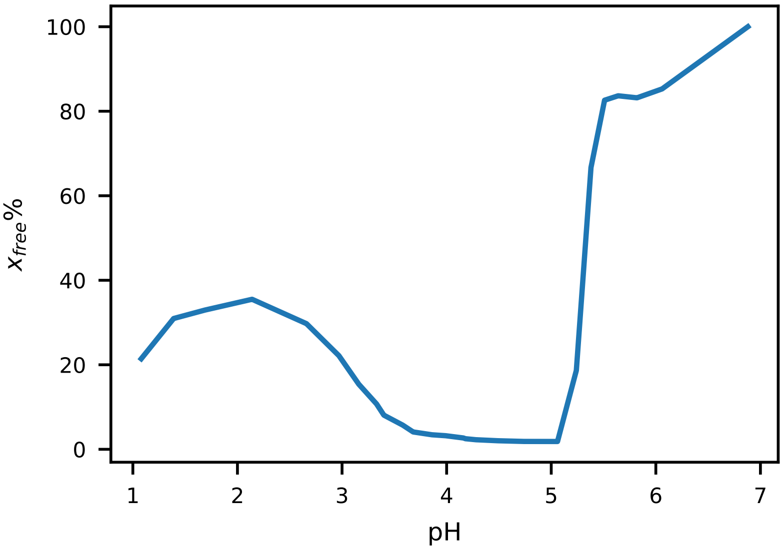

Figure 3.1: Percentage of free casein as a function of pH change obtained by addition of 1 M HCl to 4 wt% sodium caseinate solution. Data borrowed from [132]

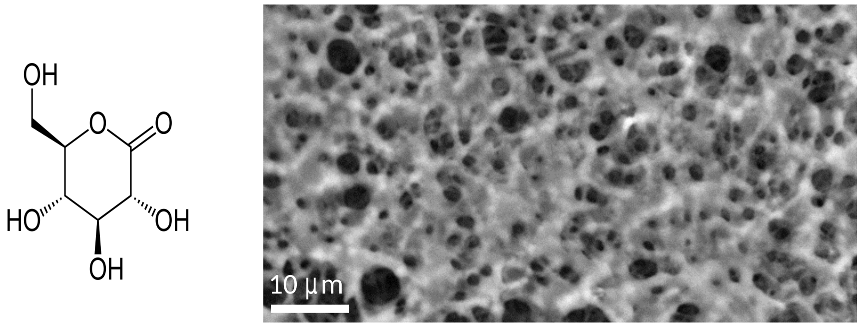

Figure 3.2: Left: Moleculart structure of GDL. Right: Micrsotructural picture of a 4%wt casein gel acidified with 1%wt GDL in water obtained using SEM (borrowed from [67])

safety measures are not required, triggering aggregation. In homogeneous acidification via bacetria culture, this process is kinetically driven by diffusion limited cluster aggregation (DLCA), leading to gelation [64]. On shifting the pH beyond the isoelectric point, the net charge of casein becomes positive enough to induce electrostatic repulsion. Hence, in Fig. 3.1, at around $\approx$ pH 3.5, the amount of free casein starts to rise and the gel (at least partially) dissolves.

Sodium caseinate is obtained by acidifying and curdling skimmed milk at pH 4.5, followed by the addition of sodium hydroxide up to a pH of 6.7 [133]. It is later pasteurized and spray dried. Depending on the ionic strength, caseinates can either be suspended individually or in aggregates of average size 11 nm, corresponding to about 15 proteins [134, 135]. Although the acid and alkaline treatment change the native structure present in milk, these aggregates still display short-range attraction along with the long-range electrostatic repulsion. Thus gelation can be induced by slow acidification.

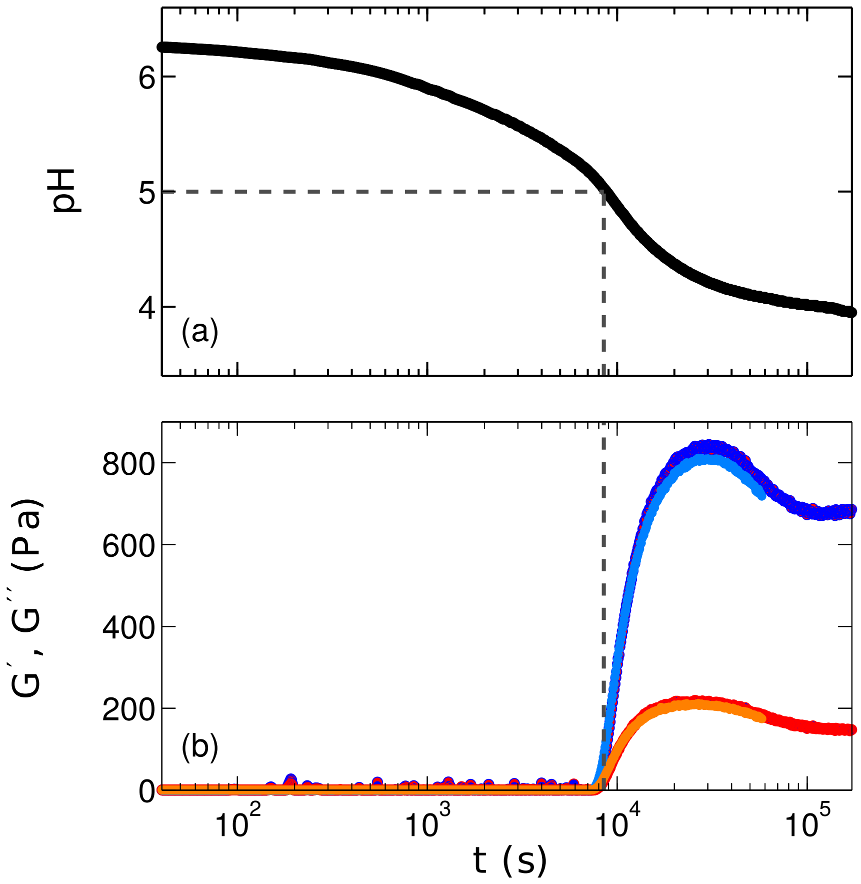

FIGURE 3.3: (a) The pH as a function of time for gelation of 4% casein acidified by 1% GDL. The black dotted line represent the first point in time and pH when they observe gelation at pH=≈ 5. (b) The corresponding elastic modulus G' and viscous modulus G'' obtained from linear viscoelasticity for a small amplitude oscillatory shear test with frequency of 1 Hz and amplitude of 0.1% with(darker) and without(lighter) polyamide sphere for ultrasound probing. Data borrowed from [132]

3.1.1 Acidification of sodium caseinate

Sodium caseinate and milk can be acidified artificially using chemicals that promote slow homogeneous acidification. Glucono-δ-lactone (GDL) an internal ester, is one such chemical (see Fig. 3.2, left). On addition to water, it undergoes hydrolysis by first-order kinetics [136]. It offers better control on the gelation process compared to lactobacillus culture: no variability due to the type of culture used and the final pH is decided by the chemical equilibrium and hence, the initial concentration of GDL. The right image on Fig. 3.2 shows an SEM image of a 4% wt casein gel obtained by addition of 1%wt GDL [67].

3.1.2 Linear rheology of casein gel during acidification

On addition of GDL to a casein solution the pH decreases limited by the first-order kinetics of hydrolysis of GDL as shown in Fig. 3.3a. At a pH close to the isoelectric point of casein (pH 5 here), the elastic modulus G' and viscous modulus G'' starts to rise with the value of $G' > G''$ signaling the onset of gelation. Finally, the pH saturates to a value close to the isoelectric point and the gel shows a plateau close to the maximum in the measured viscoelastic parameters at around approximately 8 h. To

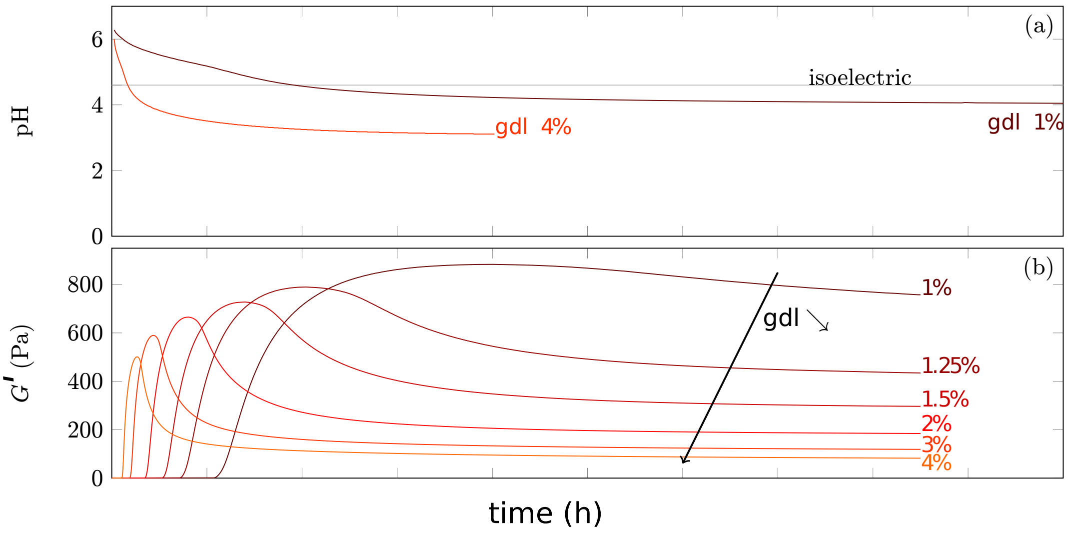

FIGURE 3.4: (a) The pH as a function of time for 4% casein acidified by 1% and 4% GDL. (b) The elastic modulus G' obtained from linear viscoelasticity for test described in Fig. 3.3 and the effect of changing the GDL concentration from 1% and 4%. Image taken from Mathieu Leocmach (unpublished).

fasten the gelation, the rate of acidification needs to be increased, which can be done by increasing the concentration of GDL. But, on increasing the GDL concentration to 4%, as shown in Fig. 3.4a, the pH lowers below 4. As seen in Fig. 3.4b, the elastic modulus decreases drastically with the plateau much smaller ($< 200\,\mathrm{Pa}$) than the maximum, implying improper gelation [132]. This is due to the over-acidification which leads to partial redissolution of the aggregates.

3.2 Controlled fast gelation

TThe over-acidification problem has led us to search for another method to fasten gelation. But, why do we need fast gelation? Taking into consideration the limitation on initial GDL concentration to prevent over-acidification, the typical gelation time is larger than 8 hours. This can be problematic for long-duration experiments as instability due to solvent loss and other factors can be introduced. Also, the caseinate aggregate might develop a gradient in concentration with height due to gravity, so having an arrested state as fast as possible is necessary. Thus, faster gelation is needed to avoid the introduction of instability, noises, and concentration gradient due to sedimentation in the experiment.

The next step for us is to decide on a method to gelify faster while avoiding over-acidification. This can be realized in two manners:

- Adding a buffer species to arrest the decrease in pH for excess GDL
- Controlling the pH through surrounding solution via diffusion.

The two methods are explained in the next section

3.2.1 Buffer addition

Buffering by a weak acid/base

This section is a small introduction to buffer chemistry. For the case of buffering by a weak acid (AH) and its conjugate base (A^-), the dissociation equation in water is given by

$$\mathrm{HA} \rightleftharpoons \mathrm{A}^- + \mathrm{H}^+, \quad Ka = \frac{[\mathrm{H}^+][\mathrm{A}-]}{[\mathrm{HA}]}. \tag{3.1}$$

Remembering that $\mathrm{pH} = -\log_{10}[\mathrm{H}^+]$ and $\mathrm{pKa} = -\log_{10} Ka$, (Eq. 3.1) becomes

$$\mathrm{pH} = \mathrm{pKa} + \log_{10}\frac{[\mathrm{A}-]}{[\mathrm{HA}]} \tag{3.2}$$

As seen from (Eq. 3.2), the buffering action is such that when the pH is close to the pKa, the pH is almost insensitive to dilution (the ratio $[\mathrm{A}-]/[\mathrm{HA}]$ remains constant) or to the consumption of a small quantity of either the acid or the base formed by other reactions (e.g. addition of a small quantity of strong acid). This is why a (close to) stoichiometric solution of a weak acid and its conjugate base is called a buffer. By contrast, for a pH far from the pKa, the acid form (respectively base form) will be in large minority and its concentration easily further decreased by other reactions, driving up (respectively down) the ratio in (Eq. 3.2). The buffering power does not apply, and the pH becomes very sensitive to other reactions. For instance, the pKa of acetic acid and acetate (noted HAc and Ac^-) is $\mathrm{pKa}_{\mathrm{Ac}} = 4.75$, which make it a good candidate to stabilise the pH near the isoelectric point of the casein (pI≈ 4.6). However at $\mathrm{pH}{=}6.75{=}\mathrm{pKa}_{\mathrm{Ac}} + 2$, acetate is the majority species by a factor of a hundred.

We can also consider the situation where a concentration C_0 of HA is put in water. At equilibrium, we have $[\mathrm{HA}] = C_0(1-y)$, $[\mathrm{A}-] = C_0 y$, and neglecting the original concentration of H^+ due to water self-protolysis $[\mathrm{H}^+] = C_0 y$. Putting these values in (Eq. 3.1) we get a second order equation in y that can in general be solved as

$$[\mathrm{H}^+] = \frac{Ka}{2}\left(-1 + \sqrt{1 + 4\frac{C_0}{Ka}}\right) \Leftrightarrow \mathrm{pH} = \mathrm{pKa} - \log_{10}\left(\frac{-1 + \sqrt{1 + 4C_0/Ka}}{2}\right) \tag{3.3}$$

However, for many cases $C_0 \gg Ka$, thus the above equation reduces to

$$[\mathrm{H}^+] \approx \sqrt{C_0 Ka} \Leftrightarrow \mathrm{pH} = \frac{1}{2}(\mathrm{pKa} - \log_{10} C_0). \tag{3.4}$$

GDL hydrolysis and pH

GDL hydrolysis into gluconic acid slowly followed by a fast equilibriation between between gluconic acid and gluconate [136]. The two reactions can be expressed as

$$\underbrace{\mathrm{GDL}}_{g(1-x)} + \mathrm{H_2O} \underset{k_1}{\overset{k}{\rightleftharpoons}} \underbrace{\mathrm{HGl}}_{gx(1-y)}, \qquad K_{\mathrm{GDL}} = \frac{[\mathrm{HGl}]_\infty}{[\mathrm{GDL}]_\infty} = \frac{k}{k_1} \approx 7.7. \tag{3.5}$$

$$\underbrace{\mathrm{HGl}}_{gx(1-y)} \rightleftharpoons \underbrace{\mathrm{Gl}^-}_{gxy} + \underbrace{\mathrm{H}^+}_{gxy}, \qquad Ka_{\mathrm{Gl}} = [\mathrm{H}^+]\frac{y}{1-y} \approx 10^{-3.70} \tag{3.6}$$

Since (Eq. 3.6) is fast, at any time, we can apply (Eq. 3.3), replacing C_0 by gx. We thus get

$$y = \frac{Ka_{\mathrm{Gl}}}{2gx}\left(-1 + \sqrt{1 + 4\frac{gx}{Ka_{\mathrm{Gl}}}}\right) \overset{x \gg Ka_{\mathrm{Gl}}/g}{\approx} \sqrt{\frac{Ka_{\mathrm{Gl}}}{gx}}. \tag{3.7}$$

or $x \approx Ka_{\mathrm{Gl}}/(gy^2)$. If we are at final equilibrium, we can input this values in (Eq. 3.5) and solve for y

$$y_\infty \approx \sqrt{\frac{1+K_{\mathrm{GDL}}}{K_{\mathrm{GDL}}}\frac{Ka_{\mathrm{Gl}}}{g}}, \tag{3.8}$$

$$x_\infty \approx \frac{K_{\mathrm{GDL}}}{K_{\mathrm{GDL}}+1} \approx 0.885. \tag{3.9}$$

The remarkable lack of dependence of x_∞ on g can also be recovered starting from (Eq. 3.5):

$$K_{\mathrm{GDL}} = \frac{x_\infty(1-y_\infty)}{1-x_\infty} \Leftrightarrow x_\infty = \frac{K_{\mathrm{GDL}}}{1+K_{\mathrm{GDL}}-y_\infty} \overset{y \ll K_{\mathrm{GDL}}+1}{\approx} \frac{K_{\mathrm{GDL}}}{K_{\mathrm{GDL}}+1}. \tag{3.10}$$

Since $[\mathrm{H}^+] = gxy$, the final pH is obtained by combining (Eq. 3.8) and (Eq. 3.9):

$$\mathrm{pH}_\infty = \frac{1}{2}(\mathrm{pKa}_{\mathrm{GDL}} - \log_{10} g), \quad Ka_{GDL} \equiv \frac{K_{\mathrm{GDL}}}{K_{\mathrm{GDL}}+1}Ka_{\mathrm{Gl}} \approx 10^{-3.75}. \tag{3.11}$$

For instance GDL (molar mass $M_{\mathrm{GDL}} = 178.14\,\mathrm{g\,mol^{-1}}$) at 1%wt corresponds to an initial GDL molar concentration of $g = 56 \times 10^{-3}\,\mathrm{mol\,l^{-1}}$. According to (Eq. 3.11) it would reach a final pH of 2.5. This predicted value is lower than the observed final pH$\approx$ 4 in the presence of 4%wt sodium caseinate. Indeed proteins are themselves weak poly(acid/base) that have an influence on the pH.

GDL and acetate buffer solution

To speed up the gelation process, we can use the buffering power of acetate (pKa= 4.75). The presence of CH_3COO^-/CH_3COOH buffer means that we can add excess of GDL which will reduce the pH faster initially until gelation but the kinetics will slow down near $\approx$ 4.75 due to the buffering power of acetate. Thus addition of excess GDL will not lead to overacidification and softening of gel. Treating analytically the pH response of sodium caseinate is too complex since it has multiple acidic and basic groups. Besides, compared to the 4%wt system used in [13, 132], we will switch to 1%wt to have a larger microstructure for better imaging. Since the GDL will be in excess, the ratio of GDL to caseinate will be higher than in [13], reducing the influence of caseinate on the final pH. Thus, we assume that the final pH is only affected by the initial concentration of acetate buffer and GDL.

From (Eq. 3.11), we know that the final $[\mathrm{H}^+]$ is given by the initial GDL and the equivalent dissociation constant $Ka_{\mathrm{GDL}} = 10^{-3.75}$. Sodium acetate trihydrate is a water soluble crystal salt which acts as a source of acetate ions. At $t = 0$, if we add g moles of GDL($M_{\mathrm{GDL}} = 178.14\,\mathrm{g\,mol^{-1}}$) and a moles of sodium acetate trihydrate ($M_{\mathrm{NaAc.3H_2O}} = 136.08\,\mathrm{g\,mol^{-1}}$)

$$\underbrace{\mathrm{GDL}}_{gM} \rightleftharpoons \mathrm{Gl}^- + \mathrm{H}^+ \tag{3.12}$$

$$\underbrace{\mathrm{Ac}^-}_{aM} + \mathrm{H}^+ \rightleftharpoons \mathrm{AcH} \tag{3.13}$$

We have at equilibrium,

$$\underbrace{\mathrm{GDL}}_{g(1-x)} \rightleftharpoons \underbrace{\mathrm{Gl}^-}_{gx} + \underbrace{\mathrm{H}^+}_{gx-ay} \tag{3.14}$$

$$\underbrace{\mathrm{Ac}^-}_{a(1-y)} + \underbrace{\mathrm{H}^+}_{gx-ay} \rightleftharpoons \underbrace{\mathrm{AcH}}_{ay} \tag{3.15}$$

From chemical equilibrium balance, we have

$$Ka_{\mathrm{AcH}} = \frac{[\mathrm{Ac}-][\mathrm{H}^+]}{[\mathrm{AcH}]} = \frac{a(1-y)[\mathrm{H}^+]}{ay}, \tag{3.16}$$

$$Ka_{\mathrm{GDL}} = \frac{[\mathrm{Gl}-][\mathrm{H}^+]}{[\mathrm{GlH}]+[\mathrm{GDL}]} = \frac{gx[\mathrm{H}^+]}{g(1-x)}, \tag{3.17}$$

where $Ka_{\mathrm{AcH}} \approx 10^{-4.75}$ and $Ka_{\mathrm{GDL}} \approx 10^{-3.75}$.

Mass balance of H^+ give us $[\mathrm{H}^+] = gx - ay$. If we assume $gx, ay \gg 10^{-\mathrm{pH}}$, we get

$$\frac{g}{a} \approx \frac{y}{x} \tag{3.18}$$

For the gelation to be proper, we need to have a final pH close to the isolectric point of 4.6. Putting this constraint on $[\mathrm{H}^+]$ and solving (Eq. 3.16), (Eq. 3.17) and (Eq. 3.18), we get

$$x \approx 0.88, \tag{3.19}$$

$$y \approx 0.59 \tag{3.20}$$

$$\frac{g}{a} \approx 0.67 \tag{3.21}$$

Thus, (Eq. 3.21) signifies that the molar ratio of GDL to Acetate in the initial solution should be approximately 0.67 for having an equilibrium pH of ≈ 4.6.

3.2.2 Diffusion control through surrounding solvent

As discussed in Chapter. 2, we surround the gel with a solvent with similar composition water based solution to nullify interfaces and hence, surface tension forces. Since the surrounding solvent is in excess, it will decide the final concentration of ions and hence, it can act as a source of H^+ via diffusion. To quantify the time scale for this gelation, we need to solve the mass transfer on applying a step concentration of H^+ for the typical length scale of the radius of head.

Diffusion characterization: Analytical

To simplify the mass transfer problem involved, we consider a simplified cylindrical geometry for the gel confined between coverslip and head as shown in Fig. 2.9. We also assume that H^+ is the only ion we are concerned with for the change of pH. We can solve the non-steady state mass transfer equation in cylindrical coordinates to get the concentration profile C with time

$$\frac{\partial C}{\partial t} = \frac{1}{r}\frac{\partial}{\partial r}\left(rD\frac{\partial C}{\partial r}\right) \tag{3.22}$$

where r is the radial distance, D is the diffusion coefficient. Using the method of separation of variable, the mass transfer equation reduces to

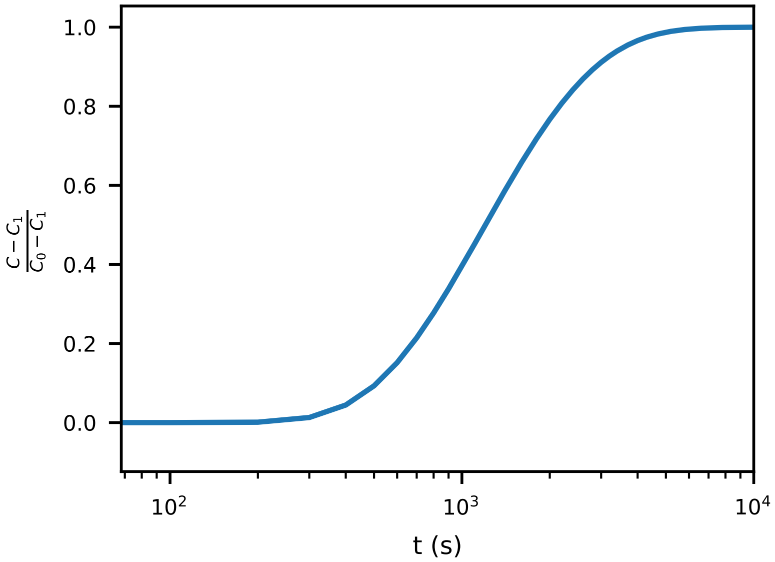

FIGURE 3.5: Normalized concentration at the center of the cylinder for the model diffusion of H^+ inside a cylinder of radius same as the head in ICAMM on introduction of a step concentration outside the confinement, solved using (Eq. 3.29).

$$C = ue^{-D\alpha^2 t} \tag{3.23}$$

where α is a distance based parameter, u is a function of radial distance r from the center satisfying the bessel equation of zero order.

$$\frac{d^2u}{dr^2} + \frac{1}{r}\frac{du}{dr} + \alpha^2 u = 0 \tag{3.24}$$

The solution to (Eq. 3.23) can also be obtained analytically if we define a model based on assumed initial and boundary conditions:

- The concentration of H^+ is constant initially between the plates

$$C = C_1,\ 0 < r < a,\ t = 0 \tag{3.25}$$

- The concentration of H^+ is constant around the cylinder i.e. in the buffer for all the time

$$C = C_0,\ r = a,\ t >= 0 \tag{3.26}$$

The solution for these boundary condition is given by [137]

$$\frac{C - C_1}{C_0 - C_1} = 1 - \frac{2}{a}\Sigma_{n=1}^{\infty} \frac{e^{-D\alpha_n{}^2 t} J_0(r\alpha_n)}{\alpha_n J_1(r\alpha_n)} \tag{3.27}$$

Here J_0 and J_1 are bessel function of first kind of order 0 and 1 respectively. The α_n are the root of the bessel funcion J_0.The solution of this for the center of the cylinder ($r = 0$) is plotted in Fig. 3.5 for the ICAMM setup ($a = 0.6$ cm). The time for equilibration is > 1.5 hour.

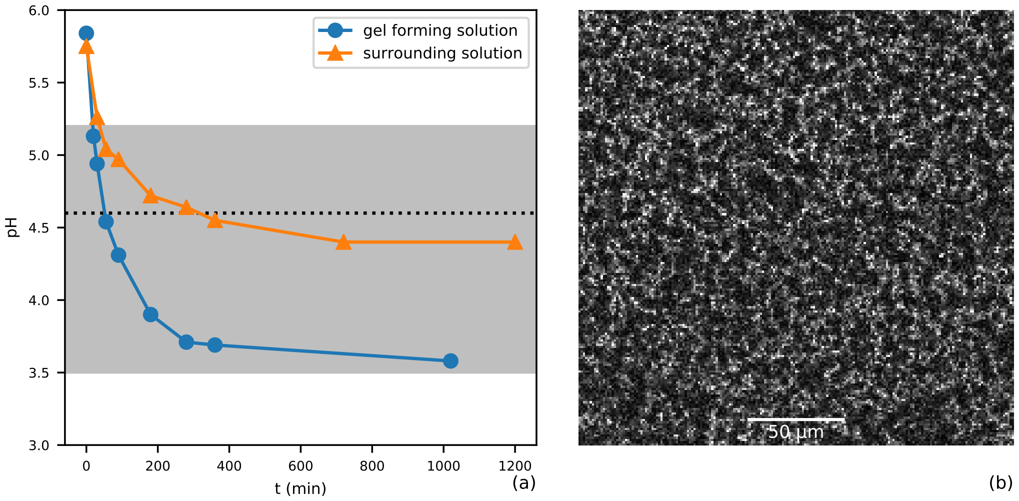

FIGURE 3.6: (a)Evolution of pH of the surrounding solution and the gel solution when not in contact with each other. The zone of pH where casein aggregation is observed.The horizontal dotted line is the isoelectric pH. (b) 2D view of the casein gel formed inside ICAMM following the protocol described in Section 3.3 at t= 20 min.

3.2.3 Gelation controlled by diffusion only

Besides the small improvement in gelation time compared to just using GDL, using a solvent-controlled diffusion method suffers from other issues. The addition of H^+ occurs through the addition of molecules of acid which makes the surrounding solvent heavier than the gel sample. Once the gel sample is sandwiched between the head and coverslip, the addition of solvent would lead to the mixing of the two since the surrounding solvent is heavier than the sample and will displace it. Furthermore, the pH of the surrounding solution should be around the isoelectric point as it will regulate the final pH of the gel. But, it also cannot be constant since it would lead to gelation happening heterogeneously at the contact between the gel-forming solution and the surrounding solution. Therefore, the pH of the surrounding solution should decrease with time, reach the gelation pH after the gel-forming solution does, and stabilize at a pH close to the isoelectric point. This calls for a method that utilizes both the buffer equilibrium and GDL kinetics with the surrounding solvent diffusion.

3.3 Experimental preparation for ICAMM

From the discussion in the last section, we summarize the experimental requirements through the following points:

1. As seen in Section 3.2.2, to control the final pH of the gel-forming solution, the surrounding solvent should contain acetate as it governs the long time scale pH through diffusion. Also the ratio of GDL to acetate should be close to the value derived in Section. 3.2.1(Eq. 3.21) to have an equilibrium pH close to the isoelectric point of casein.

2. To avoid mixing, the surrounding solvent must have an equal or lower density than the gel sample. One species which definitely increases the density is the

casein which is only present in the gel sample. The other species, GDL, and acetate in the surrounding solvent should be either higher or equal concentration to the sample.

3. The pH of the sample should decrease faster than the surrounding solvent. This happens if either acetate is lower or GDL is higher in the sample. We go for excess of GDL in the sample (compared to the surrounding solvent) while keeping the same amount of acetate in the sample and surrounding, as the short-term pH is governed by the kinetics of GDL diffusion which will be more efficient in bringing the pH down faster.

Since it is the total amount of acetate+acetic acid which governs the final pH, it is possible vary the initial stoichiometric ratio of acetate to acetic acid. For instance, an initial ratio of 9:1 decreases the initial pH to a value just above the gelation zone and thus decreases the gelation time. In practice, we prepare an acetate solution by mixing 0.764 %wt sodium acetate-trihydrate ($CH_3COONa.3H_2O$, Sigma-Aldrich CAS: 6131-90-4) and 0.320 %v of glacial acetic acid (CH_3COOH, VWR Chemicals CAS 64-19-7) in 9:1 ratio so that the molar ratio in the final solution is $[CH_3COOH]/[CH_3COO^-] = 0.1$. This solution has a pH $\approx$ 5.75. Upon addition of 0.75 %wt GDL (TCI CAS: 90-80-2), the pH decreases to 5.2 in 35 min, and then slowly converges to its equilibrium pH $\approx$ 4.4, as shown in Fig. 3.6. The chemical composition are such that the final solution has $[CH_3COO^-]/[GDL] \approx 0.69$, close to the desired value derived in (Eq. 3.21). Also the assumptions for (Eq. 3.18) are valid for these values of the concentrations.

To prepare the gel-forming solution, we dissolve 1 %wt sodium caseinate (TCI CAS: 9005-46-3) in water at room temperature and mix this solution in 1 : 1 volume ratio with an acetate solution made by mixing 1.528 %wt sodium acetate-trihydrate and 0.320 %v of acetic acid in 9 : 1 ratio. The concentration in acetate is thus similar between the gel-forming and the surrounding solution in accordance with pt. 3. The initial pH of the gel-forming solution is 5.9. Before the experimentation and addition of GDL, we add Rhodamine B dye (Sigma Aldrich CAS: 81-88-9) so that we have a concentration of 2 µmol in the gel-forming solution. We add excess to the calculated amount of GDL in the gel-forming solution (Note: $GDL_{surrounding} > GDL_{sample}$). Upon addition of 2.5 %wt GDL, the pH of an isolated gel-forming solution decreases to 5.2 in 20 min and then converges to its equilibrium pH $\approx$ 3.6, as shown in Fig. 3.6. Note that the in situ gel sample will not reach this over-acidification pH due to mass transfer with the surrounding buffer.

To prepare an experiment in ICAMM, we start from an empty tank. The head is pressed onto the bottom coverslip by physical contact between the sensors and their target. Then, we add GDL simultaneously to both the gel-forming and the surrounding solutions. After 10 s mixing, we immediately pipette 200 µl of the gel-forming solution around the head. Then we fill the tank with 50-60 ml of the surrounding solution. Part of the filling is done at a controlled flow rate of 60 ml/h, using a syringe pump and a 0.3 mm inner diameter tube ending at the end of the tank close to the head, in order to minimize the mixing with the gel-forming solution. Once the perimeter of the head is surrounded, the filling is completed manually with a pipette from the other end of the tank. When the tank is filled, we raise the head by 100 µm and wait for 40-45 min for the gelation to take place after which, we put a control loop for 135 min before any test to ensure all chemical species are in equilibrium between the surrounding and the gel. Mixing of the two solutions does occur before gelation, especially at the beginning of the filling of the tank. However, the gel-forming solution is denser and stays in the hollow around the head. Furthermore, the tight confinement by the touching sphere-plane geometry prevents

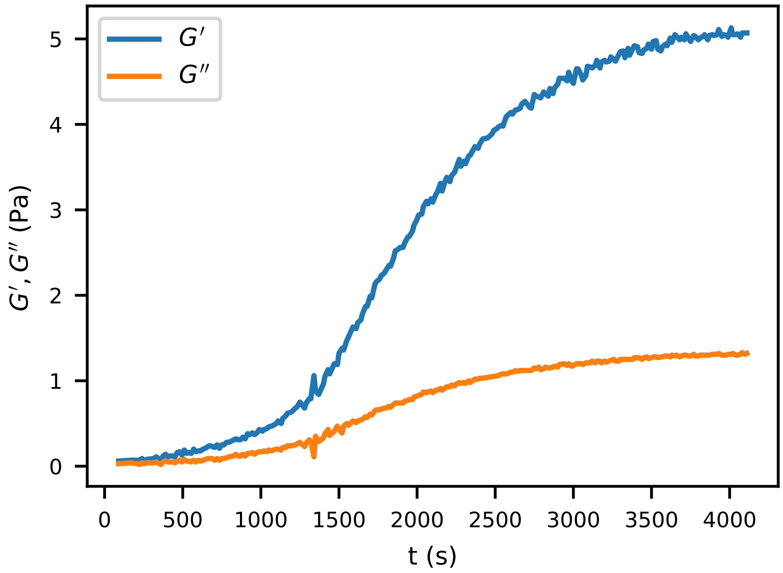

FIGURE 3.7: Evolution of elastic(G') and viscous modulus(G'' until gelation for the 1 wt% casein sample. The spike in the modulus curve at around 1400 s corresponds to the disturbance due to introduction of surrounding buffer.

mixing under the head itself. When the head is raised, the composition in the gap far from its edge is one of the pure gel-forming solutions. Indeed, as seen in Fig. 3.6, gelation in situ is observed at 20 min after mixing as in the case of pure gel-forming solution. However, long after the solutions have been put into contact, the pH of the gel-forming solution is set by the pH of the surrounding solution. Our waiting time of ≈ 3 hour is larger than the analytical estimation for hydrogen ion diffusion in Section 3.2.2. A more detailed analysis of the diffusion time based on rheometer characterization in Section 3.4.3 explains this choice.

3.4 Rheometer Characterization

We perform characterization of our system's dynamic mechanical behavior using a rheometer for three reasons:

- To determine the elastic modulus and yielding behavior.
- To see the effect of height on the modulus and verify whether having a gap of $\approx 100\,\mu$m leads to emergence of confinement effects.
- The physical chemistry of the pH changes and hence, the modulus of gel is determined by not only the dissociation but also the mass transfer. So, we try to characterize this mass transfer.

We use an Anton Paar MCR 301 rheometer with a plane-plane geometry setting with a rotor of diameter 4.3 cm. The gap between the plates is set as either 0.1 mm, 0.3 mm or 1 mm. The 1% casein sample in acetate buffer was mixed with GDL and a volume slightly in excess of the calculated amount to fill-up the gap is placed in-between the plates. Small oscillation strain of magnitude 1% and frequency 1 Hz are applied to the sample inserted. The formation of the gel can be observed with the

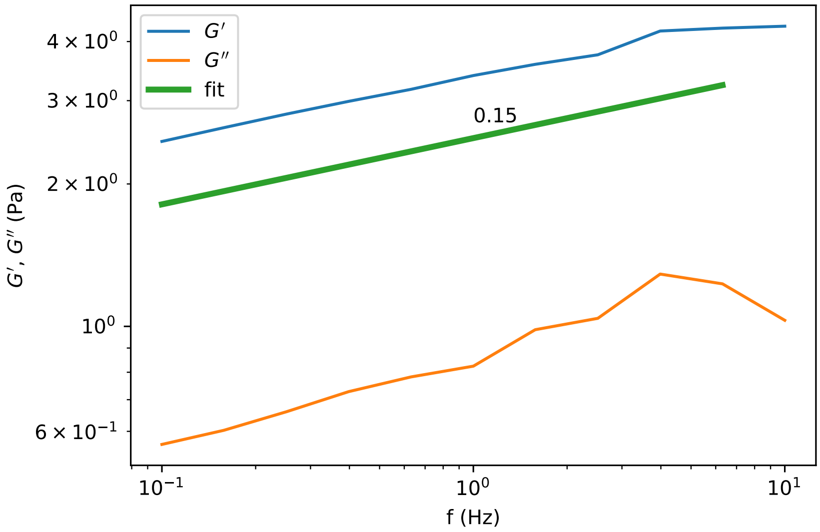

FIGURE 3.8: Evolution of elastic(G') and viscous modulus(G'' on applying a frequency sweep from 0.1 Hz to 0 Hz at strain amplitude of 1% (log-log scale). The green curve represents a power law fit of exponent 0.15

increase in G' and G'' value as seen with the plateauing in Fig. 3.7. Once $G^{'}$ reaches above 1 Pa, we fill and surround the plate-plate set-up with a large amount of surrounding solvent similar to our experiment in ICAMM. This ensures no evaporation and re-condensation of sample in addition to stabilization of the pH of the sample around the isoelectric point of casein. The oscillation experiments are stopped at a certain point in time ranging from 2 h to 15 h and creep experiments are performed until rupture.

3.4.1 Small oscillation frequency sweep

To observe the frequency dependence of G' and G'', we perform frequency sweep from 0.1 Hz to 0 Hz at strain amplitude of 1%. As seen in Fig. 3.8, the behavior of G' shows a power-law behavior with the exponent surprisingly similar to that observed by Leocmach et al [13], where the experiment was carried out on 4 wt% Casein acidified slowly by 1 wt% GDL. Thus, this indicates that our modified physical chemistry does not impact the linear rheology of our gel system.

3.4.2 Effect of gap size

For our ICAMM experiments on the microscope, we use a gap size of typically $\approx 100\,\mu m$. This is based on two factors: due to refractive index mismatch, the quality of the image degrades as we scan deeper inside the sample. With 100 µm, we are still able to observe the contrast between solvent and gel strands. Second, the acquisition time is a limiting factor in the imaging of dynamic experiments. Thus a lower gap size means a lower number of z planes in acquisition for the same z resolution. Since our gel has a pore size typical of $\approx 10\,\mu m$, we want to know how adhesion and other confinement effects might influence our experiment. To verify whether the confinement effects start dominating at lower gap size, we conduct a low strain oscillation test and creep test. The result for the two are summarized in Table 3.1 and Table 3.2 respectively.

Gap(mm)	Avg G'_{max}(Pa)
1.0	7.05 ± 0.25
0.3	6.3
0.1	7.38 ± 2.60

TABLE 3.1: Average elastic modulus at local maximum for different gap size. The number of experiments at 0.3mm was just one so we do not have an estimation of error.

Gap(mm)	σ(Pa)	$\gamma_c(\%)$	t_c(s)
1.0	20	125	15
0.3	13	130	120
0.1	18	230	1400

TABLE 3.2: Three creep experiment at different gap size and σ such that $\gamma = \frac{\sigma}{G'_{max}} \approx 200\%$. The γ_c and t_c are the strain and time of rupture respectively

As seen in Table 3.1, the maximum of the elastic modulus does not vary significantly with gap size. The value for 0.1 mm is averaged over five experiments while it is two and one experiments for 1 mm and 0.3 mm respectively. Thus the behavior of the gel in the linear regime remains unaffected and the dynamics are still governed by the bulk

By contrast, the creep behavior depends significantly on the gap size. In table 3.2 we see that the breaking time increases by two orders of magnitude between gap 1mm and gap 0.1mm, while the critical strain roughly doubles. This can be attributed to the higher number of defects in a larger volume sample, which can increase the probability of precursor nucleation and faster catastrophic failure [138].

3.4.3 Diffusion characterization: from experiments

Fig. 3.9a shows the long-term behavior of the elastic modulus. Initially, the pH inside an isolated gel (without surrounding solvent) continues to decrease towards the isoelectric point as seen in Fig. 3.6 and reaches the isoelectric point in approximately 60 min. The elastic modulus is expected to reach its maximum around this time but as seen in the inset of Fig 3.9a, it takes $\approx$ 100 min due to the simultaneous mass transfer happening due to the introduction of the surrounding buffer. This introduces an important question. How long does the pH take to reach equilibrium with simultaneous dissociation and mass transfer?

We can try to answer this question by dividing the gel behavior we observe in Fig. 3.9 into two zones. We obtain the initial time until $\approx 10^4$ s which is dominated by the dissociation and the modulus reaches the maximum and starts to go down due to the pH going below the isoelectric point. Then between $\approx 10^4$ s and $\approx 10^5$ s, we have the contribution of both dissociation and diffusion. Finally, at around $\approx 10^5$ s, diffusion of H^+ starts dominating, where we can work on the assumption that everything is dissociated and the only factor to account for is the diffusion of ions.

Taking the above assumption and additionally assuming that H^+ is the only ion we are concerned with for the change in pH (diffusion of GDL will affect the pH too, but it is at least three orders slower than H^+ [139]). We can solve the non-steady state mass transfer equation in cylindrical coordinate akin to the method described in Section 3.2.2 to get the concentration profile with time.

From (Eq. 3.23), we see that the solution depends on the radial position but the time constant of the decay is independent of it and hence, we can get an idea of the

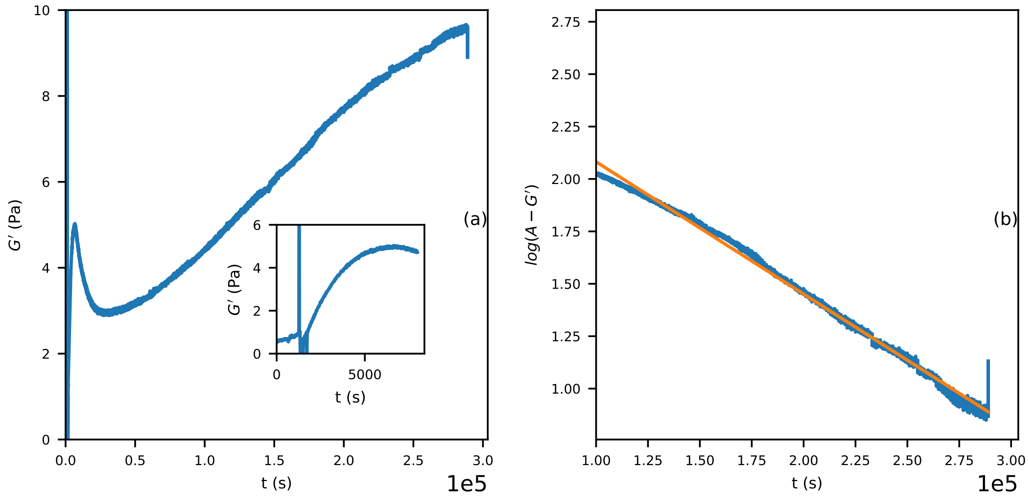

FIGURE 3.9: (a) Evolution of elastic modulus (G') on long time scale (over 5 decades in seconds). Inset: G' plotted for $t < 7000$ s (b) An exponential decay fit for (G') with the best fit for the ending (diffusion governed t>10^5 s) obtain for A = 12. The decay constant $\tau \approx 158 \times 10^3$ s (44 h) is given by the slope of the plot.

real-time constant if we fit the elastic modulus curve in the diffusion dominant zone with an exponential such that

$$G = A - Be^{\frac{-t}{\tau}} \tag{3.28}$$

where τ defines the characteristic decay time of the modulus. We need an estimate for A (in Pascal) before we can estimate B and τ through fit. For $A = 12$, we have a good fit applying best at higher time decades when this model should fit better with the real experiment. The result of the fit is shown in Fig. 3.9b. The value of τ from the fit is $\approx$ 44 h. hence, τ is equivalent to the unsteady state decay constant $\frac{1}{D\alpha^2}$ in (Eq. 3.23). α has units of m^{-2} and hence, we assume that its inverse is the characteristic length scale of diffusion and is equal to the radius of the cylinder, a. Thus $\tau \propto a^2$. Assuming this scaling for α , this approximates the time for stabilization below the ICAMM head of radius $a = 6$ mm to be $\approx$ 3.5 h.

An analytical solution to (Eq. 3.23) similar to the one in Section 3.2.2 is given by

$$\frac{C_1 - C}{C_1 - C_0} = 1 - \frac{2}{a}\sum_{n=1}^{\infty}\frac{e^{-D\alpha_n{}^2 t}J_0(r\alpha_n)}{\alpha_n J_1(r\alpha_n)} \tag{3.29}$$

The solutions of this for the center of the cylinder ($r = 0$) are plotted in Fig. 3.10 for the two cases we are interested in i.e. the plate-plate rheometer geometry ($a =$ 2.1 cm) and the ICAMM setup ($a = 0.6$ cm). The theoretical times of chemical equilibration differ by an order of magnitude from the times measured in experiments. However the scaling in $\tau \propto a^2$ consistently predicts the saturation at 3.5 h in ICAMM from the measurement in the rheometer.

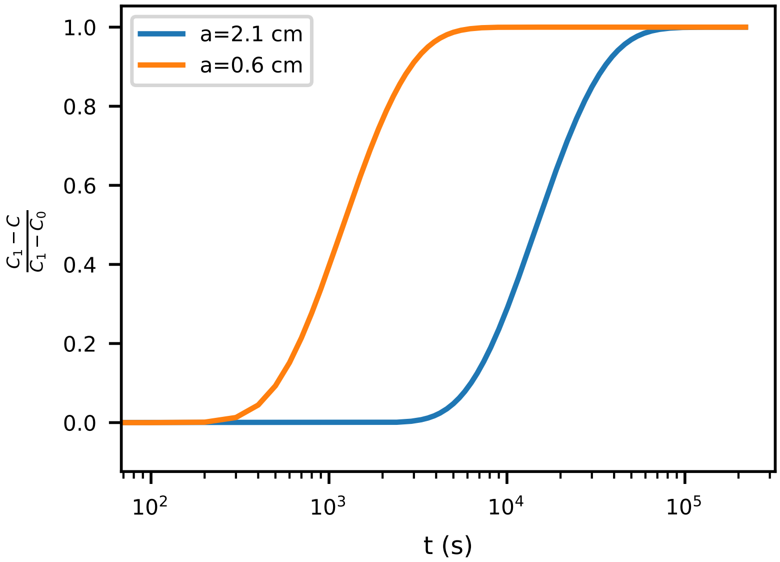

FIGURE 3.10: Normalized concentration using (Eq. 3.29) at the center of the cylinder for the model diffusion of H^+ inside a cylinder for the two radius, $a = 2.1\,\text{cm}$ and $a = 0.6\,\text{cm}$ corresponding to the rheometer upper rotor and the head of ICAMM respectively

Key concepts of the chapter: We have discussed the physical chemistry of caseinate gel system and the method we employ for experiment in ICAMM:

1. We propose a faster gelation method combining the usage of a buffer of acetate and diffusion with the surrounding buffer to arrest the drop in pH on addition of excess GDL. This will help in a fast stable in situ gelation in ICAMM.

2. We have characterized the diffusion time between the gel sample and surrounding solvent using an analytical model and experiment in rheometer.

3. Through rheometer experiments down to a gap size of 100 µm, we do not observe confinement effect on the viscoelastic linear behavior while the dependence of failure time and strain on the gap size is explained through volume effect.

> It doesn't matter how beautiful your theory is, it doesn't matter how smart you are. If it doesn't agree with experiment, it's wrong.
>
> Richard P. Feynman

Chapter 4

ICAMM: Proof of Concept

The above quote from Feynman's lecture on scientific method, defines the line of thought in how modern science is distinguished from philosophy by requiring observational/experimental validation for theories. Here instead of a theory, we test through experiments whether our cantilever-based setup ICAMM can perform rheology on the soft casein gel system, the protocol for preparation of which was defined in Chapter 3. We test small step strain response and step stress response to show the implementation of the PID control loops we developed, described in Chapter 2 and quantify the precision and sensitivity of the setup. Incremental step strain experiments or creep experiments are performed to observe the macroscopic response from linear to the non-linear regime until fracture. The ability of this setup to observe microstructural changes under shear is demonstrated by linking macroscopic behavior to microscopic softening near the head, verified using image correlation analysis in the incremental strain step experiment. Finally, a similar analysis is used in the creep experiment to infer the shortcoming of such analysis in detecting mesoscale changes in the gel and the need for finer displacement estimation techniques.

4.1 Strain control

4.1.1 Step strain

To test our control loop, we do a step strain experiment and record the stress response from the deflection of the cantilever. As shown in Fig. 4.1a, we fix a set point at $x_{\text{head/ground}} = 0\,\mu\text{m}$ for 60 s, and then update the set point to $x_{\text{head/ground}} = 3\,\mu\text{m}$. This corresponds to a shear strain of 0.03. The PID ($K_p = 0.1$, $K_i = K_d = 0$) controller acts on $x_{\text{head/ground}}$, that is to say the shear strain of the gel. The action of the proportional controller is limited by the step size of the micromanipulator motion and results in a steady state error associated with a proportional controller given by:

$$e_p = \pm\frac{1}{2K_p} \tag{4.1}$$

This is equivalent to 0.3125 µm, which is shown as the dotted red line in Fig. 4.1a and Fig. 4.1b

In Fig 4.1b, we see the zoom of Fig 4.1a ±10 s around the update time of the set point. The controlled variable $x_{\text{head/ground}}$ converges to the set point in 5 s. To speed up the response, we can increase the K_p or use a PI controller with the constraint of ensuring no overshoot in the response. Fig 4.1c shows the change in deflection $\Delta x_{\text{head/arm}}$, a measure of shear-stress. The deflection $\approx 0.5\,\mu\text{m}$ corresponds here to a shear force $\approx 1\,\mu\text{N}$ and hence, $\sigma \approx 30\,\text{mPa}$. Fig 4.1d is the zoom of Fig 4.1c on same time scale as Fig 4.1b. We see clearly a progressive stress shift at the transition

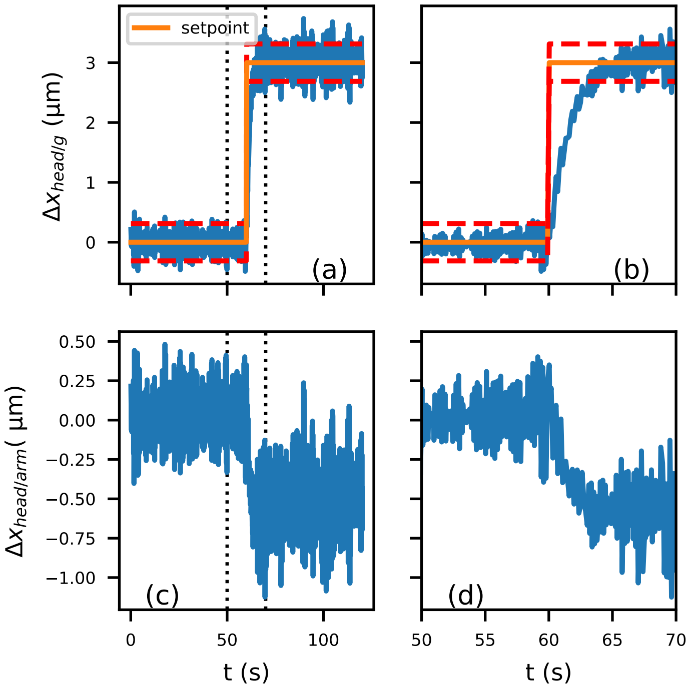

FIGURE 4.1: Step strain response: (a) The desired set-point (in orange) for a step displacement in x of 3 µm and the actual displacement response (blue) with time. The red dashed lines show the steady-state error of the proportional controller $\pm e_p$ with $K_p = 0.1$. During the entire duration, we keep the strain in z constant. (b) Zoom ±10 s (dotted lines in (a)) before and after the transition in displacement $\Delta x_{\mathrm{head/ground}}$. (c) change in deflection $\Delta x_{\mathrm{head/arm}}$ corresponding to the applied strain and (d) zoomed of $\Delta x_{\mathrm{head/arm}}$ around the transition time

confirming that the gel is attached and responding to the head motion. The standard deviation of the stress measurement over 5 s is ≈ 10 mPa. This is of the order of our theoretical precision in stress.

4.1.2 Shear strain steps

We can repeat strain steps to test the mechanical behavior of the gel at larger strains. Here, we start the test 210 min after mixing of GDL. In Fig. 4.2a, we show the strain γ_x applied using a proportional controller ($K_p = 0.1$, $K_i = K_d = 0$), in which set point for x position increases by steps of 10 µm (8.7 %) strain every 7 min until a shear strain of 174 % (set point not shown). The gap is kept constant at $h_0 = 115$ ±0.3 µm by a second proportional controller with same constant, leading to normal strain fluctuations $\delta\gamma_y \approx 0.25\%$ as shown in Fig. 4.2b. After each step, the shear stress shown in Fig. 4.2c displays the same non-linear viscoelastic relaxation as reported in Ref. [47] (see Section 1.4.1). Because of this unsteady value, the error in stress measurement is better estimated at a long time when the rate of change is the lowest. Indeed, during the last 10 s of the first step ($\gamma = 8.7$ %), the standard deviation of the stress is ≈ 5 mPa, comparable to the theoretical uncertainty predicted in Section 2.3.4, and half of the value measured in Section 4.1.1. We guess that this previously measured larger uncertainty was actually due to the drifting mean because of the viscoelastic relaxation.

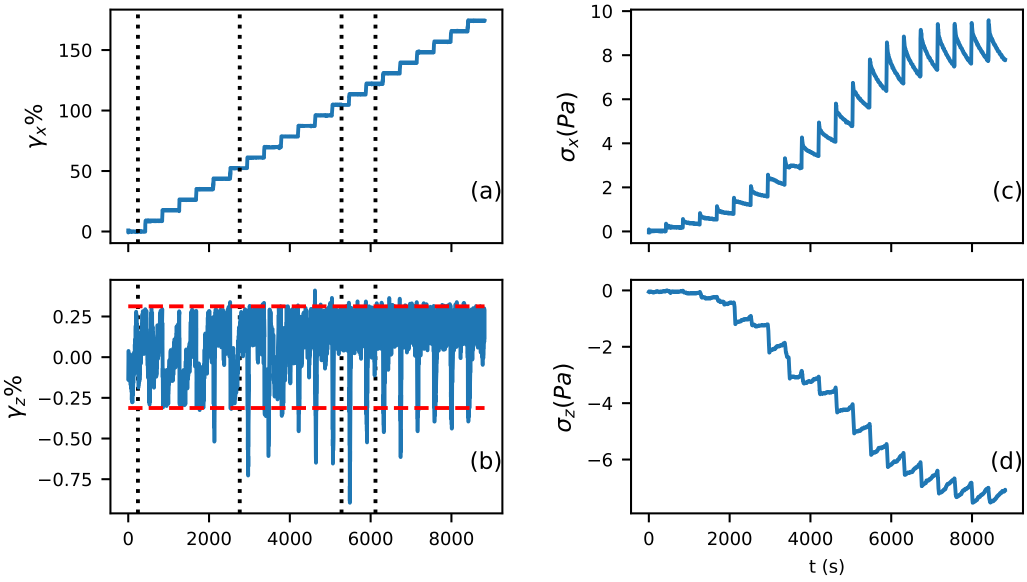

FIGURE 4.2: Behavior at large strain: shear strain setpoint increasing in steps of 8.7 % every 420 s from 0% to 183% for a constant normal strain setpoint. (a) Measured shear stain. (b) Measured normal strain. The red dotted line indicate the steady-state error of the proportional controller (c) The measured shear stress and (d) normal stress variation with time. Dotted vertical lines in (a) and (b) mark the times of the pictures in Fig. 4.6.

By averaging the last 10 s of each step, we obtain the stress-strain dependence (Fig. 4.3). Overall, the gel is strain hardening between 34 % and 121 %, and strain softening at larger strains instead of undergoing a sudden drop in stress as expected from the brittle fracture in these system [47] . Compared to Ref. [47], where they observe the relaxation of step strain, our gel displays a much larger strain hardening domain. This is expected as due to the four-time lower casein concentration, there are less topological restrictions on stretching of the gel leading to a longer non-linear hardening phase without breaking [72]. From the linear regime at strain below 34 %, we extract an elastic modulus $G' = 1.986 \pm 0.085$ Pa by applying a linear fit to the average of stress value for the last 10 s as a function of strain as shown in Fig. 4.4. The error includes systematic uncertainty (see Section 2.3.4). Taking into account the $G \propto \omega^{0.15}$ scaling of casein gels [13] and the low equivalent frequency of our measurements ($\approx 1/7$ min), the rheometer measurement at 1 Hz (≈ 7 Pa see Section 3.3) interpolates to ≈ 2.9 Pa. The lower value measured by strain steps can be attributed to two factors: 1) the difference in gelation and later rheology procedures in the two experiments and 2) normal force conditions: it has been shown that gels like protein and polymer gels show variation in shear modulus and breaking time-based on the normal force condition they are constrained by during their aging (For instance no control, constant strain, constant stress in the normal direction) [140, 141]. Here, our gel is under constant shear and normal stress after the gelation (≈ 40 min) and before the creep (≈ 210 min), while in the rheometer experiment, we are always under constant normal strain. For polysaccharide gels, the sol/gel transition is associated with a reduction in volume, and under constant strain conditions, lead to the stretching of gel inducing hardening and drift of G' to higher values.

Fig. 4.2d shows that the normal stress is also reliably measured, and follows the shear stress. As seen in Fig. 4.3b, the normal stress gradually increases from zero in the linear regime to a negative value. The large magnitude of the negative

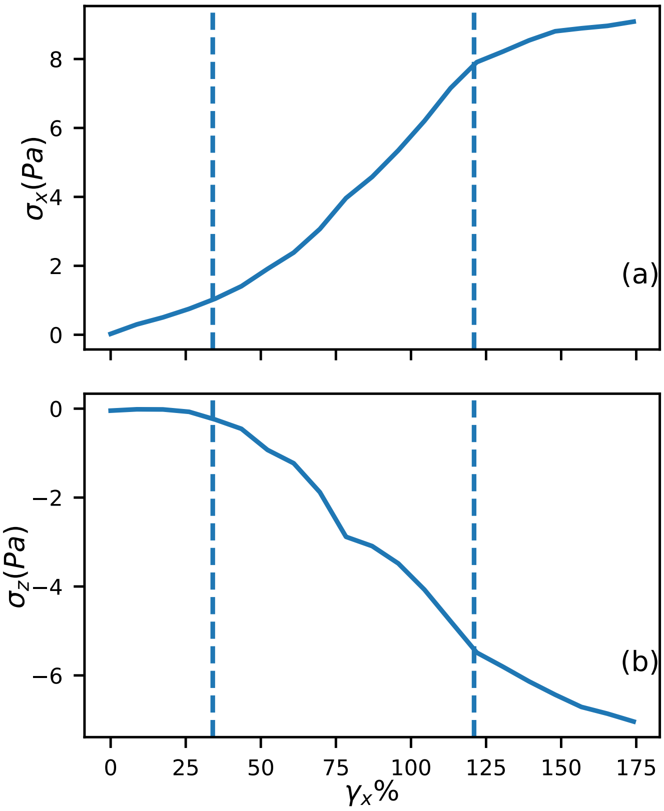

FIGURE 4.3: Behavior at large strain: shear strain setpoint increasing in steps of 8.7 % every 420 s from 0% to 183% for a constant normal strain setpoint. (a) Shear stress and (b) Normal stress as a function of applied shear strain. Both the stresses are obtained by averaging over the last 10 s of the step Dotted vertical lines in (a) and (b) represent strain at 34% and 121%

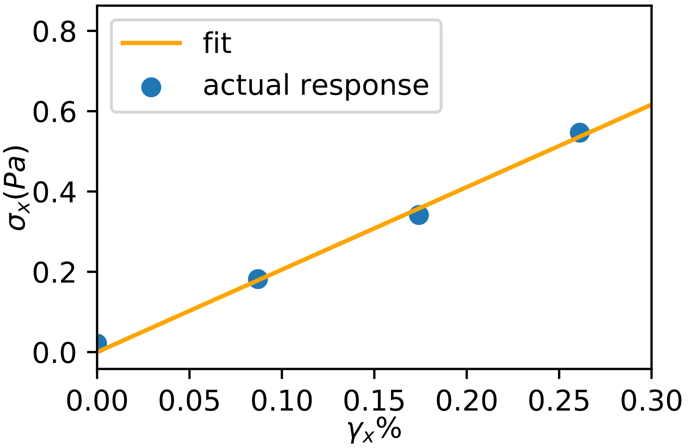

FIGURE 4.4: The stress-strain points (filled circle) obtain by averaging over the last 10 s of the stress relaxation for strain step in the linear regime corresponding to $\gamma_x < 34\%$. The linear-fit corresponds to the best fit with a slope representing the elastic modulus $G' = 1.986 \pm 0.085\,\text{Pa}$

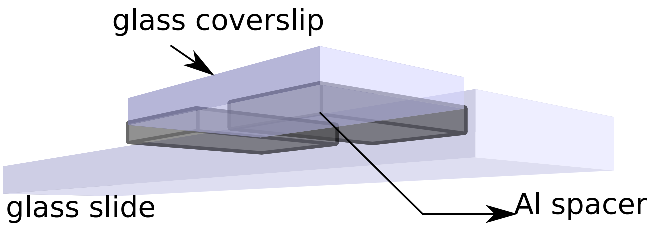

FIGURE 4.5: Schematic representation of the calibration setup used to get the axial scaling factor required to obtain the correct z distances

value is linked to the same reasoning as strain hardening in the non-linear regime i.e. the non-linear stretching of the gel strand in the extensional direction (see Section 1.4.1) [76, 142].

4.1.3 Simultaneous confocal acquisition

As a proof of concept, we performed three-dimensional confocal acquisition (Leica SP5, 488 nm excitation). Crucially, we use here an objective lens without immersion fluid (Leica HC PL APO 40× NA=0.95 CORR). Previous attempts with oil or water immersed objectives have revealed that the immersion fluid was transmitting enough force from the z-scanning objective to bend the coverslip by a few micrometers and perturb the mechanical measurement. Without optical immersion fluid, there is no signature of the z-scanning cycle on the measurements shown in Fig. 4.2.

Z calibration

Due to the difference in the refractive index of air and our sample, a shift of objective focus lead to the gap size measured between the coverslip and the head being incorrect, specifically smaller than the real gap size in our case. The measured gap size is also affected by the deterioration of the point spread function(PSF) leading to a decrease in resolution. Thus an axial scaling factor needs to be introduced for all the distances measured in the z direction. Simple scaling of the distances based on geometric optics requires measurement of the refractive index of our gel sample. It can also lead to overestimation of the axial factor in case of high numerical aperture objective [143].

To avoid this we rely on experimental measurements similar to Ref. [143] to get the precise axial calibration. To do this we make a custom cell by sticking two aluminum foil spacers followed by a coverslip on the top, as seen in Fig. 4.5. The spacer is bonded to the glass slide and the coverslip using UV glue (Norland Optical Adhesive 65). The gap size is decided by the thickness of the spacer as well as the thickness of the UV glue layer. The gap in the empty calibration cell is measured to be 113 µm using the confocal in reflection mode. It is then filled with the casein sample and the distance is measured in fluorescence mode using the 40x objective to be 73 µm. The ratio of the two measurements gives the axial factor as ≈ 1.55. In the following, all distances in the z direction will be scaled by this factor.

Microscopic picture

We start each stack at the 4$^{\text{th}}$ minute of each step. The full $228 \times 228 \times 139$ µm stack is acquired in 120 s and is centered on the axis of the sphere-plane geometry. In this way, we obtain a 3D stroboscopic view of the microstructure responding to shear.

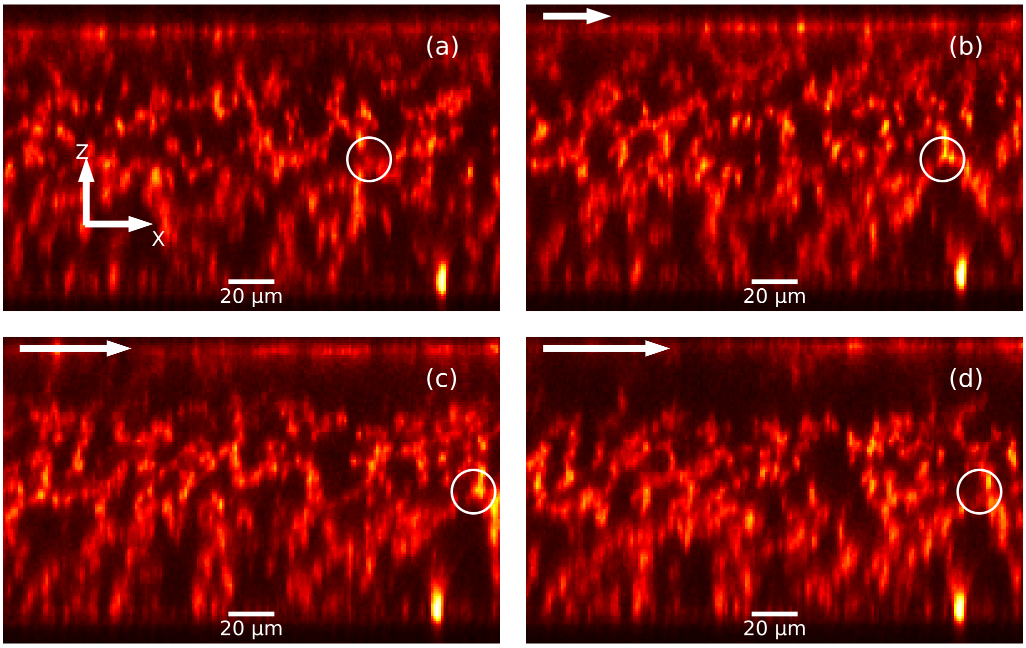

FIGURE 4.6: Microstructure visualisation during strain steps. From (a) to (d): Cut in the shear plane (x, z) from 3D confocal acquisition at 0%, 52%, 104% and 121% of strain respectively. The top of the panel is the head and the bottom the coverslip. The magnitude and direction of shear strain applied to the head is indicated by the white arrows at the top of each panel and by the dotted vertical lines in Fig. 4.2. Displayed images are the average of 10 (x, z) planes of the confocal stack for a total thickness of 4.45 µm. The white circle tracks a section of the gel and its approximate trajectory.

In Fig. 4.6, we show a cut through the acquired volume in the shear (x, z) plane at four different steps: $\gamma = 0\%$, 51%, 102% and 121%. In Fig. 4.6a, we qualitatively observe that the density in protein is not constant along z: there is an adsorbed layer on both the coverslip at the bottom and on the head at the top. Furthermore a few microns below the head, the density seems to be lower than in the bulk of the gel. Between Fig. 4.6a and c, we observe the progressive shear of the gel network. At $\gamma = 111\%$, the adsorbed layer on the head is completely detached from the bulk of the gel in the observable zone and as seen in Fig. 4.6d, the bulk of the gel undergoes viscoelastic recoil. Since we do not observe a corresponding drop in the macroscopic shear stress response expected with complete failure (see Fig. 4.3a), we think that the fracture does not reach the edge of the head. Indeed, as detailed in Section 2.3.3, further away from the axis of the geometry the gap is larger and the strain and stress are smaller, so that it may not be enough for the fracture to propagate.

2D image correlation

From the confocal images, we can obtain the displacement profile in the gel (Fig. 4.7). We use plane by plane 2D image phase correlation (See Chapter 5) for details of the method) between consecutive stacks [144], and accumulate these displacements from 0 to γ_x to obtain a displacement profile $\Delta x(z)$ at each step γ_x. Since the scanning direction and the shear direction are well aligned, displacements along y are at least two orders of magnitude smaller than along x and are thus not significant. The image phase correlation is performed with an upsampling factor of 10, i.e. to within

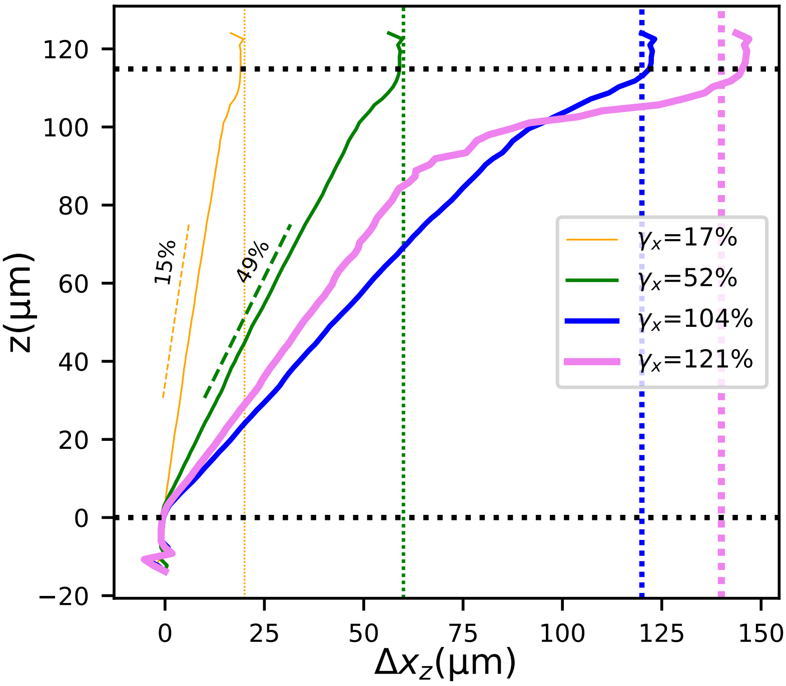

Figure 4.7: Displacement profile in the gap. The displacement in the shear direction (x) is obtained by accumulating the image correlation computed value between two consecutive time frames. The four curves are for macroscopic strains 17%, 52%, 104% and 121%. The dotted line next to the curve with slope value correspond to the best fit for the strain in the bulk of the gel. The horizontal dotted line denotes the coverslip (bottom) and the head (top) position. Vertical dotted lines denote the macroscopic imposed strain value for the four plotted curves. The error in Δx_z estimation is $\approx$ 45 nm

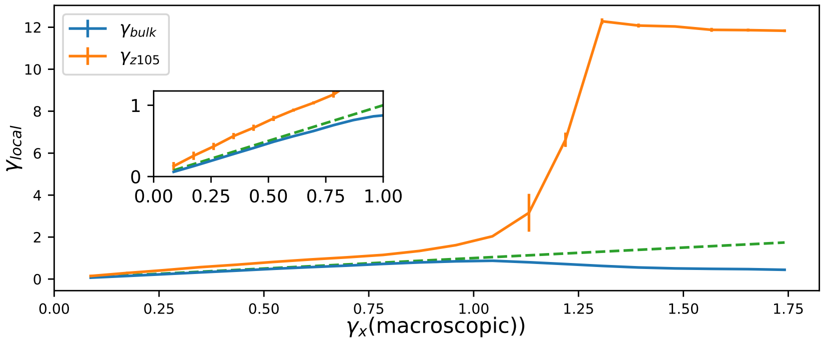

Figure 4.8: The local strain for the bulk of gel (blue cuve) and at z = 105 μm(orange) as a function of macroscopic strain (γ_x) measured by ICAMM. The bulk curve is obtained from the slope of the best fit of Fig. 4.7 in between z = 25 μm and z = 62 μm. The local strain at z = 105 μm (orange) is obtained by calculating the gradient of Fig. 4.7 between the adjacent pixels corresponding to z = 105 μm. Dotted line represent $\gamma_{local} = \gamma_x$. Inset shows zoomed in curves for ($\gamma_x < 1$)

a tenth of a pixel. Thus the error in Δx is $\approx 45\,\mathrm{nm}$. The instantaneous absolute uncertainty for the 2D image correlation in shear strain can be defined as the ratio of Δx by resolution in z which is equal to $\approx 4.5\%$.

For small strains (see e.g. the yellow curve in Fig. 4.7), we observe that the strain is almost homogeneous in the whole gap, with a linear $\Delta x(z)$ for $5\,\mu\mathrm{m} \leq z \leq 100\,\mu\mathrm{m}$. However, we notice that close to the coverslip or the head, the slope is steeper for a few microns, indicating harder materials that may correspond to the adsorbed layers of gel in the glass coverslip. Furthermore, we observe a smaller slope, i.e. a softer layer, below the head for $100\,\mu\mathrm{m} \leq z \leq 110\,\mu\mathrm{m}$. This behavior is conserved until $\gamma_x = 104\%$, with a softening of the already soft layers, probably due to damage accumulation. This can be also seen in Fig. 4.8 where the bulk strain starts to deviate from the macroscopic measured strain even before $\gamma_x = 1$ with the top soft layer becoming softer around the same point. Finally, at $\gamma_x = 121\%$ (pink curve on Fig. 4.7) we observe a complete rupture of the soft layer, where the top layer remains adsorbed on the head. This is seen also in the local strain signal for the softer portion in Fig. 4.8 were for $z = 105\,\mu\mathrm{m}$ we see an asymptotic increase in local strain signaling shear banding. By contrast, the bulk of the gel recoils viscoelastically as seen in the decrease in bulk strain in Fig. 4.8, which widens the fracture and reduces the extent of the linear zone.

This quantitative, space-resolved analysis is a proof of concept, showing that ICAMM can be integrated with confocal microscopy and yield more detailed information than what is captured by the global mechanical response alone.

4.2 Stress control

4.2.1 Step stress

By controlling the cantilever deflection, ICAMM can also perform step stress experiments and record the strain response. Here, the control on $x_{\mathrm{head/arm}}$ is ensured by a proportional-integral (PI) controller. We use a Ziegler-Nichols method [145] to optimize the constants of the controller: $K_p = 0.45 K_u$,$K_i = 0.54 K_u / T_u$, where K_u is the ultimate proportional gain at which the output displays stable oscillations and T_u is the time period of these oscillations. Since oscillations of diverging amplitude quickly destroy the gel, requiring a new sample each time, we limited ourselves to a range $0.35 < K_u < 0.5$ and $T_u \approx 40\,\mathrm{s}$. Exploring from these values, we obtain a stable response without overshoot for $K_p = 0.2$ and $K_i = 0.001$.

As shown in Fig. 4.9a, we fix a set point at $x_{\mathrm{head/arm}} = 0\,\mu\mathrm{m}$ for 300 s with a compliant PI controller ($K_p = 0.01$ and $K_i = 0.001$), and then update the set point to $x_{\mathrm{head/arm}} = 11.50\,\mu\mathrm{m}$, that is to say an effective stress $\sigma_0 = 0.79\,\mathrm{Pa}$, with the tighter controller determined above ($K_p = 0.2$ and $K_i = 0.001$). We expect a steady state error $e_p = 0.02\,\mathrm{Pa}$ (see (Eq. 4.1)), further narrowed by the integral term with a time constant of the order of 20 s.

In Fig 4.9b, we see the zoomed in version of Fig 4.9a to $\pm 25\,\mathrm{s}$ around the update of the set point. The controlled variable $x_{\mathrm{head/arm}}$ converges to the set point in 10 s and remains stable on much longer times (inset of Fig 4.9d). Fig 4.9c shows the change in position $\Delta x_{\mathrm{head/ground}}$, a measure of shear-strain. Fig 4.9d is the zoomed in version of Fig 4.9c on same time scale as Fig 4.9d. We see clearly that the strain evolves in time even after the stress has settled to its set point value.

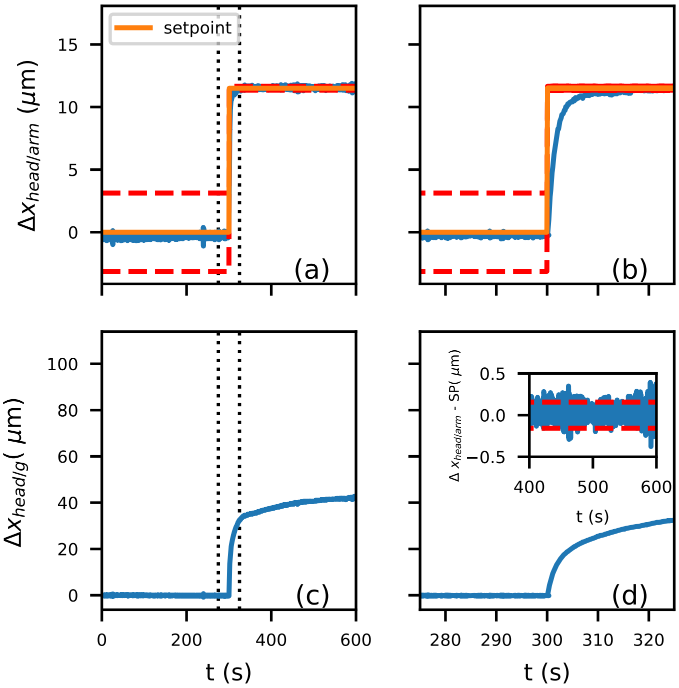

FIGURE 4.9: Step stress response: (a) The desired set-point (in orange) for a step deflection in x of 11.50 µm and the actual deflection (blue) with time. The red dashed lines show the steady-state error of the proportional controller $\pm e_p$. During the entire duration, we keep the strain in z constant. (b) Zoom ±25 s before and after the step in set point, see dotted lines in (a). (c) Change in position $\Delta x_{\text{head/ground}}$ corresponding to the applied stress and (d) zoomed-in around the transition time. Inset: Stability of the deflection around the set point at later times.

.

4.2.2 Creep tests

Finally, we demonstrate that the ICAMM is able to study the long-time response to constant shear stress. For the procedure, after mixing GDL, we keep the gel under no control for the initial 45 min and then apply zero force in both shear and normal direction for the next $\approx$ 135 min ($K_p = 0.01, K_i = 0.0005$). Then, we estimate the elastic modulus by performing small strain steps of 3% from 0% to 9% in step, 60 s each. A linear fit of the stress response (not shown) gives $G' = 1.418 \pm 0.156$ Pa

For the experiment depicted by the thin red curve in Fig. 4.10, 210 min after mixing, we change the set point in the x direction to $\sigma = 2.13$ Pa, i.e. a deflection of 31.10 µm with $K_p = 0.2$ and $K_i = 0.001$. In the y direction, the gap measured from the confocal images is kept constant $h_o = 115$ µm with $K_p = 0.1$ and $K_i = 0.001$. The actual applied stress is shown in Fig. 4.10a. It converges to its set point in $\approx$ 10 s. The same procedure is followed for the blue thick curve with the applied stress changed to $\sigma = 1.77$ Pa.

In Fig. 4.10b, we show the evolution of the strain in a log-log scale. We clearly observe at short times (< 10 s) the regime where the response is dominated by the convergence of the feedback and the gel responds elastically. At the intermediate

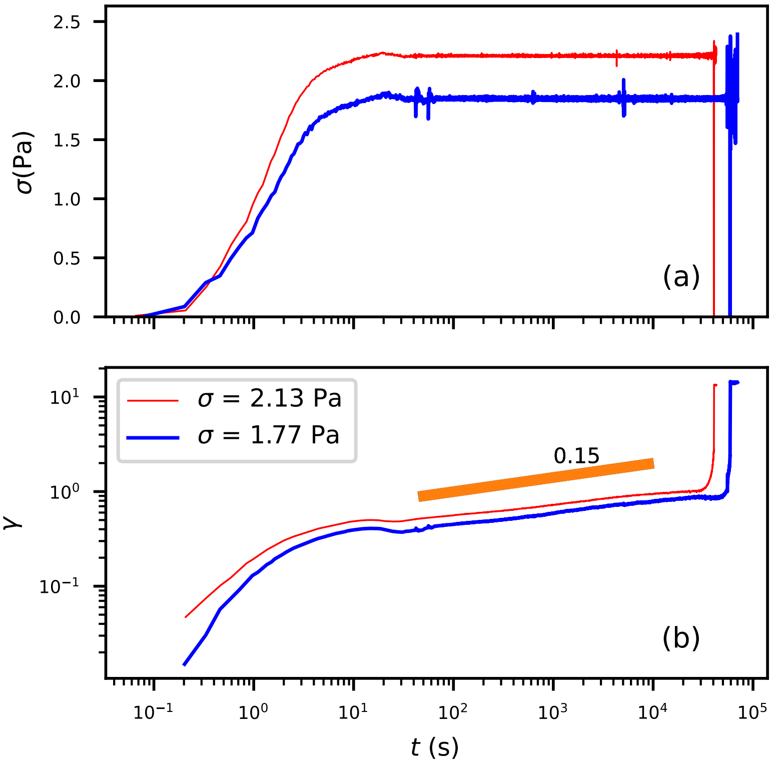

FIGURE 4.10: Constant shear experiments on a gel where $G' \approx 1.4\,\text{Pa}$. At t=0, the set point jumps from zero to $\sigma = 2.13\,\text{Pa}$ (thin red curve) or 1.77 Pa (thick blue curve). The gap is kept constant at $h_o \approx 115\,\mu\text{m}$ and 135 µm respectively. (a) The actually applied stress function of time. The set point is reached in 10 s without overshoot. (b) The shear strain response function of time in log-log scale. The straight line highlights the power-law regime after initial convergence of the feedback loop.

time scale, the stress is properly applied and can be considered constant. We observe the power-law regime characteristic of the frequency-dependent viscoelastic response of casein gels $\gamma \sim t^\alpha$ [13] (see Section 1.2.4) with a similar value of the exponent $\alpha \approx 0.15$. We demonstrated in Section that our 1 wt % shows a similar power-law, verifying that the macroscopic creep can be explained by linear viscoelasticity. Interestingly, the creep extends over four decades of time. This slow linear creep until $\gamma \approx 1$ is followed by a fast divergence of the strain that indicates nucleation and growth of fractures. Finally, the gel undergoes full rupture seen in the asymptomatic growth of the strain.

4.2.3 2D Image correlation in creep

For the experiment where we apply $\sigma = 2.13\,\text{Pa}$ on the gel (thin red curve in Fig. 4.10), we acquire 3D stack of size $228 \times 228 \times 139\,\mu\text{m}$ continuously until fracture with each stack taken in $\approx 70\,\text{s}$. Similar to Section 4.1.3, we perform plane by plane image correlation between consecutive time frames and accumulate the displacement over time. The result for some selected z position is shown Fig. 4.11a and Fig. 4.11b for both the x and y direction respectively. As seen, the displacement is mainly in the shear direction and the y displacement is at least an order of magnitude less. The curve for height 127 µm is representative of the displacement of the head and

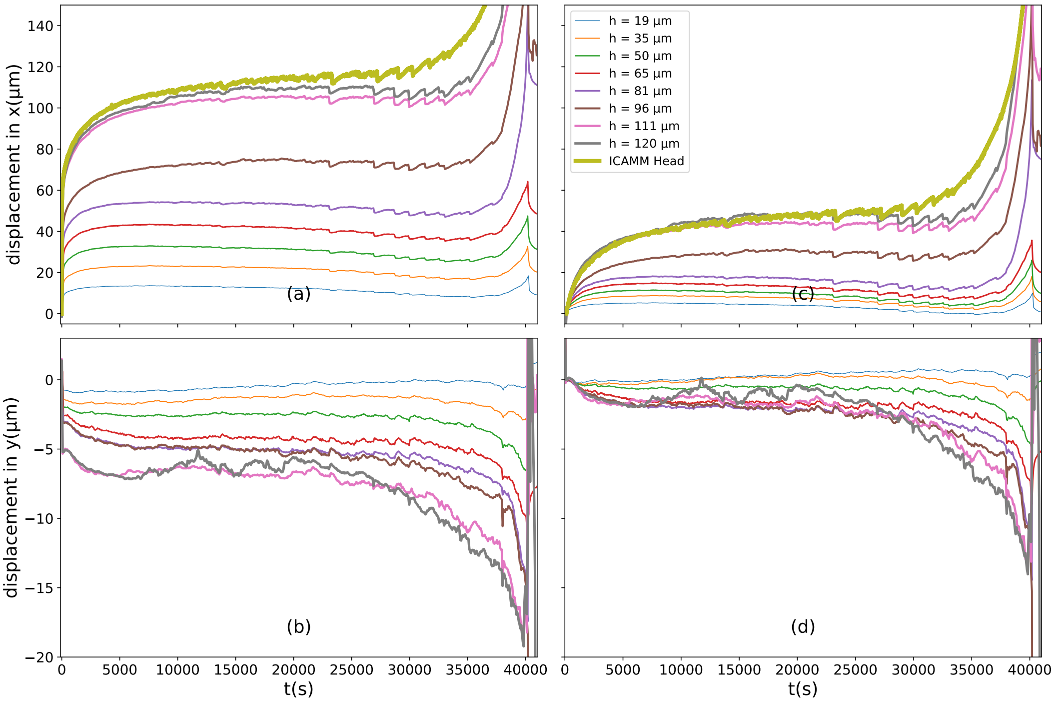

FIGURE 4.11: Result of cumulative displacement at different z inside the gel of height $\approx 115\,\mu\text{m}$ after applying $\sigma = 2.13\,\text{Pa}$ obtained by applying image correlation between consecutive time frame. (a) The displacement in shear direction (x) and (b) in orthogonal direction (y). The thick green curve in (a) is the position of the head and representative of the global shear strain. (c) and (d) are respectively the x and y cumulative displacement with respect to the position at $t_0 + 70\,\text{s}$ i.e. removing the contribution of the displacement between the two first frames.

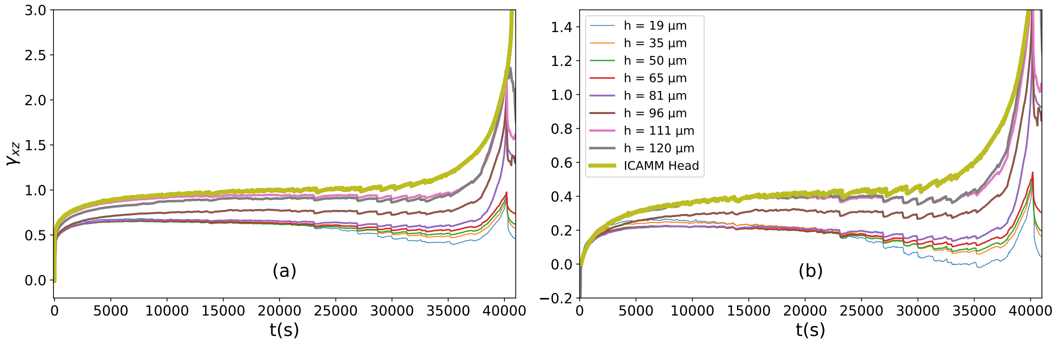

FIGURE 4.12: The cumulative strain at the height $\gamma_{xz} = \frac{\text{displacment in x}(\mu\text{m})}{z}$ at different z inside the gel of height $\approx 115\,\mu\text{m}$ after applying $\sigma = 2.13\,\text{Pa}$ obtained by applying image correlation between consecutive time frame. The thick green curve in (a) and (b) is the position of the head and representative of the global shear strain. (b) is the value $\approx 70\,\text{s}$ after the application of creep obtained by removing the contribution between the first and second time frame.

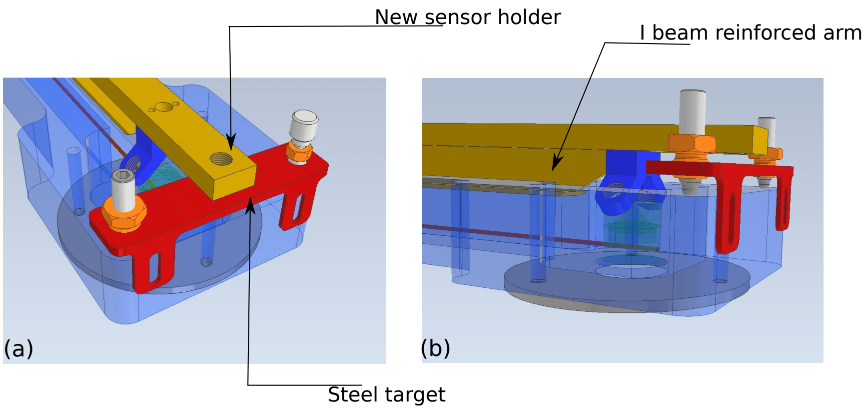

FIGURE 4.13: Additional 3^{rd} sensor to measure accurately the z position accounting for the vertical motion due to creep. (a) angled top view and (b) angled side view.

should match the magnitude of the head displacement obtained from measurement in ICAMM, shown by the thick green curve in Fig. 4.11a. The image correlation is performed with an upsampling factor of 100, i.e. to within 100th of a pixel. Thus the error for single image registration is $\approx 4.5\,\mathrm{nm}$ which will be of the order of $\approx 3\,\mu\mathrm{m}$ for a sequence with 700-time frames (approximately the number of time frames plotted in Fig. 4.11). The difference can also be accounted for by the fact that the time taken to image one plane is $\approx 0.7\,\mathrm{s}$, which is slower compared to the fast dynamics in the initial transition period (before $\approx 10\,\mathrm{s}$), making the measurements less reliable. In fact, if we measure the displacement removing the motion of the first time frame as shown in Fig. 4.11c and 4.11d, we see that the initial creep of the head and $z > 110\,\mu\mathrm{m}$ overlap.

In Fig. 4.11a and Fig. 4.11c, we observe at the resolution of the plane size that the gel follows the global shear motion but above $z = 81\,\mu\mathrm{m}$, it creeps faster than the gel below. It can be seen much clearer if we define the local strain for the gel at different z as seen in Fig. 4.12. The curves for $z \leq 81\,\mu\mathrm{m}$ overlap while the heights above display a softer behavior. Thus we hypothesize that at the end of the linear creep, nucleation and fracture proceeds at this z leading to an asymptomatic increase in strain for the gel above z = 81 μm while the gel below z = 81 μm breaks and undergoes elastic recoil. Also around the midway ($t \approx 20\,000\,\mathrm{s}$) of the creep, we observe a small decrease in the displacement, the origin of which is explained in the next section and will be quantified in Section 6.1. Any detail about the x,y location of the nucleation and the mechanism leading to the shear banding is hard to infer from the plane by plane image correlation and we need to obtain displacement within the plane at least of the scale of the pore size of the gel. A particle-level tracking algorithm is not possible for our caseinate gel. Thus, analysis technique for estimation of small-displacement locally or simplification of our gel into node and edges can help capture local rearrangements or rupture events, which will be the focus of the next chapter.

4.3 Position control in z

At the start of this year, we discovered that the position of our head is changing i.e. moving in the upward direction even when we have a control loop acting on it. This can be seen by the slight shift in head position in Fig. 4.6. Although it seems quite insignificant here, over the duration of a creep test which lasts almost 10× longer, it can be quite larger. Over a long time, this affects our claim of precise control as well can impact fracture nucleation mediated by the change in normal strain.

We have discovered that the source of it is the creep in the duralumin arm shown in Fig. 2.3. To account for the vertical creep motion of the plate, we change our measurement method by introducing a third sensor as seen in Fig. 4.13. The sensor is fixed at the end of the arm. It measures the position of a steel target fixed to the tank, shown in red in Fig. 4.13. This gives us the accurate position of the arm w.r.t ground i.e. $z_{\mathrm{arm/ground}}$. Considering the arm plate is creeping, we have to account for the two-position separately: the base of the arm which is attached to the micromanipulator, and the end of the arm which is close to the sensor. The actual deflection of the head in the z direction can thus be given by $z_{\mathrm{head/armBase}}$ which is equivalent to

$$z_{\mathrm{head/armBase}} = z_{\mathrm{head/armEnd}} + z_{\mathrm{armEnd/armBase}} \tag{4.2}$$

We don't know $z_{\mathrm{armEnd/armBase}}$ but it can be reduced to known quantities such that

$$z_{\mathrm{head/armBase}} = z_{\mathrm{head/armEnd}} + z_{\mathrm{armEnd/ground}} - z_{\mathrm{armBase/ground}} \tag{4.3}$$

$z_{\mathrm{head/armEnd}}$ is known from the calibration matrix of the original two sensors, $z_{\mathrm{armEnd/ground}}$ is known from the third sensor and $z_{\mathrm{armBase/ground}}$ from the micromanipulator. Similarly, the actual position of the head is given by

$$z_{\mathrm{head/ground}} = z_{\mathrm{head/armEnd}} + z_{\mathrm{armEnd/ground}} \tag{4.4}$$

Thus, any change in position due to creep of the arm plate is accounted for. Since the x component is not affected by the vertical movement, we assume that the value derived from the micromanipulator position and head position from the two original sensors is adequate.

Also, another design change we have inculcated is to use a stainless steel arm plate instead of a dural plate. Since the surrounding solution is acidic, it causes corrosion in the dural plate due to the inability to form a protective oxide layer. The steel plate is also reinforced with an I beam as seen in Fig. 4.13b. The reinforced beam resists bending due to the coupling of bending of the arm plate and the I beam. The choice of the I beam for reinforcement is based on the fact that the I beam can resist the maximum amount of bending load while using the least amount of material due to a large second moment of area (see (Eq. 2.1)).

Key concepts of the chapter: We have demonstrated the effective operation of our device ICAMM through feedback loops either by stress measurement in a strain-controlled experiment or vis-versa:

1. The response time is $\approx 10\,\mathrm{s}$ in both constant shear strain and creep mode. A faster response can be obtained by changing the parameter of the PID controllers
2. Practical resolution in stress measurement is $\approx 6\,\mathrm{mPa}$, similar to the theoretical value
3. The behavior of the gel under shear is reminiscent of previous work on this material under constant strain [47] and creep [13]. Under creep, it shows the saw viscoelastic exponent as shown for Ref. [13].
4. Microscopic visualization and image correlation of xy plane resolved in z axis and time offer insight into failure. Under constant strain steps, we obtain a progressive softening near the headway before the non-linear regime.
5. However, the approach does not offer insight into any local plastic activity inside the gel during the power-law regime of the creep, thus requiring finer estimation of local strain using other techniques.

Chapter 5

What shall we take as an Event?

The ecological approach to visual perception (1979), J. Gibson

Analysis Tools

J. Gibson, an American psychologist introduced the concept of optical flow which is a popular technique in the computer vision domain. He argued that visual perception is direct and all the information required for it is already present in the environment and requires no extra learning from the brain. He describes there are certain cues in the environment like intensity change, which helps in our perception. In our confocal imaging, we see visually strand breaking events, nucleation of fracture, and other phenomena on applying a deformation to our system. In this chapter we translate the cues in our images, to estimate where and when these events are happening and whether they are correlated to each other.

We aquire either consecutive (for creep experiments) or periodic (for strain steps experiments) 3D time frames of confocal data. From this aquisition, we need to identify fracture precursors and quantify local dynamics. Since our gel network is too heterogenoeus, feature based tracking is not suitable to capture local dynamics. We try two methods here: 1) A direct measurement of spatio-temporal gradient in pixel intensity to obtain velocity field and 2) reducing our gel to a simple network using morphological skeletonization and graph theory. We perform our analysis and plotting using python via Anaconda distribution [146] using libraries `opencv` [147], `openpiv` [148], `numpy` [149], `scipy` [150], `pandas` [151], `h5py` [152], `networkx` [153], `trackpy` [154] and `matplotlib` [155], scripts and modules we have developed. A typical 3D stack is generally $512\,\mathrm{px} \times 512\,\mathrm{px} \times 100\,\mathrm{px}$ in xyz and $20 - 1000$ frames in time. For reading and slicing the confocal data in lif format to array, we use the library `read_lif`[156]. The computations are done on our local workstation (12-cores @2.20 GHz, 64GB ram, 500GB + 4TB of HDDs).

5.1 Motion estimation

Motion estimation techniques are used to determine how things are moving in a sequence of images. One class of motion estimation methods is called feature based methods. They are generally used for large motion detection. The method relies on the extraction of certain features such as corners and later tracks them from one frame to another. A well-known method using this is the Crocker–Grier algorithm [157] for tracking blob-like features in images. Since our gel is heterogeneous, defining good features is tough. So we progressed with utilizing another class of motion estimators called direct or dense methods. In these methods, we estimate the motion of pixels by approximating the motion field from variation in time of the intensity field. Thus, it relies on the spatial and temporal gradient of the image intensity field (in grayscale) to estimate the velocity field. If we express the spatial and temporal variation of the first image by $I(x,y,t)$, and say at time $t+dt$, the pixels is displaced by dx, dy, the second image is obtained as $I(x+dx, y+dy, t+dt)$. Optical-flow methods work on three key assumptions:

1. The lighting in the image or the pixel intensities remain the same between the two images.
2. The motions of the pixels are small.
3. There is spatial coherence in the motion of the pixels i.e. all the pixels in the neighborhood move similarly.

Using the first assumption, we can equate the intensities in the two images:

$$I(x,y,t) = I(x+dx, y+dy, t+dt) \tag{5.1}$$

In real images, the first assumption of no intensity change does not hold true, Hence, the methods look for dx, dy such that $I(x,y,t)$ and $I(x+dx, y+dy, t+dt)$ show best correspondence. The definition of best is heuristic and depends on the method used. We try two different methods:

1. Particle image velocimetry (PIV) based on applying image correlation between two images or sub-images and computing it in Fourier space. We use the OpenPIV implementation of it in python [148] for our analysis. The significance of the parameters in the implementation is discussed in Section 5.1.1.
2. Dense optical-flow algorithm by Gunner Farneback [158] based on estimating the motion for each pixel computed in real space. In Section 5.1.2, we discuss the algorithm in detail and look at the corresponding parameters in its 2D implementation in opencv [147]. We also discuss the pyramid-based subsampling algorithm in Section 5.1.2. It can be used for estimating large displacements in PIV too to overcome the limitation of small motion in these dense methods.

5.1.1 Particle Image Velocimetry (PIV)

Since its first mention in 1984 [159], particle image velocimetry(PIV) was originally a way of obtaining the velocity field in a fluid seeded with tracer particles by correlating two images separated by a short time interval dt. Its algorithm is now used for detecting displacement and velocity field in other systems where imaging with intensity contrast is possible. The analysis involves cross-correlating the two images. Suppose, $f(x,y)$ and $g(x,y)$ are the intensity at location (x,y) for the first and second image of size (M,N) respectively, the discrete cross correlation $c(x,y)$ is calculated as,

$$c(x,y) = \frac{\sum_{m=1}^{m=M}\sum_{n=1}^{n=N} |f(m,n) - \bar{f}||g(m+x, n+y) - \bar{g}|}{\sqrt{\sum_{x=1}^{x=M}\sum_{y=1}^{y=N} |f(x,y) - \bar{f}|^2 |g(x,y) - \bar{g}|^2}} \tag{5.2}$$

where $\bar{f}$ and $\bar{g}$ are the mean of $f(x,y)$ and $g(x,y)$ respectively. The terms at the bottom of the division are the standard deviation for both the images used to normalize the cross-correlation. The upper cross correlation can be visualized as a mapping built by sliding one image over the other, and adding the multiplication of overlapped pixel to quantify the amount of matching. Calculation in the real

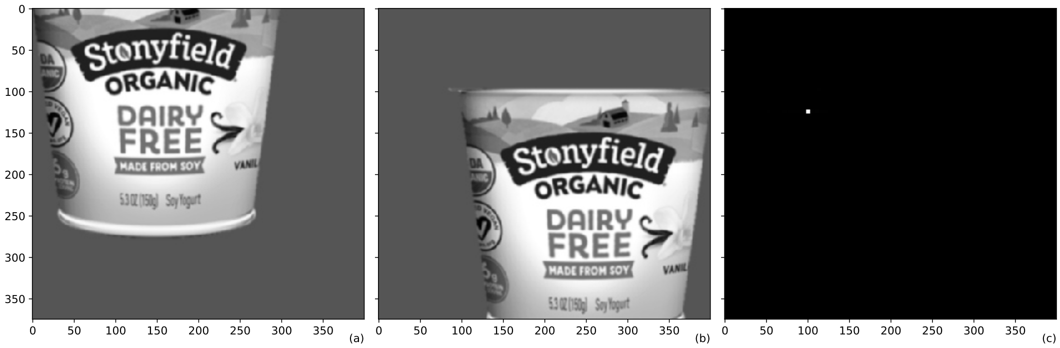

FIGURE 5.1: PIV operation: (a) and (b) are the same image shifted by 75 px and 100 px in horizontal and vertical axis respectively. (c) represent the cross-correlation field $c(x, y)$ between the two images. The white dot is the maximum with estimated shift 74.5 px and 100 px.

space can be computationally expensive. Analogous to the convolution theorem, in Fourier space, the additive multiplication reduces to simple multiplication,

$$F\{c\} = F\{f\}.F\{g\}^* \tag{5.3}$$

where F denotes the discrete Fourier transform and $F\{g\}^*$ is the complex conjugate of Fourier transform of $g(x, y)$. Applying a reverse Fourier transform, we obtain its real space value

$$c(x, y) = F^{-1}\{F\{c\}\} \tag{5.4}$$

The coordinates (x, y) at which $c(x, y)$ is maximum gives us the best match for the displacement. Fig. 5.1 demonstrate the result of operating (Eq. 5.2), (Eq. 5.3), and Eq.(5.4) on an image shifted in space. The white dot in Fig. 5.1c denotes the maximum in cross-correlation and hence, the actual shift between the images.

To make the method applicable for local velocity, PIV algorithms divide the image into windows and track the local displacement of these windows between different time frames. We use the OpenPIV implementation of it in python [148]. In the method, the image is divided into interrogation windows using the parameter `window_size`. The `overlap` parameter decides how much will the interrogation windows overlap. The `search_area_size` decides the window size for the second image offering the possibility to search an extensive area for a possible large shift.

5.1.2 Farneback algorithm

The second method is to use the Farneback algorithm [158]. Farneback in his thesis proposed the idea to approximate an image or subset of an image with a quadratic polynomial and see how this polynomial undergoes transformation on applying a displacement on it.

Quadratic approximation in 1D

Consider a polynomial function at time t $f_1(x) = A_1x^2 + b_1x + c_1$ and its form at time $t + \Delta t$ as $f_2(x) = A_2x^2 + b_2x + c_2$. If $f_2(x)$ is a pure translation of $f_1(x)$. Then, $f_2(x) = f_1(x - d)$, where d is the global displacement representing the translation. On substituting $f_1(x - d)$ and equating we get,

$$A_1 = A_2 = A \tag{5.5}$$

$$b_2 = b_1 - 2A_1 d \tag{5.6}$$

Hence,

$$d = \frac{b_1 - b_2}{2A} \tag{5.7}$$

However, in real world, no transformation is pure translation. So, in practice we take,

$$A = \frac{A_1 + A_2}{2} \tag{5.8}$$

Thus, we can get the translation d from the coefficient of the quadratic polynomial combining (Eq. 5.7) and (Eq. 5.8). Also, we see that it is independent of the constant term c so from here on, I ignore it in the description.

Application to image translation

For real image, Farneback gives a description which can be applied for any N dimension quadratic polynomial (for 2D, $N = 2$). Besides, assuming a global displacement d for an entire image is impractical. Hence, Farneback replaced the global polynomial with a local polynomial description depending on the position $\underline{x}$ in the image. For an N dimensional image, the local quadratic polynomial representation can be given by $f_1(\underline{x}) = \underline{x}^T A_1(\underline{x})\underline{x} + b_1(\underline{x})^T \underline{x} + c_1(\underline{x})$, where $A_1(\underline{x})$ is a $N \times N$ matrix, and both $\underline{x}$ and $b_1(\underline{x})$ are $N \times 1$. If the 2nd image is given by $f_2(\underline{x}) = \underline{x}^T A_2(\underline{x})\underline{x} + b_2(\underline{x})^T \underline{x} + c_2(\underline{x})$, similar to the Section. 5.1.2 applying elementary matrix operations, the local displacement $d(\underline{x})$ can be given by

$$A(\underline{x}) = \frac{A_1(\underline{x}) + A_2(\underline{x})}{2} \tag{5.9}$$

$$A(\underline{x})d(\underline{x}) = \Delta b(\underline{x}) \tag{5.10}$$

Where $\Delta b(\underline{x}) = -\frac{1}{2}(b_2(\underline{x}) - b_1(\underline{x}))$. Similar to (Eq. 5.7), we get

$$d(\underline{x}) = A(\underline{x})^{-1} \Delta b(\underline{x}) \tag{5.11}$$

for the case if 2D image, (Eq. 5.9), (Eq. 5.10) and (Eq. 5.11) are given as

$$A(x,y) = \frac{A_1(x,y) + A_2(x,y)}{2} \tag{5.12}$$

$$d(x) = A(x,y)^{-1} \Delta b(x,y) \tag{5.13}$$

Hence, the displacement is a function of space. This local polynomial is used as the parameter `poly_n` in the opencv implementation of the algorithm.

The result obtained by such spatial computation of d for each pixel is quite noisy and might be computationally expensive. To solve this, Farneback, based on the 3rd assumption of optical-flow, assumed that the displacement is spatially coherent and variation over a neighborhood is slow. For this, he introduced a window $w(\Delta x, \Delta y)$ over which the displacement $d(x,y)$ remains the same.In case of a 2D image of size

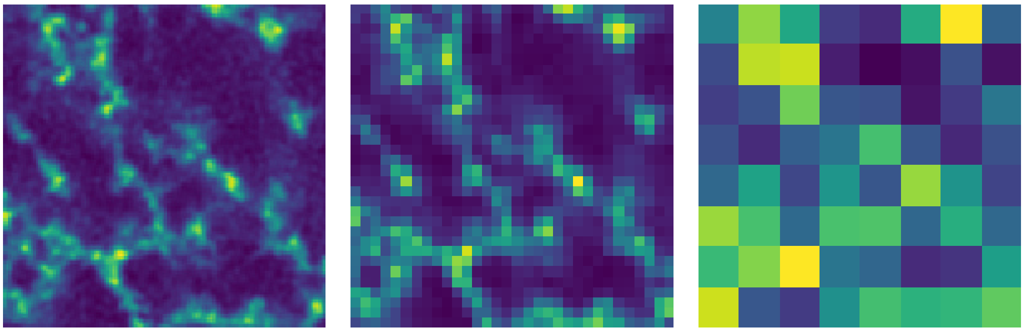

FIGURE 5.2: A xy plane cut section of the gel downscaled by a factor of 4 to go from 128 px × 128 px to 8 px × 8 px to make a three level pyramid.

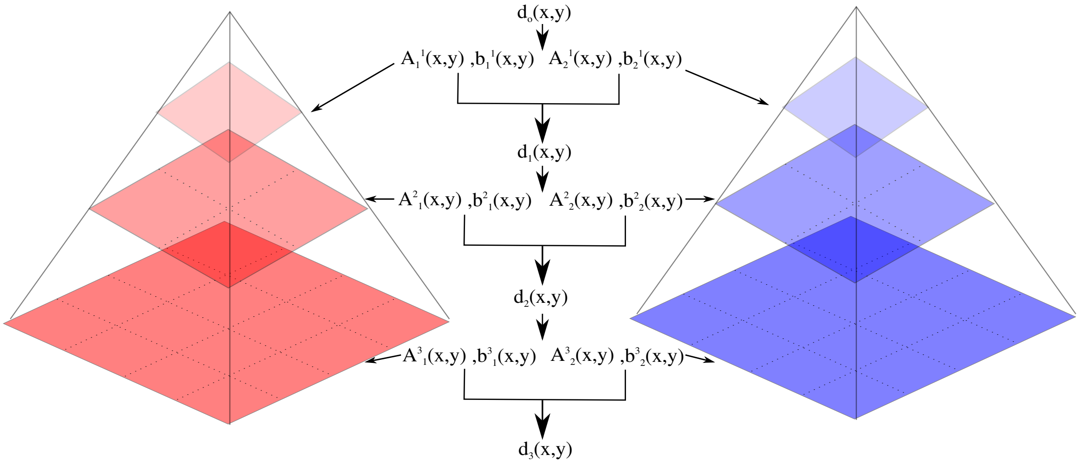

FIGURE 5.3: Schematic representing of Farneback's operation on a three level sub-sampling of a 16 px 2D image such that each level down has four times the pixel of the previous level as shown in Fig. 5.2. The local polynomial is estimated separately for each level and the estimated displacement is passed down to the next level as the initial guess. Subscript on the coefficients denote the image while superscript denotes the level of the pyramid.

(N, M), the solution is obtained by minimizing the error in (Eq. 5.10) over the neighborhood,

$$\sum_{\Delta x \in N} \sum_{\Delta y \in M} w(\Delta x, \Delta y) || A(x + \Delta x, y + \Delta y) d(x, y) - \Delta b(x + \Delta x, y + \Delta y) ||^2 \tag{5.14}$$

The solution to Eq. 5.15 is given by

$$d(x, y) = (\sum_{\Delta x \in N} \sum_{\Delta y \in M} w A^T A)^{-1} (\sum_{\Delta x \in N} \sum_{\Delta y \in M} w A^T \Delta b) \tag{5.15}$$

In the `opencv` implementation, the parameter `winsize` accounts for the square neighborhood (N, N). The window can be any weighted function and by default is a box filter but can be set to gaussian to have more weight on pixel closer to the center pixel. It should be noted that the description here is well suited for the 2D translation case which is the implementation in opencv. For a more general N-dimensional arbitrary transformation, Farneback provides a general solution, the steps for which have been skipped here. Farneback also mentioned that we can obtain the minimum value of (Eq. 5.14) and use it as a confidence value for our computation. The `opencv` implementation does not offer it as an option in the output.

Until now, Farneback's algorithm only account for small displacements. To improve the method for large displacements and to reduce errors, Farneback introduced iterative refinement by adding the prior known knowledge of the displacement. If we know a priori that there is a shift of $\tilde{d}(x, y)$, we can compare the polynomial at x, y and $x + \tilde{x}, y + \tilde{y}$. This modifies (Eq. 5.12) and $\Delta b(x, y)$ as

$$A(x, y) = \frac{A_1(x, y) + A_2(x + \tilde{d}(x), y + \tilde{d}(y))}{2} \tag{5.16}$$

$$\Delta b(x, y) = -\frac{b_2(x + \tilde{d}(x), y + \tilde{d}(y)) - b_1(x, y)}{2} + A(x, y)\tilde{d}(x, y) \tag{5.17}$$

Thus the actual displacement $d(x, y)$ can be obtained in same method as (Eq. 5.15). This process can be iterated multiple times with output $d(x, y)$ after an iteration acting as $\tilde{d}(x, y)$ for the next. In `opencv` this is implemented using the parameter `iterations`.

Another improvement for measuring large-scale displacement is by using coarser images to estimate the larger displacement. We can construct a multi-scale pyramid of such coarser images by using a lowband-pass filter and subsampling the images. An example of subsampling is shown in Fig. 5.2. In the coarser image on the extreme right, the displacement can get reduced by a factor of 8 and the small displacement approximation of the algorithm can hold true. These can be passed down to the finer image as the known a priori shift, $\tilde{d}(x, y)$. It requires estimation of the polynomial coefficients at each scale, but this does not affect the time or space complexity significantly. In `opencv`, parameters `pyr_scale` and `levels` decide the amount of subsampling and levels in the computational pyramid. An example of a three-level pyramid subsampling is shown in Fig. 5.3. The three-level in the Fig. 5.3 can be the images in Fig. 5.2 and its displaced counterpart (not shown).

5.2 Performance of PIV and optical-flow for 2D images

In this section, we optimize the parameter choices and compare the two above described methods to see which performs optimally for our system. For each example we take a 2d cut of the xy plane of 256 px × 256 px with pixel size 0.446 µm. We show through the example how optical flow is more precise in determining the velocity field and its pixel-level computation makes it more robust to estimating local changes in the velocity field.

5.2.1 Simple translation

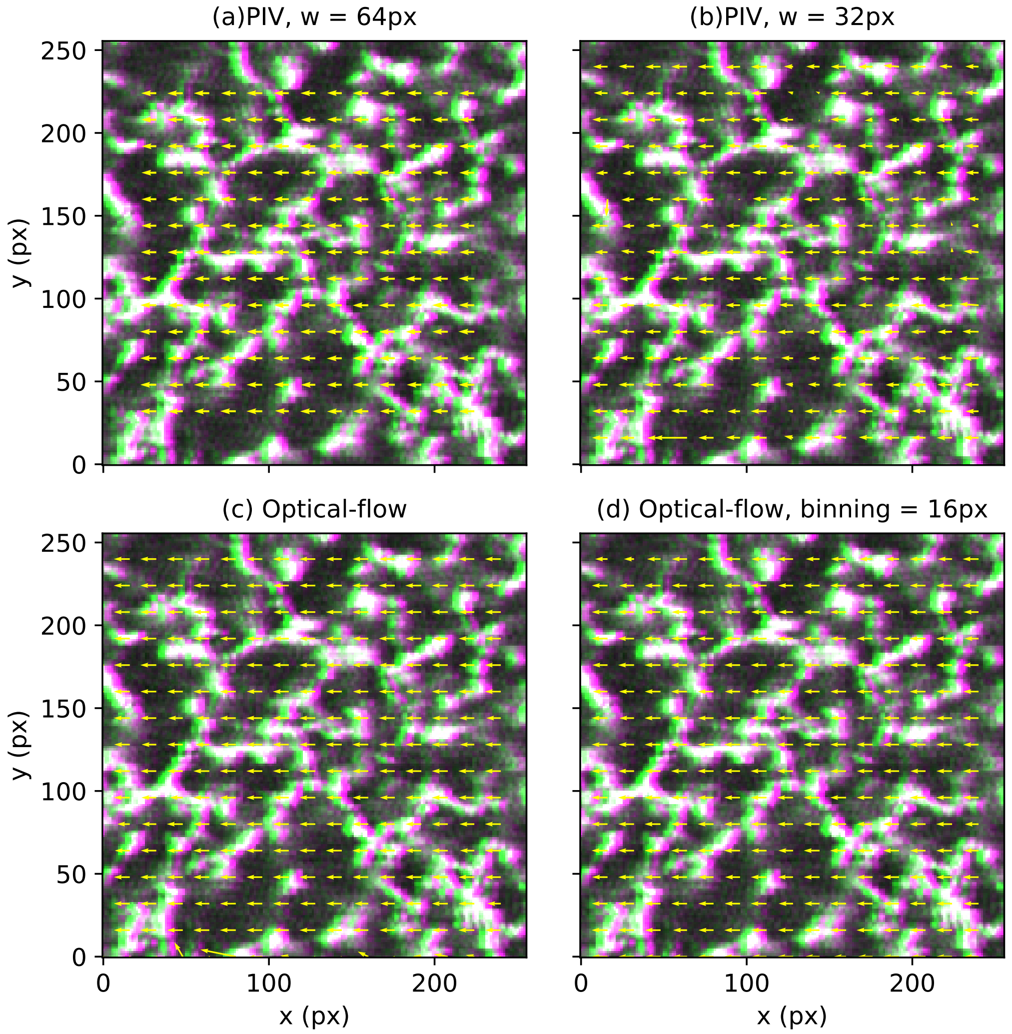

FIGURE 5.4: Superimposition of a section of the xy cut for two grayscale images (pixel size = 0.446 µm) plotted in magenta (red+blue) and green colormap. The green image is obtained by an artificial displacement on the magenta colormap image of 5 µm in the negative x direction. The quiver are the displacement field estimations by varying the method and parameter. (a) Result from PIV, obtained with window of size 64 px with the average displacement in x of 4.80 µm ± 0.11 µm and 0.01 µm ± 0.03 µm in y. (b) PIV obtained with window of size 32 px with the average estimated displacement in x 4.65 µm ± 0.44 µm and 0.02 µm ± 0.43 µm in y. (c) and (d) Result from optical-flow. To simplify the quiver plotting in (c) we plot just the quiver at every 16 px while in (d) we average over bin of size 16 px. Average displacement estimated with optical-flow in x is 4.96 µm ± 0.14 µm and 0.00 µm ± 0.04 µm in y.

We try to optimize the parameters for PIV and optical flow and compare the method for a case of an artificially shifted image. As seen in Fig. 5.4, we have the original grayscale image plotted in magenta colormap overlapped with the image shifted by 5 µm in the negative x-direction. The shifted image is superimposed over the original image in the green colormap. Hence, the gel strands turn grey in the region of overlap, but we can distinctly see green and magenta hue over the edges of the strands. We tried removing the background by using a low pass Gaussian filter but it does not impact the displacement estimation. The high pass filter is good in removing noise in the image and we saw improvement in the displacement estimation. Thus all the images in Fig. 5.4 are obtained after applying Gaussian filter of 1 px to the original images.

For PIV, choosing `window_size` lower than 32 px leads to large noises and deviation in velocity field estimation so, we are limited to a `window_size` 32 px . In general in our experiments, the displacements are not significantly large compare to the `window_size`, so we choose to keep the `search_area_size` same as the `window_size`. This is good for consistency if we want to treat a large number of images. The `overlap` parameter can be non-zero to allow more windows and hence, denser field. For the purpose of consistency we choose it to be such that we have a velocity estimation at every $16^{\text{th}}s$ pixel for every PIV example. Hence, for a `window_size` of 64 px as seen in Fig. 5.4a the `overlap` is 48 px and in Fig. 5.4b for `window_size` of 32 px it is 16 px. As we see in Fig. 5.4a and 5.4b, on changing the `window_size` from 64 px to 32 px, the displacement field shows inconsistency as can be seen in the plotted quivers which are non-uniform. This can also be seen in the average x displacement where it has higher off-set from expected estimation as well as higher standard deviation in x and y displacements in case of 32 px compare to 64 px.

Fig. 5.4c shows our result for optical-flow with the quiver plotted at every 16 px. Based on the recommendation from the python library and after testing, the size of the neighborhood to estimate the polynomial function for the pixel or `poly_n` is chosen to be 5 px. The neighborhood over which we approximate spatial coherence or the `winsize` parameter is taken to be 15 px, which is better compared to the typical window size we are able to reach using PIV and is of the scale of events we are interested in as will be seen in the next Section 5.2.2. Also, we use a gaussian window instead of the default box filter to have a smoother transition between the displacement field. We do a multiscale analysis with a pyramid of size 4. The subsampling is such that each level down is twice the number of pixels as the previous i.e. we start with a coarser 32 px × 32 px image to the original 256 px × 256 px. At each level, we iterate 3 times with the parameter `iterations` to have more precise results. The parameter `poly_sigma` decides the size of the Gaussian used to smooth the derivatives which are the basis of the polynomial expansion and we choose it to be 1.2. In Fig. 5.4d, we average the obtained displacement over bins of 16 px × 16 px. This is to test the impact of averaging the result over a bin size as storage of data for every pixel especially with 3D time acquisition would be heavy on the memory. The average displacements for optical flow are more precise in both x and y directions and less noisy compared to the PIV cases. Computational time for PIV for the case of `window_size` of 32 px is 16.5 ms and for Farneback algorithm is 14.6 ms.

5.2.2 Breaking precursors detection

When we have a strand breaking event, the velocity field around the strand is expected to distort. Using this information, we can have spatial and temporal data of all these events and derive statistical data which can indicate where do these events

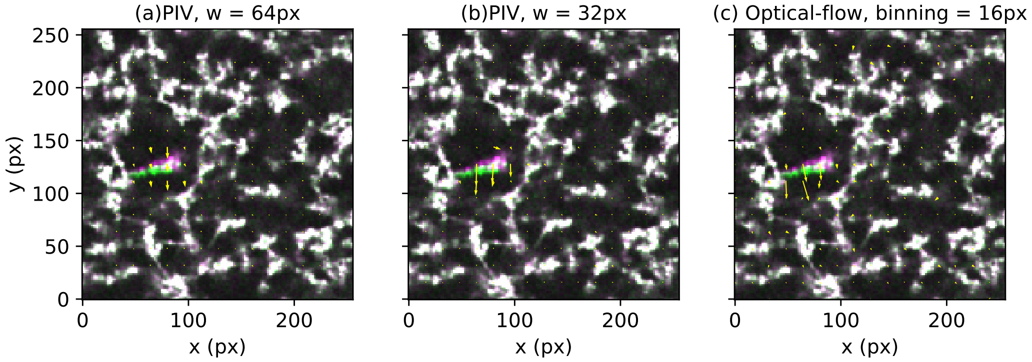

FIGURE 5.5: Superposition of a section of the xy cut for two grayscale images (pixel size = 0.446 µm) obtained from consecutive 3D acquisition plotted in magenta (red+blue) and green colormap. The breaking event corresponds to the region of non-overlap and hence, segregation of the colors. (a) and (b) Result from PIV plotted as quiver over the images with window size of 64 px and 32 px respectively,(c) Result from optical flow averaged over bin of size 16 px.

lead to the catastrophic failure of gel. Here, we check the applicability of PIV and optical flow in discovering these distortions in the velocity field.

As seen in Fig. 5.5 we have a strand breaking event which is the non-overlapped colored zone. The acquisition is in 3D and here, we have a 2D slice of the actual image. Fig. 5.5a is the quiver ploted for a `window_size` of 64 px. The parameter chosen are the same as in Section 5.2.1. Fig. 5.5b has the `window_size` equal to 32 px. We see the velocity field around the event larger in both cases, with the quiver location more precise in Fig. 5.5b.

For the optical flow, the parameters are the same as in Section 5.2.1. We show the result for the average over a bin of size 16 px. Due to the spatial coherence assumption of the algorithm, we observe high flow in the neighborhood of the strand which introduces noise in our measurement. But the method is more robust, irrespective of the strand size compared to PIV due to preserving pixel-level information. To demonstrate this in Fig. 5.6, we show another slice with strand breaking events. As seen in Fig. 5.6a and Fig. 5.6b corresponding to `window_size` of 32 px and 16 px respectively, reducing the `window_size` in PIV leads to large error. The optical flow estimates the velocity field correctly around the breaking neighborhood even for an average over 16 px. We can reduce the averaging parameter further to have information at smaller scales. Thus, we decided to focus on the analysis using optical flow.

5.3 3D implementation of optical-flow

Since we are dealing with 3D acquisition, the `opencv` implementation which works for 2D images is insufficient. One way to go forward is to extend Farneback's implementation to 3D as the algorithm initially deals with any N-dimensional signal. Another method can be to use the geometry of our shear flow to our advantage. We apply the `opencv` implementation for each xy cut plane. Assuming the global displacements in y are small since our system is in Couette geometry, we unshear each xy plane by the average displacement in x and then apply the optical flow in the yz and xz cut planes to obtain the z velocities. The second method is better since the displacements in the three directions are not of the same scale due to our shear

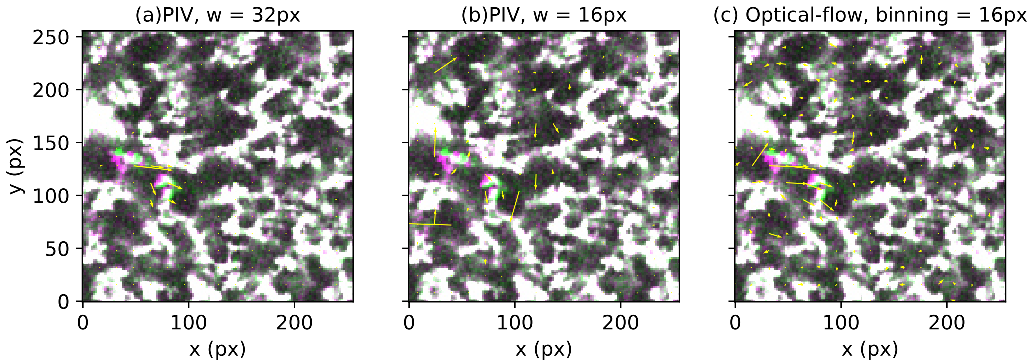

FIGURE 5.6: Superposition of a section of the xy cut for two grayscale images (pixel size = 0.446 µm) obtained from consecutive 3D acquisition plotted in magenta (red+blue) and green colormap. The breaking event corresponds to the region of non-overlap and hence, segregation of the colors. (a) and (b) Result from PIV plotted as quiver over the images with window size of 32 px and 16 px respectively,(c) Result from optical flow averaged over bin of size 16 px.

geometry. Besides, this choice seemed faster to implement the 2D implementation already existing in `opencv`. We keep the optical flow parameter the same as decided in Section 5.2.1 for the optical-flow computed irrespective of the direction.

We used the `read_lif` library to import the lif file and read the 3D continuous time acquisition data in array format I_{xyzt} with dimension (t, z, y, x).The output is the velocity field V_{xyzt} computed between consecutive time frame stored in weight averaged bins over 8 pixels in x and y using hdf (Section 5.3.4). The size of it is $(t-1, z, \frac{y}{8}, \frac{x}{8})$.

5.3.1 Applying 2D xy optical flow

Before any operation, we blur the noises in our image with a gaussian of size 1 px in all three directions. Also, due to the refractive index mismatch between the solvent and the gel, there is a loss in signal with height (z direction). Hence, we need to normalize the intensity profile in the z direction to prevent the Farneback algorithm to discard low-intensity pixels. The normalization is done by multiplying with the maximum value of intensity for a grayscale 8-bit image (255) and dividing by the maximum pixel intensity for that xy plane

$$I_{xy|z} = \frac{255 I_{xy|z}}{\mathrm{max}(\mathrm{I}_{\mathrm{xy|z}})} \tag{5.18}$$

where $|$ denotes that the operation is done for every xy plane at a fixed z. Later for each xy cut plane, we apply optical flow. This gives us the velocity profile for each pixel in x and y direction, $V_{xy|z}$. Velocity for each pixel leads to two problems.

- We encounter storage problem if we save the velocity field for each pixel and store further operation such as the gradient of the velocity field
- As seen in Section 5.2.2, due to the spatial coherence, we have velocity profile in blank spaces where we do not have gel or any breaking event

Thus, it is essential to average the velocity field, especially in x, y where we have 512 px each with more weight given to important pixels i.e. pixel with intensity.

5.3.2 Weighted averaging

A better method to average would be to have a weighted average based on pixel intensity. This way, we eliminate the influence of not so important pixels which are not actually a strand of the gel. The weight we chose is based on the feature detection method by Shi-Tomasi [160]. The method is based on the idea that at the edge or corner of a feature, there will be a large intensity difference and hence, a large gradient associated with it. Around a pixel P at position (x, y), the difference in intensity can be modeled as

$$E_{x,y} = \sum_{\Delta x \in N} \sum_{\Delta y, N} w(x,y)(I(x + \Delta x, y + \Delta y) - I(x,y))^2 \tag{5.19}$$

Where w is the gaussian weight assigned to the neighborhood pixels. On applying first order taylor series expansion approximation the formulation simplifies to

$$E_{x,y} = \Delta^T M \Delta \tag{5.20}$$

where $\Delta = \begin{bmatrix} \Delta x & \Delta y \end{bmatrix}$ and M is the covariance matrix of the derivative over the neighborhood given as

$$\sum_{\Delta x \in N} \sum_{\Delta y, N} w(x,y) \begin{bmatrix} \nabla_x I^2 & \nabla_x I \nabla_y I \\ \nabla_x I \nabla_y I & \nabla_y I^2 \end{bmatrix} \tag{5.21}$$

Here $I = I(x,y)$ is the intensity and ∇_x and ∇_y are its gradient in x and y respectively. If λ_1 and λ_2 are the eigen values of the matrix M, then the Shi-Tomasi gives a score to the pixel P as the minimum from the two eigen-value. In the `opencv` implementation we can choose the neighborhood size (N) as `blockSize`, and the sobel operator size, `ksize`, to calculate the gradient. We choose them as 3 px. The weight matrix in xy is denoted by $w_{xy|z}$ at a particular z. The binned xy velocity field thus is given by

$$V_{\frac{x}{b}\frac{y}{b}|z} = \frac{\sum_{p\in\frac{x}{b}} \sum_{q\in\frac{y}{b}} w_{pq|z} V_{pq|z}}{\sum_{p\in\frac{x}{b}} \sum_{q\in\frac{y}{b}} w_{pq|z}} \tag{5.22}$$

Where b is the number of pixels over which we average and denoted by `binning` in our program. By default, its value is 8.

5.3.3 Estimating z velocity field

Once we have the x and y velocities, the z velocities are obtained by removing the large displacement associated with x velocity which is in the shear direction. The assumption here is that y velocities are small, and hence, the neighborhood remains the same in y. Thus by shifting the 2^{nd} image in the x direction, we are restoring the neighborhood. The shift in x (shiftx) is approximated as the weighted average velocity in x obtained from the optical flow in xy direction. Note that the shiftx is calculated for each xy plane and hence is a function of z.

$$\text{shiftx} = \frac{\sum_{p\in x} \sum_{q\in y} w_{pq|z} V_{p|z}}{\sum_{p\in x} \sum_{q\in y} w_{pq|z}} \tag{5.23}$$

For computing the z velocities, we apply 2D optical flow on the x shifted xz and yz planes and take a weighted mean for the z velocities.

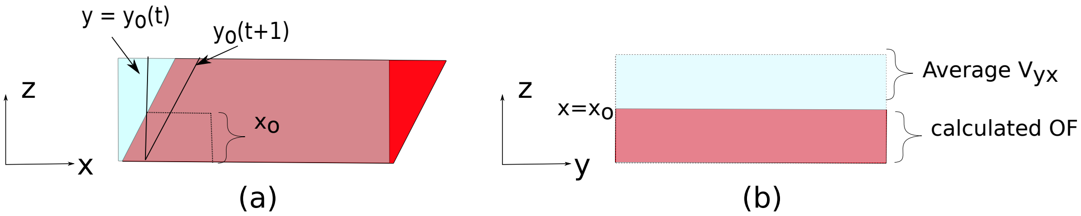

FIGURE 5.7: Schematic representation of estimation of z velocity V_z: (a) the (x, z) visualization of the gel image. The light-colored represents gel at time frame t and the dark at the next time frame $t+1$. The overlapping region is the only part of the gel common between the two images. the darkest (red) has moved out of the visualization zone and the lightest (blue) has moved into the visualization zone. We estimate the xshift which is the average displacement for each xy frame, equivalent to the known overlapping region of the image, and remove this affine displacement. For estimating the z velocity in special case: the y plane y_o, represented by a line here at the two times t and $t+1$. The portion of it until $x = x_o$ is there in the gel at both the time frame. As seen in (b), the V_z until $x = x_o$ is estimated by applying optical flow in the sheared back yz plane. For the portion above x_o, which just entered the visualization at $t+1$, it is estimated by approximating to the average V_z estimated for the plane.

$$V_z = \frac{\sum_{p\in x}\sum_{r\in z} w_{pr|y} V_r + \sum_{q\in y}\sum_{r\in z} w_{qr|x} V_r}{\sum_{p\in x}\sum_{r\in z} w_{pr|y} + \sum_{q\in y}\sum_{r\in z} w_{qr|x}} \tag{5.24}$$

For computing the optical flow in yz, we have to note that due to the shifting in x, some pixels in the x direction will not correspond between the original and the second image as seen in Fig. 5.7a. This is due to some pixels moving out of the field of view and some new pixels introduced. Thus, the optical flow is computed slice by slice in x direction for each yz frame only for the pixels where correspondence is possible. For the pixel where there is no correspondence, we assign the average V_z value corresponding to that plane. Note that we smoothen the velocity profile in yz with a high-frequency gaussian filter of size 1 px as the shifting process is an assumption and the flow profile can be noisy compared to the one we compute with the optical flow in xy planes. This operation can be visualized in the schematic Fig. 5.7. Similarly, the V_z profile is obtained. Later, the final V_z is estimated by taking a weighted average of the two as shown in (Eq. 5.24). The weight is obtained by Shi-Tomasi in xz and yz planes respectively.

5.3.4 Data storage and slicing using HDF

The large size of our acquisition with the additional load of flow dimensions added to it can make an array quite heavy to operate on memory as well as big for storing on the disk. To operate with this huge amount of data, we will store our flow profile and other data in Hierarchical Data Format(HDF). HDF format allows large data storage in a form similar to a file directory. We have groups that act like folders and can contain another folder or datasets. Dataset is the actual data being stored. The format is self-describing as each group or dataset can be allotted metadata that describes what it is exactly. HDF format allows data slicing which means we can pick up, read or write a part of the dataset and operate on it instead of importing the entire data into memory. We use the python implementation of version 5 of the format, `h5py` [152].

Thus, for every consecutive time frame we operate on to calculate the flow profile, we store the result in an HDF dataset whose metadata is `FlowField3D`. For x and y velocities, before storing we do a weighted average of the velocity data over

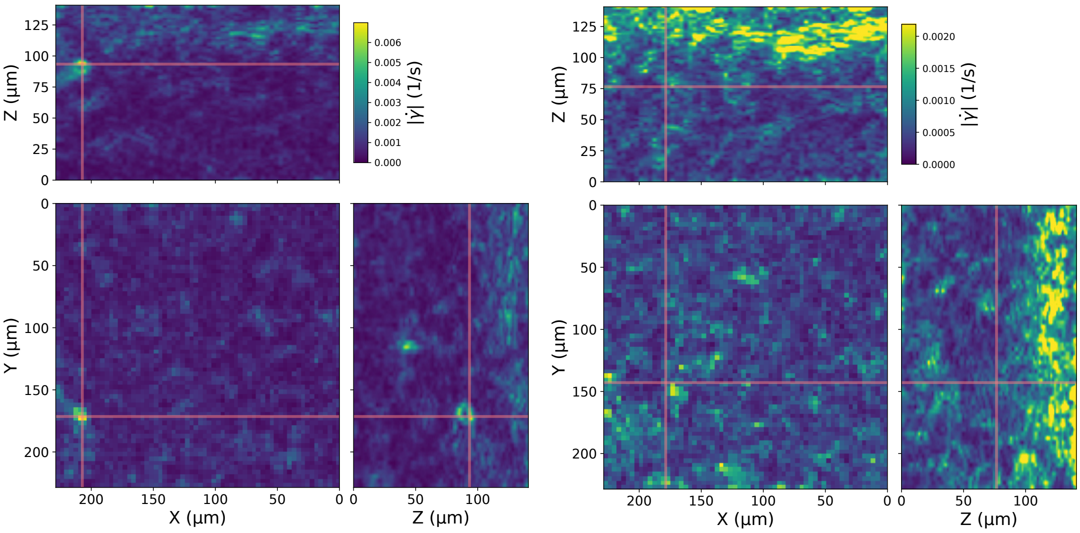

(a) (b)

FIGURE 5.8: *x*,*y*,*z* cut planes of norm of the strain field between two consecutive time frame (a) at a location where we detect an event using the algorithm and (b) where no event is detected. Notice the gradual increase in global intensity with *z* for both the cases

a few pixels and bin the result as discussed in Section 5.3.2. The *z* velocity is stored after a weighted averaging as shown in Section 5.3.3. Every time we need to operate on the flow profile, the HDF can come in handy since instead of inputting the entire flow array, we can work on slices and put the output back to the disk, keeping the Random Access Memory (RAM) relatively free.

5.3.5 Spatial gradient of velocity field

As seen in Fig. 5.5 and Fig. 5.6, the velocity field near strand breaking event show large gradient. Extracting the gradient of the velocity field can thus help us locate such strand breaking events inside the gel. More meaningful information can be obtained from the strain rate field, which is the symmetric component of the velocity gradient field given by

$$\dot{\gamma} = \frac{\nabla V + \nabla V^T}{2} \tag{5.25}$$

where, $\nabla V = \nabla_i V_j$ is a tensor field and the V^T denotes the transpose of V. It should be taken into consideration that we do not have same pixel size in *z* direction as *x*,*y*. so while taking the gradient we need to multiply by the right pixel size in the velocity term and the gradient term.

$$\nabla V_{ij} = \frac{\partial}{\partial(x_i p_i b_i)}(V_j p_j) \tag{5.26}$$

Where p is the pixel size and b is the binning size in the axis direction. We use the `gradient` method from the `numpy` library in our code. The dataset is added to the HDF file with metadata `gradient_flow`.

5.4 Finding fracture precursors

As seen in Fig. 5.5 and Fig. 5.6, around a strand breaking event, we have a large gradient in velocity field. Thus, local maximas in velocity gradient field and hence,

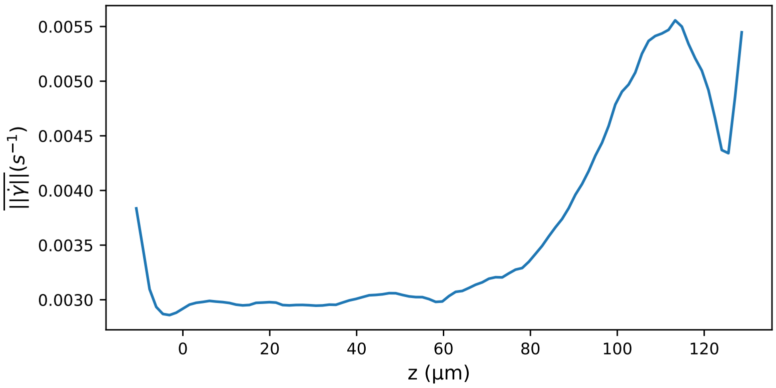

FIGURE 5.9: Normalized norm of the strain field averaged over xy plane and plotted as a function of z. The increase in signal intensity is observed between any time frames irrespective of whether there is an event or not and is attributed to the poor image signal to noise ratio deep inside the gel.

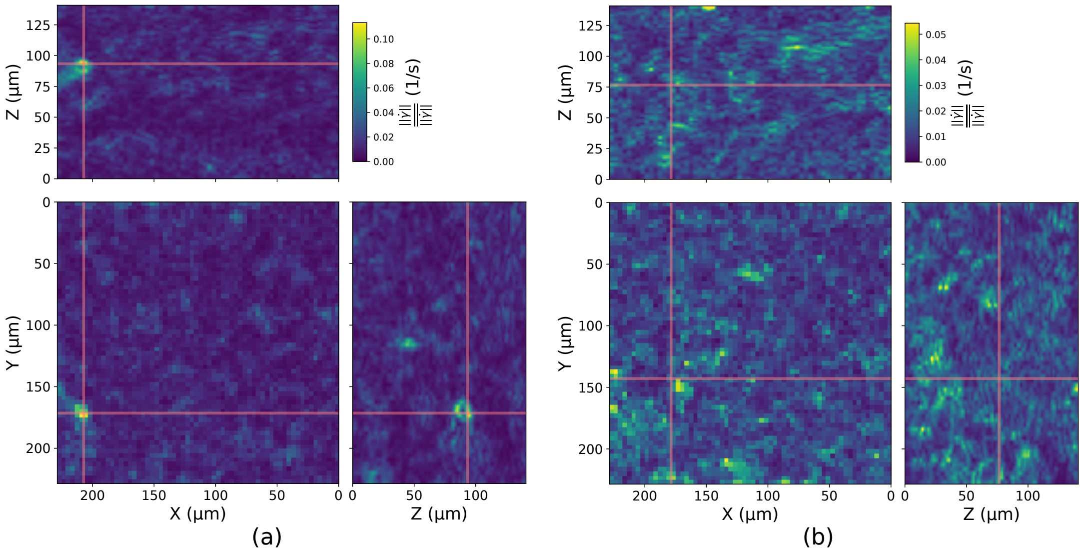

FIGURE 5.10: x,y,z cut planes of norm of the strain field between two consecutive time frame (a) at a location where we detect an event using the algorithm and (b) where no event is detected. Notice the gradual increase in global intensity with z for both the cases

in strain field, should correspond to a strand breaking event. The strand breaking events are the precursors to the catastrophic fracture and identifying them can help us understand how these events lead to the final macroscopic breaking. We calculate the strain rate field from the velocity gradient field as shown in (Eq. 5.25). To quantify this strain field we take the norm of it, $\|\dot{\gamma}\|$, where $\|\|$ denotes the matrix norm.

To find local maximas corresponding to strand breaking in $\|\dot{\gamma}\|$, we compare the morphological dilated form of $\|\dot{\gamma}\|$ with itself to find the sites which are local maximas in a neighborhood. We use the function `grey_dilation` from the `scipy` library. The dilation size by default is 3 times the `binning`, i.e the size of our velocity averaging. Later, we give a threshold to cutoff local maximas above a certain value. One of the local maxima located using this method is shown in Fig. 5.8.

As seen in Fig. 5.8, there is a gradual increase in intensity of $\|\dot{\gamma}\|$ This increase in intensity is due to the poor quality of image deeper inside the gel due to refractive index mismatch. The poor quality introduces noise in velocity estimation and hence, larger gradients. We define the xy average norm field, $\overline{\|\dot{\gamma}\|}$, which is obtained as the average for a xy plane for a particular z. As seen in Fig. 5.9, the profile of $\overline{\|\dot{\gamma}\|}$ after $z \sim 40$ px starts to increase and we observe this pattern for every strain rate between two consecutive time frames. Thus, we define normalization of the norm strain rate field by $\|\hat{\gamma}\|$ obtained as

$$\|\hat{\gamma}\| = \frac{\|\dot{\gamma}\|}{\overline{\|\dot{\gamma}\|}} \tag{5.27}$$

(Eq. 5.27) signifies normalizing each xy plane by the average of it. We compute the $\hat{\gamma}$ and $\|\hat{\gamma}\|$ by slicing the velocity gradient field dataset `gradient_flow` in the HDF file, computing and storing them in the same HDF file as dataset `strain_field` and `norm_strain` respectively. To find the localized high strain events, the default dilation size is 3 times the parameter `binning` defined in Section 5.3.2 and the threshold is $\|\hat{\gamma}\| = 0.1$. The $\|\hat{\gamma}\|$ map in the case where an event is located and where mo event is located are shown in Fig. 5.10a and Fig. 5.10b respectively. The magnitude of $\|\hat{\gamma}\|$ becomes locally larger than 0.1, which is our criteria for detecting an event, while in case of no event, value of $\|\hat{\gamma}\|$ is approximately half of it.

5.5 Skeletonize and network analysis

Alternatively, We tried to develop a network analysis algorithm of our system where our gel at each time frame can be visualized as a system of nodes and edges and thus, quantify the change in these edges and nodes between frames for local information. To do so, we apply morphological skeletonization to our gel to simplify before defining nodes and edges using graph theory. I describe the method in detail here. The simplified topology makes for some good visualization of the gel network, the analysis turned out to be a dead end since the edges and nodes defined for each time frame where not conserved in the other perfectly. This happens especially near the head due to poor resolution. Still, for a refractive index matched system of network gel, this technique can simplify the analysis of local changes.

5.5.1 Skeletonization

To have a network structure, we skeletonized the 3D image for each time frame. We denote the time frame here by fr. Skeletonization reduces the features in the image to a 1-pixel width object while preserving the link between pixels. We use

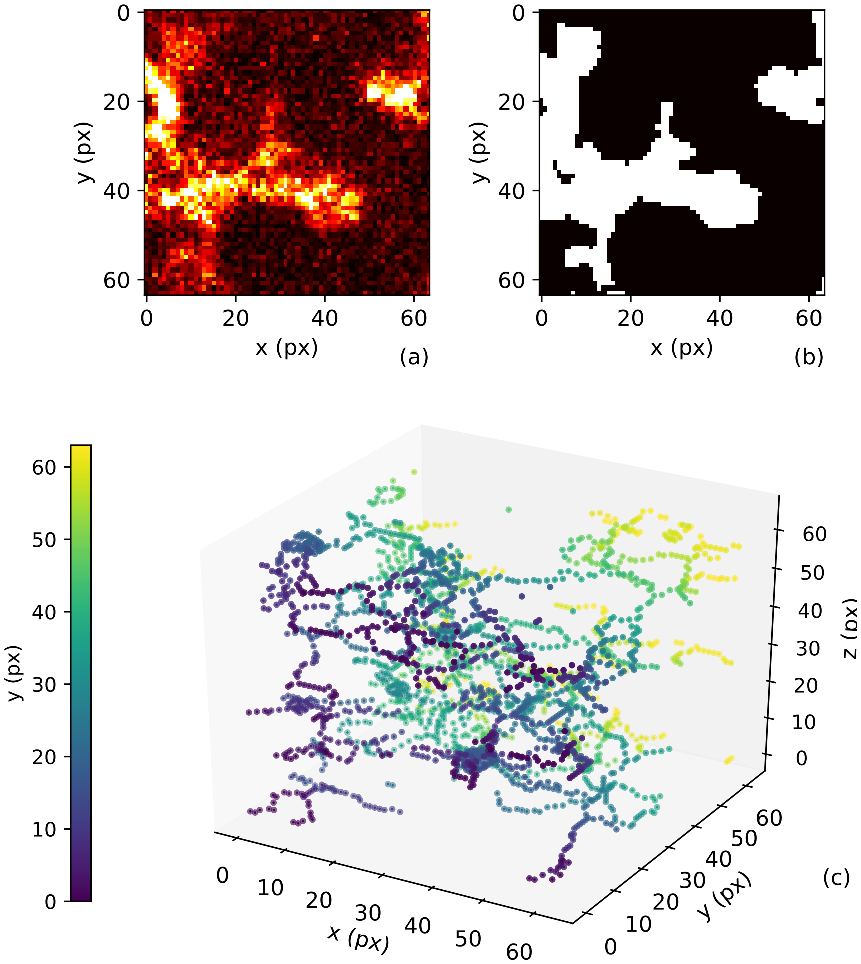

FIGURE 5.11: (a) A 64 px × 64 px cut of the original xy plane at z = 50 px. (b) Binarization result of (a) for a threshold `thr` = 1.3. (c) 3D plot of the skeletonization result for the 64 px × 64 px cut in xy and 60 px in z with colormap based on y position. Plotted scatter points enlarged to size of 5 px^2

Lee's method [161], which can be applied in 3D and has a python implementation in `skimage` library. Before skeletonization, we need to remove noise and binarize the image. We do the binarization operation on each xy plane separately as we have a loss of signal in z.

We apply a high-frequency gaussian blur of 1 px to smoothen the image. The binarization for each xy plane is done by filtering out pixels with intensity less than a threshold times the mean intensity of the plane (Fig. 5.11 b). The threshold is denoted by `thr` in our program and generally, we see good preservation of structure with a value between $1.2 - 1.3$. We perform morphological skeletonization in 3D and obtain an image of 1-pixel thick network structure as seen in Fig. 5.11c.

5.5.2 Defining a graph

Our skeletonized network is still complex and to simplify further, we can define a graph after identifying pixels as either nodes or edges. We use the `NetworkX` package [153] to define a graph after all the edges and nodes are identified and to define their connection. Edges are a continuous chain of pixels where every pixel has two neighbors. Nodes are any pixel with either more than two neighbors or any pixel

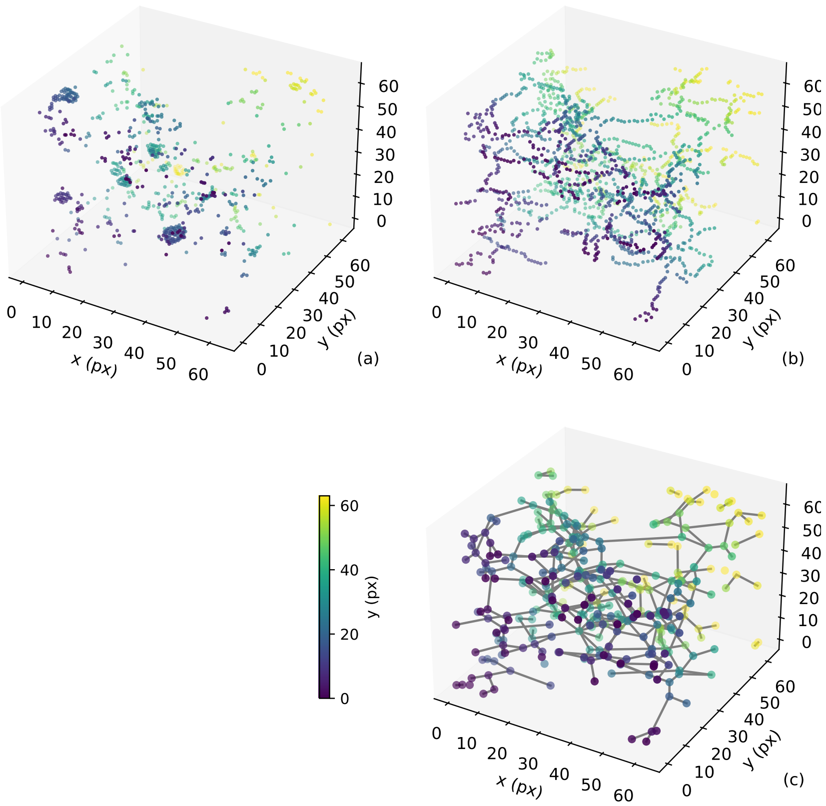

FIGURE 5.12: 3D plot of the (a) nodes and (b) edges result for 64 px × 64 px cut in xy and 60 px in z with colormap based on y position. Plotted scatter points enlarged to 5 px^2. (c) a 3D plot of the network with the nodes as scattered point with the same colormap along y.

at the end of an edge with one neighbor. To pass on the node object to the graph we define its position as the center of mass of all the pixels in the node object. We pass on the edge object after identifying how they are connected between two nodes. Also, we take care to handle exceptional cases where the two connected nodes are the same which is the case of an isolated loop. We treat it as an edge starting and ending at the same node in the graph. In Fig. 5.12 we see the result of these operations. Fig. 5.12a Fig. 5.12b show the isolated nodes and edge objects and Fig. 5.12c is the simplified graph representing our skeletonized gel in Fig. 5.11c.

5.5.3 Problem with this analysis

Ideally, topological changes should capture local plasticity by a change in the number of edges and nodes. However, the microstructure of our gel is not so well defined compared to spherical particle gels with distinguishable fractal structure as seen in the work of Ref. [95, 94]. The signal-to-noise ratio is also distorted by the refractive index mismatch. The origin of the problem lies at the step where we skeletonize our gel as can be seen in Fig. 5.13. As seen for the change in strain from $\gamma = 0\%$ to $\gamma = 17.4\%$ the global change in the microstructure position is captured qualitatively by the skeletonization. However, The local structure is not preserved and becomes worse as we go higher in z. Thus, making any further pursuit of analysis with this method futile.

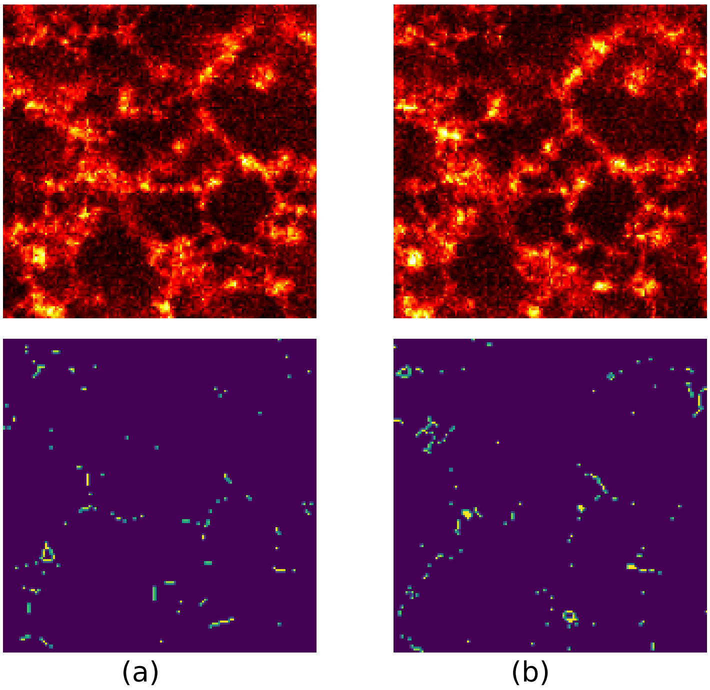

FIGURE 5.13: xy Microstructure of the gel and its corresponding skeletonization at $z = 30\,\text{px}$ for the incremental strain step experiment described in Section 4.1.2 at strain of (a) 0% and (b) 17.4%

Key concepts of the chapter: The plane by plane image correlation described in Section 4.2.3 is not sufficient to capture local plastic events. These events are visually confirmed to be the breaking of gel strands. In this chapter we developed the analysis required:

1. To estimate the velocity field using a small displacement methods such as Farneback's algorithm and PIV. We find Farneback more accurate in terms of the global as well as local velocity field.
2. The Farneback algorithm available in the python library is in 2D. We have developed a 3D algorithm by taking advantage of the shear geometry in our case.
3. From the velocity field we can have the velocity gradient and hence the strain rate field. The resolution of these fields can be adjusted with the method parameters such as the size of averaging. By default, we look at things on mesoscale of $\approx 3\,\mu\text{m}$ since the displacement estimation beyond this is noisy and expensive on the memory.
4. The strand breaking event manifests through the generation of large gradients locally. Thus, using morphological operations we can detect them as local maximas. An event is counted each time the normalized strain is larger than 0.1 We will use this to get temporal and spatial statistics on these events.

> Everything is related to everything else, but near things are more related than distant things
>
> Waldo Tobler

Chapter 6

Detection of Precursor to Fracture

The above statement is known as the First Law of Geography and laid the foundation for the concept of spatial autocorrelation. In this chapter, the analysis method developed based on the small motion estimation technique of optical described in Chapter. 5 is applied to the two creep experiments presented in Chapter 4. We validate the optical-flow method by getting the global velocity estimation and comparing it to the plane by plane image correlation, shown in Chapter 4. We apply the local strain field and detecting precursor algorithm to extract Spatio-temporal statistics on strand breaking events. We further notice the difference in events nucleation in the two experiments, namely in the bulk and near the head. We then describe the spatial autocorrelation method and how its applications to extract local coupling in amorphous systems. We then apply the 3D spatial autocorrelation to observe whether we observe similar coupling in our system.

6.1 Global displacement estimation from optical-flow

To observe the global estimation using Farneback's algorithm, we accumulate the average displacement in the three directions for different xy planes and compare it with the global mechanical displacement obtained from ICAMM measurements (Fig. 6.1). Thus, we have an additional velocity component to analyze compared to the planar image correlation we used in Section 4.2.3. Similar to Fig. 4.11 , we see a growth in displacement at different heights tracing the global strain with the final fracture seen in the fast rise of displacement in the three direction at $t > 39\,000\,\mathrm{s}$ as seen in Fig. 6.1. In Fig. 6.1a, the x displacement for height 120 µm obtained from optical flow matches with the actual displacement of head (thick green curve) until $t \approx 20\,000\,\mathrm{s}$. This estimation of the height is slightly off than our estimation from the z calibration (Section 4.1.3) which gives the height of gel as 115 µm.

Fig. 6.1d shows the average strain γ_{yz} computed using the new method for each of the plane similar to Fig. 4.12. The strain data collapses for $z \leq 96\,\mu\mathrm{m}$. Thus, the faster creeping zone is observed above $z = 96\,\mu\mathrm{m}$ as compare to $z = 81\,\mu\mathrm{m}$ seen with planar image correlation in Section 4.2.3. At the end of creep and start of growth of fracture, the difference between x displacement for z above 96 µm and z below 96 µm is more gradual compare to the estimation by image correlation (Fig. 4.11c). This can be due to the correction in the position of plane introduced by the estimation of z velocity in the optical-flow as seen in Fig. 6.1c. This difference in strain points towards the nucleation growing of fracture around the z plane at height between $\approx 96\,\mu\mathrm{m}$, as discussed in Section 4.2.3.

The estimation in z offers quantification of the problem of undesired creep in our setup as discussed in Chapter 4. We have applied constant strain in the z direction but observe the z is increasing, i.e. the head is going upwards. The source of this abnormal z displacement is the slow creep of the duralumin arm shown in Fig. 2.3.

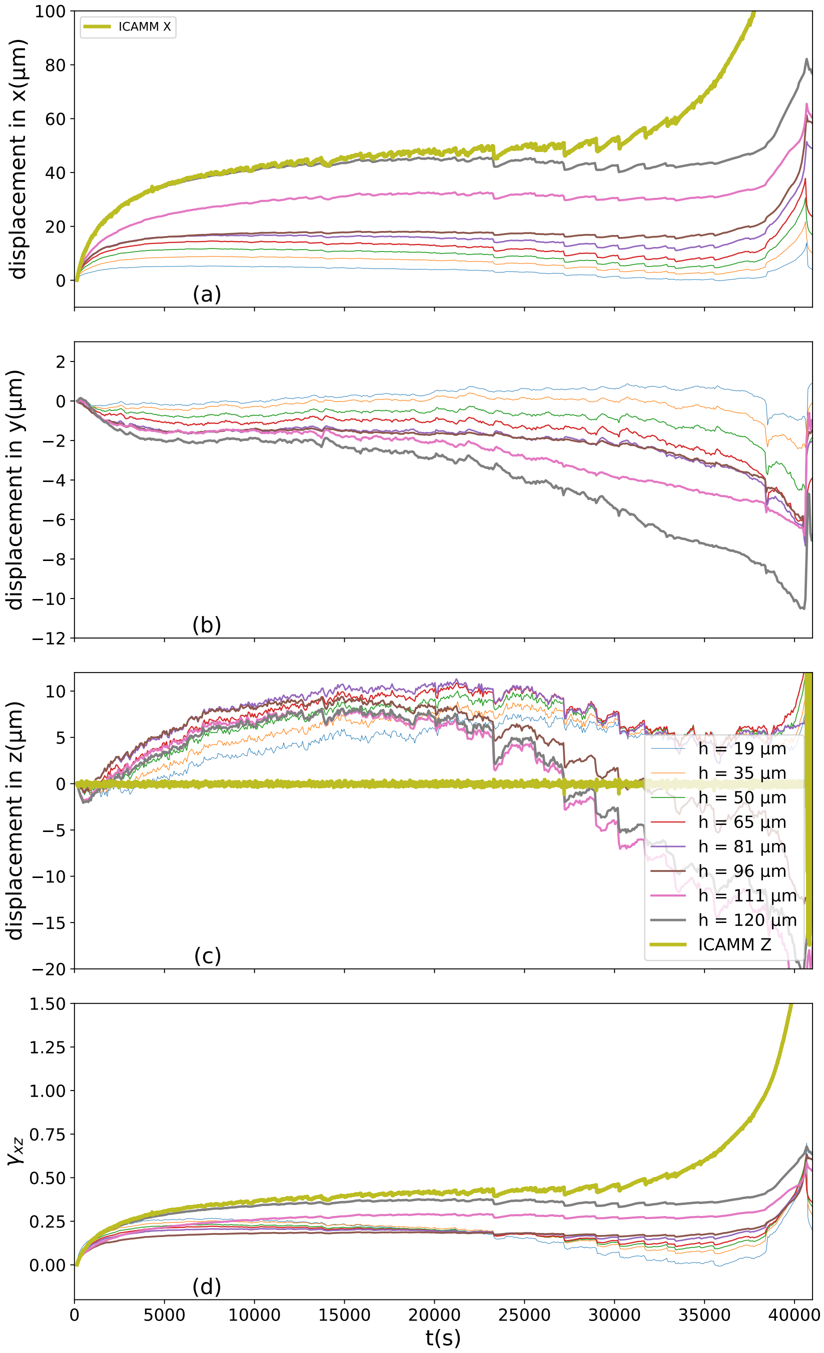

FIGURE 6.1: The cumulative displacement as a function of time at different height averaged over $xy \approx 70$ s after application of creep, obtained by applying Farneback's optical flow between consecutive time frames. (a), (b), and (c) represent the displacement in shear (x), orthogonal (y) and gradient (z) direction respectively. (d) is the strain component γ_{zx} at the different height The thick green curve in (a),(d) and (c) is the displacement of the head in x and z respectively obtained from measurement by ICAMM.

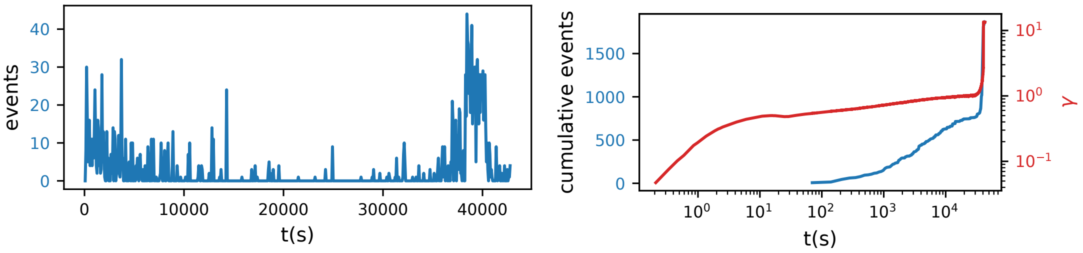

(a) (b)

FIGURE 6.2: Temporal evolution of strand breaking events in the test with $\sigma = 2.13\,\mathrm{Pa}$. (a) Frequency of events (b)Cumulative number of events plotted against the macroscopic creep in log time scale.

As discussed in Chapter 4, the latest iteration of the setup accounts for this creeps and adds in a correction. From the average z displacement from Fig 6.1c, it seems the shift is of the order of 0.5 µm in 1000 s. Thus, around $t \approx 20\,000\,\mathrm{s}$, midway through the creep, instead of the macroscopic normal strain $\gamma_{zz} = 0$, we have $\gamma_{zz} \approx 0.1$. This can trigger local strand breaking in the already stretched gel which might explain the observed onset of dropping in displacement in z seen in Fig. 6.1c at $t > 20\,000\,\mathrm{s}$. This might also explain the change in the average y displacement seen in Fig. 6.1b which still remains $10\times$ smaller compare to the x displacement

Here again, we observe a deviation from the global creep with the average plane creep starting to decrease for $t > 20\,000\,\mathrm{s}$ as seen in Fig. 6.1a. A hypothesis we have is that the net difference only starts to appear at $t = 20\,000\,\mathrm{s}$. As the creep starts to slow down, the strand breaking events are inducing more local damage and their recoil due to loss of stored elastic energy as well as gravitational settling is registered by the image analysis methods leading to a decrease in z and x displacement. Another reason for the x movement might be due to the creep of the arm. Although the creep is vertical, the sensors are not equidistant from the head. A movement of the arm will lead to a change in distance with respect to the one for which the calibration is performed leading to minor movement in the x-direction. In fact in our image, qualitatively we just see the movement of the head in the vertical direction and a very minor movement in the shear direction.

6.2 Spatio-temporal evolution of fracture

Using the method described in Section 5.4, we find local strand breaking events from the location of large divergence in strain field, described in Section 5.3.5. For the two creep experiment shown in Fig. 4.10, we observe different spatio-temporal evolution of fracture, one concentrated in the bulk and the other near the head. It should be noted though the criteria of determining an event i.e. $\|\hat{\gamma}\| > 0.1$ (Section 5.4) is quite robust in catching all the strand breaking events but sometimes may correspond to local rearrangements or noise. We have not yet figured out what these other local maxima in strain field might correspond to but statistically, with this high threshold, they are insignificant.

6.2.1 Nucleation in the bulk

Fig. 6.2a shows the temporal frequency of the strand breaking events. We observe the strand breaking events in the linear viscoelastic regime [13] way before the final catastrophic failure. The events are plotted after the first time frame i.e. $\approx 70\,\mathrm{s}$ as the first creep time frame is noisy due to the fast dynamics compared to the scanning rate of the CLSM. The detection at the later time during the fast propagation of fracture and asymptotic increase in strain ($t > 39\,000$ s) is noisy but shows a burst of events leading to failure. This experiment shows large number of events at the start of the creep for time less than 10 000 s. The Fig. 6.2b shows the cumulative sum of the events in comparison to the measured strain.

The existence of multiple microscopic strand breaking events remarkably does not affect the macroscopic behavior in the primary regime, which is still governed by linear viscoelasticity. Contrary to previous observation using ultrasound probe [13, 70], and scattering technique [53], the strain field at the mesoscale shows local heterogeneity related to plastic rupture events in the primary power-law creep.

The spatial location of these events and their evolution in time can be seen in Fig. 6.3b, which helped us locate the site of nucleation in the actual confocal images at around y= 145 µm, which can be observed through the (x, z) projection around this y as seen in Fig. 6.3a. The shear plane (x, z) images are obtained by averaging 10 (x, z) planes around y= 145 µm. At $t = 0$ s, we see a bright impurity marked by the white circle shown in Fig. 6.3a. This impurity can be an external contamination or a large aggregate of the gel caused by local inhomogeneous gelation while the addition of GDL to the casein acetate solution. At the start of the creep, we see scattered strand-breaking events which qualitatively seemed to avalanche. In Fig. 6.3b, we already start to see a cluster of events at $t \approx 3010$ s which correspond to the location near the impurity, seen in the confocal image panel in Fig. 6.3b. This localized breaking can be attributed to the presence of impurity. As seen from the microstructure in Fig. 6.3a, after the initial orientation due to shear, the overall structure reaches an arrested state of slow creep with low global movement ($t \approx 200$ s to $t \approx 35\,000$ s. The local plastic strand breaking events, however, continue to be registered but at a lower frequency. At $t \approx 15\,800$ s, we already see the presence of a crack near the impurity in Fig. 6.3a. The events occur all across the gel but are concentrated more near the impurity increasing the cluster size around it as seen in Fig. 6.3b. At the end of the linear regime at $t > 35\,000$ s, the frequency of events again starts to increase (Fig. 6.2a) which also corresponds to the increase in the global strain. Finally, the gel undergoes irreversible rupture due to a fast increase in rupture events around the impurity and near the top. We infer from the work of Ref. [72] that the existence of the stiffer impurity facilitates fracture nucleation due to higher topological constraints on the gel surrounding it. The gel remains firm after rupture compared to cluster densification and fluidization observed in failure of reversible gel [94, 95].

6.2.2 Nucleation near the head

To demonstrate the fracture nucleation in a cleaner experiment i.e. without any visible microscopic impurity, we take the other experiment with the applied $\sigma = 1.77$ Pa. We acquire the continuous confocal images over a larger area of x and y dimension 388 µm × 388 µm. The time evolution of event and the corresponding macroscopic creep response are plotted in Fig. 6.4. Statistically, we get similar result from obtaining optical-flow data binned over ≈ 3 µm × 3 µm × 1.5 µm (`binning` parameter 4) versus data averaged over ≈ 6 µm × 6 µm × 1.5 µm (`binning` parameter 8). The nature of the temporal event evolution is different than what we observe in the case of Fig. 6.2. For $t < 300$ s, no events are seen compared to the initial burst of events in the previous case. The frequency of events start increasing gradually and reach a maximum at $t \approx 30\,000$ s before slowing down all within the primary creep regime.

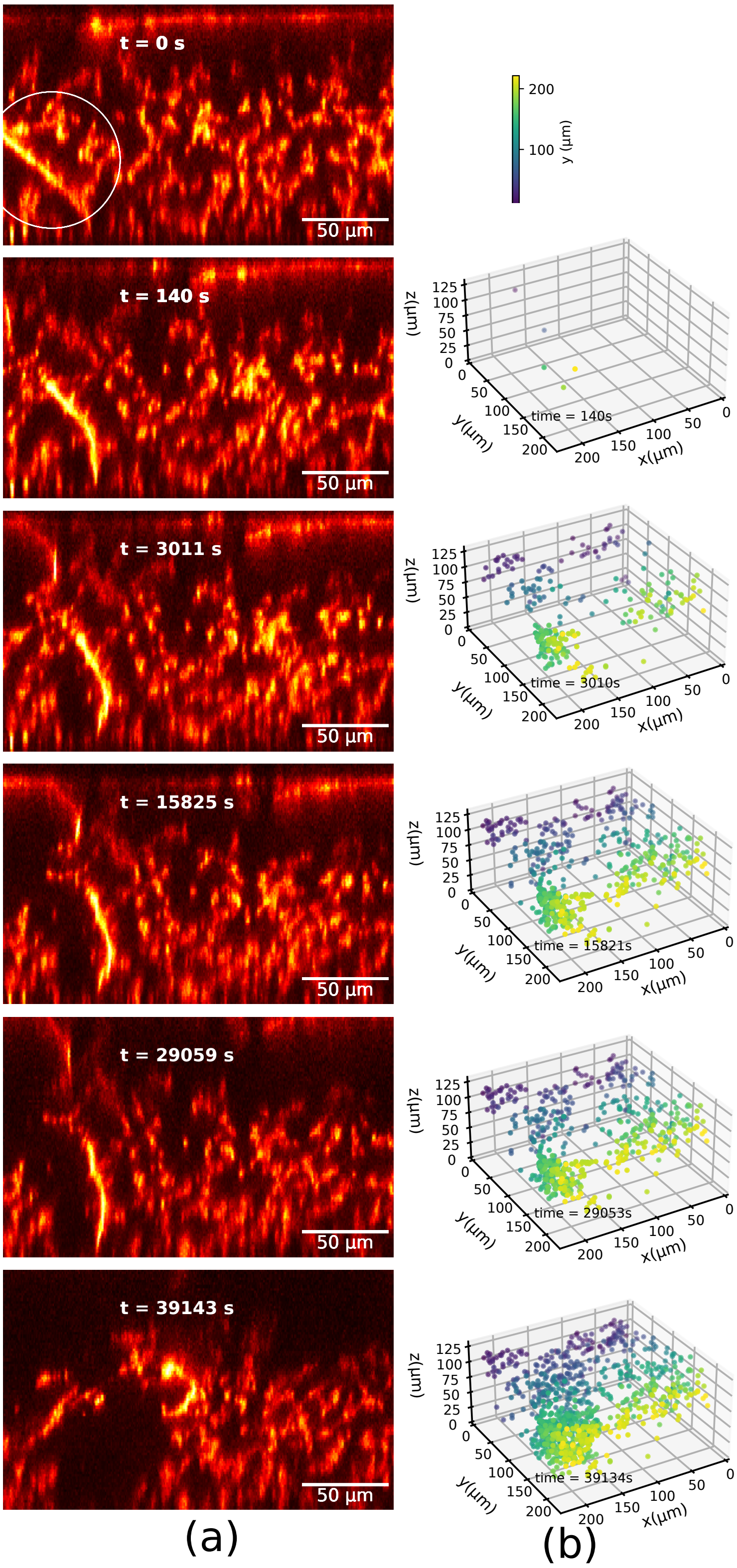

FIGURE 6.3: Microscopic visualization during creep for $\sigma = 2.13\,\mathrm{Pa}$. (a) Cut in the shear plane (x, z) around $y = 145\,\mu\mathrm{m}$ and (b) The evolution of strand breaking events with time in 3D plotted as sphere. We observe nucleation and growth of fracture around a defect (bright strand highlighted by the white circle in (a)) in the bulk in (a) which is correctly estimated by the accumulation of events detected by our method

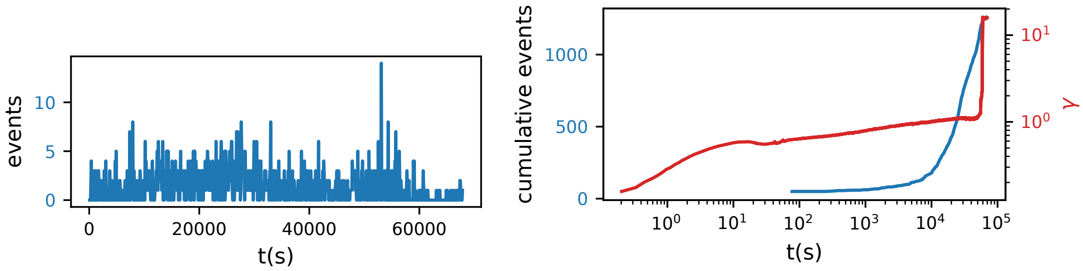

(a) (b)

FIGURE 6.4: Temporal evolution of strand breaking event in the test with $\sigma = 1.77\,\mathrm{Pa}$. (a) Frequency of events (b)Cumulative number of event plotted against the macroscopic creep in log time scale.

Finally at the end of the linear regime, the number of events start to rise again until nucleation and macroscopic fracture. The cumulative number of events against the strain is shown in (Fig. 6.4)b. The total strand breaking events observed until $t = 10\,000\,\mathrm{s}$ is an order lesser than in Fig. 6.2b.

As seen in Fig. 6.5, the nucleation site is smaller and situated at the corner of the observation zone, and difficult to locate without the help of the precursor detection algorithm. As seen in Fig. 6.5b, the events are scattered and qualitatively more independent than cascading. At $t \approx 5600\,\mathrm{s}$, as seen in Fig. 6.5b, we see a small amount of damage accumulating at the site of nucleation. At around order of 10 000 s, the damage accumulated at the site where nucleation happens becomes larger than the other accumulation cluster. Already at $t \approx 16\,000\,\mathrm{s}$, the damage at the site seemed to have grown larger than other clusters and we can see that the damage is no longer free of memory as suggested by Bailey's criteria [57] discussed in Section 1.2.5. Finally, the fracture enters the crack growth regime and goes out of the observable zone leading to macroscopic failure at $t \approx 55\,000\,\mathrm{s}$. Hence, the number of events detected at rupture as seen in Fig. 6.5a is not relatively too large compared to the case of bulk growth (Fig. 6.2a).

6.3 Spatial correlation

After finding the localized events, the next step is to understand how they are linked to each other. It has been shown through simulations [162] and experiments [163, 164, 165, 166, 167] that in amorphous materials these events induce deformation locally which creates internal stresses leading to long-range correlations. These stresses lead to other failure events due to elastic coupling. In colloidal glass this coupling between these highly localized events or shear transformation zones (STZ) have been experimentally described [164, 165, 167] using Eshelby's inclusion analysis [168, 169]. This section contains a brief description of the Eshelby analysis, and the spatial autocorrelation method used to observe it from the experiment.

6.3.1 Eshelby analysis

Eshelby through a thought experiment analytically determined the strain, stress, and displacement field inside a linear elastic material or 'inclusion' surrounded by another linear elastic material or 'medium' [168]. Due to the deformation constrain from the surrounding medium as seen in Fig. 6.6, the inclusion is under a stress $\sigma^*_{ij} = C_{ijkl}\gamma^*_{ij}$, where C_{ijkl} is the elastic modulus and γ^*_{ij} is the unconstrained uniform

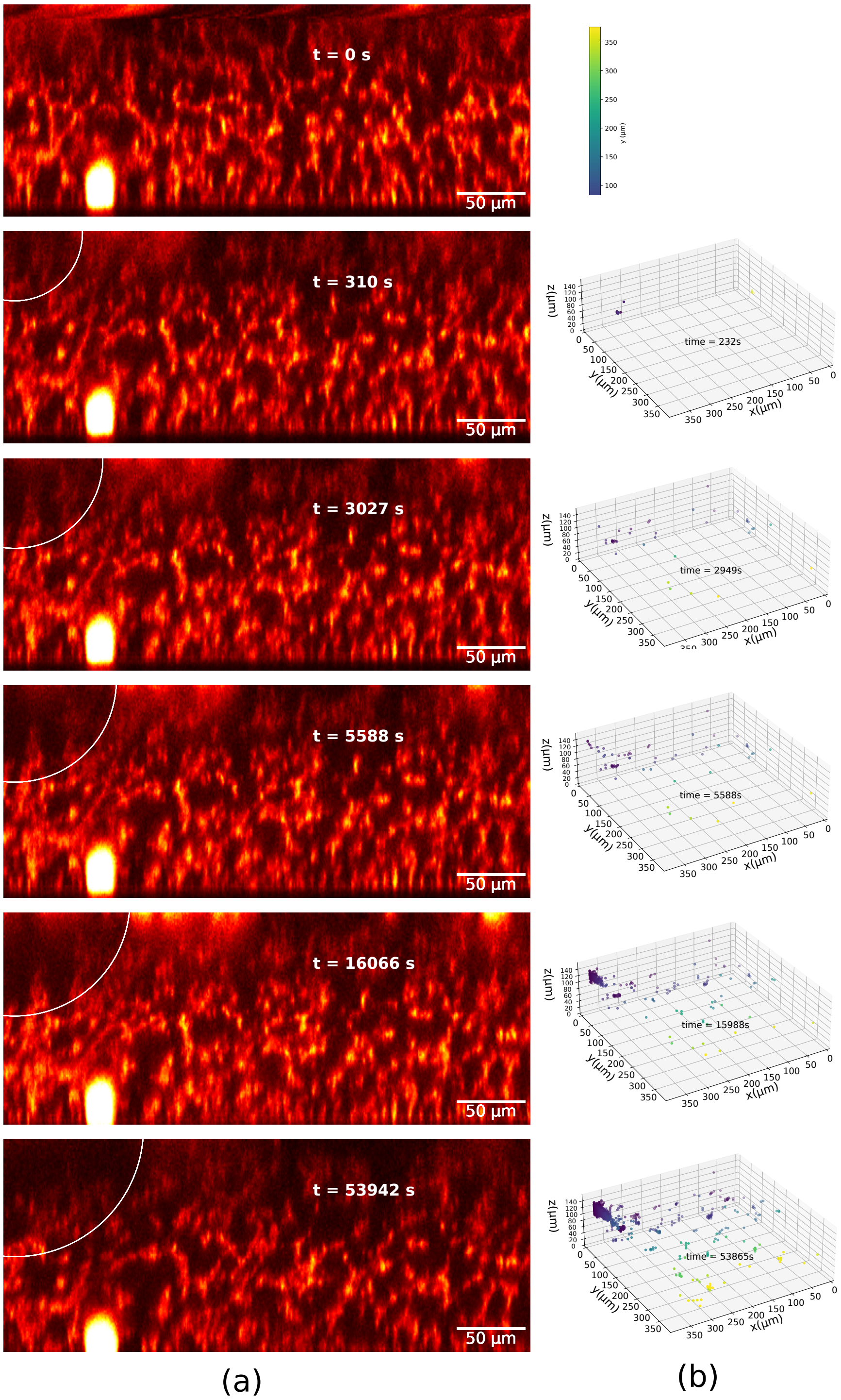

FIGURE 6.5: Microscopic visualization during creep for $\sigma = 1.77\,\mathrm{Pa}$. (a) Cut in the shear plane (x,z) around $y = 11\,\mu\mathrm{m}$ and (b) The evolution of strand breaking event with time in 3D plotted as sphere. We observe nucleation and growth of fracture around a top left corner near the head in (a) which is correctly estimated by the accumulation of event detected by our method

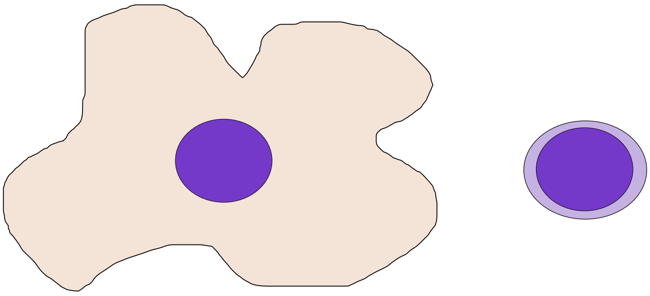

FIGURE 6.6: Eshelby's though experiment of an inclusion inside a medium to understand the stress and strain due to change of form assuming linear elastic behavior

strain i.e. if the inclusion was free. If the inclusion is an ellipsoid, and the medium is infinite, the strain field inside the inclusion is uniform. In the case of shear transformation of the spherical inclusion of radius a, with unconstrained transformation shear strain $\gamma^*_{xz} = \frac{\epsilon}{2}$, and if the elastic constant is the same for the inclusion and medium, the principal shear strain component xz component is given by [167].

$$\gamma_{xz}(r) = \begin{cases} \gamma^o_{xz} & \text{for } r < a \\ \frac{\gamma^o_{xz} a^3}{4r^5}[9a^2c - (2+3c)r^2 - 15c(7a^2 - 5r^2)\cos(4\theta)] & \text{for } r \geq a \end{cases} \tag{6.1}$$

where $\gamma^o_{xz} = \epsilon\frac{4-5v}{15(1-5v)}$, $c = \frac{1}{4(4-5v)}$, v is the Poisson ratio, r is the position vector from the origin of the inclusion and $\theta = \cos^{-1}(z/r)$

This $\cos(4\theta)$ results in a fourfold quadrupolar pattern in the xz plane outside the inclusion zone. Thus in any material, the presence of this pattern signifies Eshelby type elastic coupling between the surrounding and the local plastic zone.

6.3.2 Spatial autocorrelation

Spatial autocorrelation examines how one data point is similar to other data points around it. Mathematically it is mapped similar to cross-correlation as seen in Section 5.1.1 such that if $f(x,y)$ describes a 2D signal its spatially autocorrelation $a(x,y)$ is given by

$$a(x,y) = \sum_{m=1}^{M}\sum_{n=1}^{N}(f(m,n))(f(m+x,n+y)) \tag{6.2}$$

Note that compared to (Eq. 5.2), the definition here does not account for the subtracted average term and the normalization term in the denominator. This does not change the signal qualitatively. Similar to (Eq. 5.3) and (Eq. 5.4), the autocorrelation can be calculated using fast Fourier transform and later converted to real space.

6.3.3 Eshelby from autocorrelation

In experiments, the strain field can be analyzed by spatial correlation function. The 3D spatial autocorrelation of the the strain field γ_{xz} described by eq 6.1 can be seen in Fig. 6.7. The xz projection shown by Fig. 6.7 is special because it encapsulates the

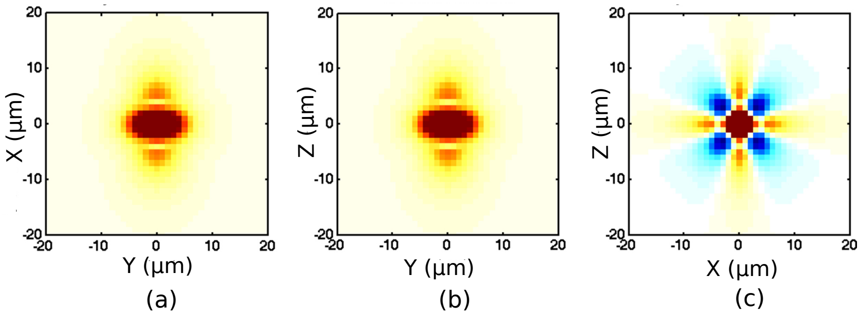

FIGURE 6.7: The crosssection representing the (a) xy, (b) yz, and (c) xz cut for the spatial correlation of γ_{xz} for an Eshelby inclusion given by (Eq. 6.1). The size of the inclusion is 2.25 µm and the isotropic medium surrounding the inclusion has a poisson ratio of $v = \frac{1}{3}$. Notice the quadrupolar pattern in (c), the characteristic pattern of an Eshelby inclusion. Figure adapted from Ref. [167].

characteristic quadrupolar pattern of negative correlation in strain around the inclusion. Red signifies a positive correlation while blue indicates negative correlation i.e the strain is of opposite sign to that inside the inclusion.

To capture the effect of localized shear transformation in our experiment, we look at the spatial correlation of the non-affine component of principle strain component defined as $\Delta\gamma_{xz} = \gamma_{xz} - \bar{\gamma_{xz}}$ where $\bar{\gamma_{xz}}$ is the average of the component.

6.4 Result from spatial correlation

Understanding how the strand breaking events interact with each other and the surrounding intact gel should help us explain why fracture nucleates in some specific regions. As seen in Section 6.3, Eshelby inclusions can be thought of as localized plastic core embedded in an elastic homogeneous surrounding and has been studied in several amorphous systems to understand at mesoscale how these local events are elastically coupled. We compute the unnormalized 3D spatial correlation of the non-affine part of the (x, z) component of the strain $\Delta\gamma_{xz} = \gamma_{xz} - \overline{\gamma_{xz}}$, to see evolution of local pattern. The strain data is averaged over a bin of size 3 µm × 3 µm × 1.5 µm, which sets the resolution of the autocorrelation. For all the plots, the colormap scales between $\pm 0.1\Delta\gamma_{xz}$ so that the maximum dynamic range in the pattern is visible.

We first test the experiment undergoing bulk nucleation and fracture ($\sigma = 2.13$ Pa). For the autocorrelation between time frames where we have no strand breaking event detected, we she the quadrupolar pattern which is regular Eshelby like behavior as seen in Fig. 6.8. Strangely, as seen in Fig. 6.9, between time frames where we observe strand breaking events, a significant number show distorted quadrupole, with a weaker anti-correlation in the extensional direction than the one in compression. The same is not observed for spatial correlation between time frame with events for experiment with nucleation near the head ($\sigma = 1.77$ Pa) as seen in Fig. 6.10. The distortion points towards the impurity-driven nucleation violating the Eshelby analysis in multiple ways: The inclusion having an elastic modulus different from the surrounding medium and/or the strain field inside the plastic inclusion being non-uniform. For now, we do not have a strong explanation for this.

Fig. 6.11 shows the autocorrelation before the application of the stress. Over a longer length scale, it is quite noisy with large magnitudes. However, over a shorter distance, we observe a strong Eshelby pattern of alternating positive and negative

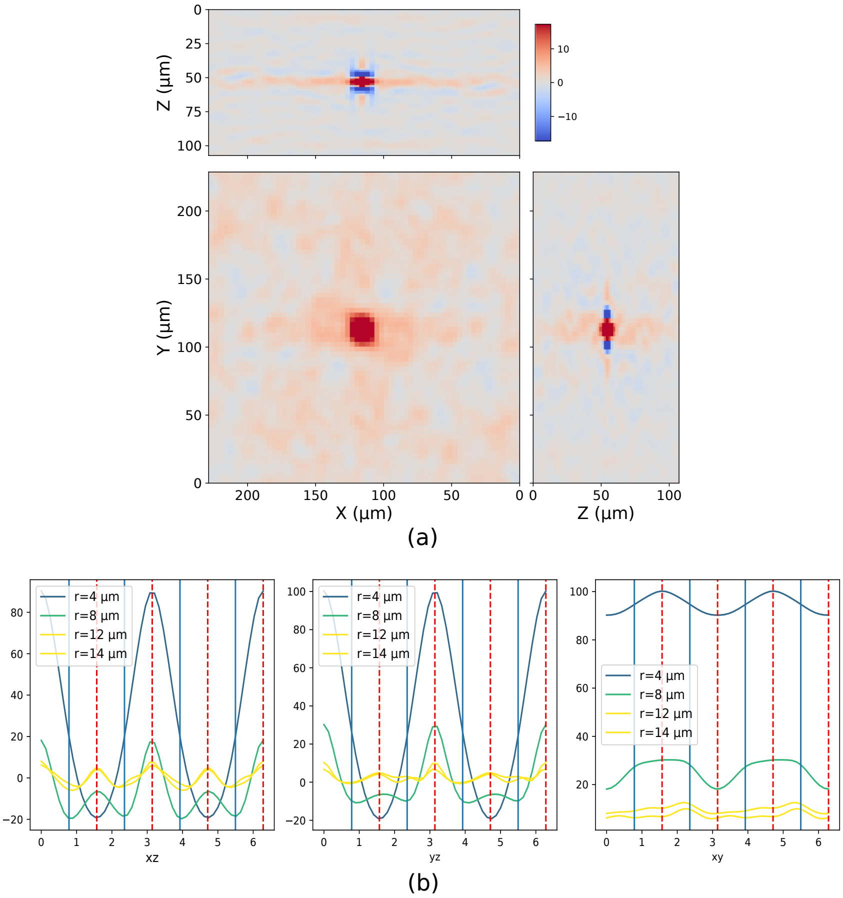

(a)

(b)

FIGURE 6.8: 3D spatial autocorrelation on $\Delta\gamma_{xz}$ between two consecutive time frame where we have no strand breaking event for the experiment with bulk failure ($\sigma = 2.13\,\mathrm{Pa}$). (a) Orthogonal projection of the spatial correlation: Notice the four fold quadrupolar pattern in the xz projection, a signature of Eschelby inclusion. (b) 2D projection of the angular variation of the autocorrelation.

correlation surrounding the positive core in the (x,z) projection of the autocorrelation. It is similar qualitatively and in magnitude to the one shown in Fig. 6.10, which is between two-time frames after the application of shear where we see an event. Quiescent colloidal glass [167] show similar development of correlation where thermal energy is the driving force but is an order of magnitude smaller than that of sheared colloidal glass. The presence of stronger attractive potential compared to the thermal energy and hence, the stronger elastic nature of the arrested gel can explain this difference.

Around the failure, the autocorrelation becomes noisy. Once the brittle fracture either in the bulk or near the head takes place, we still observe the Eshelby like pattern which means the fractured gel is still having elastic nature with shear transformation zones.

6.5 Conclusion

We have established strand-breaking events as the precursor to fracture in the gel. These events are identified through a high local gradient in the strain field, which is derived from Farneback's algorithm for displacement estimation. Through this displacement estimation technique, we get a picture of global displacement as well

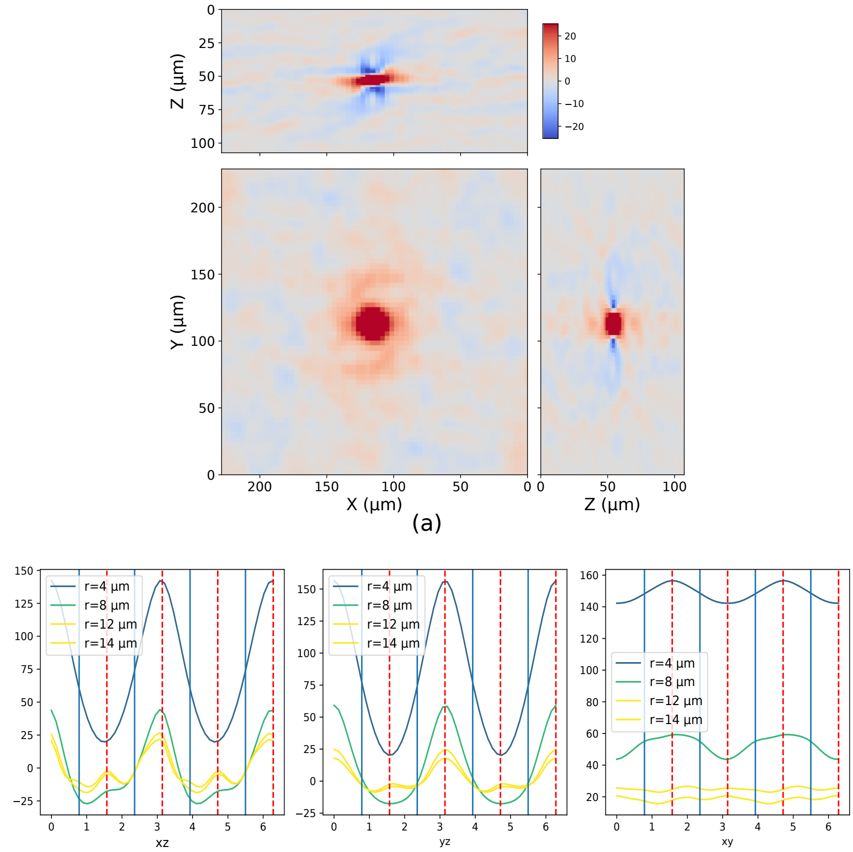

(a)

(b)

FIGURE 6.9: 3D spatial autocorrelation n $\Delta\gamma_{xz}$ between two consecutive time frame where we detect strand breaking events for the experiment with bulk failure ($\sigma = 2.13\,\mathrm{Pa}$). (a)Orthogonal projection of the spatial correlation: Notice the distorted four fold quadrupolar pattern in the xz projection. (b) 2D projection of the angular variation of the autocorrelation. For all the strand breaking events we see this significant distortion in the four fold pattern.

by averaging obtain the displacement of each (x, y) plane. This led us to discover a problem with our setup: The arm to which the sensors are attached is not perfectly fixed but displays creep in the vertical direction. This leads to majorly vertical and some minor motion in x direction. This problem is elaborated in Chapter 4 and we have also provided the solution for it. Until the end of this Ph.D., our task will be to obtain a cleaner experiment and verify our results discussed in this chapter.

Keeping the error in the current experiments in mind, we provide evidence of precursor events in the linear viscoelastic regime of a gel under constant stress. The nature of the nucleation, whether it is in the bulk or at the interface needs further clean experiments to explore the reason for it. Here, we provide one experiment governed by bulk due to the presence of impurity while another where we have nucleation near the head. We performed other creep experiments but the nucleation of the precursor events was not observed besides in these two cases discussed. This is expected as strand-breaking events are rare. In fact, through numerical simulations, it has been shown that failure under creep for colloidal gels can occur by breaking just $\approx 0.1\%$ of the particle bonds [89]. From (Eq. 2.12) the area under which strain can be considered homogeneous is $\approx 13\,\mathrm{mm}^2$. Thus, the area under observation through imaging with the current design of the head is $\leq 1\%$ of the total area where stress is significant, making the probability of observing fracture nucleation

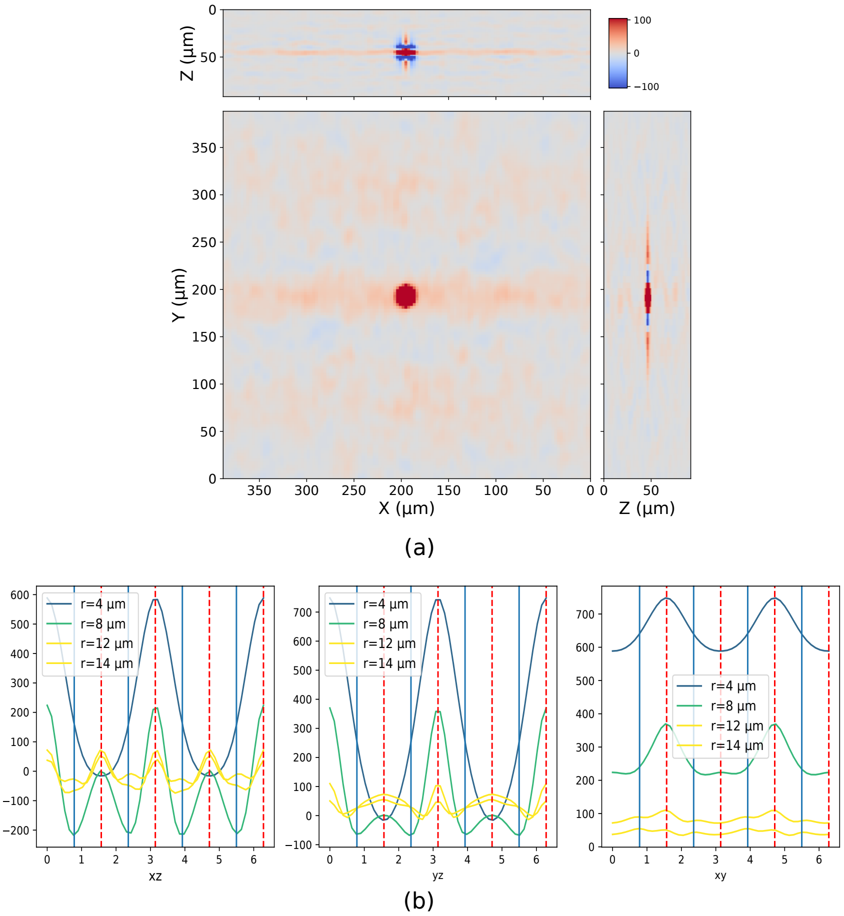

(a)

(b)

FIGURE 6.10: 3D spatial autocorrelation $\Delta\gamma_{xz}$ between two consecutive time frame where we detect strand breaking events for the experiment with failure near the head ($\sigma = 1.77\,\mathrm{Pa}$). (a)Orthogonal projection of the spatial correlation (b) 2D projection of the angular variation of the autocorrelation with no distortion in xz compared to Fig. 6.9.

low. Thus, design changes need to be made which can increase the percentage of area under observation with significant strain and hence, probability of observing events nucleation.

Besides the temporal and spatial statistics, we try spatial correlation to understand the nature of this localized high strain zone due to plastic strand breaking events. We discover through the spatial correlation of the γ_{yz} that these shear transformation zones act like Eshelby's inclusion with the correlation showing the typical quadrupolar behavior. These inclusions are present even before the application of stress and due to the strong elastic nature of protein gel, and hence, show similar magnitude before and after the stress is applied. The observation of distorted non-Eshelby like quadrupolar patterns in the bulk nucleation of events is linked to the plasticity governed by the artifact and is not observed in the other experiment. This has been verified for other experiments as well where we see no nucleation either in bulk or near the interface, but observe strand breaking events.

Finally, we need to look into the pattern observed in planes other than shear which can answer how these events are linked to each other through the elastic network. Also, autocorrelation on the γ_{yz} component of the strain should be tried since the displacement in this plane is non-affine. A problem with the current analysis using optical flow is the prediction of large displacement in the portion where the gel is not present as seen in Fig. 5.5c. This noise is observed even after the weighted

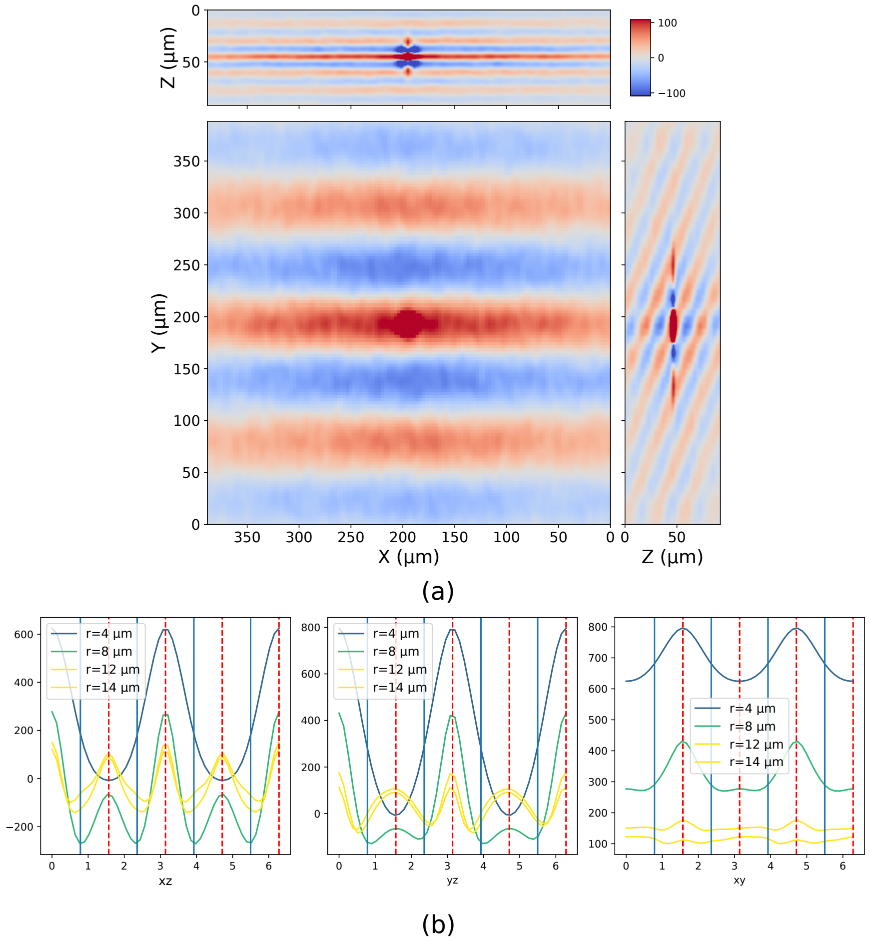

FIGURE 6.11: 3D spatial autocorrelation $\Delta\gamma_{xz}$ between two consecutive time frame before the start of the creep test for the experiment with failure near the head ($\sigma = 1.77\,\mathrm{Pa}$). (a)Orthogonal projection of the spatial correlation (b) 2D projection of the angular variation of the autocorrelation. Notice the similarity with Fig. 6.10.

averaging operation and might lead to noise in autocorrelation signal larger than the resolution of the autocorrelation ($\approx 3\,\mu\mathrm{m}$) as seen in the large positive correlation at the center of the order $10\,\mu\mathrm{m}$. Currently, we are not sure whether this large correlation is linked to the size of the inclusion or just noise from Farneback's optical flow algorithm. A more precise displacement field estimation is needed to further explore this.

Key concepts of the chapter: Applying the analysis we developed based on Farneback's small-displacement estimation method, we observe the three regimes of fracture in our experiment on casein gel under creep and made some interesting observations:

1. The implementation we developed offers insight into the displacements in the z direction as well. We observe and quantify the problem of the undesired z displacement from the average z displacement of the xy planes at different heights.
2. We have two experiments where the nucleation of fracture is in the observable zone of the microscope. The first one has damage accumulation due to strand-breaking precursors in the bulk. However, this is not a clean experiment as we observe an impurity over which this damage concentrates and nucleate.
3. However, in the other experiment, where the damage is accumulated near the head, the temporal growth of fracture is more gradual. The site of nucleation accumulates enough damage to be larger than other clusters of damage accumulation way before in the primary regime of the creep associated with this gel. Finally, in the tertiary regime of creep, it shows faster nucleation followed by crack growth leading to the fracture of the gel.

To understand the nature of the interaction between the accumulated damage, we apply 3D spatial correlation on the non-affine principle shear component γ_{yz}. Our preliminary observations are:

1. We observe a quadrupolar pattern in the correlation in the xz plane. This quadrupole corresponds to the Eshelby kind of interaction where local zones of high plastic activity exist coupled elastically to the surrounding medium.
2. The Eshelby exist over all the time: Before or after the application of creep, and when we have strand breaking event or when we have none. This points to the pre-existence of this 'weak' region in these largely heterogeneous materials.
3. For the case of impurity mediated nucleation in the bulk, we observe a distorted Eshelby pattern whenever we detect precursor events.

Chapter 7

Our nature consists in motion;
complete rest is death

Blais Pascal

Conclusion and perspectives

This work on micromechanics of gel rupture consists of two-part:

- Developing the required instrumental setup which can apply and measure stress and strain on soft gels, and developing the appropriate physical chemistry and experimental procedure for the gel system to work with this setup.
- Performing controlled shear stress and strain experiment while simultaneously observing the microstructure in soft casein gels which show characteristics of brittle fracture, to identify the fracture precursor and how they interact leading to nucleation and finally catastrophic failure.

7.1 Novel setup

We have developed a robust setup to probe the long-term mechanical response of soft materials to steady mechanical stimuli while having a direct microscopic visualization of the structural changes happening inside them. The deflections are measured using eddy-based sensors which offer currently an accuracy of up to 6 mPa **on stress measurement. This is at least an order of magnitude better than published shear cells [79, 80] and of the same order as commercial rheometers**. This can be further improved by changing the cantilever dimensions thus making it possible to work with softer systems. The additional benefit is the presence of two sensors, having the same precision in both the shear and normal directions. The usage of PID control loops allows stress and strain control independently in both directions. The large dynamic range of the sensors can help explore materials ranging from very soft (10 mPa) to soft (10 Pa).

The gel system we decided to work with is 1% sodium caseinate. The pore size in this protein gels is of the size $\approx 10\,\mu\text{m}$ allowing for visualization of microstructure with good resolution. We have discussed the physical chemistry of this system and based on a combination of buffer mediated acidification and mass transfer with the surrounding solvent, we have developed a fast in-situ gelation method. The typical time for the gelation is ≈ 20 min and the mass transfer is estimated to equilibrate in 210 min. The in-situ gelation lays down the procedure to possible studies on fracture in colloidal gel systems such as PMMA particle gels.

We demonstrate the effectiveness of our setup by performing controlled strain and stress experiments. The microscopic behavior can be perfectly visualized through the 3D stroboscopic view of the microstructure. Indeed combined with simple 2D image correlation, it offers insight into how the presence of a softer layer near the head mediates the catastrophic failure of the material under constant strain stairs. This soft layer is thin and can be a result of partial sedimentation during the 20 min of gelation. The softness of this zone grows gradually with the step increment in strain.

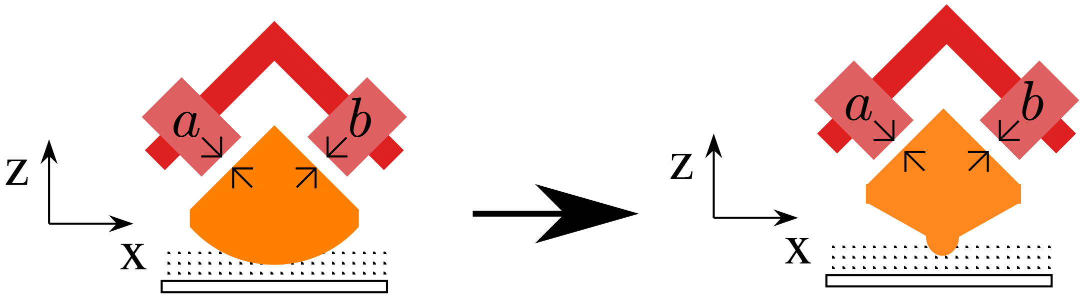

FIGURE 7.1: Schematic representation of the change in radius of curvature

7.2 Scope for setup design improvement

The setup we have developed has potential for several studies in soft solid rheology but suffers from two problems:

- Although we have quite good control on position and stress, we observe a drift in the z position during long-duration creep experiment of the order 0.5 µm in 1000 s (see Section 6.1). This affects our claim of precise control as well can impact fracture nucleation mediated by the change in normal strain.
- In Section 2.3.3, we have defined a critical length x_c (Eq. 2.12) away from the head center, over which we can consider that the strain is homogeneous. Beyond this, due to the curvature of the head, the strain is considerably smaller than that at the center. Thus with the current radius of curvature $R_o = 20\,\text{mm}$, we have $x_c = 2\,\text{mm}$. Assuming circular symmetry,the area under observation with the (x,y) image size of 388 µm × 388 µm is $\approx$ 1% of the total area over which the stress is concentrated. This is really a small probability of observing nucleation events and in fact, over multiple experiments, I just came across two, where I see the nucleation of precursors leading to fracture.

We are currently working on solving these two problems. The reason and the solution for the first have been discussed in Section 4.3. The mechanical parts are already fabricated. Here I present the solution to the second problem in brief.

7.2.1 Head design

As seen in (Eq. 2.12), the critical distance x_c is proportional to the radius of curvature. A decrease in radius of curvature of the head can concentrate stress in a smaller region. Thus, we have made a change in the head design as seen in the schematic Fig. 7.1 by changing R_o from 20 mm to 1 mm. This leads to an increase in the observable percentage of area under effective strain homogeneity to 24%.This increases our probability of observing nucleation of strand-breaking events.

An issue which will arise on using this head is the proportional reduction in the precision of stress measurement. This is because a reduction in radius will lead to a reduction in effective are (A_{eff}) and hence, the deflection required to apply the same stress as before would be smaller, thus reducing the precision. Specifically, the reduction will be from 6 mPa to 170 mPa. To address this we can either reduce the cross-section area of the cantilever or make a stiffer gel by changing to a higher concentration sodium caseinate gel. We are currently proceeding with the latter by increasing the concentration to 2 wt% sodium caseinate. Based on (Eq. 1.27), our mesh size should scale down to approximately 6 µm which is still large enough to be observable with the resolution of our microscope.

7.2.2 Other design challenges

One drawback of our design is the long $\approx 10\,\mathrm{s}$ response time of ICAMM. This makes our apparatus unsuited for steady shear-rate experiments or for oscillatory rheology at high frequencies. The response time could be shortened by using a different actuator with faster electronics. However, the inertia of the cantilever and viscous forces acting on the head would set a lower bound for the response time.

Although ICAMM has high precision in stress measurement of 6 mPa, its precision in stress application is slightly lower at 20 mPa as it is limited by the action of the micromanipulator and the PID control loop we use. Without causing overshoot in the control action, we can improve this by shifting to an actuator more precisely than the current micromanipulator.

Currently, all our operations are done in a room at temperature 18°. More precise temperature control could be implemented provided a lack of vibration, e.g. using Peltier elements or laminar flow around the tank. Since the materials used for the different components of the apparatus are subject to thermal dilation, calibrations should be done anew at every 'large' temperature change. This might be an issue if one intends to control the temperature dynamically, e.g. to quench a sample.

7.3 Precursors to fracture

Our decision to use sodium caseinate gel due to its simpler physical chemistry and ease of integration to the setup comes up with additional challenges in deriving local information compared to colloidal gel systems. In Chapter 5, we described different small-displacement estimation techniques which extract the local displacement or velocity from the intensity change namely PIV and Farneback's optical flow algorithm. We concluded that Farneback's algorithm is more accurate and faster compared to PIV. A 3D implementation of the algorithm was developed based on the plane Couette geometry of our shear experiments. The velocity field can be used to obtain the local strain rate field. Thus, we have the measurement of local strain rate which can give information about the local plastic events.

Specifically, in our creep experiments, we observe scattered strand-breaking events that manifest in the velocity field through the presence of high local velocities. Thus, a maximum in local velocity gradient and specifically in the norm of strain rate field is used to detect spatially and temporally the distribution of these strand breaking events. In fact, when we track these detected events, we made some interesting observations (for the clean experiment discussed in Chapter 6) :

- The strand breaking events start to occur soon after ($t \approx 300\,\mathrm{s}$) the application of the sub-critical stress and continue to occur throughout the duration of the creep without impacting the global linear viscoelastic behavior.
- These events are spread across the gel and qualitatively show independent accumulation with no cascading effects.
- Around $t \approx 10\,000\,\mathrm{s}$ and still in the linear viscoelastic regime, we start to see one of the accumulations grow larger in size than the others. Correspondingly in the gel, we see a crack nucleating near the head of the gel (see Fig. 6.5).
- Outside the linear regime, we observe fast nucleation at the above-mentioned site, and finally the fast crack growth regime leads to the macroscopic fracture of gel (at $t \approx 55\,000\,\mathrm{s}$).

Thus, we provide the first experimental evidence of strand breaking events as fracture precursors for physical gel under creep, as well as the observation of the three regimes of fracture. The question that arises next is how can we quantify the nature of the interaction of the damage accumulation due to strand breaking events i.e. how are they correlated? The second question is how and when does the damage accumulation become large enough to transitions to the nucleation regime?

Because our temporal resolution currently is approximately 70 s, observation of a short temporal correlation is not possible. But, with a faster spinning disk confocal microscope the lab has recently acquired, the temporal resolution should improve by a factor of at least 10. We tried to see if there is a local spatial correlation. We looked at the non-affine part of the principle shear component, γ_{xz}. We are able to see Eshelby type interactions that explain the existence of shear transformation zones within the gel that undergo plastic rearrangements coupled to the surrounding elastic medium. We discover that they exist even before the gel is sheared, which in cases of colloidal glass have been identified as prospective flaw zones which suffer plastic rearrangements upon undergoing shear [167]. However, we cannot prove this claim for our gel as the resolution of measuring local shear is at the mesoscale for our analysis and due to the more heterogeneous nature of our gel. The low resolution of local strain measurement arises from the flaw in the small displacement estimation by Farnebacks' algorithm which predicts displacement around a plastic strand breaking event in zones where we have no gel, which leads to noise in the autocorrelation. Besides, we have worked with a version of Farneback where local motion is just pure translational. Thus, There is scope for improvement by considering other local transformations such as rotation. The best would be to have some analysis similar to Ref. [170], where in addition, local plasticity can be quantified. The method, however, requires traceable centers of the discrete unit such as cells, foam, and particle and identification of links with the neighbors. This, although far from the microscopic picture of our gel can be realized by placing a grid of regularly spaced points in our system and identifying grid points that are important, based on whether they are inside the gel matrix or not. Implementation of this method for gel has been done by Mathieu Leocmach but its validation is still in the early stage.

Another aspect I would like to explore is looking at the component γ_{yz} which should inherently have no affine component and hence, a higher signal for the presence of correlation. The ultimate aim of the correlation study would be to connect with the observation of Bailey's criteria in this gel system, and to see if the local measurement corresponds to the assumption of independent, irreversible damage accumulation (see Section. 1.2.5). This would make for some good parallels with fracture in hard brittle systems which also follow this criterion.

Besides, the study in fracture of gels can be advanced by looking at fracture of colloidal gel system with large particle such as PMMA particle gel where the analysis should be relatively easier since particle tracking is possible. A comparison of the microscopic development during creep in this system should help to explain the difference of rheological behavior observed in these gels undergoing reversible fluidization vs the brittle fracture ones.

7.4 Looking beyond (i.e. before) fracture

Besides the fracture, with this setup, we have the potential to explore the microscopic reason for other non-linear phenomena observed in gels. The dependence of gel's linear and non-linear rheology on the normal stress/strain condition it is exposed to during aging of the gel has been explored [140, 141]. We ourselves have observed (data not shown in this thesis) fracture time reduced to half on changing the condition from no control during gelation to strain control in the normal (z) direction. The high precision in the stress measurement in the normal direction along with the microscopic picture in these materials can expand the understanding of aging in these systems. Another idea that can be explored is the understanding of the origin of reversible softening observed in the work of Ref [47] on increasing the amplitude of the step strain. Ultimately, the combination of fast confocal microscopy with our setup can serve as a tool to understand the microstructural origin of phenomena in viscoelastic systems across domains.

Bibliography

[1] P. G. de Gennes. "Soft Matter". In: *Reviews of Modern Physics* 64.3 (July 1, 1992), pp. 645–648. DOI: 10.1103/RevModPhys.64.645. URL: https://link.aps.org/doi/10.1103/RevModPhys.64.645 (visited on 10/17/2021).

[2] Luca Cipelletti, Kirsten Martens, and Laurence Ramos. *Microscopic Precursors of Failure in Soft Matter*. Sept. 26, 2019. arXiv: 1909.11961 [cond-mat]. URL: http://arxiv.org/abs/1909.11961 (visited on 10/03/2019).

[3] Stephen Timoshenko. *History of strength of materials: with a brief account of the history of theory of elasticity and theory of structures*. Courier Corporation, 1983.

[4] L. T. Wardhaugh and D. V. Boger. "The Measurement and Description of the Yielding Behavior of Waxy Crude Oil". In: *Journal of Rheology* 35.6 (Aug. 1, 1991), pp. 1121–1156. ISSN: 0148-6055. DOI: 10.1122/1.550168. URL: http://sor.scitation.org/doi/abs/10.1122/1.550168 (visited on 10/13/2021).

[5] Kyu Hyun et al. "A Review of Nonlinear Oscillatory Shear Tests: Analysis and Application of Large Amplitude Oscillatory Shear (LAOS)". In: *Progress in Polymer Science* 36.12 (Dec. 2011), pp. 1697–1753. ISSN: 00796700. DOI: 10.1016/j.progpolymsci.2011.02.002. URL: https://linkinghub.elsevier.com/retrieve/pii/S0079670011000281 (visited on 10/08/2021).

[6] B. N. J. Persson. "On the Mechanism of Adhesion in Biological Systems". In: *The Journal of Chemical Physics* 118.16 (Apr. 22, 2003), pp. 7614–7621. ISSN: 0021-9606. DOI: 10.1063/1.1562192. URL: http://aip.scitation.org/doi/abs/10.1063/1.1562192 (visited on 10/16/2021).

[7] James P. Sethna, Karin A. Dahmen, and Christopher R. Myers. "Crackling Noise". In: *Nature* 410.6825 (6825 Mar. 2001), pp. 242–250. ISSN: 1476-4687. DOI: 10.1038/35065675. URL: https://www.nature.com/articles/35065675 (visited on 10/12/2021).

[8] Alex Hansen, Per Christian Hemmer, and Srutarshi Pradhan. *The fiber bundle model: modeling failure in materials*. John Wiley & Sons, 2015.

[9] Louis-Joseph Vicat. *Recherches expérimentales sur les phénomènes phisiques qui précedent et accompagnent la rupture ou l'affaissement d'une certaime classe de solides*. Fain, 1833.

[10] Jean-Paul Poirier. *Creep of crystals: high-temperature deformation processes in metals, ceramics and minerals*. Cambridge University Press, 1985.

[11] Michael P C Conrad, Gregory D Smith, and Goran Fernlund. "FRACTURE OF SOLID WOOD: A REVIEW OF STRUCTURE AND PROPERTIES AT DIFFERENT LENGTH SCALES". In: *WOOD AND FIBER SCIENCE* 35 (2003), p. 15.

[12] H. Nechad et al. "Creep Ruptures in Heterogeneous Materials". In: *Physical Review Letters* 94.4 (Jan. 31, 2005), p. 045501. ISSN: 0031-9007, 1079-7114. DOI: 10.1103/PhysRevLett.94.045501. URL: https://link.aps.org/doi/10.1103/PhysRevLett.94.045501 (visited on 08/06/2021).

[13] Mathieu Leocmach et al. “Creep and Fracture of a Protein Gel under Stress”. In: *Physical Review Letters* 113.3 (July 2014), p. 038303. ISSN: 0031-9007. DOI: `10.1103/PhysRevLett.113.038303`. arXiv: `1401.8234`.

[14] T. Sentjabrskaja et al. “Creep and Flow of Glasses: Strain Response Linked to the Spatial Distribution of Dynamical Heterogeneities”. In: *Scientific Reports* 5.1 (2015), p. 11884. ISSN: 2045-2322. DOI: `10.1038/srep11884`. URL: `http://www.nature.com/articles/srep11884` (visited on 02/22/2021).

[15] Jürg Schweizer. “Snow Avalanche Formation”. In: *Reviews of Geophysics* 41.4 (2003), p. 1016. ISSN: 8755-1209. DOI: `10.1029/2002RG000123`. URL: `http://doi.wiley.com/10.1029/2002RG000123` (visited on 10/04/2021).

[16] Leonardo da Vinci. *The mechanical books, in the ordered reconstruction by Arturo Uccelli, preceded by a critical introduction and an examination of the sources.* 1972.

[17] William Barclay Parsons. *Engineers and Engineering in the Renaissance*. Williams & Wilkins, 1939.

[18] Frederick Thomas Peirce. “Tensile tests for cotton yarns:“the weakest link” theorems on the strength of long and of composite specimens”. In: *J. Textile Inst* 17 (1926), pp. 355–368.

[19] Waloddi Weibull. “A statistical theory of strength of materials”. In: *IVB-Handl.* (1939).

[20] JAY R. LUND and JOSEPH P. BYRNE. “Leonardo Da Vinci’s Tensile Strength Tests: Implications for the Discovery of Engineering Mechanics”. In: *Civil Engineering and Environmental Systems* 18.3 (June 1, 2001), pp. 243–250. ISSN: 1028-6608. DOI: `10.1080/02630250108970302`. URL: `https://doi.org/10.1080/02630250108970302` (visited on 10/15/2021).

[21] John Price Hirth, Jens Lothe, and T Mura. “Theory of dislocations”. In: *Journal of Applied Mechanics* 50.2 (1983), p. 476.

[22] P. Schall et al. “Visualization of Dislocation Dynamics in Colloidal Crystals”. In: *Science* 305.5692 (2004), pp. 1944–1948.

[23] Zhiwei Shan et al. “Grain boundary-mediated plasticity in nanocrystalline nickel”. In: *Science* 305.5684 (2004), pp. 654–657. ISSN: 0036-8075, 1095-9203. DOI: `10.1126/science.1098741`. URL: `https://www.sciencemag.org/lookup/doi/10.1126/science.1098741` (visited on 02/25/2021).

[24] Marc André Meyers and Krishan Kumar Chawla. *Mechanical behavior of materials*. Cambridge university press, 2008.

[25] Loïc Vanel et al. “Time-Dependent Rupture and Slow Crack Growth: Elastic and Viscoplastic Dynamics”. In: *Journal of Physics D: Applied Physics* 42.21 (Nov. 7, 2009), p. 214007. ISSN: 0022-3727, 1361-6463. DOI: `10.1088/0022-3727/42/21/214007`. URL: `http://stacks.iop.org/0022-3727/42/i=21/a=214007?key=crossref.3c55a97e13c7b51c326fcbdaead59ad2` (visited on 12/11/2018).

[26] Alan Arnold Griffith. “VI. The phenomena of rupture and flow in solids”. In: *Philosophical transactions of the royal society of london. Series A, containing papers of a mathematical or physical character* 221.582-593 (1921), pp. 163–198.

[27] Costantino Creton and Matteo Ciccotti. “Fracture and Adhesion of Soft Materials: A Review”. In: 79.4 (Mar. 2016), p. 046601. ISSN: 0034-4885. DOI: `10.1088/0034-4885/79/4/046601`. URL: `https://doi.org/10.1088/0034-4885/79/4/046601` (visited on 10/14/2021).

[28] Grigory Isaakovich Barenblatt. "The mathematical theory of equilibrium cracks in brittle fracture". In: *Advances in applied mechanics*. Vol. 7. Elsevier, 1962, pp. 55–129.

[29] Yves Pomeau. "Recent Progress in the Moving Contact Line Problem: A Review". In: *Comptes Rendus Mécanique* 330.3 (Jan. 1, 2002), pp. 207–222. ISSN: 1631-0721. DOI: `10.1016/S1631-0721(02)01445-6`. URL: `https://www.sciencedirect.com/science/article/pii/S1631072102014456` (visited on 10/17/2021).

[30] A. Guarino et al. "Failure Time and Critical Behaviour of Fracture Precursors in Heterogeneous Materials". In: *The European Physical Journal B - Condensed Matter and Complex Systems* 26.2 (Mar. 1, 2002), pp. 141–151. ISSN: 1434-6036. DOI: `10.1140/epjb/e20020075`. URL: `https://doi.org/10.1140/epjb/e20020075` (visited on 10/17/2021).

[31] Daniel Bonn et al. "Delayed Fracture of an Inhomogeneous Soft Solid". In: *Science* 280.5361 (Apr. 10, 1998), pp. 265–267. DOI: `10.1126/science.280.5361.265`. URL: `http://www.science.org/doi/full/10.1126/science.280.5361.265` (visited on 10/15/2021).

[32] WF Busse et al. "Fatigue of fabrics". In: *Journal of Applied Physics* 13.11 (1942), pp. 715–724.

[33] F. Bueche. "Tensile Strength of Plastics below the Glass Temperature". In: *Journal of Applied Physics* 28.7 (July 1, 1957), pp. 784–787. ISSN: 0021-8979. DOI: `10.1063/1.1722855`. URL: `http://aip.scitation.org/doi/10.1063/1.1722855` (visited on 10/17/2021).

[34] S. N. Zhurkov. "Kinetic Concept of the Strength of Solids". In: *International journal of fracture mechanics* 1.4 (Dec. 1, 1965), pp. 311–323. ISSN: 1573-2673. DOI: `10.1007/BF03545562`. URL: `https://doi.org/10.1007/BF03545562` (visited on 10/17/2021).

[35] Bikas K. Chakrabarti, Soumyajyoti Biswas, and Srutarshi Pradhan. "Cooperative Dynamics in the Fiber Bundle Model". In: *Frontiers in Physics* 8 (Feb. 15, 2021), p. 613392. ISSN: 2296-424X. DOI: `10.3389/fphy.2020.613392`. URL: `https://www.frontiersin.org/articles/10.3389/fphy.2020.613392/full` (visited on 10/10/2021).

[36] Ferenc Kun et al. "Scaling Laws of Creep Rupture of Fiber Bundles". In: *Physical Review E* 67.6 (June 23, 2003), p. 061802. ISSN: 1063-651X, 1095-3787. DOI: `10.1103/PhysRevE.67.061802`. URL: `https://link.aps.org/doi/10.1103/PhysRevE.67.061802` (visited on 08/06/2021).

[37] E. A. Jagla. "Creep Rupture of Materials: Insights from a Fiber Bundle Model with Relaxation". In: *Physical Review E* 83.4 (Apr. 25, 2011), p. 046119. ISSN: 1539-3755, 1550-2376. DOI: `10.1103/PhysRevE.83.046119`. URL: `https://link.aps.org/doi/10.1103/PhysRevE.83.046119` (visited on 08/06/2021).

[38] S. Pradhan, P. Bhattacharyya, and B. K. Chakrabarti. "Dynamic Critical Behavior of Failure and Plastic Deformation in the Random Fiber Bundle Model". In: *Physical Review E* 66.1 (July 23, 2002), p. 016116. ISSN: 1063-651X, 1095-3787. DOI: `10.1103/PhysRevE.66.016116`. URL: `https://link.aps.org/doi/10.1103/PhysRevE.66.016116` (visited on 08/09/2021).

[39] F. Kun et al. "Universality behind Basquin's Law of Fatigue". In: *Physical Review Letters* 100.9 (Mar. 4, 2008), p. 094301. ISSN: 0031-9007, 1079-7114. DOI: `10.1103/PhysRevLett.100.094301`. URL: `https://link.aps.org/doi/10.1103/PhysRevLett.100.094301` (visited on 08/25/2021).

[40] Oskar Emil Meyer. "Zur Theorie der inneren Reibung." In: 1874.78 (Jan. 1, 1874), pp. 130–135. ISSN: 1435-5345. DOI: `10.1515/crll.1874.78.130`. URL: `http://www.degruyter.com/document/doi/10.1515/crll.1874.78.130/html` (visited on 10/17/2021).

[41] Nicholas W Tschoegl. *The phenomenological theory of linear viscoelastic behavior: an introduction*. Springer Science & Business Media, 2012.

[42] A. Bonfanti et al. "Fractional Viscoelastic Models for Power-Law Materials". In: *Soft Matter* 16.26 (2020), pp. 6002–6020. ISSN: 1744-683X, 1744-6848. DOI: `10.1039/D0SM00354A`. URL: `http://xlink.rsc.org/?DOI=D0SM00354A` (visited on 03/26/2021).

[43] Aditya Jaishankar and Gareth H. McKinley. "Power-Law Rheology in the Bulk and at the Interface: Quasi-Properties and Fractional Constitutive Equations". In: *Proceedings of the Royal Society A: Mathematical, Physical and Engineering Sciences* 469.2149 (Jan. 8, 2013), p. 20120284. ISSN: 1364-5021, 1471-2946. DOI: `10.1098/rspa.2012.0284`. URL: `https://royalsocietypublishing.org/doi/10.1098/rspa.2012.0284` (visited on 05/05/2021).

[44] Saad A. Khan, Carol A. Schnepper, and Robert C. Armstrong. "Foam Rheology: III. Measurement of Shear Flow Properties". In: *Journal of Rheology* 32.1 (Jan. 1988), pp. 69–92. ISSN: 0148-6055, 1520-8516. DOI: `10.1122/1.549964`. URL: `http://sor.scitation.org/doi/10.1122/1.549964` (visited on 10/07/2021).

[45] Ronald G Larson. *The structure and rheology of complex fluids*. Vol. 150.

[46] T.J. Faber, A. Jaishankar, and G.H. McKinley. "Describing the Firmness, Springiness and Rubberiness of Food Gels Using Fractional Calculus. Part II: Measurements on Semi-Hard Cheese". In: *Food Hydrocolloids* 62 (Jan. 2017), pp. 325–339. ISSN: 0268005X. DOI: `10.1016/j.foodhyd.2016.06.038`. URL: `https://linkinghub.elsevier.com/retrieve/pii/S0268005X16302880` (visited on 10/07/2021).

[47] Bavand Keshavarz et al. "Nonlinear Viscoelasticity and Generalized Failure Criterion for Polymer Gels". In: *ACS Macro Letters* 6.7 (July 18, 2017), pp. 663–667. ISSN: 2161-1653, 2161-1653. DOI: `10.1021/acsmacrolett.7b00213`. URL: `https://pubs.acs.org/doi/10.1021/acsmacrolett.7b00213` (visited on 10/18/2019).

[48] G. W. Scott Blair and B. C. Veinoglou. "A Study of the Firmness of Soft Materials Based on Nutting's Equation". In: 21.9 (Sept. 1944), pp. 149–154. ISSN: 0950-7671. DOI: `10.1088/0950-7671/21/9/301`. URL: `https://doi.org/10.1088/0950-7671/21/9/301` (visited on 10/18/2021).

[49] G. W. Scott Blair and J. Burnett. "On the Creep, Recovery, Relaxation and Elastic "Memory" of Some Renneted Milk Gels". In: 10.1 (Jan. 1959), pp. 15–20. ISSN: 0508-3443. DOI: `10.1088/0508-3443/10/1/304`. URL: `https://doi.org/10.1088/0508-3443/10/1/304` (visited on 10/17/2021).

[50] S. Aime, L. Cipelletti, and L. Ramos. “Power Law Viscoelasticity of a Fractal Colloidal Gel”. In: *Journal of Rheology* 62.6 (Nov. 2018), pp. 1429–1441. ISSN: 0148-6055, 1520-8516. DOI: `10.1122/1.5025622`. URL: `http://sor.scitation.org/doi/10.1122/1.5025622` (visited on 10/07/2021).

[51] Pierre Lidon, Louis Villa, and Sébastien Manneville. “Power-Law Creep and Residual Stresses in a Carbopol Gel”. In: *Rheologica Acta* 56.3 (Mar. 2017), pp. 307–323. ISSN: 0035-4511, 1435-1528. DOI: `10.1007/s00397-016-0961-4`. URL: `http://link.springer.com/10.1007/s00397-016-0961-4` (visited on 10/07/2021).

[52] Moutushi Dutta Choudhury et al. “Forced Spreading and Rheology of Starch Gel: Viscoelastic Modeling with Fractional Calculus”. In: *Colloids and Surfaces A: Physicochemical and Engineering Aspects* 407 (Aug. 2012), pp. 64–70. ISSN: 09277757. DOI: `10.1016/j.colsurfa.2012.05.008`. URL: `https://linkinghub.elsevier.com/retrieve/pii/S0927775712003378` (visited on 10/07/2021).

[53] Stefano Aime, Laurence Ramos, and Luca Cipelletti. “Microscopic Dynamics and Failure Precursors of a Gel under Mechanical Load”. In: *Proceedings of the National Academy of Sciences* 115.14 (2018), pp. 3587–3592. ISSN: 0027-8424, 1091-6490. DOI: `10.1073/pnas.1717403115`. arXiv: `1804.01810`. URL: `http://arxiv.org/abs/1804.01810` (visited on 12/11/2018).

[54] M.-Carmen Miguel et al. “Dislocation Jamming and Andrade Creep”. In: *Physical Review Letters* 89.16 (Sept. 26, 2002), p. 165501. ISSN: 0031-9007, 1079-7114. DOI: `10.1103/PhysRevLett.89.165501`. URL: `https://link.aps.org/doi/10.1103/PhysRevLett.89.165501` (visited on 08/06/2021).

[55] OH Basquin. “The exponential law of endurance tests”. In: *Proc Am Soc Test Mater*. Vol. 10. 1910, pp. 625–630.

[56] F. Kun et al. “Universality behind Basquin’s Law of Fatigue”. In: *Physical Review Letters* 100.9 (Mar. 4, 2008), p. 094301. DOI: `10.1103/PhysRevLett.100.094301`. URL: `https://link.aps.org/doi/10.1103/PhysRevLett.100.094301` (visited on 10/17/2021).

[57] James Bailey. “An attempt to correlate some tensile strength measurements on glass: III”. In: *Glass Ind* 20.3 (1939), p. 95.

[58] A. D. Freeds and A. I. Leonov. “The Bailey Criterion: Statistical Derivation and Applications to Interpretations of Durability Tests and Chemical Kinetics”. In: *Zeitschrift für angewandte Mathematik und Physik ZAMP* 53.1 (1 Jan. 1, 2002), pp. 160–166. ISSN: 1420-9039. DOI: `10.1007/s00033-002-8148-5`. URL: `http://link.springer.com/article/10.1007/s00033-002-8148-5` (visited on 10/15/2021).

[59] A. Ya. Malkin and C. J. S. Petrie. “Some Conditions for Rupture of Polymer Liquids in Extension”. In: *Journal of Rheology* 41.1 (Jan. 1997), pp. 1–25. ISSN: 0148-6055, 1520-8516. DOI: `10.1122/1.550881`. URL: `http://sor.scitation.org/doi/10.1122/1.550881` (visited on 10/10/2021).

[60] Raffaele Mezzenga and Peter Fischer. “The Self-Assembly, Aggregation and Phase Transitions of Food Protein Systems in One, Two and Three Dimensions”. In: *Reports on Progress in Physics* 76.4 (Apr. 1, 2013), p. 046601. ISSN: 0034-4885, 1361-6633. DOI: `10.1088/0034-4885/76/4/046601`. URL: `https://iopscience.iop.org/article/10.1088/0034-4885/76/4/046601` (visited on 01/19/2021).

[61] J.P. Gong et al. "Double-Network Hydrogels with Extremely High Mechanical Strength". In: *Advanced Materials* 15.14 (July 17, 2003), pp. 1155–1158. ISSN: 09359648, 15214095. DOI: 10.1002/adma.200304907. URL: http://doi.wiley.com/10.1002/adma.200304907 (visited on 02/11/2021).

[62] Tristan Baumberger, Christiane Caroli, and David Martina. "Solvent Control of Crack Dynamics in a Reversible Hydrogel". In: *Nature Materials* 5.7 (July 2006), pp. 552–555. ISSN: 1476-1122, 1476-4660. DOI: 10.1038/nmat1666. URL: http://www.nature.com/articles/nmat1666 (visited on 08/06/2021).

[63] Wei-Heng Shih et al. "Scaling Behavior of the Elastic Properties of Colloidal Gels". In: *Physical Review A* 42.8 (Oct. 1, 1990), pp. 4772–4779. ISSN: 1050-2947, 1094-1622. DOI: 10.1103/PhysRevA.42.4772. URL: https://link.aps.org/doi/10.1103/PhysRevA.42.4772 (visited on 08/09/2021).

[64] Leon G. B. Bremer, Ton van Vliet, and Pieter Walstra. "Theoretical and Experimental Study of the Fractal Nature of the Structure of Casein Gels". In: *Journal of the Chemical Society, Faraday Transactions 1: Physical Chemistry in Condensed Phases* 85.10 (1989), p. 3359. ISSN: 0300-9599. DOI: 10.1039/f19898503359. URL: http://xlink.rsc.org/?DOI=f19898503359 (visited on 05/28/2021).

[65] Frédéric Cardinaux et al. "Interplay between Spinodal Decomposition and Glass Formation in Proteins Exhibiting Short-Range Attractions". In: *Physical Review Letters* 99.11 (Sept. 13, 2007), p. 118301. DOI: 10.1103/PhysRevLett.99.118301. URL: https://link.aps.org/doi/10.1103/PhysRevLett.99.118301 (visited on 10/17/2021).

[66] T. Gisler, R. C. Ball, and D. A. Weitz. "Strain Hardening of Fractal Colloidal Gels". In: *Physical Review Letters* 82.5 (Feb. 1, 1999), pp. 1064–1067. ISSN: 0031-9007, 1079-7114. DOI: 10.1103/PhysRevLett.82.1064. URL: https://link.aps.org/doi/10.1103/PhysRevLett.82.1064 (visited on 10/08/2021).

[67] Thomas Gibaud, Thibaut Divoux, and Sébastien Manneville. *Nonlinear Mechanics of Colloidal Gels: Creep, Fatigue and Shear-Induced Yielding*. 2020. arXiv: 2011.06921 [cond-mat]. URL: http://arxiv.org/abs/2011.06921 (visited on 08/05/2021).

[68] Paulina J. Skrzeszewska et al. "Fracture and Self-Healing in a Well-Defined Self-Assembled Polymer Network". In: *Macromolecules* 43.7 (Apr. 13, 2010), pp. 3542–3548. ISSN: 0024-9297, 1520-5835. DOI: 10.1021/ma1000173. URL: https://pubs.acs.org/doi/10.1021/ma1000173 (visited on 08/06/2021).

[69] Christophe Perge et al. "Time dependence in large amplitude oscillatory shear: A rheo-ultrasonic study of fatigue dynamics in a colloidal gel". In: *Journal of Rheology* 58.5 (2014), pp. 1331–1357. DOI: 10.1122/1.4887081. URL: https://sor.scitation.org/doi/abs/10.1122/1.4887081.

[70] Vincent Grenard et al. "Timescales in Creep and Yielding of Attractive Gels". In: *Soft Matter* 10.10 (2014), p. 1555. ISSN: 1744-683X, 1744-6848. DOI: 10.1039/c3sm52548a. URL: http://xlink.rsc.org/?DOI=c3sm52548a (visited on 08/06/2021).

[71] Thomas Gibaud et al. "Multiple Yielding Processes in a Colloidal Gel under Large Amplitude Oscillatory Stress". In: *Soft Matter* 12.6 (2016), pp. 1701–1712. ISSN: 1744-683X, 1744-6848. DOI: 10.1039/C5SM02587G. URL: http://xlink.rsc.org/?DOI=C5SM02587G (visited on 08/12/2021).

[72] Mehdi Bouzid and Emanuela Del Gado. "Network Topology in Soft Gels: Hardening and Softening Materials". In: *Langmuir* 34.3 (Jan. 23, 2018), pp. 773–781. ISSN: 0743-7463, 1520-5827. DOI: 10.1021/acs.langmuir.7b02944. URL: https://pubs.acs.org/doi/10.1021/acs.langmuir.7b02944 (visited on 08/10/2021).

[73] Matthieu Pouzot et al. "Strain Hardening and Fracture of Heat-Set Fractal Globular Protein Gels". In: *Journal of Colloid and Interface Science* 293.2 (Jan. 2006), pp. 376–383. ISSN: 00219797. DOI: 10.1016/j.jcis.2005.06.074. URL: https://linkinghub.elsevier.com/retrieve/pii/S0021979705007344 (visited on 08/09/2021).

[74] Jader Colombo and Emanuela Del Gado. "Stress Localization, Stiffening, and Yielding in a Model Colloidal Gel". In: *Journal of Rheology* 58.5 (Sept. 2014), pp. 1089–1116. ISSN: 0148-6055, 1520-8516. DOI: 10.1122/1.4882021. URL: http://sor.scitation.org/doi/10.1122/1.4882021 (visited on 08/09/2021).

[75] Cornelis Storm et al. "Nonlinear Elasticity in Biological Gels". In: *Nature* 435.7039 (May 2005), pp. 191–194. ISSN: 0028-0836, 1476-4687. DOI: 10.1038/nature03521. URL: http://www.nature.com/articles/nature03521 (visited on 08/09/2021).

[76] Paul A. Janmey et al. "Negative Normal Stress in Semiflexible Biopolymer Gels". In: *Nature Materials* 6.1 (Jan. 2007), pp. 48–51. ISSN: 1476-1122, 1476-4660. DOI: 10.1038/nmat1810. URL: http://www.nature.com/articles/nmat1810 (visited on 08/24/2021).

[77] Oleg V. Kim et al. "Structural Basis for the Nonlinear Mechanics of Fibrin Networks under Compression". In: *Biomaterials* 35.25 (Aug. 2014), pp. 6739–6749. ISSN: 01429612. DOI: 10.1016/j.biomaterials.2014.04.056. URL: https://linkinghub.elsevier.com/retrieve/pii/S0142961214004542 (visited on 08/22/2021).

[78] Abderrahim Ed-Daoui and Patrick Snabre. "Poroviscoelasticity and Compression-Softening of Agarose Hydrogels". In: *Rheologica Acta* 60.6-7 (July 2021), pp. 327–351. ISSN: 0035-4511, 1435-1528. DOI: 10.1007/s00397-021-01267-3. URL: https://link.springer.com/10.1007/s00397-021-01267-3 (visited on 08/22/2021).

[79] Neil Y C Lin et al. "A Multi-Axis Confocal Rheoscope for Studying Shear Flow of Structured Fluids." In: *The Review of scientific instruments* 85.3 (Mar. 2014), p. 033905. ISSN: 1089-7623. DOI: 10.1063/1.4868688.

[80] S. Aime et al. "A Stress-Controlled Shear Cell for Small-Angle Light Scattering and Microscopy". In: *Review of Scientific Instruments* 87.12 (Dec. 2016), p. 123907. ISSN: 0034-6748. DOI: 10.1063/1.4972253. arXiv: 1603.06703.

[81] Manfred Wilhelm. "Fourier-Transform Rheology". In: *Macromolecular Materials and Engineering* 287.2 (2002), pp. 83–105. ISSN: 1439-2054. DOI: 10.1002/1439-2054(20020201)287:2<83::AID-MAME83>3.0.CO;2-B. URL: http://onlinelibrary.wiley.com/doi/abs/10.1002/1439-2054%2820020201%29287%3A2%3C83%3A%3AAID-MAME83%3E3.0.CO%3B2-B (visited on 10/17/2021).

[82] Manfred H. Wagner et al. "Analysis of Medium Amplitude Oscillatory Shear Data of Entangled Linear and Model Comb Polymers". In: *Journal of Rheology* 55.3 (May 2011), pp. 495–516. ISSN: 0148-6055, 1520-8516. DOI: 10.1122/1.3553031. URL: http://sor.scitation.org/doi/10.1122/1.3553031 (visited on 10/09/2021).

[83] J Schijve. "Fatigue of Structures and Materials in the 20th Century and the State of the Art". In: (), p. 52.

[84] V. Gopalakrishnan and C. F. Zukoski. "Delayed Flow in Thermo-Reversible Colloidal Gels". In: *Journal of Rheology* 51.4 (July 2007), pp. 623–644. ISSN: 0148-6055, 1520-8516. DOI: 10.1122/1.2736413. URL: http://sor.scitation.org/doi/10.1122/1.2736413 (visited on 08/06/2021).

[85] Stefan B. Lindström et al. "Structures, Stresses, and Fluctuations in the Delayed Failure of Colloidal Gels". In: *Soft Matter* 8.13 (2012), p. 3657. ISSN: 1744-683X, 1744-6848. DOI: 10.1039/c2sm06723d. URL: http://xlink.rsc.org/?DOI=c2sm06723d (visited on 02/22/2021).

[86] N. Koumakis and G. Petekidis. "Two Step Yielding in Attractive Colloids: Transition from Gels to Attractive Glasses". In: *Soft Matter* 7.6 (2011), p. 2456. ISSN: 1744-683X, 1744-6848. DOI: 10.1039/c0sm00957a. URL: http://xlink.rsc.org/?DOI=c0sm00957a (visited on 08/09/2021).

[87] Brice Saint-Michel, Thomas Gibaud, and Sébastien Manneville. "Predicting and Assessing Rupture in Protein Gels under Oscillatory Shear". In: *Soft Matter* 13.14 (2017), pp. 2643–2653. ISSN: 1744-683X, 1744-6848. DOI: 10.1039/C7SM00064B. URL: http://xlink.rsc.org/?DOI=C7SM00064B (visited on 09/10/2020).

[88] Jan Maarten van Doorn et al. "Strand Plasticity Governs Fatigue in Colloidal Gels". In: *Physical Review Letters* 120.20 (May 18, 2018), p. 208005. ISSN: 0031-9007, 1079-7114. DOI: 10.1103/PhysRevLett.120.208005. URL: https://link.aps.org/doi/10.1103/PhysRevLett.120.208005 (visited on 08/10/2021).

[89] Benjamin J. Landrum, William B. Russel, and Roseanna N. Zia. "Delayed Yield in Colloidal Gels: Creep, Flow, and Re-Entrant Solid Regimes". In: *Journal of Rheology* 60.4 (July 2016), pp. 783–807. ISSN: 0148-6055, 1520-8516. DOI: 10.1122/1.4954640. URL: http://sor.scitation.org/doi/10.1122/1.4954640 (visited on 08/09/2021).

[90] S. Manneville, L. Bécu, and A. Colin. "High-Frequency Ultrasonic Speckle Velocimetry in Sheared Complex Fluids". In: *The European Physical Journal - Applied Physics* 28.3 (Dec. 2004), pp. 361–373. ISSN: 1286-0042, 1286-0050. DOI: 10.1051/epjap:2004165. URL: http://www.cambridge.org/core/journals/the-european-physical-journal-applied-physics/article/abs/highfrequency-ultrasonic-speckle-velocimetry-in-sheared-complex-fluids/7E218429E127BF7F77C5B5C330604938 (visited on 10/17/2021).

[91] Thomas Gibaud, Damien Frelat, and Sébastien Manneville. "Heterogeneous Yielding Dynamics in a Colloidal Gel". In: *Soft Matter* 6.15 (2010), p. 3482. ISSN: 1744-683X, 1744-6848. DOI: 10.1039/c000886a. URL: http://xlink.rsc.org/?DOI=c000886a (visited on 08/09/2021).

[92] Ali Mohraz and Michael J. Solomon. "Orientation and Rupture of Fractal Colloidal Gels during Start-up of Steady Shear Flow". In: *Journal of Rheology* 49.3 (May 2005), pp. 657–681. ISSN: 0148-6055, 1520-8516. DOI: 10.1122/1.1895799. URL: http://sor.scitation.org/doi/10.1122/1.1895799 (visited on 08/09/2021).

[93] Michael C. Rogers et al. “Echoes in X-Ray Speckles Track Nanometer-Scale Plastic Events in Colloidal Gels under Shear”. In: *Physical Review E* 90.6 (Dec. 22, 2014), p. 062310. ISSN: 1539-3755, 1550-2376. DOI: `10.1103/PhysRevE.90.062310`. URL: `https://link.aps.org/doi/10.1103/PhysRevE.90.062310` (visited on 08/09/2021).

[94] Kasper Masschaele, Jan Fransaer, and Jan Vermant. “Direct Visualization of Yielding in Model Two-Dimensional Colloidal Gels Subjected to Shear Flow”. In: *Journal of Rheology* 53.6 (Nov. 2009), pp. 1437–1460. ISSN: 0148-6055, 1520-8516. DOI: `10.1122/1.3237154`. URL: `http://sor.scitation.org/doi/10.1122/1.3237154` (visited on 08/09/2021).

[95] Bharath Rajaram and Ali Mohraz. “Microstructural Response of Dilute Colloidal Gels to Nonlinear Shear Deformation”. In: *Soft Matter* 6.10 (2010), p. 2246. ISSN: 1744-683X, 1744-6848. DOI: `10.1039/b926076e`. URL: `http://xlink.rsc.org/?DOI=b926076e` (visited on 02/24/2021).

[96] Priya Varadan and Michael J. Solomon. “Direct Visualization of Long-Range Heterogeneous Structure in Dense Colloidal Gels”. In: *Langmuir* 19.3 (Feb. 1, 2003), pp. 509–512. ISSN: 0743-7463. DOI: `10.1021/la026303j`. URL: `https://doi.org/10.1021/la026303j` (visited on 10/17/2021).

[97] L. C. Hsiao et al. “Role of Isostaticity and Load-Bearing Microstructure in the Elasticity of Yielded Colloidal Gels”. In: *Proceedings of the National Academy of Sciences* 109.40 (2012), pp. 16029–16034. ISSN: 0027-8424, 1091-6490. DOI: `10.1073/pnas.1206742109`. URL: `http://www.pnas.org/cgi/doi/10.1073/pnas.1206742109` (visited on 02/22/2021).

[98] Mehdi Bouzid et al. “Elastically Driven Intermittent Microscopic Dynamics in Soft Solids”. In: *Nature Communications* 8.1 (Aug. 2017), p. 15846. ISSN: 2041-1723. DOI: `10.1038/ncomms15846`. URL: `http://www.nature.com/articles/ncomms15846` (visited on 08/10/2021).

[99] Misaki Ozawa et al. “Random Critical Point Separates Brittle and Ductile Yielding Transitions in Amorphous Materials”. In: *Proceedings of the National Academy of Sciences* 115.26 (June 26, 2018), pp. 6656–6661. ISSN: 0027-8424, 1091-6490. DOI: `10.1073/pnas.1806156115`. URL: `http://www.pnas.org/lookup/doi/10.1073/pnas.1806156115` (visited on 08/09/2021).

[100] Didi Derks et al. “Confocal Microscopy of Colloidal Dispersions in Shear Flow Using a Counter-Rotating Cone–Plate Shear Cell”. In: *Journal of Physics: Condensed Matter* 16.38 (2004), S3917–S3927. ISSN: 0953-8984, 1361-648X. DOI: `10.1088/0953-8984/16/38/010`. URL: `https://iopscience.iop.org/article/10.1088/0953-8984/16/38/010` (visited on 02/25/2021).

[101] P. Ballesta et al. “Slip and Flow of Hard-Sphere Colloidal Glasses”. In: *Physical Review Letters* 101.25 (2008), p. 258301. ISSN: 0031-9007, 1079-7114. DOI: `10.1103/PhysRevLett.101.258301`. URL: `https://link.aps.org/doi/10.1103/PhysRevLett.101.258301` (visited on 02/24/2021).

[102] S. K. Dutta et al. “Development of a Confocal Rheometer for Soft and Biological Materials”. In: *Review of Scientific Instruments* 84.6 (2013), p. 063702. ISSN: 0034-6748, 1089-7623. DOI: `10.1063/1.4810015`. URL: `http://aip.scitation.org/doi/10.1063/1.4810015` (visited on 02/16/2021).

[103] Richard C Arevalo et al. “Stress heterogeneities in sheared type-I collagen networks revealed by boundary stress microscopy”. In: *PloS one* 10.3 (2015), e0118021. DOI: `https://doi.org/10.1371/journal.pone.0118021`.

[104] P. A. Smith et al. "Yielding and Crystallization of Colloidal Gels under Oscillatory Shear". In: *Physical Review E* 76.4 (2007), p. 041402. ISSN: 1539-3755, 1550-2376. DOI: 10.1103/PhysRevE.76.041402. URL: https://link.aps.org/doi/10.1103/PhysRevE.76.041402 (visited on 02/25/2021).

[105] José Paredes, Noushine Shahidzadeh-Bonn, and Daniel Bonn. "Shear Banding in Thixotropic and Normal Emulsions". en. In: *Journal of Physics: Condensed Matter* 23.28 (June 2011), p. 284116. ISSN: 0953-8984. DOI: 10.1088/0953-8984/23/28/284116. URL: https://doi.org/10.1088/0953-8984/23/28/284116 (visited on 07/27/2021).

[106] Hubert K. Chan and Ali Mohraz. "A Simple Shear Cell for the Direct Visualization of Step-Stress Deformation in Soft Materials". In: *Rheologica Acta* 52.5 (2013), pp. 383–394. ISSN: 0035-4511, 1435-1528. DOI: 10.1007/s00397-013-0679-5. URL: http://link.springer.com/10.1007/s00397-013-0679-5 (visited on 02/19/2021).

[107] Rut Besseling et al. "Quantitative Imaging of Colloidal Flows". In: *Advances in Colloid and Interface Science* 146.1-2 (2009), pp. 1–17. ISSN: 00018686. DOI: 10.1016/j.cis.2008.09.008. URL: https://linkinghub.elsevier.com/retrieve/pii/S000186860800167X (visited on 02/26/2021).

[108] Pierre Ballesta et al. "Slip of Gels in Colloid–Polymer Mixtures under Shear". In: *Soft Matter* 9.12 (2013), p. 3237. ISSN: 1744-683X. DOI: 10.1039/c3sm27626k.

[109] Itai Cohen et al. "Slip, Yield, and Bands in Colloidal Crystals under Oscillatory Shear". In: *Physical Review Letters* 97.21 (2006), p. 215502. ISSN: 0031-9007, 1079-7114. DOI: 10.1103/PhysRevLett.97.215502. URL: https://link.aps.org/doi/10.1103/PhysRevLett.97.215502 (visited on 02/25/2021).

[110] Vijayakumar Chikkadi and Peter Schall. "Nonaffine Measures of Particle Displacements in SheNeil Y.C. Linared Colloidal Glasses". In: *Physical Review E* 85.3 (Mar. 2012), pp. 1–5. ISSN: 1539-3755. DOI: 10.1103/PhysRevE.85.031402.

[111] J.-B. Boitte, M. Hayert, and C. Michon. "Observation of Wheat Flour Doughs under Mechanical Treatment Using Confocal Microscopy and Classification of Their Microstructures". In: *Journal of Cereal Science* 58.3 (2013), pp. 365–371. ISSN: 07335210. DOI: 10.1016/j.jcs.2013.07.009. URL: https://linkinghub.elsevier.com/retrieve/pii/S0733521013001252 (visited on 02/19/2021).

[112] E. D. Knowlton, D. J. Pine, and L. Cipelletti. "A Microscopic View of the Yielding Transition in Concentrated Emulsions". In: *Soft Matter* 10.36 (2014), pp. 6931–6940. ISSN: 1744-683X, 1744-6848. DOI: 10.1039/C4SM00531G. URL: http://xlink.rsc.org/?DOI=C4SM00531G (visited on 02/19/2021).

[113] Hideyo Tsurusawa et al. "Direct Link between Mechanical Stability in Gels and Percolation of Isostatic Particles". In: *Science Advances* 5.5 (May 2019), eaav6090. ISSN: 2375-2548. DOI: 10.1126/sciadv.aav6090. arXiv: 1804.04370.

[114] K. N Pham et al. "Yielding of Colloidal Glasses". In: *Europhysics Letters (EPL)* 75.4 (Aug. 2006), pp. 624–630. ISSN: 0295-5075. DOI: 10.1209/epl/i2006-10156-y.

[115] G. Binnig, C. F. Quate, and Ch. Gerber. "Atomic Force Microscope". In: *Physical Review Letters* 56.9 (Mar. 1986), pp. 930–933. DOI: 10.1103/PhysRevLett.56.930.

[116] Galileo Galilei. *Discorsi e dimostrazioni matematiche intorno a due nuove scienze attenenti alla mecanica ed i movimenti locali*. Gli Elsevirii, 1638.

[117] P. L. Bransby and G. W. E. Milligan. "Soil Deformations near Cantilever Sheet Pile Walls". In: *Géotechnique* 25.2 (June 1975), pp. 175–195. ISSN: 0016-8505. DOI: `10.1680/geot.1975.25.2.175`.

[118] David Tabor and R. H. S. Winterton. "The Direct Measurement of Normal and Retarded van Der Waals Forces". In: *Proceedings of the Royal Society of London. A. Mathematical and Physical Sciences* 312.1511 (Sept. 1969), pp. 435–450. DOI: `10.1098/rspa.1969.0169`.

[119] Jacob N Israelachvili and Gayle E. Adams. "Measurement of Forces between Two Mica Surfaces in Aqueous Electrolyte Solutions in the Range 0–100 Nm". en. In: *Journal of the Chemical Society, Faraday Transactions 1: Physical Chemistry in Condensed Phases* 74.0 (1978), pp. 975–1001. DOI: `10.1039/F19787400975`.

[120] Jürgen Fritz. "Cantilever Biosensors". en. In: *Analyst* 133.7 (2008), pp. 855–863. DOI: `10.1039/B718174D`.

[121] R. Kassies et al. "Combined AFM and Confocal Fluorescence Microscope for Applications in Bio-Nanotechnology". In: *Journal of Microscopy* 217.1 (Jan. 2005), pp. 109–116. ISSN: 0022-2720, 1365-2818. DOI: `10.1111/j.0022-2720.2005.01428.x`.

[122] Jack R. Staunton et al. "Correlating Confocal Microscopy and Atomic Force Indentation Reveals Metastatic Cancer Cells Stiffen during Invasion into Collagen I Matrices". In: *Scientific Reports* 6.1 (Apr. 2016), p. 19686. ISSN: 2045-2322. DOI: `10.1038/srep19686`. URL: `http://www.nature.com/articles/srep19686`.

[123] P. Marmottant et al. "The Role of Fluctuations and Stress on the Effective Viscosity of Cell Aggregates". en. In: *Proceedings of the National Academy of Sciences* 106.41 (Oct. 2009), pp. 17271–17275. ISSN: 0027-8424, 1091-6490. DOI: `10.1073/pnas.0902085106`.

[124] Tomita Vasilica Stirbat et al. "Fine Tuning of Tissues' Viscosity and Surface Tension through Contractility Suggests a New Role for α-Catenin". en. In: *PLOS ONE* 8.2 (Feb. 2013), e52554. ISSN: 1932-6203. DOI: `10.1371/journal.pone.0052554`.

[125] Abbas Mgharbel, Hélène Delanoë-Ayari, and Jean-Paul Rieu. "Measuring Accurately Liquid and Tissue Surface Tension with a Compression Plate Tensiometer." In: *HFSP journal* 3.3 (June 2009), pp. 213–21. ISSN: 1955-2068. DOI: `10.2976/1.3116822`.

[126] Baudouin Géraud et al. "Capillary Rise of Yield-Stress Fluids". In: *EPL (Europhysics Letters)* 107.5 (Sept. 2014), p. 58002. ISSN: 0295-5075. DOI: `10.1209/0295-5075/107/58002`.

[127] Loren Jørgensen et al. "Yield Stress and Elasticity Influence on Surface Tension Measurements". In: *Soft Matter* 11.25 (2015), pp. 5111–5121. ISSN: 1744-683X. DOI: `10.1039/C5SM00569H`.

[128] Gerhard Meyer and Nabil M. Amer. "Novel Optical Approach to Atomic Force Microscopy". In: *Applied Physics Letters* 53.12 (Sept. 1988), pp. 1045–1047. ISSN: 0003-6951. DOI: `10.1063/1.100061`.

[129] Santanu Kundu and Alfred J. Crosby. “Cavitation and Fracture Behavior of Polyacrylamide Hydrogels”. In: *Soft Matter* 5.20 (2009), pp. 3963–3968. DOI: `10.1039/B909237D`.

[130] J.A. Lucey and H. Singh. “Formation and Physical Properties of Acid Milk Gels: A Review”. In: *Food Research International* 30.7 (Aug. 1997), pp. 529–542. ISSN: 09639969. DOI: `10.1016/S0963-9969(98)00015-5`.

[131] S.P.F.M. Roefs, A.E.A. De Groot-Mostert, and T. Van Vliet. “Structure of Acid Casein Gels 1. Formation and Model of Gel Network”. In: *Colloids and Surfaces* 50 (Jan. 1990), pp. 141–159. ISSN: 01666622. DOI: `10.1016/0166-6622(90)80259-7`.

[132] Mathieu Leocmach et al. “Hierarchical Wrinkling in a Confined Permeable Biogel”. In: *Science Advances* 1.9 (Oct. 2015), e1500608. ISSN: 2375-2548. DOI: `10.1126/sciadv.1500608`.

[133] John E. Kinsella and Charles V. Morr. “Milk Proteins: Physicochemical and Functional Properties”. In: *C R C Critical Reviews in Food Science and Nutrition* 21.3 (Jan. 1984), pp. 197–262. ISSN: 0099-0248. DOI: `10.1080/10408398409527401`.

[134] Abdelkader HadjSadok et al. “Characterisation of Sodium Caseinate as a Function of Ionic Strength, pH and Temperature Using Static and Dynamic Light Scattering”. In: *Food Hydrocolloids* 22.8 (Dec. 2008), pp. 1460–1466. ISSN: 0268005X. DOI: `10.1016/j.foodhyd.2007.09.002`. URL: `https://linkinghub.elsevier.com/retrieve/pii/S0268005X07002202` (visited on 07/08/2021).

[135] Anne Pitkowski, Dominique Durand, and Taco Nicolai. “Structure and Dynamical Mechanical Properties of Suspensions of Sodium Caseinate”. In: *Journal of Colloid and Interface Science* 326.1 (Oct. 2008), pp. 96–102. ISSN: 00219797. DOI: `10.1016/j.jcis.2008.07.003`. URL: `https://linkinghub.elsevier.com/retrieve/pii/S0021979708008059` (visited on 07/08/2021).

[136] Donald T Sawyer and John B Bagger. “The Lactone-Acid-Salt Equilibria for D-Glucono-d-Lactone and the Hydrolysis Kinetics for This Lactone”. In: 81 (1959), p. 5. DOI: `10.1021/ja01529a014`.

[137] John Crank. *The mathematics of diffusion*. Oxford university press, 1979.

[138] W Weibull. “The phenomenon of rupture in solids”. In: *Handlingar* 153 (1939).

[139] Dietmar Fink et al. “Diffusion Kinetics of the Glucose/Glucose Oxidase System in Swift Heavy Ion Track-Based Biosensors”. In: *Nuclear Instruments and Methods in Physics Research Section B: Beam Interactions with Materials and Atoms* 398 (May 2017), pp. 21–26. ISSN: 0168583X. DOI: `10.1016/j.nimb.2017.03.050`. URL: `https://linkinghub.elsevier.com/retrieve/pii/S0168583X17302896` (visited on 07/07/2021).

[140] Bosi Mao, Thibaut Divoux, and Patrick Snabre. “Normal Force Controlled Rheology Applied to Agar Gelation”. In: *Journal of Rheology* 60.3 (May 2016). Comment: 19 pages, 15 figures - accepted for publication in Journal of Rheology, pp. 473–489. ISSN: 0148-6055, 1520-8516. DOI: `10.1122/1.4944994`. arXiv: `1508.01689`. URL: `http://arxiv.org/abs/1508.01689` (visited on 09/08/2020).

[141] Angelo Pommella, Luca Cipelletti, and Laurence Ramos. "Role of Normal Stress in the Creep Dynamics and Failure of a Biopolymer Gel". In: *Physical Review Letters* 125.26 (Dec. 31, 2020). Comment: accepted for publication in Physical Review Letters, p. 268006. ISSN: 0031-9007, 1079-7114. DOI: `10.1103/PhysRevLett.125.268006`. arXiv: `2012.09827`. URL: `http://arxiv.org/abs/2012.09827` (visited on 01/07/2021).

[142] C. P. Broedersz and F. C. MacKintosh. "Modeling Semiflexible Polymer Networks". In: *Reviews of Modern Physics* 86.3 (July 24, 2014), pp. 995–1036. ISSN: 0034-6861, 1539-0756. DOI: `10.1103/RevModPhys.86.995`. URL: `https://link.aps.org/doi/10.1103/RevModPhys.86.995` (visited on 08/24/2021).

[143] T.H. Besseling, J. Jose, and A. Van Blaaderen. "Methods to Calibrate and Scale Axial Distances in Confocal Microscopy as a Function of Refractive Index". In: *Journal of Microscopy* 257.2 (Feb. 2015), pp. 142–150. ISSN: 0022-2720, 1365-2818. DOI: `10.1111/jmi.12194`. URL: `https://onlinelibrary.wiley.com/doi/10.1111/jmi.12194` (visited on 09/05/2021).

[144] Stefan Van der Walt et al. "scikit-image: image processing in Python". In: *PeerJ* 2 (2014), e453.

[145] J. G. Ziegler and N. B. Nichols. "Optimum Settings for Automatic Controllers". In: *Journal of Dynamic Systems, Measurement, and Control* 115.2B (June 1993), pp. 220–222. ISSN: 0022-0434, 1528-9028. DOI: `10.1115/1.2899060`.

[146] *Anaconda Software Distribution*. Version Vers. 2-2.4.0. 2020. URL: `https://docs.anaconda.com/`.

[147] Itseez. *Open Source Computer Vision Library*. 2015. URL: `https://github.com/itseez/opencv`.

[148] Alex Liberzon et al. *OpenPIV/openpiv-python: OpenPIV - Python (v0.22.2) with a new extended search PIV grid option*. Version 0.22.2. July 2020. DOI: `10.5281/zenodo.3930343`. URL: `https://doi.org/10.5281/zenodo.3930343`.

[149] Travis Oliphant. *NumPy: A guide to NumPy*. USA: Trelgol Publishing. [Online; accessed <today>]. 2006–. URL: `http://www.numpy.org/`.

[150] Eric Jones, Travis Oliphant, Pearu Peterson, et al. *SciPy: Open source scientific tools for Python*. 2001–. URL: `http://www.scipy.org/`.

[151] Wes McKinney et al. "Data structures for statistical computing in python". In: *Proceedings of the 9th Python in Science Conference*. Vol. 445. Austin, TX. 2010, pp. 51–56.

[152] Andrew Collette. *Python and HDF5*. O'Reilly, 2013.

[153] Aric A. Hagberg, Daniel A. Schult, and Pieter J. Swart. "Exploring Network Structure, Dynamics, and Function using NetworkX". In: *Proceedings of the 7th Python in Science Conference*. Ed. by Gael Varoquaux, Travis Vaught, and Jarrod Millman. Pasadena, CA USA, 2008, pp. 11 –15.

[154] Daniel B. Allan et al. *soft-matter/trackpy: Trackpy v0.5.0*. Version v0.5.0. Apr. 2021. DOI: `10.5281/zenodo.4682814`. URL: `https://doi.org/10.5281/zenodo.4682814`.

[155] John D. Hunter. "Matplotlib: A 2D Graphics Environment". In: *Computing in Science Engineering* 9.3 (2007), pp. 90–95. DOI: `10.1109/MCSE.2007.55`.

[156] Mathieu Leocmach and Yushi Yang. 2019. URL: `https://github.com/MathieuLeocmach/read_lif`.

[157] John C. Crocker and David G. Grier. “Methods of Digital Video Microscopy for Colloidal Studies”. In: *Journal of Colloid and Interface Science* 179.1 (1996), pp. 298–310. ISSN: 0021-9797. DOI: `https://doi.org/10.1006/jcis.1996.0217`. URL: `https://www.sciencedirect.com/science/article/pii/S0021979796902179`.

[158] Gunnar Farnebäck. “Polynomial expansion for orientation and motion estimation”. PhD thesis. Linköping University, Computer Vision, 2002, p. 181. ISBN: 91-7373-475-6.

[159] R. J. Adrian. “Twenty Years of Particle Image Velocimetry”. In: *Experiments in Fluids* 39.2 (Aug. 2005), pp. 159–169. ISSN: 0723-4864, 1432-1114. DOI: `10.1007/s00348-005-0991-7`. URL: `http://link.springer.com/10.1007/s00348-005-0991-7`.

[160] Jianbo Shi and Tomasi. “Good features to track”. In: *1994 Proceedings of IEEE Conference on Computer Vision and Pattern Recognition*. 1994, pp. 593–600. DOI: `10.1109/CVPR.1994.323794`.

[161] C.N. Chu T.C. Lee R.L. Kashyap. “Building Skeleton Models via 3-D Medial Surface Axis Thinning Algorithms”. In: *CVGIP: Graphical Models and Image Processing* 56 (1994), pp. 462–478. ISSN: 1049-9652. DOI: `https://doi.org/10.1006/cgip.1994.1042`. URL: `https://www.sciencedirect.com/science/article/abs/pii/S104996528471042X`.

[162] A. Tanguy, F. Leonforte, and J. L. Barrat. “Plastic Response of a 2D Lennard-Jones Amorphous Solid: Detailed Analysis of the Local Rearrangements at Very Slow Strain Rate”. In: *The European Physical Journal E* 20.3 (July 2006), pp. 355–364. ISSN: 1292-8941, 1292-895X. DOI: `10.1140/epje/i2006-10024-2`. URL: `http://link.springer.com/10.1140/epje/i2006-10024-2` (visited on 09/29/2021).

[163] Alexandre Kabla, Julien Scheibert, and Georges Debregeas. “Quasi-Static Rheology of Foams. Part 2. Continuous Shear Flow”. In: *Journal of Fluid Mechanics* 587 (Sept. 25, 2007), pp. 45–72. ISSN: 0022-1120, 1469-7645. DOI: `10.1017/S0022112007007276`. URL: `https://www.cambridge.org/core/product/identifier/S0022112007007276/type/journal_article` (visited on 09/29/2021).

[164] P. Schall, D. A. Weitz, and F. Spaepen. “Structural Rearrangements That Govern Flow in Colloidal Glasses”. In: *Science* 318.5858 (Dec. 21, 2007), pp. 1895–1899. ISSN: 0036-8075, 1095-9203. DOI: `10.1126/science.1149308`. URL: `https://www.sciencemag.org/lookup/doi/10.1126/science.1149308` (visited on 09/26/2021).

[165] Vijayakumar Chikkadi et al. “Long-Range Strain Correlations in Sheared Colloidal Glasses”. In: *Physical Review Letters* 107.19 (Nov. 4, 2011), p. 198303. ISSN: 0031-9007, 1079-7114. DOI: `10.1103/PhysRevLett.107.198303`. URL: `https://link.aps.org/doi/10.1103/PhysRevLett.107.198303` (visited on 09/26/2021).

[166] Antoine Le Bouil et al. “Emergence of Cooperativity in Plasticity of Soft Glassy Materials”. In: *Phys. Rev. Lett.* 112 (24 2014), p. 246001. DOI: `10.1103/PhysRevLett.112.246001`. URL: `https://link.aps.org/doi/10.1103/PhysRevLett.112.246001`.

[167] K. E. Jensen, D. A. Weitz, and F. Spaepen. "Local Shear Transformations in Deformed and Quiescent Hard-Sphere Colloidal Glasses". In: *Physical Review E* 90.4 (Oct. 10, 2014), p. 042305. ISSN: 1539-3755, 1550-2376. DOI: `10.1103/PhysRevE.90.042305`. URL: `https://link.aps.org/doi/10.1103/PhysRevE.90.042305` (visited on 11/19/2020).

[168] John Douglas Eshelby. "The determination of the elastic field of an ellipsoidal inclusion, and related problems". In: *Proceedings of the royal society of London. Series A. Mathematical and physical sciences* 241.1226 (1957), pp. 376–396.

[169] John Douglas Eshelby. "The elastic field outside an ellipsoidal inclusion". In: *Proceedings of the Royal Society of London. Series A. Mathematical and Physical Sciences* 252.1271 (1959), pp. 561–569.

[170] F. Graner et al. "Discrete Rearranging Disordered Patterns, Part I: Robust Statistical Tools in Two or Three Dimensions". In: *The European Physical Journal E* 25.4 (Apr. 2008), pp. 349–369. ISSN: 1292-8941, 1292-895X. DOI: `10.1140/epje/i2007-10298-8`. URL: `http://link.springer.com/10.1140/epje/i2007-10298-8` (visited on 01/24/2019).